

# Analysis and Quality Assessment of LEO GPS Data for Geophysical and Ionospheric Applications

Inauguraldissertation  
der Philosophisch-naturwissenschaftlichen Fakultät  
der Universität Bern

vorgelegt von

**Lucas Schreiter**

aus Deutschland

Leiter der Arbeit:

Prof. Dr. Adrian Jäggi  
Astronomisches Institut der Universität Bern

Co-Leiterin der Arbeit:

Prof. Dr. Claudia Stolle  
Deutsches Geoforschungszentrum Potsdam, Geomagnetismus  
und Universität Potsdam



This work is licensed under a  
<http://creativecommons.org/licenses/by-nc-nd/4.0/> International License.

---



# Scientific environment

The author has carried out the research reported in this dissertation at the Astronomical Institute of the University of Bern (AIUB) and Section 2.3 at the German Center for Geoscience (GFZ) in Potsdam.

This research project was funded by the Swiss National Science Foundation (SNSF) grant 200021\_169035: "Low Earth Orbiters and the Ionosphere's Stochastic Properties."



# Acknowledgements

I want to thank the Swiss National Science Foundation for funding this thesis. I would also like to acknowledge the University of Bern and GFZ Potsdam for hosting me during my thesis.

I also want to thank my supervisors Adrian Jäggi and Claudia Stolle, for their support, expertise, and opportunity to conduct this research. Special thanks are to Pieter Visser for his precise and constructive feedback on evaluating this work.

I want to thank Oliver Montenbruck, Christian Siemes, and Franz Zangerl as external collaborators. A large part of this work would have been impossible without their valuable input and contributions.

I am very thankful for the fruitful discussions and the input from my colleagues. Here I want to name the LEO group of the AIUB under the chair of Daniel Arnold for the productive discussions during the weekly meetings and the GPS group chaired by Rolf Dach. I also want to thank the colleagues from AIUB and GFZ, Section 2.3, for their help and support.

I also want to thank FFG, ESA, ISSI, and AUSTROSPACE for allowing me to participate in the Alpbach Summer School and the Post Alpbach Workshop. I also want to acknowledge the DFG for allowing me to join the SPP 1788 Meetings, Summer and Winter schools.





# Abbreviations

AIUB	Astronomical Institute of the University of Bern
ASU	Astronomical Institute of the Czech Academy of Science
BSW	Bernese GNSS Software
CHAMP	Challenging Minisatellite Payload
CODE	Center for Orbit Determination Europe
COSMIC	Constellation Observing System for Meteorology, Ionosphere and Climate
COSPAR	Committee for Space Research
COST-G	Combination Service for Time-variable Gravity Fields
CP	Counter-Rotation Processor
CRV	Code Range Variation
CU	Continuous Update
DCB	Differential Code Bias
DMSP	Defense Meteorological Satellite Program
DU	Discrete Update
EISCAT	European Incoherent Scatter Scientific Association
ERP	Earth Rotation Parameters
ESA	European Space Agency
ESR	EISCAT Svalbard Radar
FFT	Fast Fourier Transform
GFZ	German Research Centre for Geosciences Potsdam
GLONASS	Globalnaja Nawigazionnaja Sputnikowaja Sistema
GNSS	Global Navigation Satellite System
GOCE	Gravity field and steady state Ocean Circulation Explorer
GPS	Global Positioning System
GRACE	Gravity Recovery And Climate Experiment
hl-SST	High-Low Satellite to Satellite Tracking
HOI	Higher Order Ionosphere/Ionospheric
IfG	Institute for Geodesy, Hannover
IGG	Institute for Geodesy and Geoinformation, Bonn
IGS	International GNSS Service
ILRS	International Laser Ranging Service
IRI	International Reference Ionosphere
ITSG	Institute of Geodesy at Graz University of Technology
JPL	Jet Propulsion Laboratory

KBR	K-band Ranging System
KN	Kinematic
LEO	Low Earth Orbit
ll-SST	Low-Low Satellite to Satellite Tracking
LSA	Least Squares Adjustment
mlat	Magnetic Latitude
mLT	Magnetic Local Time
NCO	Numerically Controlled Oscillator
PCV	Phase Center Variation
(D)PLL	(Digital) Phase Lock Loop
POD	Precise Orbit Determination
RD	Reduced Dynamic
RINEX	Receiver Independent Exchange Format
ROT	Rate Of TEC
ROTI	Rate Of TEC Index
RPI	Rapid Plasmaspheric Imager
RUAG	Rüstung Unternehmen AG
SLR	Satellite Laser Ranging
TEC	Total Electron Content
TECU	TEC Unit ( $10^{16} el/m^3$ )
TL	Tracking Loop
TP	Tracking Processor
TUM	Technical University of Munich
URSI	International Union of Radio Science





# Contents

<b>Scientific environment</b>	<b>i</b>
<b>Acknowledgements</b>	<b>iii</b>
<b>Abbreviations</b>	<b>v</b>
<b>1 Introduction</b>	<b>1</b>
<b>2 The ionosphere and plasmasphere</b>	<b>5</b>
2.1 Ionization and recombination . . . . .	6
2.2 Altitudinal development . . . . .	6
2.2.1 Ion composition . . . . .	8
2.2.2 Profiler functions . . . . .	8
2.3 Frequencies . . . . .	9
2.4 Electron and ion drift . . . . .	10
2.5 Appleton anomaly . . . . .	10
2.6 Ionospheric plasma depletions . . . . .	12
2.7 Measurement types . . . . .	13
2.7.1 Radar . . . . .	13
2.7.2 Ionosonde . . . . .	14
2.7.3 Sounding rockets . . . . .	14
2.7.4 Satellites . . . . .	14
2.7.5 Ground-based GPS/GNSS . . . . .	15
2.8 Characterization of the topside ionosphere and plasmasphere . . . . .	15
2.8.1 IRI model . . . . .	15
2.8.2 NeQuick model . . . . .	16
2.8.3 Neustrelitz Plasmasphere Model . . . . .	17
2.8.4 TUM model approaches . . . . .	18
2.8.5 CODE TEC maps . . . . .	18

<b>3</b>	<b>Ionospheric effects on GNSS data</b>	<b>21</b>
3.1	Least-squares adjustment . . . . .	21
3.2	The Global Positioning System . . . . .	23
3.3	GLONASS . . . . .	24
3.4	Galileo . . . . .	24
3.5	Modeling the GPS/GNSS observables . . . . .	25
3.6	First and higher order ionospheric terms . . . . .	27
3.7	Computation of slant- and vertical TEC . . . . .	29
3.7.1	Melbourne-Wuebbena based screening . . . . .	30
3.7.2	Code range variation . . . . .	31
3.7.3	Mapping functions . . . . .	32
3.7.4	Leveling and bias estimation . . . . .	34
3.7.5	Error sources . . . . .	37
3.7.6	Rate Of TEC Index . . . . .	38
3.8	The International GNSS Service . . . . .	38
3.9	Bernese GNSS software . . . . .	39
<b>4</b>	<b>Low Earth Orbiters using GPS/GNSS</b>	<b>41</b>
4.1	CHAMP . . . . .	41
4.2	GOCE . . . . .	42
4.3	Swarm . . . . .	43
4.4	GRACE . . . . .	43
4.5	GRACE Follow-On . . . . .	44
4.6	Sentinel . . . . .	44
4.7	DMSP . . . . .	45
4.8	COSMIC . . . . .	46
4.9	COSMIC-2 . . . . .	46
<b>5</b>	<b>Precise orbit and gravity field determination using Low Earth Orbiters</b>	<b>47</b>
5.1	Measurement principles . . . . .	48
5.1.1	High-low-SST . . . . .	48
5.1.2	Low-low-SST . . . . .	48
5.1.3	Satellite based gradiometry . . . . .	49
5.1.4	SLR validation . . . . .	49
5.2	Gravitational acceleration . . . . .	50
5.3	Modeling satellite motion for LEO satellites . . . . .	52
5.4	Orbit representations . . . . .	54
5.4.1	Dynamic orbits . . . . .	54
5.4.2	Kinematic positions . . . . .	54

5.4.3	Reduced-dynamic orbits . . . . .	55
5.5	Orbit estimation . . . . .	55
5.6	Bernese Processing Engine for LEO POD . . . . .	57
5.7	Gravity field estimation . . . . .	58
5.8	Orbit differences and phase residuals . . . . .	59
5.9	Models and Settings used for Swarm . . . . .	59
5.9.1	Swarm Precise orbit determination . . . . .	60
5.9.2	Swarm Gravity field estimation . . . . .	60
5.10	Gravity field comparison . . . . .	61
5.11	Comparing the Swarm and GRACE monthly gravity fields . . . . .	62
<b>6</b>	<b>Identification and mitigation of problematic GPS observations</b>	<b>65</b>
6.1	Ionospheric artifacts in Swarm kinematic positions and gravity fields . . . . .	66
6.1.1	Radial variances . . . . .	68
6.1.2	Comparing to slant TEC . . . . .	72
6.1.3	AIUB standard screening . . . . .	72
6.2	Appropriate weighting of the GPS phase observations . . . . .	72
6.2.1	Computation of derivatives for the geometry-free linear combination . . . . .	73
6.2.2	Weights for the GPS phase observations . . . . .	74
6.2.3	Identification using the Rate of TEC index . . . . .	75
6.2.4	Geographical restriction of down-weighting . . . . .	77
6.2.5	Combination of methods . . . . .	77
6.3	Gravity field recovery using weighted GPS data . . . . .	77
6.3.1	GPS-only Gravity field recovery using weighted GPS data . . . . .	77
6.3.2	Weighted observations . . . . .	79
6.3.3	Orbit . . . . .	83
6.3.4	Covariances . . . . .	83
6.3.5	SLR validation . . . . .	87
6.3.6	Weighted observations and solar activity . . . . .	90
6.4	ROTI modification for identifying equatorial plasma depletion . . . . .	91
6.4.1	qROTI/ROTI in equatorial regions . . . . .	92
6.4.2	Comparing qROTI to IBI . . . . .	93
6.4.3	Distribution in geomagnetic latitude and local time . . . . .	94
<b>7</b>	<b>GPS/GNSS tracking using Phase Lock Loops</b>	<b>99</b>
7.1	Digital Phase Lock Loops (DPLL) design . . . . .	99
7.1.1	Discrete update loops . . . . .	100
7.1.2	Continuous update approximation . . . . .	100
7.1.3	L1 aided L2 tracking . . . . .	101

7.2	Swarm loop filter characterization . . . . .	103
7.2.1	Simulation . . . . .	105
7.2.2	Transfer function approximation . . . . .	105
7.2.3	Loop filter inversion . . . . .	109
7.2.4	Correction of the L2 phase observable . . . . .	109
7.3	Impact on orbit and gravity field determination . . . . .	111
<b>8</b>	<b>Measuring and modelling the ionosphere using LEO-GPS</b>	<b>121</b>
8.1	Topside formulation . . . . .	122
8.2	Model approach . . . . .	124
8.2.1	Consideration regarding slant TEC . . . . .	125
8.2.2	Tracing and integration . . . . .	126
8.2.3	Order of the numerical integration . . . . .	127
8.2.4	Parameters . . . . .	127
8.2.5	Parameter estimation . . . . .	129
8.2.6	Regularization . . . . .	130
8.3	Results . . . . .	131
8.3.1	Quality of fit . . . . .	132
8.3.2	Choice of regularization parameter . . . . .	132
8.3.3	Evaluation of electron density using IRI . . . . .	135
8.3.4	Evaluation of electron density using DMSP . . . . .	137
8.3.5	Comparison to CODE TEC maps . . . . .	137
8.3.6	Storm response . . . . .	139
8.3.7	P1-P2 receiver bias . . . . .	140
8.3.8	Geometry-free PCV maps . . . . .	141
8.3.9	Outlook . . . . .	143
8.4	Application: Tomography using Swarm . . . . .	143
8.4.1	Ray geometry . . . . .	144
8.4.2	Removing the topside . . . . .	144
8.4.3	Mapping and masking . . . . .	146
8.4.4	Algorithm description and reconstruction . . . . .	146
<b>9</b>	<b>Summary, Conclusions and Outlook</b>	<b>151</b>
	<b>Bibliography</b>	<b>155</b>
	<b>Publications</b>	<b>179</b>

# List of Figures

2.1	Temperature and ionization profiles [Kelley, 1989]	7
2.2	Chemical composition with altitude [Kelley, 1989].	7
2.3	Electron and ion drift depending on collision frequency and electric field [Kelley, 1989].	10
2.4	Plasma drift in $\mathbf{E} \times \mathbf{B}$ direction at the magnetic equator and gradient driven plasma drift along the magnetic field lines [Kelley, 1989].	11
2.5	CODE global ionosphere map for the 1st of March 2015 8:00 UT. The Appleton anomaly is visible as a the double peak near the geomagnetic equator.	11
2.6	Vertical drift as observed by the Jicamarca radio observatory (Peru) [Kelley, 1989].	12
3.1	Sky plot of the sum of the higher order ionospheric corrections for the ionosphere-free (left) and the geometry-free (right) linear combination. An azimuth of $0^\circ$ equals geographic north.	29
3.2	Melbourne Wuebbena and differences of mean values over time windows of 2 s, 10 s, and 20 s (bottom) for Swarm A GPS observations of PRN G01, on 1st of March 2015. The Melbourne-Wuebbena linear combination was centered around 0.	31
3.3	P1 Code range variation maps for GRACE-A and GRACE-B in Azimuth and Elevation. The strong pattern in the GRACE B CRV map is related to the occultation antenna switched on.	33
3.4	Determination of the ionospheric pierce point and zenith angles [Schaer, 1999].	34
3.5	Single layer, modified single layer, and slab layer mapping function.	35
3.6	Simulated DCB estimation for assumed 1 Hz sampling with 2000 pairs (orange) and 0.1 Hz sampling wit 200 pairs (blue) using 1000 simulated estimatios. The true bias is 3 TECU.	37
4.1	Artist's impression of the CHAMP satellite [DLR, 2020a].	41
4.2	GOCE (left [ESA, 2020b]) and Swarm (right [ESA, 2020f]).	42
4.3	GRACE (left [NASA, 2020]) and GRACE-FO (right [JPL, 2020]).	43

4.4	Sentinel-1 (left [ESA, 2020g]), Sentinel-2 (center [ESA, 2020h]), Sentinel-3 (right [ESA, 2020i]). . . . .	44
4.5	DMSP-5P Satellite [NOAA, 2020]. . . . .	45
4.6	COSMIC (left [NSPO, 2020]) and COSMIC-2 (right [UCAR, 2020]). . . . .	46
5.1	Definition of the orbital elements $a, e, i, \Omega, \omega, u(t_0)$ and the state vector $\mathbf{r}(t), \dot{\mathbf{r}}(t)$ [Prange, 2010]. . . . .	53
5.2	Scheme of the POD for LEO satellites at AIUB (following Jäggi [2006]). . . . .	58
6.1	Geoid height differences between the monthly Swarm GPS-only gravity field and the JPL-GRACE-RL06 for March 2015. . . . .	66
6.2	Radial differences between Swarm reduced dynamic orbits and kinematic positions for Swarm A and Swarm C (top). The bottom plot shows the ambient plasma density as measured by the Swarm Langmuir probes. . . . .	67
6.3	Ionosphere-free phase residuals of Swarm A reduced dynamic orbits (top) and first (D1), second (D2) and third (D3) time derivatives of the geometry-free linear combination using smoothing and a Savitzky-Golay filter for 1st of November 2014 (doy 305). . . . .	68
6.4	Mean radial variances (left) and mean spreading of phase residuals (right) in magnetic coordinates for the analyzed test period. . . . .	69
6.5	Radial variances binned for a longer time span in geographic coordinates, Nov. 2013 - Dec. 2017. . . . .	71
6.6	Percentage of rejected GPS-observations rejected in the preprocessing for the analyzed test period. Left: geographic coordinates, right: magnetic coordinates. . . . .	71
6.7	Tests on synthetic data for the first (D1), second (D2), and third (D3) time derivative of the geometry-free linear combination. Red points show the true analytic noise-free derivative, green the computed derivatives from noisy data using the filter settings from Tab. 6.1 and blue points the three-point derivative scheme. The noise in the second and third plots, visible as blue points, exceeds the axis's limit. The right side shows a zoom to compare the true derivative with the Gauss-Savitzky-Golay filtered derivative. . . . .	74
6.8	From top to bottom: Ionosphere-free phase residuals, AIUB-ROTI variance, Graz-ROTI variance, and AIUB-ROTI combined with the second derivative. The time span from 1.8 h UT to 2.0 h UT corresponds to an equatorial pass, and from 2.1 h UT to 2.4 h UT corresponds to a polar pass. The ROTI variances are larger at the polar region. The second derivative with a fixed sigma square exceeded the threshold (bottom) in near-equatorial regions. Only variance unequal to $1\text{mm}^2$ were plotted. . . . .	76

6.9	Two years (2015/2016) of monthly Swarm gravity fields for Swarm A and Swarm C compared to monthly JPL GRACE-RL06 solutions using the wRMS. With and without applying weights. Because of ground track resonance in January and February 2015, the more robust CSR GRACE-RL06 solution [Bettadpur, 2018] is used for these two months . . . . .	80
6.10	Geoid height differences between monthly Swarm A gravity field to the corresponding JPL-GRACE-RL06 solution for March 2015. Gravity field differences were computed up to degree 70. . . . .	81
6.11	Difference (solid lines) and formal error (dashed lines) degree Amplitude for monthly Swarm A gravity field w.r.t. AIUB-GRACE03S, March 2015. . . . .	82
6.12	Percentage of weighted raw GPS measurements for the analyzed test period binned to the corresponding LEO position. Top: first derivative D1 $L_{GF}$ (left), second derivative D2 $L_{GF}$ (right), middle: third derivative D3 $L_{GF}$ (left), ROTI>2 mm <sup>2</sup> (right), bottom: ROTI>5 mm <sup>2</sup> . Bin-size 1° mlat × 0.2 h mLT. . . . .	84
6.13	Kinematic minus reduced dynamic positions in radial, along- and cross-track direction. For both, kinematic and reduced dynamic positions, the same weighting was applied. . . . .	85
6.14	Differences between the uniformly weighted positions of reduced dynamic (left) and kinematic (right) orbits. All orbits were compared to the uniformly weighted case. . . . .	86
6.15	Number of kinematic positions for the analyzed test period, un-screened (left) and with AIUB standard screening (right). Binned in 1° × 1° grid. . . . .	88
6.16	Radial variances for the analyzed test period, global. Top: AIUB standard screening (left), AIUB-ROTI (right), bottom: Graz-ROTI (left), second derivative (eq.)+AIUB-ROTI (right). The clearly visible ground track (top, left) is due to a large RMS for Swarm A, 29th of March 2015 . . . . .	88
6.17	Radial variances in magnetic coordinates. Top: AIUB standard screening (left), AIUB-ROTI (right), bottom: Graz-ROTI (left), second derivative (eq.)+AIUB-ROTI (right). . . . .	89
6.18	Percentage of screened position in comparison to the $F_{10.7}$ and $K_p$ indices. . . .	91
6.19	Classical ROTI and qROTI under quiet conditions (top). In situ plasma density measurements (bottom). The equatorial ionization anomaly is clearly visible, but no depletions. The response of the classical ROTI approach may be seen near the ionization peaks. . . . .	93
6.20	ROTI and qROTI response to a severe plasma depletion (top). In situ plasma density measured by the Swarm Langmuir probes (bottom). The depletion is clearly visible in both ROTI approaches. . . . .	94
6.21	GBI compared to IBI for the same time window as shown in Fig. 6.20. . . . .	95

6.22	Relative number of detections binned by $1^\circ$ in latitude and $2^\circ$ in longitude for the IBI-index (left) and the derived GBI index (right), November 2014. . . . .	96
6.23	Relative number of detections binned by $1^\circ$ in magnetic latitude and 12 min in magnetic local time for the IBI-index (left) and the derived GBI index (right), November 2014. . . . .	97
6.24	Relative number of GBI detections made by GOCE binned by $1^\circ$ in latitude and $2^\circ$ in longitude (left) and in magnetic coordinates binned in $1^\circ$ in magnetic latitude and in 12 min in magnetic local (right), November 2011. . . . .	97
7.1	Model of a DPLL including separation in CP and TP, from Thomas [1998]. . . . .	101
7.2	Simplified tracking processor with third-order loop filter, adopted from Fig. 3.1 in Thomas [1998]. . . . .	104
7.3	Amplitude and phase response for the different L1 TL setting used by the Swarm receivers. . . . .	106
7.4	Amplitude and phase response for the different L2 TL setting used by the Swarm receivers. . . . .	107
7.5	TL response and differences for different bandwidths to a synthetic cosine-shaped pulse. . . . .	108
7.6	Amplitude and phase response for the $B_L = 0.25$ Hz for the empirical transfer function, CU approximation and the fitted transfer function. . . . .	109
7.7	Inversion of the $B_L = 0.25$ Hz loop filter using the inverse transfer function with 1 Hz data sampling. . . . .	110
7.8	Impact of four different methods to treat the edges (Swarm A, 1st of March 2015) for G01. Option 1: no extrapolation, Option 2: 300 seconds of zero values, Option 3: point mirroring at the edges, Option 4: 60 second linear polynomial with 10 second blending. . . . .	112
7.9	TL corrections scaled to IF linear combination and IF Phase residuals for G01 and G23 to a reduced dynamic orbit for Swarm A, 1st of November 2014. . . . .	113
7.10	Number of observation usable for reduced dynamic orbit fit. . . . .	114
7.11	Posteriori RMS reduced dynamic orbit (left) and kinematic orbit (right) fit. . . . .	115
7.12	Number of ambiguities set up. . . . .	116
7.13	Geoid height differences for a Swarm A GPS-only gravity field solution compared to the monthly GRACE JPL-RL06 solution. The original reference scenario is shown on the left, based on L2 corrected RINEX files in the middle and the gravity field obtained using weighting on the right. . . . .	119
7.14	Difference- (solid) and error degree (dashed) amplitude for a Swarm A GPS-only gravity field solution for March 2015 (left) and a Swarm C GPS-only gravity field for August 2015 (right). . . . .	120



8.1	Changes in the profile function when adjusting the parameters $hm$ , $H_0$ , and $\alpha$ . $Nm$ is fixed to $e^{10}/4 \text{ m}^{-3}$ , $H_0 = 50 \text{ km}$ , $\alpha = 1$ and $hm = 350 \text{ km}$ unless varied.	124
8.2	Relative numerical integration error tested on Epstein layer function. Note that in case of the separate integration the number of support points in each interval is the number of function evaluation divided by 2.	128
8.3	Positions of the sampled points in mlat/mLT for 2nd of July 2019 from 00:00 UT to 03:00 UT. The blue dots originate from the CODE TEC map, which is a rough constraint for the large unobserved areas. Furthermore, the figure includes the satellites from Tab. 8.1. This includes Sentinel 1 A/B, 2 A/B, 3 A/B as S1A, S1B, S2A, S2B, S3A, S3B, Swarm A/B/C as A, B, C, and GRACE-FO as GC and GD.	131
8.4	Norm of post-fit residuals compared to the norm of the scaled parameter vector. The black line indicates the mean values. Solution for the 1st and 2nd of July 2019 considered.	133
8.5	Observed TEC versus model TEC for Swarm A and Sentinel 3A (2nd of July 2019, doy 183).	133
8.6	Differences between observed and model TEC versus elevation. 2nd of July 2019 from 00:00 UT to 03:00 UT.	134
8.7	Electron density predicted by the IRI model (left) and by the LEO GPS reconstruction at an altitude of 500 km. For 2nd of July 2019 valid from 03:00h to 06:00h.	135
8.8	Electron density difference in percent relative to IRI at an altitude of 500 km. For the 2nd of July 2019 valid from 03:00h to 06:00h.	136
8.9	DMSP observations compared to IRI-2016 Electron density and the model predictions, 1nd of July 2019. The correlation between observations and IRI is 86 %, whereas to the proposed model the correlation is 83.5 %.	138
8.10	TEC of the CODE TEC map (left) and the proposed model (right) for 2nd of July 2019, at 01:30 UT. Evaluated from 90 km to approximately GPS altitude (20000km). White areas in the CODE TEC map are negative values.	138
8.11	Estimated global TEC map for 4th (left), 5th (middle), and 6th (right) of August 2019, at 12:00 UT.	139
8.12	Estimated electron density for 4th (left), 5th (middle), and 6th (right) of August 2019, at 12:00 UT and 500 km altitude.	139
8.13	Estimated Receiver biases for Sentinel 1A/1B/2A/2B/3A/3B, Swarm A/B/C and GRACE C/D. Also the estimated offsets for the CODE TEC maps are shown. Time period used: 1st of July 2019, 00:00 UT to 03:00 UT.	140
8.14	Ionosphere-free (top, left), geometry-free (top, right), L1 (bottom, left) and L2 (bottom, right) PCV maps. July and August 2019.	142
8.15	Observational scenario for tomography using a vertical grid.	144

8.16	Real observational scenario with boxes increasing exponentially in height for Swarm A, 2nd of November 2014. Equator crossing at 1:12 UT. The rays were mapped to the vertical plane. . . . .	145
8.17	GPS TEC observed by Swarm with and without plasmaspheric electron content. 10th of May 2017, equatorial pass at 2:40 UT (9:05 LT) . . . . .	146
8.18	Rejected observations(red) and accepted observations (blue) with respect to elevation and azimuth. . . . .	147
8.19	Electron density of the reconstruction before MART is applied, based on Langmuir probe measurements at the bottom-side of the reconstruction plane (10th of May 2017). . . . .	149
8.20	MART applied to unweighted (left) and weighted (right) Swarm GPS observations using the prior given by the Langmuir probes (10th of May 2017). . . . .	149

# List of Tables

6.1	Filter settings . . . . .	73
6.2	Gravity field evaluation and SLR-Residuals statistics for Swarm A, March 2015. . . . .	79
6.3	Gravity field evaluation and SLR-Residuals statistics for Swarm A, June 2016. . . . .	79
6.4	Correlation coefficient between the relative number of weighted observations and the $F10.7$ index. . . . .	91
6.5	Local time at middle of the month . . . . .	92
7.1	PLL TL bandwidths of the Swarm satellites [ESA, 2015a,b, 2016, van den IJssel et al., 2016]. . . . .	103
7.2	Third-order DPLL loop coefficients ( $K_1$ , $K_2$ , $K_3$ ) for different design bandwidths $B$ based on Stephens and Thomas [1995]. The values apply for rate-only numerically controlled oscillator (NCO) updates, super-critical damping, and a one-step computational delay. For comparison, continuous-update loop coefficients $\omega_0$ , $a$ , and $b$ as defined in Ward et al. [2006] are provided for the respective update intervals $T$ (see Eq. 7.16) . . . . .	105
7.3	SLR residual statistics for March 2015, Swarm reduced dynamic orbits. . . . .	115
7.4	SLR residual statistics for March 2015, Swarm kinematic orbits. . . . .	116
7.5	SLR residual statistics for Aug. 2015, Swarm reduced dynamic orbits. . . . .	116
7.6	SLR residual statistics for Aug. 2015, Swarm kinematic orbits. . . . .	117
7.7	SLR residual statistics for Nov. 2016, Swarm reduced dynamic orbits. . . . .	117
7.8	SLR residual statistics for Nov. 2016, Swarm kinematic orbits. . . . .	117
7.9	Gravity field comparison for March 2015 . . . . .	119
7.10	Gravity field comparison for August 2015 . . . . .	120
8.1	Observation types used for fitting the topside ionosphere-plasmasphere model. The in situ plasma density is taken from the Swarm Langmuir Probes. The $N_e$ values obtained by the Langmuir probes are corrected by the factors published in Lomidze et al. [2018]. . . . .	125

8.2	Correlation coefficient for different regularization parameters $\lambda$ between the derived model and DMSP observations for 2nd of July 2019. . . . .	134
-----	---	-----

# Chapter 1

## Introduction

The ionosphere is of dispersive nature for electromagnetic waves as they are used for signal transmission in Global Navigation Satellite Systems (GNSS). Since its impact on pseudorange or carrier phase measurements obtained using GNSS is frequency-dependent, typically, a dual-frequency combination is used to largely eliminate the ionosphere's impact in geodetic applications. Still, even when using dual-frequency observations, the so-called higher-order ionospheric terms can not be eliminated. Besides, side effects introduced by the ionospheric signal content's temporal dynamics may occur depending on the implementation of the tracking processor.

For many Low Earth Orbit (LEO) satellite missions, a geodetic type dual-frequency GPS/GNSS receiver is used to obtain highly accurate three-dimensional positions on the centimeter level. Such accurate positions are primarily required for altimetry missions and also allow to derive GPS-only gravity field solutions. In a near-earth environment with the presence of ionized plasma, such accuracy can not be achieved using single-frequency GNSS observations. In turn, the dual-frequency may also be used to mitigate and quantify the ionospheric code delay or phase advance. This information then can be converted into a slant measurement of the total electron content along the line of sight between the LEO satellite receivers and the GPS satellite transmitters. A large fleet of LEO satellites in operation nowadays allows for three-dimensional monitoring and quantifying the plasma-density in the upper ionosphere and plasmasphere. This application is of particular interest since the available observations apart from GPS/GNSS are sparse and of limited geographical coverage, e.g., radar measurements and rocket sounding, or they can only reach up to the ionization peak as is the case for ionosonde measurements.

In this work, first the theoretical background is addressed. This includes the ionosphere, the measurement technique, important satellite missions and the background on orbit and gravity field estimation. Three specific topics have been investigated. The first topic is about ionospheric artifacts and their mitigation for Swarm gravity field determination (Chap. 6). It will be briefly introduced, how those artifacts can be observed by comparing the Swarm gravity fields to more

accurate solutions obtained by other missions. This issue is approached by investigating the origin of those artifacts. Appropriate criteria are developed based on derivatives of linear combinations to identify suspicious phase observations and to derive appropriate empirical weights in order to mitigate their impact on orbit and gravity field solutions. The obtained results are again evaluated by comparing Swarm gravity fields to superior GRACE solutions. In addition, a criteria used for weighting of GPS observations is further developed to identify ionospheric plasma depletions.

The second topic investigates the technical cause for tracking related errors for the Swarm GPS receiver (Chap. 7). The aim is to better understand the cause of the phenomenon addressed in Chap. 6. The methods are introduced, that are specifically used for the correction and inversion in frequency space using the tracking loop specific transfer-function. They are refined by comparing to phase residuals from the orbit processing. Eventually, as a result the impact on orbit and gravity field estimation is studied.

The third topic is to estimate topside electron density from LEO GPS observations (Chap. 8). The methods presented here contain the model design, as well as considerations on how to compare slant TEC values to the model electron density. The results obtained from the estimation are compared to independent measurements and models. Finally, it will be shown, how ionospheric tomography benefits from a plasmasphere model and how the results from Chap. 6 can be utilized to improve the tomography.

Consequently, the key questions for the presented investigations are:

- How can unreliable GPS phase observations be identified ahead of orbit processing and how can their impact be mitigated?
- What causes the artifacts in the Swarm-GPS observations? Is this behaviour deterministic and can it be corrected?
- Can LEO GPS TEC significantly help to better observe the topside ionosphere? Can LEO satellites be used to generate three-dimensional extensions of global TEC maps?

Let us conclude with an outline of the subsequent chapters:

Chapter 2, *The ionosphere and plasmasphere*, is a short introduction to the basic properties and underlying physical processes in the upper atmosphere, causing the ionosphere and plasmasphere formation. Some basic features like the Appleton anomaly, post-sunset plasma depletions in the equatorial ionosphere, referred to as plasma bubbles, will be briefly explained because they are known to affect GPS/GNSS measurements. A small overview of measurement techniques to determine the state of the ionosphere together with their limitations is given to point out where the largest benefit is expected when making use of space borne GPS/GNSS receivers on-board LEO satellite missions.

- 
- Chapter 3, *GPS/GNSS ionosphere interactions*, is pointing out the basic principles of GPS/GNSS positioning and the impact of ionized plasma on the code and phase observations. Also, the composition of the ionospheric part in the observational equations is studied in detail to estimate its impact on common linear combinations. It is also addressed that the provided observations in the observation files may be affected by the pre-processing performed ahead of publication. Besides, this chapter includes a short outline on least-squares adjustment.
- Chapter 4, *Low Earth Orbiters using GPS/GNSS*, introduces the different satellite missions used in the subsequent chapters. Their mission concepts will be outlined together with their orbit characteristics and their key instruments. Different measurement scenarios will be presented as well.
- Chapter 5, *Precise orbit and gravity field determination using Low Earth Orbiters*, outlines the methods used to obtain precise reduced-dynamic and kinematic orbits from zero-difference GPS data. The GPS carrier phase residual screening will be discussed in more detail. Satellite Laser Ranging (SLR) measurements will be used for the validation of the computed orbits. Furthermore, this chapter recapitulates the Celestial Mechanics Approach (CMA) used to determine gravity fields. Other measurement principles like the GOCE gradiometer or the GRACE(-FO) K-band Ranging System (KBR) are briefly introduced since gravity field solutions using these methods are used as a reference due to their superior quality compared to GPS-only solutions.
- Chapter 6, *Identification and mitigation of problematic GPS observations*, shows how presumably erroneous GPS observations affect the orbit solutions and propagate into the gravity field solutions for the GOCE and Swarm Mission. Criteria are developed to identify these GPS observations based on the geometry-free linear combination of the original dual-frequency carrier phase observations. Weights will be derived and introduced to mitigate their impact on the orbit and gravity field solutions. In addition, an approach is derived to identify ionospheric plasma depletions in the GPS phase observables for the GOCE and Swarm missions.
- Chapter 7, *GPS/GNSS tracking using phase lock loops*, discusses the tracking GPS/GNSS phase observables using phase lock loops. This tracking scenario is implemented for the Swarm GPS receivers and presumably also for several other GPS/GNSS receivers. For the Swarm mission, the implementation details are provided. It is demonstrated how the tracking responds to ionospheric stimuli, and also a loop filter inversion is performed to recover an estimate of the true phase observation. Eventually, the benefits of using corrected GPS data for obtaining orbit and gravity field solutions are demonstrated.
- Chapter 8, *Measuring and modeling the ionosphere using LEO-GPS*, points out how the GPS-TEC measurements obtained by LEO satellites may be used to generate a three-dimensional model of the topside ionosphere and plasmasphere. Special emphasis is given to the absolute lev-

eling of slant TEC measurements. The model developed in this chapter is making use of several LEO constellations, among others Swarm, GRACE-FO, and the Sentinel fleet, to obtain the altitude dependency. A simple tomographic approach for Swarm is exercised. The ionosphere's topside model may be used to remove the plasmaspheric contribution of the observed slant TEC to improve the tomography.

Chapter 9, *Summary, Conclusions, and Outlook*, summarizes the essential results and conclusions of this work.



## Chapter 2

# The ionosphere and plasmasphere

The essential sources of ionization and the plasma dynamics in the upper atmosphere are this chapter's topics. The primary source of information presented in this chapter is the book "The Earth's Ionosphere", [Kelley \[1989\]](#). In the upper atmosphere, the molecules are ionized by solar radiation, mainly in the extreme ultraviolet (EUV) and X-ray spectrum. The radiation density increases with altitude because of less radiation being absorbed in higher altitudes. The atmospheric density decreases with altitude and, in turn, limits the electron and ion density in higher altitudes. Consequently, the electron density profile shows a peak at a height where the ionization maximizes. The electron density equals approximately the ion density and will thus be used to describe the plasma density. The chemical composition, however, is not homogeneous. These different compositions cause different ionization and recombination rates with altitude. Depending on those properties, the electron density profile may be separated into various layers concerning their day-night characteristics in ionization/recombination rates, chemical composition, and altitude.

The Earth's atmospheric layer that ranges from roughly 80 km up to 1000 km contains weakly ionized plasma ( $\sim 0.1\%$  ionization [[Kelley, 1989](#)]) and is called the ionosphere. Ranging up from roughly 1000 km to a few Earth radii (2-5) and mostly also bound to magnetic field lines, a weakly ionized, co-rotating plasma is present, called the plasmasphere. The height, at which  $H^+$  becomes the dominant ion species, is usually used to define the transition between the ionosphere and plasmasphere. For many applications, a fixed transition altitude is considered (e.g., 1000 km [Jakowski and Hoque \[2018\]](#)). Several processes contribute to the state of the ionosphere and plasmasphere. There is the generation of ions, primarily due to photo-dissociation, the recombination, neutral winds, and also up and down-welling, which may cause changes in the ion composition and several other phenomena like plasma depletions or polar patches (e.g., [Kelley \[1989\]](#), [Rodríguez-Zuluaga et al. \[2019\]](#), [Spicher et al. \[2015\]](#)) The ionization process is primarily solar-driven. Transport processes are driven via neutral winds, which are caused by thermal expansion and are thus, to a large extent, also solar driven. In polar regions also ionization by particle precipitation (e.g. polar patches) is present. The conductivity can change drastically between day

and night side, depending on the ion composition and the recombination rates. In addition, instabilities like for example equatorial plasma bubbles can occur (e.g. [Whalen \[2000\]](#), [Stolle et al. \[2006b\]](#)). Also, external forcing from atmospheric waves caused by earthquakes or the plasmasphere's compression may travel through the ionosphere and affect the electron density distribution [[Chen et al., 2011](#), [Tanimoto et al., 2015](#)]. Such processes cause the ionosphere to have a high variability concerning day and night, seasonal, daily, and down to time scales of seconds. In the plasmasphere on top of the ionosphere, less variability is caused by ionization and recombination than in the ionosphere. However, external forcing caused by the solar wind becomes a key driver [[Jakowski and Hoque, 2018](#)]. This chapter will shortly describe the ionosphere and plasmasphere and introduce the altitude profiles of electron density. Two of the most prominent phenomena that can be well observed using GPS/GNSS will be explained in more detail: The ionization crest near the geomagnetic equator, a day-side feature, visible as two prominent peaks, and plasma depletions that are known to scatter electromagnetic waves [[Kintner et al., 2007](#)]. The first causes large-scale spatial gradients in electron density, whereas the latter exists in both, the equatorial and polar regions. The depletions typically extend from several hundreds of kilometers down to a few kilometers [[Xiong et al., 2016a](#)]. Measurement techniques will be briefly discussed to outline where ionospheric observations obtained by Low Earth Orbiting (LEO) satellites can contribute most and point out limitations of specific measurement types.

## 2.1 Ionization and recombination

The two primary sources for ionization are photo-ionization and ionization due to high energetic particles. Photo-ionization is present on the day-side, whereas the latter occurs at the polar regions and near the South Atlantic Anomaly [[Mironova et al., 2019](#), [Zmuda, 1966](#)]. Wavelengths carrying sufficient energy to separate an electron from an atom or molecule are in the ultraviolet, X-ray, or higher energetic spectrum. For several applications, the F10.7 index is used to predict ionization. The index is the radiation density at a wavelength of 10.7 cm. The wavelength is too long to perform ionization. However, it is a well-established proxy to predict solar activity and the impact of radiation having shorter wavelengths on the Earth's atmosphere.

## 2.2 Altitudinal development

The chemical composition of the ionosphere is mostly determined by the altitude and the respective scale height. The scale height defines the height, where the gas density is reduced by a factor of  $1/e$ . The scale height may be expressed as a solution of the hydro-static differential equation

$$dP = -\rho g dz, \quad (2.1)$$

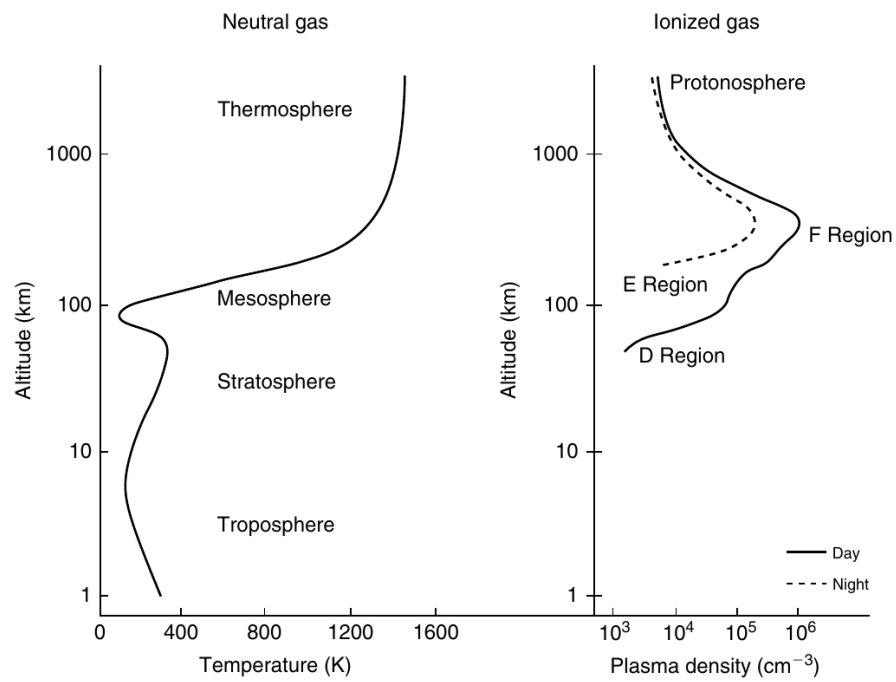


Figure 2.1: Temperature and ionization profiles [Kelley, 1989]

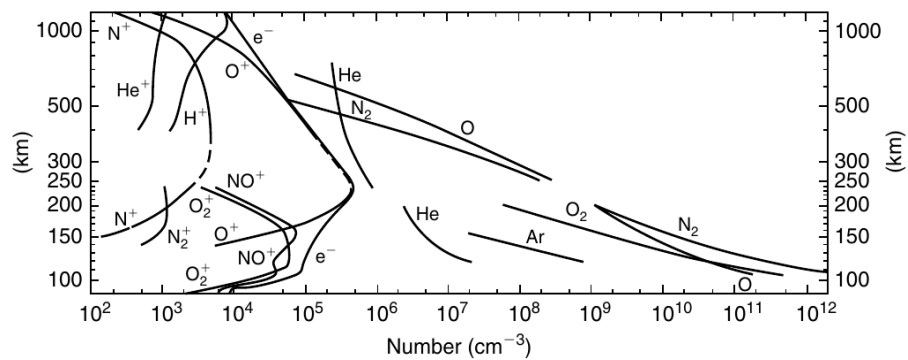


Figure 2.2: Chemical composition with altitude [Kelley, 1989].

where  $P$  is the pressure,  $\rho$  the density, and  $g$  the gravitational acceleration. The measure  $dz$  is the increment with altitude. With

$$P = \frac{\rho}{\mu m_H} k_B T, \quad (2.2)$$

where  $m_H$  is the mass of a hydrogen atom,  $\mu$  is the average mass of the particles in the gas,  $k_B$  is the Boltzmann constant, and  $T$  is the temperature in Kelvin. The solution to the differential equation is thus given as

$$P = P_0 e^{-\frac{\mu m_H}{k_B T} z} = P_0 e^{-\frac{z}{H}}, \quad (2.3)$$

with  $P_0$  being the pressure at altitude  $h_0$  and the scale height  $H = \frac{k_B T}{\mu m_H}$ . From that equation, two conclusions may be drawn. First, the lighter the gas molecules' mass, the larger the scale height, and consequently, lighter molecules reach larger altitudes. Therefore hydrogen is dominating in high altitudes (see Fig. 2.2). Besides, also the temperature has an impact. The higher the temperature, the larger the scale height and thus implying an expansion of the atmosphere.

### 2.2.1 Ion composition

The ion composition depends on the chemical composition that also defines the recombination rates. Most of the ions are generated by photo-dissociation, which takes place on the day-side. The ionization is counteracted by recombination. The recombination-rate depends on the chemical composition. Molecular oxygen, e.g., recombines much faster than atomic oxygen. Since the composition is altitude-dependent, this leads to layers of different characteristics. The highest layer, called F-layer, is present during day and night with only small electron density changes. Below the F-layer, the E-layer is located. In the E-layer, the ionization maximizes during the day but because the dominant ion species are ions of molecular oxygen ( $O_2^+$ ) it recombines after sunset almost immediately. Therefore the ionization in the E-layer shows a strong variability concerning the day- and night-side. This can also be seen in Fig. 2.1. Below 100 km, the D-layer is located, which is only existing on the day-side. Sometimes the F-layer is again separated into  $F_1$ - and  $F_2$ -layer, depending on the altitude regions.

### 2.2.2 Profiler functions

Two classical profiler functions are introduced: The formulation of the density profile as Chapman layer and the Epstein layer function. For the sake of simplicity, the reduced height is used,

$$z = \frac{h - h_m}{H}, \quad (2.4)$$

where  $h$  is the altitude,  $h_m$  is the altitude of the layers maximum electron density and  $H$  is the scale height. The electron density  $N_e$  in the Chapman layer [Chapman, 1931, Pi et al., 2008] is

described as

$$N_e(z) = N_m e^{k \cdot (1 - z - e^{-z} \sec(\chi))}, \quad (2.5)$$

where  $\sec(\chi) = 1/\cos(\chi)$  is the secant function.  $N_m$  is the maximum electron density at altitude of the peak  $h_m$  and  $\chi$  is the solar zenith angle. For  $k = 1$  the layer is called  $\alpha$ -Chapman layer, for  $k = 0.5$  the layer is called  $\beta$ -Chapman layer [Anderson et al., 1987, Olivares-Pulido et al., 2016]. The assumptions for the Chapman layer are only one type of gas, monochromatic light with parallel beams and a constant scale height of the gas density. The Chapman profile is derived by comparing the ionization rate to the gas density. The gas density drops with altitude. In contrast, the intensity of radiation increases with altitude as less absorption takes place. Eventually, a layer having an ionization peak at a specific altitude and an exponential decay in higher altitudes is formed.

A second commonly used function to describe the electron density profile is the semi-Epstein layer [Rawer, 1983, Pezzopane and Pignalberi, 2019]. For the Epstein layer the electron density is expressed using

$$N_e(z) = 4N_m \frac{e^z}{(1 + e^z)^2}. \quad (2.6)$$

This expression is widely used, e.g., in the NeQuick topside modeling [Radicella and Zhang, 1995].

## 2.3 Frequencies

Two frequencies describing the plasma are of particular interest for the propagation of electromagnetic waves: First, the plasma frequency  $f_p$ , which directly depends on the electron-density  $N_e$ . The plasma frequency is important for the higher-order ionospheric terms in signal propagation, the altitude of reflection for ionosonde measurements, and calibrating Langmuir probes. The gyro-frequency also impacts the higher-order ionospheric terms and impacts the direction of motion of the plasma drift.

$$f_p^2 = \frac{e^2 N_e}{4\pi\mu_0 m_e} = A_p N_e, \quad (2.7)$$

and second the gyro-frequency  $f_g$  in presence of a magnetic field

$$f_g = -\frac{e}{2\pi m_e} B = A_g B. \quad (2.8)$$

Here  $e$  is the electron charge,  $m_e$  is the electron mass,  $\mu_0$  is the permeability of free space and  $B$  the strength of the magnetic field. The value of the constants is  $A_p = 80.62 \text{m}^3 \text{s}^{-2}$  and  $A_g = 2.8 \cdot 10^{10} \text{sA/kg}$ .

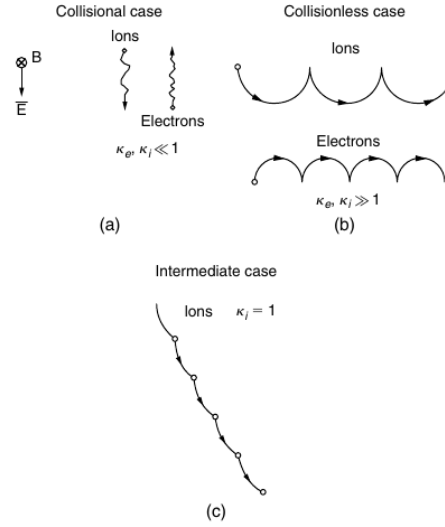


Figure 2.3: Electron and ion drift depending on collision frequency and electric field [Kelley, 1989].

## 2.4 Electron and ion drift

The frequency of collisions with neutral molecules  $f_c$  and the gyro-frequency  $f_g$  are relevant to explain the electron and ion drift. The ratio  $\kappa = f_g/f_c$  defines the direction of motion for ions and electrons. In case the collision frequency tends to infinity, many collisions occur and the motion for electrons and ions is defined by the electric field (see Fig. 2.3). In a collision-free plasma  $\kappa$  tends to infinity. If a particle with charge  $q$  is moving the Lorentz force  $\mathbf{F}_l = q \cdot (\mathbf{v} \times \mathbf{B})$  is forcing the particle on a circular trajectory. Only a half-circle can be performed due to the electric field present, and the motion is reinitialized. This results in half-cycles and consequently a drift in  $\mathbf{E} \times \mathbf{B}$  direction. In case the gyro frequency matches the collision frequency, the direction of movement is at a  $45^\circ$  angle.

## 2.5 Appleton anomaly

The Appleton anomaly is easily seen in global TEC maps. An example is shown for the 1st of March 2015 in Fig. 2.5. It is a characteristic feature resulting in a double peak on the day-side to pre-midnight [Lühr et al., 2003]. It is a regular large-scale phenomenon. On the day-side, an eastward electric field is present. The plasma is subject to a drift given in  $\mathbf{E} \times \mathbf{B}$  direction. In combination with the northward pointing magnetic field, this results in an upward plasma drift. Subsequently, the plasma is carried to higher altitudes until an equilibrium of the uplifting force and the gradient of the plasma density is reached (see. Fig. 2.4). From that on, the plasma sinks

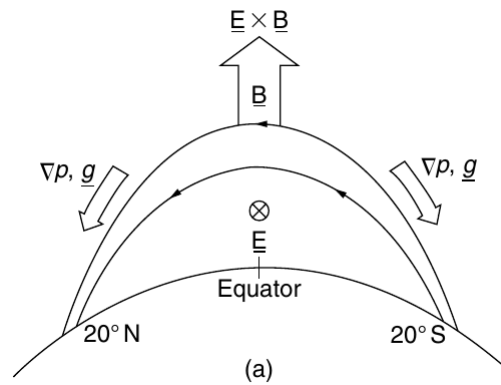


Figure 2.4: Plasma drift in  $\mathbf{E} \times \mathbf{B}$  direction at the magnetic equator and gradient driven plasma drift along the magnetic field lines [Kelley, 1989].

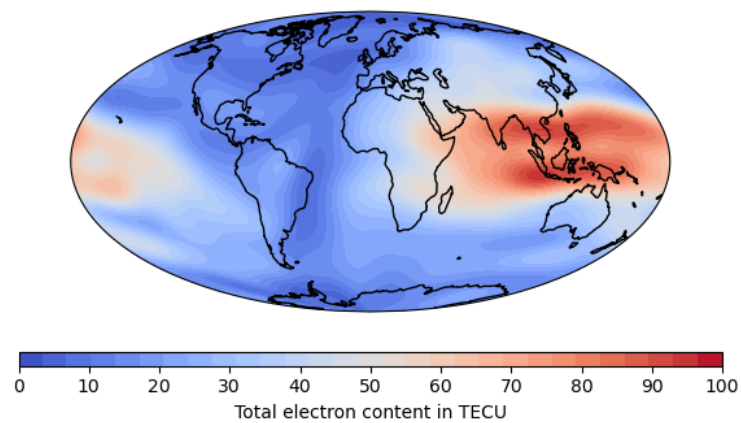


Figure 2.5: CODE global ionosphere map for the 1st of March 2015 8:00 UT. The Appleton anomaly is visible as a the double peak near the geomagnetic equator.

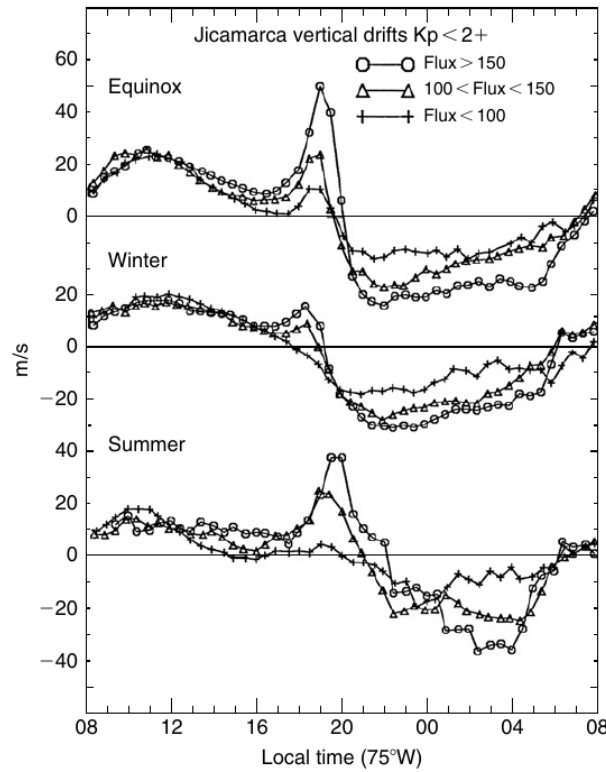


Figure 2.6: Vertical drift as observed by the Jicamarca radio observatory (Peru) [Kelley, 1989].

again to lower altitudes along the magnetic field lines. The result is an accumulation of plasma at approximately  $\pm 5$  to  $15$  degrees in magnetic latitude, depending on solar and geomagnetic conditions. Near the dusk terminator, a second effect amplifies the uplift. Given certain seasonal and solar conditions, the plasma's vertical drift velocity increases rapidly before sunset and is inverted afterwards. This effect is called the pre-reversal enhancement. Observations of the vertical drift taken by the Jicamarca radio observatory in Peru are shown in Fig. 2.6. In this figure, the vertical plasma drift is shown. The daytime upward drift corresponds to an eastward electric field, whereas the downward nighttime drift corresponds to a westward field. Near the dusk terminator, a strong amplification in the vertical drift is observed depending on the season and solar flux.

## 2.6 Ionospheric plasma depletions

Near the geomagnetic equator strong changes in the vertical drift of the plasma occur after sunset (see Fig. 2.6). The pre-reversal enhancement after sunset triggers the growth rate of the Rayleigh-Taylor instability in the lower F region [Whalen, 2000, Stolle et al., 2006b]. The instability can



cause compact volumes of lower plasma density to rise from the E-F boundary into the F-layers. The electron density is several orders lower inside the depletion. Because of conservation of plasma pressure to first order

$$\nabla \left( \frac{B^2}{2\mu_0} \right) + \nabla [N_e(T_e + T_i)] = 0, \quad (2.9)$$

such a depletion leads also to fluctuations in the magnetic field [Park et al., 2013]. Here  $B$  is the magnetic field strength,  $\mu_0$  the magnetic permeability of the free space,  $N_e$  is the electron density and  $T_e, T_i$  the electron and ion temperatures. This effect is then utilized to identify such depletions in the magnetic field measurements [DISC, 2017a, Stolle et al., 2006b, Park et al., 2013]. The detection is discussed in more detail in Sect. 6.4.3. Equatorial bubbles are well known to cause fluctuations in GPS/GNSS, VHF, and several other frequency-dependent measurements [Aarons, 1977, Aarons et al., 1981]. Several studies were made to derive the climatology of those perturbations on the GPS observations taken by LEO satellites (e.g., Xiong et al. [2016b]).

## 2.7 Measurement types

### 2.7.1 Radar

Radar measurements are the gold standard of ionospheric measurements. They can measure the electron density without altitudinal limitation using reflection, and by using Doppler shift also the winds can be measured. A few of the most famous incoherent scatter radars are Jicamarca in Peru, where the measurements for Fig. 2.6 were taken, Milestone Hill in Massachusetts, USA, and the EISCAT Svalbard radar (ESR) as part of the European Incoherent Scatter Scientific Association (EISCAT) in Svalbard, Norway. The total number of radar stations is very limited (ten radars were used for the International Reference Ionosphere (IRI) model [Bilitza, 2018]), and also, the observations are always taken from the identical latitude and longitude. A great effort is required to build and run incoherent scatter radars. They provide an important opportunity to calibrate measurements, e.g., electron density obtained via KBR by GRACE(-FO), calibrating Langmuir probes on Satellites [Lomidze et al., 2018] and also for validating ionospheric models. On 10th of August 2020, the famous Arecibo radar, build in 1969 in Puerto Rico, was severely damaged as one of the wires carrying the instrument platform snapped. Several weeks later on 6th of November 2020, a second wire snapped. As stability could not be ensured, a repair became too risky, and eventually, the radar was to be decommissioned [Witze, 2020]. On 2nd of December 2020, the telescope finally collapsed.

### 2.7.2 Ionosonde

Ionosondes are relatively simple sounders compared to incoherent scatter radars with variable frequency. In case the frequency matches the plasma-frequency, the signal is reflected, and thus the altitude of that specific electron density is obtained. This reflection, however, does not allow for sounding above the maximum electron density peak. A great effort was made to establish a network during the Geophysical year 1980. Several of those stations are still operational. They are an essential source for investigating the bottom-side and low ionosphere. Ionosondes were also used on-board satellite missions, e.g., ISIS-2 (International Satellites for Ionospheric Studies), and used extensively to characterize the topside ionosphere for construction of the IRI model [Bilitza et al., 2011].

### 2.7.3 Sounding rockets

Profiles of the electron density and chemical composition can also be obtained by sounding rockets. Typically, sounding rockets are used for altitude regimes between 50 km and 250 km as those altitude regimes are too high for balloons and too low for satellites [ISAS, 2020]. However, the time of measurements is rather short, typically in the range of a few minutes. Sounding rockets provide very localized measurements. Phenomena to be studied by sounding rockets are e.g., the auroral electrojet, as its typical altitudes are in the range of 100 km to 150 km [Potter, 1970]. However, the proposed Daedalus satellite mission aims for altitudes down to only 120 km using a highly elliptical orbit [Sarris et al., 2020]. A phase-0 study was recently concluded, but it did not enter the phase-A study for the European Space Agency (ESA) Earth Explorer 10 mission [Doornbos, 2021, ESA, 2021].

### 2.7.4 Satellites

Some satellites carry special equipment to measure electric fields, electron density, ion drift, and other parameters. A few examples are dedicated magnetic field missions like Oerstedt, CHAMP, Swarm, and the RPI (Rapid Plasmaspheric Imager) mission. A typical instrument type choice is Langmuir probes, which can extract the electron density using an electric potential, magnetometers, and thermal ion imagers. Most LEO satellites also carry a dual-frequency GPS/GNSS receiver for orbit determination. GNSS data provided by these receivers may also be used to extract the integral electron density. Those include dedicated gravity field missions like GOCE and GRACE and altimetry missions, e.g., ESA's Sentinel 3 satellites or the TOPEX/Poseidon and Jason missions.

### 2.7.5 Ground-based GPS/GNSS

For geodetic applications, large GNSS receiver networks were implemented, and the data is provided nearly continuously and with only short delays. One of the more extensive global and well-organized receiver networks is coordinated by the International GNSS Service (IGS, [Johnston et al. \[2017\]](#)). The network consists of more than 400 stations to determine the orbits of the GNSS satellites and derive various geodetic, geophysical, and atmospheric parameters, e.g., station coordinates, Earth rotation parameters, and total zenith path delay. Numerous regional networks exist, e.g. the European EUREF (Reference Frame Sub-commission for Europe [\[Bruyninx et al., 2009\]](#)) network containing around 200 stations or local networks like the AGNES (Automated GNSS Network for Switzerland) network with 30 stations distributed in Switzerland. GNSS networks can also be used to derive global or regional maps of integral electron density. A global estimation of the vertical total electron content is the routinely processed CODE (Center for Orbit Determination in Europe) TEC map (see Fig. 2.5), where the underlying GNSS observations are taken from the IGS network. Based on TEC maps, corrections can be applied to the GNSS observations to improve the station coordinate estimation [[Garcia-Fernández and Montenbruck, 2006](#)].

## 2.8 Characterization of the topside ionosphere and plasmasphere

The models presented in this section are selected because of their application in GNSS positioning or because they follow similar approaches as the model developed in Sect. 8.2 or the tomographic approach used in Sect. 8.4. The complex physics-based Whole Atmosphere Community Climate Model with thermosphere and ionosphere extension (WACCM-X [\[Liu et al., 2018\]](#)) is not considered as its maximum altitude is in the range of 500 km to 700 km. Furthermore, the tomographic approach Multi-Satellite ionosphere-plasmasphere Electron density reconstruction (MuSE [\[Gerzen et al., 2017\]](#)) is discussed instead of the Multi Instrument Data Analysis System (MIDAS) [\[Mitchell and Cannon, 2002\]](#) because in this work, a multiplicative approach is used. In contrast, the MIDAS approach employs an inversion with truncated singular value decomposition.

### 2.8.1 IRI model

The IRI [\[Rawer et al., 1978, Bilitza, 2018\]](#) model is a joint project of the Committee for Space Research (COSPAR) and the International Union of Radio Science (URSI). The current version is the IRI-2016 [\[Bilitza et al., 2017\]](#). The IRI model is mainly based on ionosonde observations and includes radar observations, even if the number of available radar stations is limited. IRI provides monthly mean ionosphere maps using the solar flux index F10.7 and the Kp-Index and the R12 sunspot number as input parameters or other equivalent input parameters. The topside estimation is currently based on the topside sounding missions ISIS-2 ionosonde measurements,

and comparisons were carried out using TOPEX radar-derived TEC [Bilitza et al., 2011]. The topside electron density is modeled using NeQuick [Bilitza et al., 2017]. As skeleton profiler the Epstein layer is used, the scale height, however, is varied with altitude:

$$H(h) = H_0 \left( 1 + \frac{rg(h - h_m F_2)}{rH_0 + g(h - h_m F_2)} \right), \quad (2.10)$$

where

- $H_0$  is the reference scale height, and
- $h_m F_2$  is the altitude of the peak density of the F2 layer.

For the parameters  $r$  and  $g$  values of  $r = 100$  and  $g = 0.125$  were found suitable in the studies of Radicella and Leitinger [2001] and Coisson et al. [2006]. Earlier IRI versions used an exponential decay, as it is also stated in Coisson et al. [2006] and Bilitza [2004].

### 2.8.2 NeQuick model

The NeQuick or the more recent NeQuick-2 model is an empirical model mostly based on ionosonde data. Three-layer functions with specific anchor points are used. The model parameters are given in the critical frequencies  $f_oE$ ,  $f_oF1$ ,  $f_oF2$ , and  $M(3000)F2$ . External drivers are the monthly mean sunspot number and the solar flux index F10.7. A modification of the NeQuick model, the NeQuick-G, is used to correct the ionospheric path delay and phase advance. Coefficients are transmitted together with the Galileo satellites' navigation message [Montenbruck and González Rodríguez, 2020], allowing to apply ionospheric corrections directly without external input. The capability to correct for those effects is especially important for the users of single-frequency receivers since no ionosphere-free linear combination can be formed to mitigate the ionospheric error in positioning. The NeQuick model is using the DGR profiler, which consists of a combination of Epstein layers [Radicella and Zhang, 1995]

$$\begin{aligned} N_e(h) &= NF_2(h) + NF_1(h) + NE(h) \\ &= \frac{4Nm * F_2}{\left(1 + \exp\left(\frac{h - hmF_2}{B_2}\right)\right)} \exp\left(\frac{h - hmF_2}{B_2}\right) \\ &+ \frac{4Nm * F_1}{\left(1 + \exp\left(\frac{h - hmF_1}{B_1}\right)\right)} \exp\left(\frac{h - hmF_1}{B_1}\right) \\ &+ \frac{4Nm * E}{\left(1 + \exp\left(\frac{h - hmE}{B_E}\right)\right)} \exp\left(\frac{h - hmE}{B_E}\right). \end{aligned} \quad (2.11)$$

The parameters

- $Nm * F_2$ ,  $Nm * F_1$ , and  $Nm * E$  are variations of the  $Nm$  of the given layer with respect to contributions of other layers.
- $B_2$ ,  $B_1$ , and  $B_E$  are empirically determined values for the scale height, whereas especially the parameter  $B_2$  includes a diurnal and seasonal variation using a specific shape parameter.
- $hmF_2$ ,  $hmF_1$  and  $hmE$  are the altitudes of the peaks of the corresponding layer.

More details on the definition of these parameters may be found in [Radicella and Zhang \[1995\]](#). They rely on empirical approximations using ionogram inversion and are thus fitted to match the topside ionospheres shape. A recent study performed by [Montenbruck and González Rodríguez \[2020\]](#) on Swarm C when only using L1 C/A pseudo-range for positioning showed how the NeQuick-G can be used for single-frequency receivers positioning in low Earth orbit to correct for ionospheric effects. The results showed that under high solar flux conditions (e.g., in 2014), the positioning error could be reduced from roughly 5 m down to 2 m. For low solar flux (e.g. in 2017), the positioning error could be reduced in the range of several centimeters. This study and a correction model will be of major interest for the increasing number of cube-sat missions. Most of their receivers are only capable of single frequency tracking and therefore need external input to compensate for the first-order ionospheric phase advance. Another variation of the NeQuick topside is also employed in the high latitude Empirical Canadian High Arctic Ionospheric Model (E-CHAIM [[Themens et al., 2017, 2018](#)]) for the topside.

### 2.8.3 Neustrelitz Plasmasphere Model

The Neustrelitz Plasmasphere Model was developed by [Jakowski and Hoque \[2018\]](#). Only one external parameter, the F10.7 index, is used, 40 additional parameters were fitted using GPS TEC observations obtained from the CHAMP mission during the years 2000-2005 (solar maximum conditions). It uses the sum of two layer functions, which both describe an exponential decay, whereas the decay in  $N_{ePL}$  is dependent on the L-shell (Apex altitude of the magnetic field line in Earth radii  $R_E$ ) and in  $N_{ePh}$  on altitude

$$N_{ePL}(L) = N_{ePL1} \cdot \exp\left(\frac{R_E(1-L)}{H_{PL}}\right) \quad (2.12)$$

$$N_{ePh}(h) = N_{ePh0} \cdot \exp\left(\frac{-h}{H_{Ph}}\right). \quad (2.13)$$

The electron density is then obtained using the relation  $N_e = N_{ePh} + N_{ePL}$ . The key parameters are

- $N_{ePL1}$ ,  $N_{ePh0}$  as reference densities,

- $H_{PL}$ , and  $H_{Ph}$  as scale heights.

$N_{ePL1}$  is the electron density at  $L = 1$  and  $N_{ePh0}$  the electron density at  $h = 0$ . Their variation is modeled using dipole latitude, diurnal, semi-diurnal and ter-diurnal variations, annual and semi-annual variations, the solar zenith angle and a fixed plasmopause location at  $L = 5$ . The validation was performed using electron density data obtained by IMAGE/RPI. This model is a mean plasmasphere model and intended to be used as a background model for GPS positioning and topside modeling.

### 2.8.4 TUM model approaches

The model developed by the Technical University of Munich (TUM) is an empirical model based on ground-based vertical TEC [Erdogan et al., 2020, Goss et al., 2020]. For smoothing and interpolation, a two-dimensional B-spline representation is used. This procedure allows to estimate regional maps and global maps and make use of local densification. A second approach followed by TUM is the three dimensional reconstruction [Gerzen and Minkwitz, 2016, Gerzen et al., 2017]). In that approach, the NeQuick model serves as a background and is adjusted by proper scaling using vertical TEC observations from ground stations. Furthermore, LEO TEC obtained from POD and occultation antennas are utilized in a Kalman-filter approach using a variation of the multiplicative algebraic reconstruction technique (MART). The Neustrelitz models for F2 peak height and density [Hoque and Jakowski, 2011, 2012] are also employed as a background for adjusting the IRI values [Gerzen et al., 2017].

### 2.8.5 CODE TEC maps

The TEC maps routinely generated by CODE model vertical TEC. Slant TEC derived from dual frequency GNSS observations are converted to vertical TEC via the modified single layer mapping function (see Sect. 3.7.3). The vertical TEC map itself is modeled using spherical harmonic expansion up to degree 15 in a sun-fixed frame and with magnetic dipole latitude. The model is purely empirical, and the model parameters are estimated piecewise linear with a time resolution of one hour. The timestamp  $h_0$  means that slant TEC observations up to one hour before and after  $h_0$  were used to estimate the model coefficients at  $h_0$ . The weighting function

$$w(h) = \max(0, 1 - |h - h_0|), \quad (2.14)$$

where  $h$  is the hour of the used measurement, is used to increase the impact of observations taken close to the reference time. Sub-hourly resolution is realized by the piecewise linear model coefficients. The code biases of the receiving ground stations are estimated daily for the TEC map estimation. For most applications they are later combined to monthly values [Schaer, 1999, Schaer et al., 1996]. It was also shown that either the ambiguities or the DCB's to obtain absolute slant

TEC values have to be known or estimated. The CODE TEC maps' main focus is to derive approximations for higher-order ionospheric corrections, which cannot be eliminated when using the ionosphere-free linear combination. Several studies showed that the station coordinates might change in the range of a few millimeters [[Fritsche et al., 2005](#)]. An example of a code TEC is shown in Fig. [2.5](#).





# Chapter 3

## Ionospheric effects on GNSS data

Even though it is not GPS specific, this chapter starts with a small introduction to least squares adjustment, as this tool is required throughout this work and is already applied in TEC and multi-path estimation introduced in this chapter.

After briefly introducing the GPS, GLONASS, and Galileo Global Navigation Satellite Systems (GNSS), the observation equations and essential linear combinations are outlined. Eventually, the computation of GNSS-derived TEC is discussed in this chapter. Even though other (G)NSS exist, e.g., the local Japanese Quasi-Zenith Satellite System (QZSS) or the Chinese Beidou System, they will be omitted as they are not tracked by the LEO satellites used in this work. Furthermore, the signal content of the carrier phase observables and linear combinations are discussed and how they can be used for specific applications, including, e.g., preprocessing. Eventually, the computation of TEC and TEC-derived indices will be discussed, focusing on calibration-related uncertainties, e.g., the uncertainty in the code leveling and the receiver bias estimation.

### 3.1 Least-squares adjustment

In order to adjust orbit or gravity field parameters, or ionospheric models, the technique of least squares adjustment (LSA) is used (see e.g. [Tapley et al. \[2004b\]](#) and [Jäggi \[2006\]](#)). The mathematical model is

$$\mathbf{F}(\mathbf{x}) = \mathbf{y} + \boldsymbol{\epsilon}. \quad (3.1)$$

Here  $\mathbf{F}$  is the observational model,  $\mathbf{x}$  contains the model parameters,  $\mathbf{y}$  the observations, and  $\boldsymbol{\epsilon}$  the observational noise (Gaussian, zero mean). Model deficiencies can also be included in  $\boldsymbol{\epsilon}$  causing non Gaussian residuals. The parameter vector  $\mathbf{x}$  is a solution, if  $\mathbf{x}$  solves

$$\|\mathbf{F}(\mathbf{x}) - \mathbf{y}\|_P \rightarrow \min. \quad (3.2)$$

Here  $\|\mathbf{v}\|_P^2 = \mathbf{v}^T \mathbf{P} \mathbf{v}$  is the  $L^2$  norm weighted with the matrix  $\mathbf{P}$ . In case of a linear function  $\mathbf{F}(\mathbf{x}) = \mathbf{J}\mathbf{x}$ , a solution is given by

$$\mathbf{x} = (\mathbf{F}^T \cdot \mathbf{F})^{-1} \mathbf{F}^T \mathbf{y}. \quad (3.3)$$

If  $\mathbf{F}$  is non-linear,  $\mathbf{F}$  is linearized as  $\mathbf{F}(\mathbf{x}) \approx \mathbf{F}(\mathbf{x}_0) + \mathbf{J}(\mathbf{x} - \mathbf{x}_0)$ , where the Jacobian matrix  $\mathbf{J}$  contains the partial derivatives

$$\mathbf{J}_{i,j} = \frac{\partial \mathbf{F}_i}{\partial \mathbf{x}_j}(\mathbf{x}_0). \quad (3.4)$$

Now the linearized problem can be solved. Depending on the quality of the initial guess  $\mathbf{x}_0$  this can be iterated until convergence.

The observational error can be of different variance and also the observations can be correlated. This is taken into account by

$$\mathbf{P} = \mathbf{Q}_{yy}^{-1} = \sigma_0^2 \mathbf{C}_{yy}^{-1}, \quad (3.5)$$

Where  $\mathbf{P}$  is the weight matrix of observations,  $\mathbf{Q}_{yy}$  is the cofactor matrix,  $\sigma_0$  the a priori standard deviation of unit weight, and  $\mathbf{C}_{yy}$  the covariance matrix. In case all observations are considered to be independent  $\mathbf{P}$  becomes a diagonal matrix with the entries  $\sigma_0^2 / \sigma_{x_i}^2$ , where  $\sigma_{x_i}^2$  is the observation specific variance. Extensive use of observation specific weighting will be made in Chap. 6. Eventually the normal equation system is set up, with

$$(\mathbf{J}^T \mathbf{P} \mathbf{J})(\mathbf{x} - \mathbf{x}_0) - \mathbf{J}^T \mathbf{P}(\mathbf{F}(\mathbf{x}_0) - \mathbf{y}) = \mathbf{N}\mathbf{x} - \mathbf{b} = \mathbf{0}. \quad (3.6)$$

Here  $\mathbf{N}$  is the normal equation matrix and  $\mathbf{b}$  is the right-hand side of the normal equation system. The a posteriori standard deviation can eventually be computed making use of the student T-distribution and may be computed as

$$m_0 = \sqrt{\frac{\boldsymbol{\epsilon}^T \mathbf{P} \boldsymbol{\epsilon}}{n - u}}, \quad (3.7)$$

where  $\boldsymbol{\epsilon}$  are the post-fit residuals,  $n$  is the number of observations and  $u$  the number of model parameters (unknowns). The covariance matrix  $\mathbf{C}_{xx}$  (and the cofactor matrix  $\mathbf{Q}_{xx}$ ) of the adjusted model parameters is eventually given as

$$\mathbf{C}_{xx} = m_0^2 \mathbf{Q}_{xx} = m_0^2 \mathbf{N}^{-1}. \quad (3.8)$$

In case observations cause the matrix become singular or have small Eigen-values in the normal equation system, it is useful to constrain those parameters. Two types of constraints are introduced here: absolute and relative constraints. An absolute constraint can be realized by adding artificial observations of the type such as:

$$x_i = 0, \quad (3.9)$$

together with the weight  $\sigma_0^2/\sigma_i^2$ , where  $\sigma_i^2$  is the a priori variance of the  $i$ -th parameter. The same way, one may introduce relative constraints, by adding equations like

$$x_i - x_j = 0, \quad (3.10)$$

also with appropriate weights. The constraints can be summarized by a constraining matrix  $\Omega$  together with the artificial observations  $\mathbf{0}$ . The least squares problem to be solved is now

$$\|\mathbf{F}(\mathbf{x}) - \mathbf{y} - \boldsymbol{\epsilon}\| + \|\Omega\mathbf{x}\| \rightarrow \min. \quad (3.11)$$

## 3.2 The Global Positioning System

The Global Positioning System is a global satellite-based navigation system developed during the 1970s by the US military and reached full operational capability, i.e., 24 active satellites for global coverage, in mid-1995<sup>1</sup>. Today typically, up to 32 satellites are active. The GPS satellites transmit an encoded, right-hand polarized signal on two frequencies, namely the L1 (1575.42 MHz) and L2 (1227.60 MHz) frequency (see, e.g., [Kaplan and Hegarty \[2017\]](#)). The information required to identify the GPS satellite is included in the publicly available Coarse Acquisition-Code (C/A) signal. The signal is modulated on the L1 frequency using bi phase-shift keying, the accuracy for the code itself was worsened until mid-2000 by artificial noise<sup>2</sup>. Higher accuracy code, the so-called P-code, is available on both the L1 and the L2 frequency. The P-code is encrypted and not available for public use, but the encrypted Y-code can be tracked. Apart from the code measurements also the carrier phase can be extracted. The carrier phase offers high accuracy in the millimeter range. However, only a relative change of range is provided by the phase measurements. Making use of dual-frequency can be used to largely remove the ionospheric contribution. Therefore, dual-frequency measurements are preferred by the geodetic community aiming for the highest possible accuracy. Due to the encrypted signal on the L2 frequency, code-less tracking techniques have been developed and implemented. Standard techniques are to square the signal or to make use of correlations (see, e.g., [Woo \[2000\]](#)). The modernized GPS satellites (block-typed IIR-M, II-F, III-A, III-F) also provide a publicly available signal on the L2 frequency, denoted as L2C<sup>3</sup>. The newest operational generation (block-type IIF) also transmits its signals on a third L5 (1176.45 MHz) frequency.

The GPS satellites orbit the Earth in near-circular orbits at approximately 20,200 km altitude in six different orbital planes separated by 60° each, the revolution time is 11:58 h, and the inclination is 55°. Therefore the coverage in the polar regions lacks high elevation data. The ground tracks

<sup>1</sup><https://www.navcen.uscg.gov/?pageName=global>, accessed 8.12.2020

<sup>2</sup><https://www.gps.gov/systems/gps/modernization/sa/>, accessed 29th of December 2020

<sup>3</sup><https://www.gps.gov/systems/gps/modernization/civilsignals/>, accessed 8th of December 2020

are repeating after two orbital revolutions, which corresponds to one sidereal day. For most space-borne receivers, GPS is still the standard. Only very few satellite missions also support other GNSS systems. One example is the satellites of the COSMIC-2 mission [Weiss et al., 2019]). Their TriRO-GNSS also supports the Russian GLONASS and the European Galileo system for radio occultation measurements [Esterhuizen et al., 2009]. Another example of multi GNSS capable receivers is the RUAG PODRIX on-board Sentinel-6, which tracks GPS and Galileo satellites [ESA, 2020a].

### 3.3 GLONASS

The GLONASS (Globalnaja nawigazionnaja sputnikowaja sistema, Revnivkykh et al. [2017]) system is the Russian pendant to the US-American GPS system. The orbital altitude is approximately 19,100 km and the inclination almost  $65^\circ$ , which allows a better coverage in high latitude regions [Revnivykh et al., 2017]. The GLONASS satellites are distributed in 3 orbital planes, separated by  $120^\circ$  each. The satellites are almost equally distributed in each orbital plane. The ground tracks repeat after 17 revolutions. Given the revolution time of 11h 16 min, which corresponds to  $8/17$  of a sidereal day, this results in approximately eight days. Also, a minimum of 24 satellites is necessary for nominal operation. GLONASS also uses two main carrier frequencies. However, each satellite transmits on an own channel. That means that the frequency is shifted by a fixed step depending on the channel number. The frequencies for GLONASS are  $G1 = 1602 \text{ MHz} + k \cdot 562,5 \text{ kHz}$  and  $G2 = 1246 \text{ MHz} + k \cdot 437,5 \text{ kHz}$ , where  $k$  is given by the channel number [Revnivykh et al., 2017]. The GLONASS system first reached full operational capability in 1993 and again in 2012.

### 3.4 Galileo

Galileo is a civilian European GNSS system developed by ESA and the European Commission, in contrast to the GPS and GLONASS systems operated by the military [Falcone et al., 2017]. The satellites are equally distributed in circular orbits in three orbital planes separated by  $120^\circ$  at an orbital altitude of approximately 23,200 km. This results in a revolution period of 14 h 05 min and repeating ground tracks after approximately ten days. The inclination is  $55.6^\circ$ , which is slightly higher than the inclination of the GPS satellites. Since 11th of February 2019, 22 satellites are in service [GSC, 2019], the full constellation is expected in 2021. In total, a constellation of 30 satellites is planned. Galileo broadcasts on three frequencies: E1(1575.420 MHz), E5(1191.795 MHz), and E6(1278,75 MHz). The modulation used for the E1 signal is composite binary offset carrier, and bi phase-shift keying is used for E5 and E6, similar to GPS [Falcone et al., 2017].

### 3.5 Modeling the GPS/GNSS observables

The basic GNSS observables are code and phase measurements. The code measurements allow to estimate the absolute distance between the transmitter and receiver, but they are still biased by clock corrections. Moreover, the GPS signals are affected by tropospheric delays and ionospheric code delay and phase advance. Those delays are ray path dependent and the tropospheric delay can be ignored for receivers on board satellites, if no radio occultation is performed. The signal itself is modulated on the carrier frequency using bi-phase shift keying (this is shifting the phase by  $180^\circ$  if a bit shift occurs). Carrier phase observations are the integrated negative beat frequency between the received carrier of the satellite signal and the receiver-generated reference frequency. Instead of obtaining the absolute difference, only its relative phase at measurement epoch is known. The absolute distance is only obtained when adding the integer number of cycles between receiver and transmitter. This number is typically unknown and has to be estimated. The phase measurements are also affected by clock corrections, tropospheric and ionospheric effects in a similar way as the code measurements. However, there is one significant difference regarding the ionospheric signal content. Free electrons cause a delay on the code measurements but an advance in phase measurements. Only considering the first order ionospheric contribution, this leads to a change in sign considering the ionospheric component in code compared to phase measurements. Also the ionospheric component is frequency-dependent and to a first order approximation, the ionospheric component of one frequency can be expressed by the ionospheric component of the other frequency. More detail concerning ionospheric contribution will be given in Sect. 3.6. Considering these signal contributions, the pseudorange for C/A code and P code measurements  $\phi_{CA}, \phi_{P1}, \phi_{P2}$  and phase measurements  $\phi_{L1}, \phi_{L2}$  in meters can be expressed as (alternatively  $C_{1k}^i, P_{1k}^i, P_{2k}^i, L_{1k}^i$ , and  $L_{2k}^i$  can be used to underline the involved transmitter  $i$  and receiver  $k$ ):

$$\phi_{CA} = C_{1k}^i = \varrho_k^i + \frac{1}{f_1^2} I_k^i + T_k^i + c\delta_k - c\delta^i + B_{C1}^k, \quad (3.12)$$

$$\phi_{P1} = P_{1k}^i = \varrho_k^i + \frac{1}{f_1^2} I_k^i + T_k^i + c\delta_k - c\delta^i + B_{P1}^k, \quad (3.13)$$

$$\phi_{P2} = P_{2k}^i = \varrho_k^i + \frac{1}{f_2^2} I_k^i + T_k^i + c\delta_k - c\delta^i + B_{P2}^k, \quad (3.14)$$

$$\phi_{L1} = L_{1k}^i = \varrho_k^i - \frac{1}{f_1^2} I_k^i + T_k^i + c\delta_k - c\delta^i + \lambda_1 n_{1k}^i + B_{L1}^k, \quad (3.15)$$

$$\phi_{L2} = L_{2k}^i = \varrho_k^i - \frac{1}{f_2^2} I_k^i + T_k^i + c\delta_k - c\delta^i + \lambda_2 n_{2k}^i + B_{L2}^k, \quad (3.16)$$

where

- $\varrho_k^i$  denotes the slant range at signal transmission time  $t_i$  and signal reception time  $t_k$  (both in GPS-time),

- $I_k^i$  the ionospheric delay (essentially the  $q$  component, see 3.23),
- $T_k^i$  the tropospheric delay between receiver  $k$  and transmitter  $i$ ,
- $\delta_k, \delta^i$  are the clock offsets w.r.t.  $t_i$  and  $t_k$  of the receiver  $k$  and transmitter  $i$
- $B$  are the bias terms.

For the phase measurements the additional unknown integer phase ambiguity in cycles  $n_{1k}^i, n_{2k}^i$ , multiplied with the corresponding wavelengths  $\lambda_1 = c/f_1, \lambda_2 = c/f_2$  is required.

Given this formulation, one may easily form linear combinations, to retrieve different information content. For positioning the so-called ionosphere-free linear combination can be used to eliminate the first-order frequency-dependent ionospheric delay:

$$L_{if} = \frac{1}{f_1^2 - f_2^2} (f_1^2 \phi_{L1} - f_2^2 \phi_{L2}), \quad (3.17)$$

where  $f_1$  and  $f_2$  are the carrier frequencies. If the ionospheric delay shall be extracted, the geometry-free linear combination

$$L_{gf} = \phi_{L1} - \phi_{L2} \quad (3.18)$$

can be applied, because it eliminates the slant range, troposphere, and also clock corrections. Only the ionospheric delay and the ambiguity terms remain.

The wide-lane linear combination is typically used for ambiguity resolution

$$L_{wl} = \frac{1}{f_1 - f_2} (f_1 \phi_{L1} - f_2 \phi_{L2}). \quad (3.19)$$

The wide-lane linear combination has a rather large wavelength of 86 cm instead of 19 cm ( $L_1$ ) or 25 cm ( $L_2$ ) and is therefore well suited to detect cycle slips and perform wide-lane ambiguity resolution. A side effect for a later combination of code and phase observations is that the wide-lane linear combination can be used to flip the ionospheric component sign. This feature is used in the Melbourne-Wuebbena linear combination

$$L_{mw} = \frac{1}{f_1 - f_2} (f_1 \phi_{L1} - f_2 \phi_{L2}) - \frac{1}{f_1 + f_2} (f_1 \phi_{P1} + f_2 \phi_{P2}). \quad (3.20)$$

The Melbourne-Wuebbena linear combination eliminates the slant range, tropospheric and ionospheric effects and clock corrections. In case good code observations (with a noise of less than 1 m) are available, the Melbourne-Wuebbena linear combination can be used to detect cycle-slips. The low noise of the code observations is required as the wide-lane linear combination is used for the phase measurements, and thus a cycle-slip of one cycle equals a jump of 86 cm.

### 3.6 First and higher order ionospheric terms

Most of the above mentioned linear combinations make use of the first order approximation to model the ionospheric signal content. But as a matter of fact the signal also contains higher order ionospheric (HOI) terms. Following the work of [Bassiri and Hajj \[1992\]](#) (alternatively [Bassiri and Hajj \[1993\]](#)) a phase measurement  $\phi_i$  can be decomposed as:

$$\phi_{Li} = \tilde{\varrho} + n_i \lambda_i - \frac{q}{f_i^2} - \frac{s}{2f_i^3} - \frac{r}{3f_i^4}, \quad (3.21)$$

with  $\tilde{\varrho}$  containing the slant range, tropospheric delay and clock corrections. For code observations the following expression is obtained:

$$\phi_{Pi} = \varrho + \frac{q}{f_i^2} + \frac{s}{f_i^3} + \frac{r}{f_i^4}. \quad (3.22)$$

The first order term ( $q/f_i^2$ ) can be eliminated using the ionosphere-free linear combination. The remaining terms are referred to as higher order ionosphere (HOI) term. The terms can be computed using Taylor expansion and approximations regarding the refractivity index [[Petrie et al., 2011](#)]. One obtains:

$$q = \frac{1}{2} \int_{LEO}^{GPS} f_p^2 dl \frac{\text{m}^3}{\text{s}^2} = 40.3 \int_{LEO}^{GPS} N_e dl \cdot \frac{\text{m}^3}{\text{s}^2} = 40.3 \cdot TEC \frac{\text{m}^3}{\text{s}^2} \quad (3.23)$$

$$s = \int_{LEO}^{GPS} f_g f_p^2 |\cos \theta_B| dl \frac{\text{m}^2}{\text{s}^2 \cdot \text{T}} = 7527c \int_{LEO}^{GPS} N_e B |\cos \theta_B| dl \frac{\text{m}^2}{\text{s}^2 \cdot \text{T}} \quad (3.24)$$

$$r = 2437 \int_{LEO}^{GPS} N_e^2 dl \frac{\text{m}^6}{\text{s}^4} + 4.74 \cdot 10^{22} \int_{LEO}^{GPS} N_e B^2 (1 + \cos^2 \theta_B) dl \frac{\text{m}^3}{\text{s}^4 \cdot \text{T}^2} \quad (3.25)$$

where

- $N_e$  is the electron density,
- $\theta_B$  is the angle between the line of sight and the magnetic field vector,
- $B$  is the norm of the magnetic field vector,
- $TEC$  denotes the Total electron content along the line of sight (in electrons per  $\text{m}^2$ ).

The definition of the gyro frequency  $f_g$  and plasma-frequency  $f_p$  can be found in Chap. 2. A short simulation is performed to obtain a worst-case estimation of the impact on higher-order ionospheric effects on the ionosphere-free and geometry-free linear combinations. A single Epstein layer (see Eq. 2.6) is assumed, and numerical integration along the line of sight is performed to solve the

integral terms. The parameters are chosen such that with zero-elevation, the maximum slant TEC reaches up to 382 TECU ( $10^{16}$  electrons/m<sup>2</sup>), which is even higher than the maximum observed values of the Swarm mission during the solar maximum in 2014. The profile parameters are set to  $h_{max} = 350$  km,  $N_{max} = 10^{12}$  m<sup>-3</sup> and a scale height  $H = 100$  km. The altitude of the LEO satellite was set to 450 km, similar to Swarm, and an equatorial position (0° lat, 0° lon) was set because high electron densities usually occur near the geomagnetic equator. As a magnetic field model, the IGRF-13 [Thébault et al., 2015] was used with the reference date 1st of January 2005. Even under such extreme conditions, the impact on the geometry-free linear combination and the ionosphere-free linear combination is in the range of a few millimeters only if the very low elevations are not considered. The impact of the corrections for the GOCE orbit determination was negligible [Jäggi et al., 2015]. However, for ground-based GNSS receivers, the estimated station coordinates can change on mm level [Petrie et al., 2011, Garcia-Fernández and Montenbruck, 2006]. In the subsequent Chap. 7 it will be shown that tracking errors can significantly exceed the HOI contributions under such conditions. The HOI terms are therefore neglected in the following chapters. The simulation results in the antenna frame are illustrated in Fig. 3.1. An azimuth of 0° equals geographic north. The deviations increase with low elevations, and if the line of sight is almost parallel to the geomagnetic field lines (see Eq. 3.24 and 3.25). The declination for the specific location is near -7°, which means, that the line of sight near 7° and 187° is almost parallel to the geomagnetic field lines, thus maximizing the second term. In the case of TEC computations, a tracking error of 1 mm in  $L_1$  or  $L_2$  corresponds to an error in slant TEC of approximately 0.01 TECU. For comparison: the slant TEC derived from ground stations is as accurate as 0.3 TECU ([Dach et al., 2015] p.570 for ground-based stations). Therefore deviations below 30 mm in the geometry-free linear combination can be ignored at this stage. In case accuracy of less than 0.03 TECU is required, HOI corrections have to be taken into account. In such a case, also PCV maps for the geometry-free linear combination need to be considered (see Sect. 8.3.8), as their impact can also be expected to be in a similar range. Apart from the above-mentioned higher-order ionospheric terms also ray-bending is present. A study on the ray bending effects was conducted by Hoque and Jakowski [2008]. Ray-bending caused the signal path to deviate from the direct line of sight. The difference between the geometric range and the length of the ray-path is called excess path length. Making use of ray-tracing assuming a Chapman-Layer, the formula

$$d(f_i) = \frac{7.5 \cdot 10^{-5} \cdot TEC^2 \cdot e^{-2.13\epsilon}}{f_i^4 \cdot HF_2 \cdot (h_m F_2)^{1/8}} \quad (3.26)$$

was derived by Hoque and Jakowski [2008]. Here  $d(f_i)$ ,  $i = 1, 2$  is the excess path length for frequency  $i$  in meters, TEC in TECU, the elevation  $\epsilon$  in radians, the frequency  $f_i$  in GHz and the scale height and height of maximum ionization of the  $F_2$  layer ( $HF_2$  and  $h_m F_2$ ) in km. Assuming a TEC of 100 TECU, a scale height of 70 km, a peak height of 350 km, and an elevation of 0° thus maximizing the exponential function, the excess path length based on this formula is 0.84 mm for



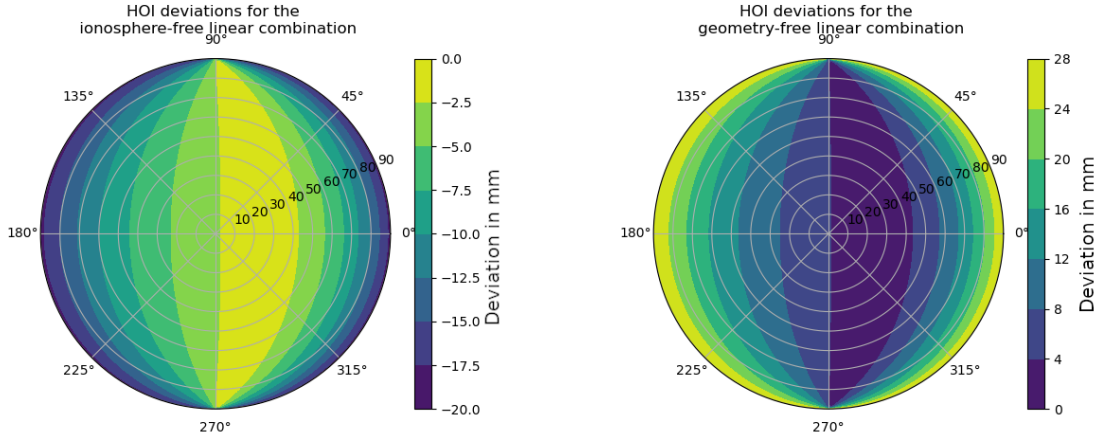


Figure 3.1: Sky plot of the sum of the higher order ionospheric corrections for the ionosphere-free (left) and the geometry-free (right) linear combination. An azimuth of  $0^\circ$  equals geographic north.

L1 and 2.26 mm for L2. These deviations translate into a deviation of -1.38 mm for the ionosphere-free linear combination and -1.43 mm for the geometry-free linear combination. This formula was derived for ground stations. For LEO satellites, the effect can be expected to be smaller because the vertical gradients in electron density are smaller and cause less refractivity.

### 3.7 Computation of slant- and vertical TEC

The geometry-free linear combination is used to derive slant TEC from GPS/GNSS observables. As can be seen in Eq. 3.23, the first-order ionospheric contribution on the code delay or phase advance is directly proportional to the TEC along the line of sight. The easiest way to obtain TEC estimates would be to directly use the geometry-free linear combination of the (semi-) codeless tracked code observables P1 and P2, or in RINEX 3 convention C1W, C2W, since no ambiguity parameters need to be estimated. Direct code tracking (C1P, C2P) is only available for military receivers. Consequently, the Y-code related observations C1W and C2W are used in this work. Only the GPS satellite-specific P1-P2 code biases of the GPS satellites need to be corrected, which are routinely processed and provided by CODE<sup>4</sup> every month [Schaer, 2012, 2011]. Only a receiver-specific P1-P2 remains and needs to be estimated. The issues regarding the estimation of the receiver-specific differential P1-P2 bias are discussed in more detail in the following sections. Furthermore, multi-path or code range variation effects need to be corrected. However, code observations are typically much noisier than phase measurements (approx. 1 m compared to mm level for phase [Dach et al., 2015]). The low noise level motivates using the carrier phase observations,

<sup>4</sup><ftp://ftp.aiub.unibe.ch/CODE/>

which requires estimating the remaining ambiguity parameter. In the following subsections, a procedure is discussed to derive slant TEC for LEO satellites. First, an outlier and cycle slip detection based on the Melbourne-Wuebbena linear combination is performed as described in Sect. 3.7.1. Additionally, the code range variation maps are computed in an antenna fixed reference frame (see Sect. 3.7.2), based on the method proposed by [Montenbruck and Kroes \[2003\]](#). An additional phase screening is performed using the ionosphere-free phase residuals from POD. Eventually, GPS satellite code biases are applied, and the geometry-free linear combination based on carrier phase observations is aligned to the code-based geometry-free linear combination in Sect. 3.7.4.

### 3.7.1 Melbourne-Wuebbena based screening

For TEC computation, both clean code and carrier phase observations on two frequencies are required. For the initial screening, the Melbourne-Wuebbena linear combination is selected because it utilizes both observation types. In case all observations are clean and multi-path corrected, the Melbourne-Wuebbena linear combination should be constant with a white noise dominated by the code noise. Since the Melbourne Wuebbena linear combination wavelength is 86 cm due to the wide-lane linear combination of the phase observations, cycle slips are easily detectable as a jump if code observation noise is not too large. A high RMS in the Melbourne-Wuebbena might indicate degraded observations in phase or code measurements. Especially for 1 Hz data collected by the Swarm receiver, the subsequent observations are highly correlated, and cycle-slips tend to become "cycle-drifts" and are smeared out over several seconds. Thus a filtering algorithm is employed that uses a boxcar smoothing of the Melbourne-Wuebbena linear combination. This method is also known as "Forward-Backward Melbourne-Wuebbena" [[Cai et al., 2013](#)]. First, the data points are averaged using symmetric 11 s boxcar smoothing. The standard deviation is also evaluated, and in case it exceeds 1 m, the observations are flagged. The averaging is performed using the sliding mean

$$L_{mw}^S(t_0) = \frac{\sum_{i=-5}^5 L_{mw}(t_i)}{11}. \quad (3.27)$$

After averaging, the difference between the smoothed value at epoch  $t - 5$  s and epoch  $t + 5$  s is computed

$$\Delta^{10} L_{mw}^S(t) = L_{mw}^S(t - 5s) - L_{mw}^S(t + 5s). \quad (3.28)$$

If the absolute of the difference is close to 86 cm or even larger, a cycle slip near epoch  $t$  is assumed. The epoch of the maximum difference between epoch  $t - 5$  s and epoch  $t + 5$  s is selected as the epoch at which the cycle slip occurs. Window size and the time difference used to compare the smoothed MW linear combination were selected based on a Swarm test case (see Fig. 3.2). Especially the L2 response takes several seconds (see Chap. 7). The time difference, therefore, has to be large enough to detect a step, but small enough not to smear out the steps. An example showing the response to a cycle-slip in the Melbourne Wuebbena linear combination with 2-, 10-,

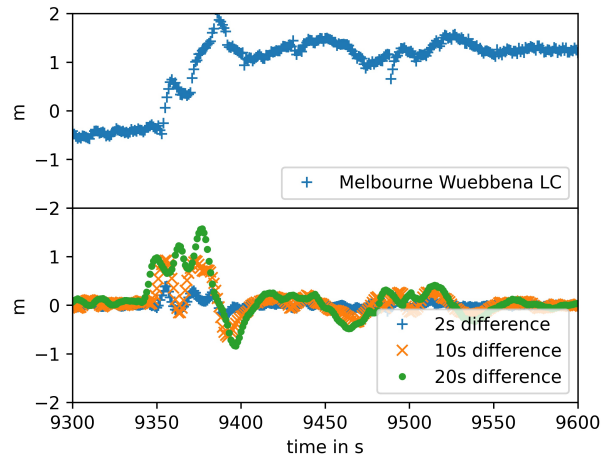


Figure 3.2: Melbourne Wuebbena and differences of mean values over time windows of 2 s, 10 s, and 20 s (bottom) for Swarm A GPS observations of PRN G01, on 1st of March 2015. The Melbourne-Wuebbena linear combination was centered around 0.

and 20-second differences is shown in Fig. 3.2. Steps are supposed to generate a difference of a multiple of 86 cm. The steps are not well visible in the two-second difference. The 20-second difference is too large to identify the epochs of the steps properly. The 10-second difference can identify the steps and is selected as the best trade-off.

This approach, however, requires the code observations to be original code observations and not being affected by already performed preprocessing steps. In the Swarm case, the code observations were smoothed using the carrier phase observations [National Space Institute - Technical University of Denmark, 2019, RUAG, 2008]. If not detected, cycle-slips can enter the code observations in the smoothing and might affect the performance of an MW-based cycle-slip detection. An additional screening is performed at a later stage using auxiliary information from POD. Based on the ionosphere-free phase residuals stemming from a reduced dynamic orbit determination, observations are rejected if a threshold of 2 cm is exceeded (this is more restrictive than the 4 cm used in POD). Those thresholds were empirically derived by analyzing the ionosphere-free phase residuals. If they exceed a few centimeters, this indicates a degradation of the observations, more precisely an issue with L1 or L2, or a misfit of the orbit model, e.g. due to maneuvers, and therefore, the observations should not be used.

### 3.7.2 Code range variation

Multi-path correction maps, expressed in an antenna fixed reference frame, are used to correct near-field multi-path effects. They are assumed to be constant in time. If receiver settings are

modified, this is not necessarily the case. For example, this effect could be observed on-board the CHAMP mission and the GRACE satellites when the occultation antenna's operational mode was switched [Montenbruck and Kroes, 2003, Dahle et al., 2019]. Following the procedure outlined in Montenbruck and Kroes [2003], the multi-path affecting the code observables may be directly estimated by forming the linear combinations

$$M_{CA} + \epsilon_{CA} \approx \phi_{CA} - \frac{2}{f_1^2 - f_2^2} (f_1^2 \phi_{L2} - f_2^2 \phi_{L1}) - \phi_{L1} - B_{CA}, \quad (3.29)$$

$$M_{P1} + \epsilon_{P1} \approx \phi_{P1} - \frac{2}{f_1^2 - f_2^2} (f_1^2 \phi_{L2} - f_2^2 \phi_{L1}) - \phi_{L1} - B_{P1}, \quad (3.30)$$

$$M_{P2} + \epsilon_{P2} \approx \phi_{P2} - \frac{2}{f_1^2 - f_2^2} (f_1^2 \phi_{L2} - f_2^2 \phi_{L1}) - \phi_{L2} - B_{P2}. \quad (3.31)$$

Here  $M_*$  denotes the multi-path, and  $\phi_*$  the code or phase observation in meters to better distinguish between the observation type. Apart from the unknown bias terms  $B_*$  and the noise terms  $\epsilon$ , one may directly obtain a multi-path estimate for the code observations. The bias term  $B$  is assumed to be constant for each connected phase arc and  $\epsilon$  to be white noise. The multi-path correction map is then computed by binning the observations in an elevation/azimuth grid ( $1^\circ \times 1^\circ$  resolution). The bias terms are estimated such that the bin-wise standard deviation is minimized using least-squares adjustment. A zero mean condition is applied to obtain a unique solution. In case disjunct districts appear (i.e., no overlapping arcs), the zero mean condition is applied to each district. Bins without any observation are constrained to zero. The multi-path maps are estimated using a larger time-span to increase robustness, e.g., two months in the following. Since the maps are assumed to be constant as long as the receiver settings do not change, or no changes in the satellite's geometry occur (for example rotating solar panels), the obtained map can be used to remove systematic code errors, which are applied in before code leveling in TEC processing. However, for CHAMP and GRACE(-FO) multi-path maps need to be computed for both operational modes of the occultation antenna [Montenbruck and Kroes, 2003]. An example of this phenomenon is shown in Fig. 3.3. The Code Range Variation (CRV) maps were computed using the months October and November 2014 for GRACE-A and GRACE-B. Due to their similar geometry in the same operational state, both satellites should have similar CRV's. However, in the selected months, the occultation antenna on-board GRACE-B was switched on, resulting in a large-scale wave pattern.

### 3.7.3 Mapping functions

A various set of mapping functions exists to approximate vertical TEC ( $vTEC$ ) from slant TEC ( $sTEC$ ). Two examples will be given here. CODE's mapping function for ground stations employs a single-layer assumption [Schaer, 1999, Dach et al., 2015]. For the Swarm operational TEC processing at GFZ, the slab layer mapping function is used [DISC, 2017b]. In the routinely processed CODE TEC maps, the single-layer model assumes that all electrons contributing to the TEC

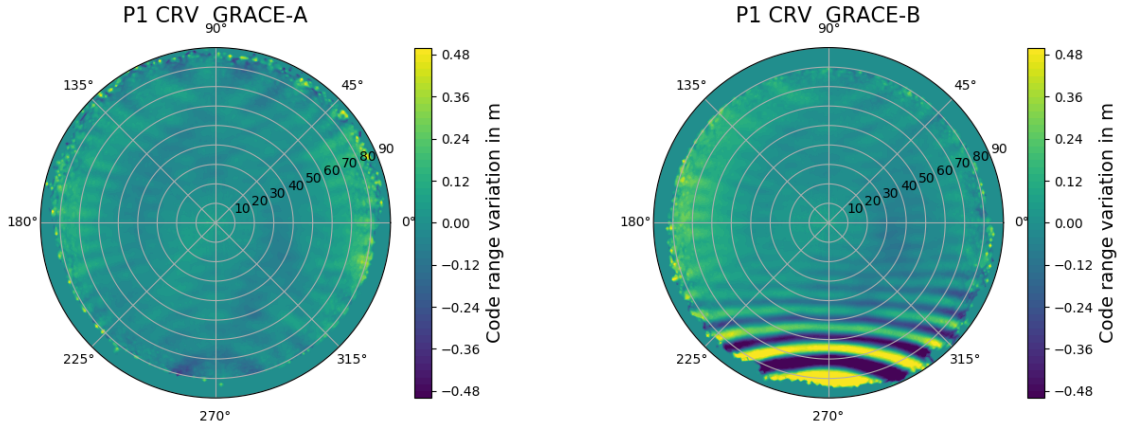


Figure 3.3: P1 Code range variation maps for GRACE-A and GRACE-B in Azimuth and Elevation. The strong pattern in the GRACE B CRV map is related to the occultation antenna switched on.

observed are concentrated in a layer of infinitesimal thickness at a given altitude  $H$  ( $H = 350$  km for CODE TEC maps). In case the slant TEC pierces the single layer orthogonal, the slant TEC equals vertical TEC. Otherwise, the slant TEC has to be scaled to obtain vertical TEC. This dependency may be formulated as

$$vTEC = \cos(z') \cdot sTEC. \quad (3.32)$$

In that specific case the elevation  $\epsilon$  dependent mapping function  $M(z) = \cos(z')$ . The zenith angle  $z'$  at the ionospheric layer may be computed from the zenith angle, see Fig. 3.4,  $z = \frac{\pi}{2} - \epsilon$  observed at the ground station using the dependency

$$\sin(z') = \frac{R}{R + H} \sin(z), \quad (3.33)$$

where  $R$  is the Earth's radius. In TEC processing the Jet Propulsion Laboratory, Pasadena, (JPL) motivated modified single layer mapping function [Coster et al., 1992, Mannucci et al., 1998] is used. The relation 3.33 is modified according to

$$\sin(z') = \frac{R}{R + H} \sin(\alpha z), \quad (3.34)$$

with an empirically determined value for  $\alpha = 0.9782$ .

A single-layer model can be considered sufficient for ground stations because of the relatively large distance between the terrestrial receiver and the ionosphere. This assumption does not hold for the Swarm mission as the Swarm satellites are orbiting the Earth within the ionosphere. Therefore an alternative mapping function was developed by Foelsche and Kirchengast [2002], the so-called slab layer is used. The layer thickness  $H_{shell}$  is assumed to be 400 km. With the radius of

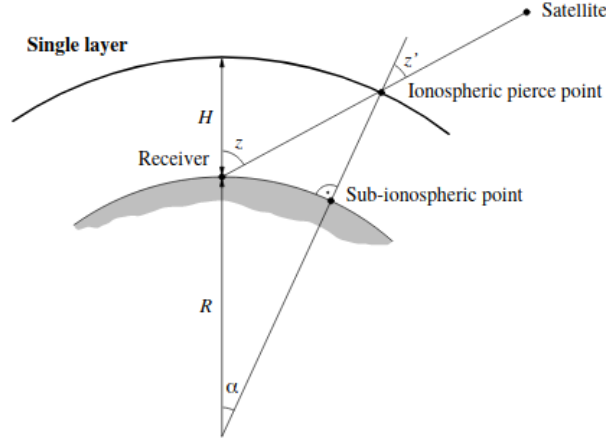


Figure 3.4: Determination of the ionospheric pierce point and zenith angles [Schaer, 1999].

the location of the satellite ( $R_{sat}$ ), the mapping function is formulated as

$$M(\epsilon) = \frac{H_{shell}}{R_{sat} + H_{shell}} \left\{ \cos(\sin^{-1}(r \cdot \cos(\epsilon))) - r \sin(\epsilon) \right\}^{-1} \quad (3.35)$$

with

$$r = \frac{R_{sat}}{R_{sat} + H_{shell}}. \quad (3.36)$$

The elevation dependency is shown in Fig. 3.5. As the elevation reaches  $90^\circ$  both mapping functions converge to 1 as slant TEC becomes vertical TEC. With lower elevations the single layer mapping function exceeds those of the slab layer mapping function. Since the uncertainties due to mapping increases with lower elevation, vertical TEC obtained by mapping is often rejected for geophysical applications. For example in Garcia-Fernández and Montenbruck [2006] an elevation mask of  $40^\circ$  is used.

### 3.7.4 Leveling and bias estimation

The geometry-free linear combination for the code measurements is compared to the phase measurements' geometry-free linear combination for code leveling. The ionosphere has the opposite effect on code compared to phase, and therefore the sign has to be flipped. The DCB for the GPS satellites needs to be applied to  $P_{gf}$ . Afterwards, the arc-wise median offset between  $L_{gf}$  and  $-P_{gf}$  is computed. The advantage of median instead of mean is the increased robustness concerning outliers. The relative slant TEC ( $rsTEC$ ) is then obtained by multiplying the cycle-slip free

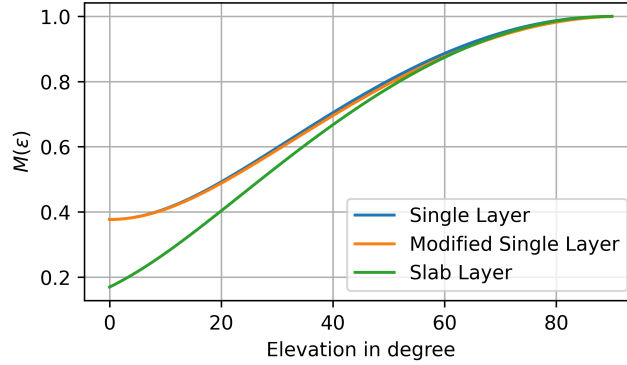


Figure 3.5: Single layer, modified single layer, and slab layer mapping function.

calibrated geometry-free linear-combination  $L_{gf}^{(cal)}$  with the constant derived from 3.23:

$$rsTEC = \frac{f_1^2 f_2^2}{f_1^2 - f_2^2} \frac{L_{gf}^{(cal)}}{40.3} \quad (3.37)$$

$L_{gf}^{(cal)}$  is  $L_{gf}$  aligned to multi-path and GPS-DCB corrected code observations. Apart from an absolute offset, the relative slant TEC already equals the slant TEC. Still, the noise in code or phase might affect the median despite its robustness. The following scenario is considered to get a grip on the expected accuracy. When considering white noise for code observations with a standard deviation of 1 m and a typical arc length of 20 minutes for LEO GPS data, an accuracy of about 3 cm ( $\sim 0.3$  TECU) can be obtained for the mean. The median can be considered at a similar level. The absolute slant TEC is the leveled relative slant TEC corrected by the LEO satellite's unknown P1-P2 receiver bias.

Several options exist to get a rough estimate of the LEO receiver bias. Since negative TEC values are physically impossible, one option is to level relative slant TEC such that the minimum value is non-negative. Alternatively, one may use a model like IRI [Bilitza et al., 2011], or the topside model NeQuick [Radicella and Zhang, 1995] to estimate the mean between relative slant TEC and model slant TEC. However, in both cases, the absolute slant TEC obtained is biased towards the assumptions. Also, the accuracy of the code-based leveling should be carefully taken into account. Such leveling errors can be expected in the range from 1.4 TECU up to 5.3 TECU [Ciraolo et al., 2007] depending on the ionosphere dynamics. Besides, the inter-day variability of the inter-frequency bias can lead to uncertainties up to 8.8 TECU, as was shown by Ciraolo et al. [2007]. It is also possible to estimate the receivers P1-P2 bias  $b$  by assuming that the mapping function  $M(\epsilon)$  (see Sect. 3.7.3) provides a realistic scaling [Yue et al., 2011]. For simultaneously collected relative slant TEC observations  $rsTEC_1 = sTEC + b$  and  $rsTEC_2 = sTEC + b$  together with



their elevations  $\epsilon_1$  and  $\epsilon_2$  thus the condition

$$M(\epsilon_1) \cdot (rsTEC_1 + b) = M(\epsilon_2) \cdot (rsTEC_2 + b) \quad (3.38)$$

can be set up. A threshold on the elevations should be applied to limit the uncertainties of the mapping function. For automated processing also additional rules may be set up to ensure quiet conditions. These include limiting the observations used for forming pairs to the night-side and observations collected in middle latitudes as this area is known for the least irregular behavior. With the formed pairs, the P1-P2 bias  $b$  can be estimated using least-squares adjustment [DISC, 2017b].

In the following, a short study is performed to assess the expected errors of the bias estimation. An absolute vertical TEC of 10 TECU is assumed. The pairs are generated by using randomly generated elevations between 70 and 90 degrees. A threshold of 70 degrees is selected to limit mapping errors and differences in slant TEC caused by spatial gradients (not considered in this example). The receiver's differential code bias (DCB) is set to 3 TECU. The relative slant TEC is now obtained by multiplication with  $1/M(\epsilon)$  and subtracting the DCB. To account for errors regarding the code leveling, white noise with a standard deviation of 1 TECU is added to the observed slant TEC values. This assumption is somewhat optimistic as it represents a best-case scenario where the leveling errors are uncorrelated. The number of formed pairs is set to 2000. For a receiver with 1 Hz sampling, as is the case for Swarm, up to 86400 epochs can be observed per day. The regional and night time limitation can be expected to reduce the number of epochs to approximately 20%. Furthermore, the elevation threshold drastically limits the number of observations that can be used for forming pairs. E.g. for Swarm A, only 310 pairs could be formed given the above-mentioned condition, i.e.,  $30^\circ < |lat| < 70^\circ$ , local time between 18 LT and 06 LT and  $70^\circ$  elevation mask, for the 16th of August 2019. If only a 0.1 Hz sampling is available, as is the case for most LEO satellite missions, the amount of pairs decreases accordingly. Given this scenario, 1000 independent runs are performed. The results are shown in Fig. 3.6. The estimations' mean value is 2.75 TECU (200 pairs) and 3.05 TECU (2000 pairs) in this simulation. The standard deviation is 4.14 TECU for 200 pairs and 1.26 TECU in the case of 2000 pairs. However, this uncertainty can be considered too large for high-flying LEO satellites like e.g., Sentinel-3, the satellite with the highest altitude used in the reconstruction in Chap. 8. Especially if the number of pairs is rather small, as the maximum TEC at these altitudes is only in the range of a few TECU (see Chap. 8). This estimation is based on a best-case scenario. In reality, a larger noise can be expected and instead of white noise systematic biases depending on the line of sight are causing an even larger uncertainty. However, an optimistic noise was selected to demonstrate, that even under an ideal situation the bias estimation based on the mapping scenario can cause significant deviations. A similar approach to solve not only for the receiver DCB, but also for the GPS DCB's is applied in Liu et al. [2020], where also vTEC obtained from mapping functions is applied to estimate the DCB's by solving a linear equation system. In case LEO satellites at different altitudes are used, two vTEC models, one for each altitude, were estimated.



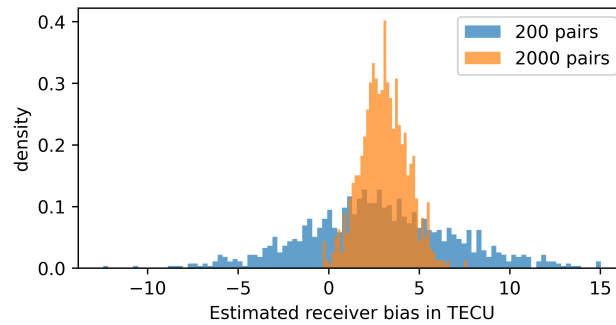


Figure 3.6: Simulated DCB estimation for assumed 1 Hz sampling with 2000 pairs (orange) and 0.1 Hz sampling with 200 pairs (blue) using 1000 simulated estimations. The true bias is 3 TECU.

### 3.7.5 Error sources

An error source, which is not removed by forming linear combinations, is the phase center variation (PCV) of the geometry-free linear combination. If PCV maps for both phase observables are available, such a correction can be directly performed. Typically, only a PCV map for the ionosphere-free linear combination is estimated in flight when using the ionosphere-free linear combination as observable for LEO POD. To obtain a PCV map for the geometry-free linear combination, one could remove most of the signal patterns by estimating an ionosphere model and analyzing the residuals. Such an approach will be applied and discussed in further detail in Chap. 8. The major uncertainty is the receiver's P1-P2 bias estimation in combination with the code leveling. An approach using both is, for example, applied in the operational Swarm TEC processing [DISC, 2017b]. The receiver DCB estimation is performed using the approach including the mapping function, see Sect. 3.7.4. Besides, the estimated TEC is checked for values smaller than 0 TECU. If such values are found and can not be considered outliers, the receiver DCB is adjusted, and the estimated TEC is shifted such that the lowest non-outlier value equals 0. This approach, however, is an underestimation, and especially when working with LEO satellites covering different altitudes, such a leveling can cause inconsistencies. The estimated DCB itself is assumed to be constant during one day, which does not account for possible changes due to temperature variations that may cause the DCB to vary [Yue et al., 2011]. An approach for a more flexible arc-wise estimation will also be given in Chap. 8.

Depending on the receiver implementation, the phase observations may show artifacts that also appear in the obtained slant TEC caused by the tracking loop. This topic will be discussed in Chap. 7, but can only partially be corrected for the Swarm mission, as the required information for other LEO missions is not publicly available.

### 3.7.6 Rate Of TEC Index

The Rate Of TEC ( $ROT$ ) is obtained by forming the difference between the  $sTEC$  values of subsequent epochs:

$$ROT = \frac{sTEC_{t_i} - sTEC_{t_{i-1}}}{t_i - t_{i-1}}. \quad (3.39)$$

$ROT$  is independent of constant biases and phase ambiguities. Therefore, it is also possible to compute  $ROT$  without any leveling applied. The standard deviation over a certain time window is then described as Rate Of TEC Index ( $ROTI$ ) [Pi et al., 1997]:

$$ROTI = \sqrt{\langle ROT^2 \rangle - \langle ROT \rangle^2}, \quad (3.40)$$

where  $\langle \cdot \rangle$  denotes the mean over a specified time window. This Index can be used to identify fluctuations in TEC as bubbles or other irregularities may induce them. The time window to choose is dependent on the application. In the Swarm operational processing, the time window is set to 61 s [DISC, 2017b] which allows detecting medium-scale irregularities with a few hundred kilometers. For irregularities having a smaller spatial scale, a smaller time window must be applied. For example, for identification and down weighting of problematic GPS observations for GOCE [Zehentner and Mayer-Gürr, 2015] a symmetrical window of 31 s is used. Since no external products are required,  $ROT$  and  $ROTI$  are highly suited to compare different preprocessing strategies. For example, one may directly compare cycle-slip detection and correction. Another possibility is to directly compare the correction multi-path effects when using code observations to compute the  $ROTI$  index.

## 3.8 The International GNSS Service

The International GNSS Service, until 2005 named as International GPS Service (IGS), is a service for providing and maintaining data products associated with the GNSS system [Beutler et al., 1996, Dow et al., 2005]. The IGS was founded by the International Association of Geodesy (IAG). The data products provided by the IGS include precise orbits and clock corrections for the GNSS satellites, precise station coordinates and clock corrections for the permanent IGS stations, Earth rotation parameters (ERP), such as polar motion and length of the day, tropospheric and atmospheric corrections. The products may be distinguished by processing latency and accuracy. The lowest latency solution, called ultra-rapid, is supposed to be available within a latency of 3-9 hours [IGS, 2020b]. The more accurate rapid solution, also containing more stations, is provided within 17-41 hours, and the final solution containing all the available stations is provided within 12-18 days. The accuracy to be expected from the final solution is around 2.5 cm for the GNSS orbits and 20 ps for the satellite and station clocks [IGS, 2020b]. Station coordinates are provided with mm accuracy, 3 mm for the horizontal and 6 mm [IGS, 2020b] for the vertical component, usually

the component being the least well determined by the GNSS tracking technique. For the ERP's, the polar motion is supposed to be as accurate as  $30 \mu\text{as}$ , the rate  $150 \mu\text{as/day}$  and the length of day with an accuracy of  $10 \mu\text{s}$  [IGS, 2020b]. Tropospheric corrections are provided with a latency of less than four weeks. The tropospheric zenith path delay can be assumed to be provided within 4 cm precision. TEC maps, usually available within 11 days, provide the gridded vertical TEC with an accuracy of 2-8 TECU [IGS, 2020b].

Several institutes worldwide contribute as analysis centers to the IGS. These are currently the Natural Resources Canada (NRCan), Wuhan University (China), Geodetic Observatory Pecny (Czech), the french CNES, the European Space Agency (ESA), subsection European Space Operations Centre in Germany (ESOC), the German Center for Geosciences (GFZ), American Jet Propulsion Laboratory (JPL), Massachusetts Institute of Technology (MIT), National Geodetic Survey (NGS), Scripps Institution of Oceanography, US Naval Observatory and the Center for Orbit Determination in Europe (CODE) located at AIUB [IGS, 2020a].

### 3.9 Bernese GNSS software

Initiated in 1980 by the former director of the Astronomical Institute of the University of Bern (AIUB), Gerhard Beutler, the Bernese GNSS Software (BSW) is a widely used tool for several high precision GNSS, and SLR-based analyses [Dach et al., 2015]. These are GNSS-based positioning, orbit determination of satellites using GNSS or SLR measurements, clock estimation, and estimation and correction of ionospheric and tropospheric effects. The current version of the Bernese GNSS Software, status March 2021, is version 5.2. For most of the applications in this work, the development version 5.3 is utilized. For the application of gravity field determination, a development version optimized for gravity field processing is used.



# Chapter 4

## Low Earth Orbiters using GPS/GNSS

In this chapter, the Low Earth Orbiting (LEO) satellites used in the following chapters and the satellites being highly suited to extend the presented work are introduced. The mission objectives of the presented missions are pretty diverse. Their mission objectives are altimetry, the determination of the Earth's gravity and magnetic field, weather prediction, and measurements of ionosphere and thermosphere. In most of the applications presented in this work, tracking data obtained from GPS is the primary source of information. For DMSP and Swarm in situ plasma density measurements are used in addition.

### 4.1 CHAMP

CHAMP (CHAllenging Minisatellite Payload [[Reigber et al., 1999](#)], see Fig. 4.1) was a satellite mission by GFZ. The satellite was dedicated to magnetic field measurements and was, in the same turn, also the first mission dedicated to gravity field retrieval using the on-board geodetic type Blackjack GPS receiver, which was also used to perform radio occultation. The satellite was launched on 15th of July 2000 into a near-polar orbit with  $87.3^\circ$  inclination and an initial altitude of about 450 km. The satellite eventually re-entered on 19th of September 2010. The CHAMP

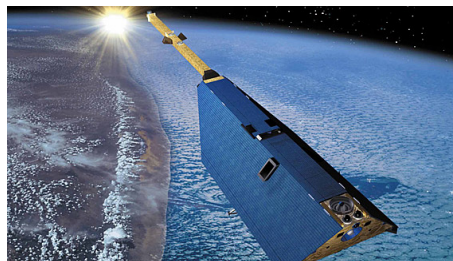


Figure 4.1: Artist's impression of the CHAMP satellite [[DLR, 2020a](#)].



Figure 4.2: GOCE (left [ESA, 2020b]) and Swarm (right [ESA, 2020f]).

satellite was equipped with an occultation antenna to retrieve atmospheric profiles [Schmidt et al., 2005]. Even though CHAMP observations are not used in this work, the approach used at AIUB for GPS-only gravity field estimation was developed for CHAMP by Prange [2010] and is applied to Swarm kinematic positions in the following chapters. The derived ionospheric bubble index (IBI) was also developed based on CHAMP magnetic field measurements [DISC, 2017a].

The magnetometers for measuring the magnetic field's direction and strength were mounted on a boom to mitigate the impact of magnetic fields caused by the satellite body on the magnetic field measurements. A similar design is also used for Swarm. Also, the GRACE satellites' design is based on the CHAMP satellite body [DLR, 2020b], but without a boom, as magnetic field measurements were not a mission objective.

## 4.2 GOCE

The Gravity field and steady-state Ocean Circulation Explorer (GOCE [Drinkwater et al., 2006]) is an ESA satellite mission, launched on 17th of March 2009 to a very low Earth orbit of only 283.5 km. After the commissioning phase, the altitude was lowered to 255 km [Jäggi et al., 2011a]. Such a low orbit made it necessary to compensate for the air drag and design the satellite in a somewhat aerodynamic shape (see Fig. 4.2, left). The satellite was equipped with an ion propulsion system to compensate for air drag. The mission's core instrument was a gradiometer consisting of six accelerometers being symmetrically placed around the center of mass [Rummel, 2010]. The distance between the accelerometer pairs was 0.5 m. Additional instruments were star cameras for precise attitude knowledge and a Lagrange GPS receiver manufactured by Laben (Thales Alenia Space) [García-Rodríguez, 2008]. The orbit was sun-synchronous but slightly drifting over 2 hours in local time during the mission duration. In October 2013, the fuel was depleted, and on 11th of November 2013, the satellite finally re-entered the atmosphere.

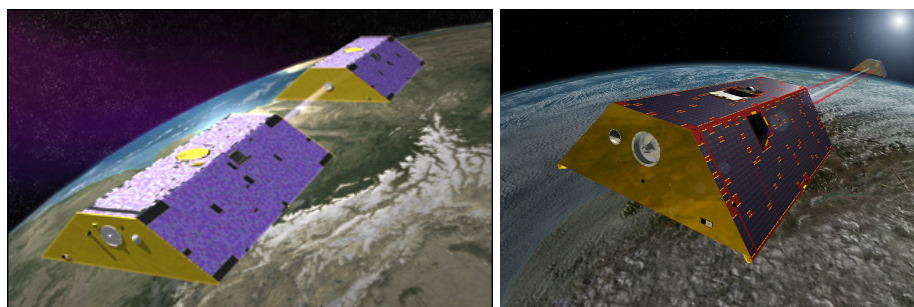


Figure 4.3: GRACE (left [NASA, 2020]) and GRACE-FO (right [JPL, 2020]).

## 4.3 Swarm

The Swarm mission [Friis-Christensen et al., 2008] consists of three identical satellites and is primarily a magnetic field mission. Like CHAMP, the magnetic field instruments are mounted on a 6 m boom To mitigate magnetic disturbances from the satellite body. The absolute scalar magnetometer sits at the boom's end, and the vector field magnetometer is mounted in its middle. The star trackers are mounted colocated with the vector field magnetometer. The electric field instrument is mounted on the satellite's ram side and consists of a thermal ion imager and two Langmuir probes. Furthermore, the satellites are equipped with accelerometers manufactured by the Czech Republic's Aerospace Research and Test Establishment (VZLU). The GPS Receiver is provided by Rüstung Unternehmen AG (RUAG)<sup>1</sup>. Two satellites (Swarm A and C) fly in close formation at initial altitudes of 475 km and separation of  $1.4^\circ$  at the equator after the commissioning phase. The third satellite (Swarm B) is orbiting the Earth at a higher altitude of about 525 km altitude (after commissioning [van den IJssel et al., 2015]). The orbits are near-polar to obtain global coverage. The Swarm mission is still operational at the time of writing. It is also serving long-wavelength gravity field determination, in particular, to bridge the gap between the two dedicated gravity missions GRACE and GRACE Follow-On [Teixeira da Encarnação et al., 2016, Lück et al., 2018].

## 4.4 GRACE

The Gravity Recovery And Climate Experiment (GRACE) [Tapley et al., 2004a] is a twin-satellite mission dedicated to the determination of the Earth's time-variable gravity field. The two satellites are following each other on the same trajectory with a separation of approximately 200 km. They are linked via K-band microwave at frequencies of 24 GHz and 32 GHz, which is the main observable for gravity field determination. The high frequencies have two benefits: First, they are

<sup>1</sup>These information are available at <https://earth.esa.int/eogateway/missions/swarm?text=Swarm>, accessed 11th of May 2021.





Figure 4.4: Sentinel-1 (left [ESA, 2020g]), Sentinel-2 (center [ESA, 2020h]), Sentinel-3 (right [ESA, 2020i]).

not as much affected by higher-order ionosphere terms, and still, because of the dual-frequency, the ionosphere-free linear combination can be used to compensate for ionospheric phase advance. This allows measuring the change of the relative distance of the satellites with an accuracy of  $1 \mu\text{m/s}$  at  $1 \text{ Hz}$  [GFZ, 2020]. Additionally, the K-band can also be used to derive the slant electron content between the satellites. Both satellites are equipped with an accelerometer to measure the non-gravitational forces [GFZ, 2020]. Additional instruments are star trackers and a BlackJack GPS receiver provided by JPL. Besides the POD antenna, the GPS receiver is also connected to an occultation antenna. GRACE was launched in a near-polar orbit with an inclination of  $89^\circ$  on 17th of March 2002 with an initial altitude of 485 km. Due to battery aging, the GRACE-B accelerometer could not be operated continuously starting in 2010 [Herman et al., 2012, Bandikova et al., 2019]. Eventually, the mission ended in October 2017 after several extensions.

## 4.5 GRACE Follow-On

GRACE Follow-On (GRACE-FO) implements the same mission design as GRACE with a few updates. Additionally to the K-band GRACE-FO is equipped with a laser ranging interferometer (LRI), which can provide additional precision due to the low noise level of only  $1 \text{ nm}/\sqrt{\text{Hz}}$  [Abich et al., 2019]. The GNSS receiver TriRO-GNSS has BlackJack heritage and can also perform radio occultation and track not only GPS but also Galileo and GLONASS simultaneously. The occultation antenna was switched on on 5th of March 2020 [Landerer et al., 2020a]. The orbits are near-polar and almost identical to those of GRACE. They have an inclination of  $89^\circ$  and an altitude of 491.5 km [Landerer et al., 2020b].

## 4.6 Sentinel

The Sentinel satellites are part of the Copernicus Earth Observation program by the European Union and ESA [Copernicus, 2020]. Only Sentinel 1 A/B, Sentinel 2 A/B, and Sentinel 3 A/B are considered in this work. Sentinel 4, 5, 5P, and 6 will not be discussed. Sentinel 1 is equipped with





Figure 4.5: DMSP-5P Satellite [NOAA, 2020].

a C-Band synthetic aperture radar [ESA, 2020c]. The first satellite (Sentinel 1A) was launched on 3rd of April 2014, whereas the second satellite (Sentinel 1B) was launched on 25th of April 2016. The orbital altitude is around 702 km with an inclination of  $98.2^\circ$ , which results in a sun-synchronous orbit. The local time is fixed to 6 LT and 18 LT. Sentinel 2 was designed to recover multi-spectral images for environmental analysis and emergency management [ESA, 2020d]. This mission also consists of two satellites in low earth orbit. They are also located in local time fixed orbits (6 LT and 18 LT) at 790 km with an inclination of  $98.6^\circ$ . The first satellite was launched on 23rd of June 2015 and the second on 7th of March 2017. Sentinel 3 is an altimetry mission and focuses on ocean temperature and sea surface height [ESA, 2020e]. It is again a twin satellite mission. The satellites are again local time fixed (10 LT and 22 LT) at an altitude of 810 km and an inclination of  $98.6^\circ$ . Sentinel 3A was launched on 16th of February 2016 and Sentinel 3B on 25th of April 2018. All Sentinel satellites are equipped with RUAG GPS receivers similar to the one used on the Swarm mission. In addition, the Sentinel 3 receivers are capable of multi GNSS tracking.

## 4.7 DMSP

Defense Meteorological Satellite Program (DMSP) is a mission program by the US military implemented in 1962 [eoPortal, 2020]. The mission objective is to scan the ocean temperature, clouds, wind, wildfires, and ice. For the ionospheric studies presented, the in situ electron density observations collected by the Langmuir probe are used. The DMSP satellites are located in sun-synchronous orbits around 800 km altitude. New satellites are regularly launched to ensure continuous observations. The newest generation is the DMSP-5P satellite (see Fig. 4.5)

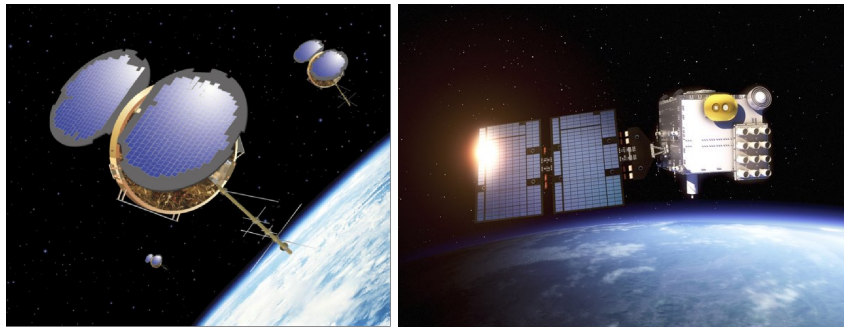


Figure 4.6: COSMIC (left [NSPO, 2020]) and COSMIC-2 (right [UCAR, 2020]).

## 4.8 COSMIC

The Constellation Observing System for Meteorology, Ionosphere and Climate (COSMIC) [Cheng et al., 2006], also known as FORMOSAT-3, is a constellation of six satellites that were launched on 15th of April 2006. The orbits have an altitude of about 500 km with inclinations of  $72^\circ$ , which causes the satellites to drift in local time. One of the key features is the GPS occultation measurements using two side-ward mounted antennas on the circular satellite body. This configuration allows the retrieval of ionospheric profiles and also, to some extent, of tropospheric parameters. Out of the initial 6 COSMIC satellites, only one is still operational (COSMIC/FORMOSAT-3 F).

## 4.9 COSMIC-2

COSMIC-2 [Cook et al., 2013] (also known as FORMOSAT-7) is the follow up mission of COSMIC (see Fig. 4.6). The inclination is only  $24^\circ$  with an altitude of 520-550 km, which provides good coverage in the equatorial region concerning local time. COSMIC-2 is also collecting occultation profiles. The receiver is the same as on GRACE-FO, but in contrast to GRACE-FO, the capability to track multi GNSS is already enabled, and apart from GPS, GLONASS is tracked by the POD antennas [Weiss et al., 2019]. COSMIC-2 was intended to consist of two satellite constellations, the one mentioned above and a second constellation at higher altitudes and inclination. If the second constellation will be launched is not yet decided. A special configuration on-board the COSMIC-2 satellites is the two GNSS antennas mounted on the satellite's sides, similar to COSMIC. As the first antenna is on the ram side, it can track GNSS satellites rising over the horizon. The tracking is then continued to larger elevations. At a certain point, the tracking is continued by the second antenna, allowing to keep the tracking until the GNSS satellite sets on the horizon.

# Chapter 5

## Precise orbit and gravity field determination using Low Earth Orbiters

Precise orbit determination (POD) is the process to determine a satellite's trajectory with high accuracy from satellite tracking data. The satellite motion itself can be described using the equations of motions, including all accelerations acting on the satellite, most prominently the acceleration caused by the Earth's gravity field. In turn, given a precise orbit, the positions can be used to estimate improvements of model parameters, such as gravity field coefficients.

Different types of tracking data (observations) are suited to perform POD. Those are satellite laser ranging (SLR), Doppler Orbitography and Radiopositioning Integrated by Satellite (DORIS), or most commonly used, GPS high-low satellite-to-satellite tracking (GPS hl-SST) using code and phase observations. In the GRACE(-FO) case, K-band low-low satellite-to-satellite tracking (ll-SST) observations may be used to determine ultra precisely the relative distance change of the satellite pair. The K-band measurements are primarily used for gravity field estimation.

Especially for altimetry missions, e.g., Sentinel-3, an orbit accuracy of less than 2 cm radial RMS is targeted, and less than 1 cm desired [[Fernandez et al., 2016](#), [Montenbruck et al., 2018](#)]. Similar requirements hold for satellite missions dedicated to the Earth's gravity field and require a precisely known orbit to estimate the low degree gravity field coefficients, e.g. GOCE, where a 1-D orbit accuracy of 2 cm was set as a mission requirement [[Bock et al., 2014](#)].

This chapter starts with an outline of different measurement techniques used for the LEO satellites considered in this work. Afterwards, gravitational accelerations acting on the satellite's center of mass are described as defining the satellite's motion to the largest extend. In this section also the representation of a gravity field using spherical harmonics will be introduced. This is continued by describing satellite motion using the Keplerian elements for the two-body problem. A set of Keplerian elements can also be used to approximate an orbit at a given time. Those are then called osculating elements and also serve as initial conditions for the equations of motion. The different orbit types, and how the orbit estimation is performed using variational equations, is introduced in

this chapter.

Precise orbit determination and gravity field estimation utilizes many models (e.g. for atmosphere, gravity field, or solar radiation). Therefore the parameters and models for Swarm POD and gravity field determination are listed in this chapter. In this work, orbit and gravity field solutions are only computed for Swarm, and external products were used for GRACE gravity fields. Since frequently used in this work, methods for gravity field comparison are briefly explained. It is outlined which performance can be expected from Swarm GPS-only gravity fields compared to the superior GRACE solutions.

## 5.1 Measurement principles

### 5.1.1 High-low-SST

The method of high-low satellite to satellite tracking (hl-SST) relying on GPS observations is used in this work to estimate precise Swarm orbits and Earth gravity field models. In this approach, the distance between GPS/GNSS and LEO satellite is used as a measure to estimate a trajectory. For gravity field estimation, the LEO satellite acts as proof mass, whereas the GPS/GNSS is used for precise point positioning (PPP [[Zumberge et al., 1997](#)]). The LEO satellite is sensitive to accelerations induced by the gravity field, which results in perturbations of the trajectory. The capability of performing space-borne geodesy using geodetic type GNSS receivers on-board LEO satellites was, among others, demonstrated using observations taken by the Blackjack receiver on-board the CHAMP satellite using a 30 s sampling [[Prange, 2010](#)]. [Jäggi et al. \[2011b\]](#) showed that increasing the observational sampling from 30 s to 10 s could strengthen the gravity field estimation and does not only increase the computational complexity. However, it was also shown that further increasing 10 s sampling for GPS-only gravity field determination to a 1 s sampling does only increase the computational effort. Hl-SST is mainly sensitive to the lower degree and order spherical harmonics, i.e., up to degree and order 20 for monthly gravity field solutions following [Teixeira da Encarnação et al. \[2016\]](#). The major limitation is the observational noise of the kinematic positions, which is at the level of centimeters.

### 5.1.2 Low-low-SST

The GRACE mission is a dedicated gravity mission. Apart from geodetic type GPS receivers, it is also equipped with an ultra-precise K-band ranging instrument, capable of measuring changes in the satellites' relative distance with  $\mu\text{m}$  precision [[Tapley et al., 2004a](#)]. The satellites follow each other on the same trajectory at a nominal separation of approximately 200 km. The ultra-precise K-band measurements' unprecedented precision allowed to obtain an accuracy of below 1 mm geoid height for the derived EIGEN-GRACE02 gravity field at 1000km resolution. That is about

one order of magnitude more accurate than the CHAMP derived GPS-only gravity fields [Reigber et al., 2005]. On more minor scales and compared to altimeter sea level measured by Jason-1 an accuracy of less than 1.8 cm for 750 km smoothing and 2.4 cm for 500 km smoothing was observed by Chambers [2006] as an average of the solutions from the three analysis centers the University of Texas at Austin, Center for Space Research (CSR), Center for Geoscience Potsdam, Germany (GFZ), and the NASA Jet Propulsion Laboratory, California Institute of Technology (JPL). In Lemoine et al. [2007] linear mass trends were derived for 3.5 years based on 10-day solutions to estimate mass gain or loss. GRACE was higher than CHAMP for most of the mission duration, making them in principle less susceptible to the gravity field's higher-order terms. Nevertheless, the ultra-precise K-band measurements in the along-track direction, combined with the accelerometers, allowed an estimation of monthly gravity fields up to degree and order 60, 90, or even 120 for certain months with non-repeating ground tracks [Mayer-Gürr et al., 2018].

### 5.1.3 Satellite based gradiometry

The Gravity field and steady-state Ocean Circulation Explorer (GOCE [Drinkwater et al., 2006]) was the first Earth explorer core mission of ESA's Living Planet Program. It was the first satellite ever equipped with a three-axis gradiometer for determining the static gravity field with an unprecedented accuracy of 1 mGal and the geoid with an accuracy of 1 cm, both at a spatial resolution of 100 km [Rummel et al., 2002]. The gradiometer core instrument consists of three accelerometer pairs with an arm length of 0.5 m [Drinkwater et al., 2006]. The difference in acceleration between six accelerometers is measured on-board, which is sensitive to gradients in the gravity field. The gradiometer is especially sensitive to higher degrees. As those degrees experience a high attenuation, a very low orbit of only 250 km was selected. Ion propulsion was implemented to compensate for the air drag to operate the mission on such a low altitude and ensure a drag-free environment for the gradiometer. It was possible to estimate gravity fields up to degree and order 300 [Förste et al., 2019]. The small distance between the accelerometers, however, made the instrument insensitive to large-scale variations. Those were supported by hl-SST or by using static gravity fields obtained by GRACE to a specific degree and substituting the estimation using a combination on the normal equation level [Förste et al., 2019].

### 5.1.4 SLR validation

The satellites' position, or more precisely the range from a ground station, equipped with an astronomical telescope to satellites can be measured using laser ranging if the satellites are equipped with retro-reflectors. A short laser pulse is transmitted from a station towards the satellite. The ground station again detects the reflected pulse. The time difference between the emission and reception of the pulse is measured, which multiplied with the speed of light results in the round-trip range. Multiple observations are screened, averaged, and stored as a normal point to reduce

observational noise, false detections, and outliers. The minimum threshold of valid data points for a normal point is three points for nighttime and six points for daytime observations. However, it is typically highly exceeded for the top-performing stations using kilohertz lasers [Sinclair/RGO, 1997]. The observed range is then compared to the theoretical range of the satellite at the same epoch. The theoretical position is given by a dynamic, reduced dynamic or kinematic orbit (see Sect. 5.4). The orbits need to be evaluated at the same epoch. Thus interpolation may be required. SLR observations depend on good atmospheric models to account for refraction. As SLR is relying on optical observations, it is also weather-dependent. The SLR network of the International Laser Ranging Service (ILRS [Pearlman et al., 2002]) is very inhomogeneous. Several stations exist in Europe, only very few near the equator and the southern hemisphere. However, the best performing SLR station Yarragadee is located in the Australian outback. Consequently, it is only little affected by cloud covering and collects more than twice as many observations as any other SLR station [Sinclair/RGO, 1997].

For LEO satellites, consistency of 1-3 cm can be observed when comparing a reduced dynamic orbit to SLR range measurements [Arnold et al., 2019]. Those measurements are used in this work for external validation of the obtained orbit solutions.

## 5.2 Gravitational acceleration

The Earth's gravity field is a potential field. This implies that the force vector  $\mathbf{F}$  acting on an infinitesimal proof-mass can be described as a vector field, which can be expressed using the gradient of a potential field  $V$ :

$$\mathbf{F} = \nabla V. \quad (5.1)$$

In the most reduced case, with the mass of the satellite negligible compared to the Earth's mass and the Earth assumed to be a point mass, the gravitational accelerations acting on the satellite can be described as

$$\ddot{\mathbf{r}} = -GM \frac{\mathbf{r}}{\|\mathbf{r}\|^3}, \quad (5.2)$$

with  $\mathbf{r}$  being the satellite's position in the geocentric frame,  $G$  is the gravitational constant, and  $M$  the Earth's mass. As is the case for LEO satellites in close vicinity to the Earth, the Earth can not be considered a point mass. Also, third body perturbations and non-gravitational accelerations need to be considered. The total acceleration acting on a proof mass at location  $\mathbf{r}$ , here the satellite, can be expressed as

$$\ddot{\mathbf{r}} = -G \int_{V_E} \rho_P \frac{\mathbf{r} - \mathbf{r}_P}{\|\mathbf{r} - \mathbf{r}_P\|^3} dV_E - G \sum_{j=1}^n m_j \left( \frac{\mathbf{r} - \mathbf{r}_j}{\|\mathbf{r} - \mathbf{r}_j\|^3} + \frac{\mathbf{r}_j}{\|\mathbf{r}_j\|^3} \right) + \mathbf{a}_{ng} \quad (5.3)$$

in the quasi-inertial geocentric coordinate system. The first term of this equation describes essentially the acceleration of the proof mass given by the mass distribution of the planet. As the planet

is not a point mass, the integral over the Earth's volume ( $V_E$ ) may be seen as the contribution of an infinite number of the infinitesimal point masses located at position  $\mathbf{r}_p$ , with the mass being the density  $\rho_P$  multiplied by the volume element  $dV_E$ . The second term denotes third body perturbations, as they act on the proof mass, but also the central body. As the external perturbations (for example Moon, Jupiter, and Saturn) are rather small, and also their distance is relatively large, they can be considered as point masses with mass  $m_j$  at location  $\mathbf{r}_j$ . This may also be seen later in Eq. 5.5, where especially higher orders are highly affected by the dampening coefficient  $(\frac{a_E}{r})^n$ , and therefore can be neglected at large distances. Eventually, all other accelerations are condensed into  $\mathbf{a}_{ng}$ . These are the accelerations, which are not contributing to the gravitational attraction and are also commonly called non-gravitational accelerations or non-conservative accelerations, e.g. solar radiation pressure, air-drag, earth albedo, etc.

To precisely measure the non-gravitational accelerations, dedicated gravity missions are equipped with high-grade accelerometers. For the Swarm mission, the accelerometers did not perform as expected. It was shown by [Teixeira da Encarnação et al. \[2020\]](#) that even for the best-performing accelerometer on Swarm C artifacts and high noise on the accelerometer measurements limit the gravimetric application. Consequently, non-gravitational accelerations have to be modeled or absorbed to the extent possible by empirical parameters.

As the source of the earth gravity field, the mass distribution (first Term in Eq. 5.3) can be contained in a compact volume, let's say a sphere or ellipsoid of sufficient radius, Gauss's formula

$$\int_V \Delta \mathbf{F} dV = \int_S \langle \mathbf{F}, \mathbf{n}_s \rangle dS \quad (5.4)$$

can be applied to link the volume integral to a surface integral. The vector  $\mathbf{n}_s$  is the radially outward pointing normal vector, and  $\langle \cdot, \cdot \rangle$  denotes the inner product. Using the Earth's equatorial radius  $a_E$  for the sphere's dimension, the gravity field on the sphere's surface may be developed into a series of spherical harmonics (see, e.g. [Heiskanen and Moritz \[1967\]](#)). With  $r$  as radius,  $\lambda$  as latitude, and  $\phi$  as longitude, the resulting potential field up to degree  $n_{max}$  is then given as

$$V(r, \lambda, \phi) = \frac{GM}{r} \sum_{n=0}^{n_{max}} \left( \frac{a_E}{r} \right)^n \sum_{m=0}^n P_n^m(\sin \phi) (C_{nm} \cos m\lambda + S_{nm} \sin m\lambda). \quad (5.5)$$

Here

$$P_n^0(x) = \sqrt{(2n+1)} P_n(x) = \sqrt{(2n+1)} \frac{1}{2^n n!} \frac{d^n}{dx^n} ((x^2-1)^n), \quad (5.6)$$

$$P_n^m(x) = \sqrt{\frac{2(2n+1)(n-m)!}{(n+m)!}} (1-x^2)^{\frac{m}{2}} \frac{d^m}{dx^m} P_n^0(x), m > 0 \quad (5.7)$$

are the fully normalized associated Legendre functions.



### 5.3 Modeling satellite motion for LEO satellites

A satellite orbit is the trajectory of a satellite. The trajectory is the result of the sum of all forces acting on the satellite causing acceleration, which is dependent on the location of the satellite (e.g., gravitational acceleration), velocity (e.g., air drag), or given time windows (e.g., propulsion). Assuming the corresponding equation of motion fully describes the motion, only the six initial conditions need to be determined for describing the orbit together with the full force model. The equation of motion is a second-order differential equation [Beutler, 2005]. The resulting initial value problem is given by

$$\ddot{\mathbf{r}}(t) = \mathbf{f}(t, \mathbf{r}, \dot{\mathbf{r}}, P) \quad (5.8)$$

$$\dot{\mathbf{r}}(t_0) = \dot{\mathbf{r}}_0 \quad (5.9)$$

$$\mathbf{r}(t_0) = \mathbf{r}_0, \quad (5.10)$$

where  $\mathbf{r}$ ,  $\dot{\mathbf{r}}$ , and  $\ddot{\mathbf{r}}(t) \in \mathbb{R}^3$  are three dimensional vectors and  $\mathbf{f}$  is a function with values in  $\mathbb{R}^3$ . The multi dimensional variable  $P$  denotes the a set of additional parameters, such as empirical accelerations, scaling factors of force models, gravity field parameters, observation-specific parameters like ambiguities and station coordinates, etc.. The initial conditions  $\mathbf{r}_0, \dot{\mathbf{r}}_0$  in Eq. 5.9 and 5.10 are the position and velocity at epoch  $t_0$ , respectively, that may be replaced by an equivalent set of parameters like initial osculating Keplerian Elements. In case of a completely undisturbed orbit with the planet and the satellite as a point mass and only gravitational accelerations considered, the orbit is fully described by the six Keplerian Elements (see Fig. 5.1). The origin of the reference coordinate system is the planet's center of mass. The x-axis points to the direction of the vernal equinox, which is the intersection of the ecliptic and the equatorial system (e.g. expressed in the J2000 reference frame [Beutler, 2005]). The z-direction is defined northwards along the Earth's rotational axis, and the y-axis is completing the right-handed system. For elliptical orbits, the Keplerian elements are then defined as

- $a$ : is the semi-major axis, thus defining the maximum diameter of the elliptical orbit
- $e$ : is the numerical eccentricity. It is defined as the distance from the center to the focal point divided by the semi-major axis. An eccentricity of 0 leads to a circular orbit, whereas a value close to 1 creates a highly elliptical orbit.
- $i$ : is the inclination, which is the angle of intersection of the equatorial plane with the orbital plane.



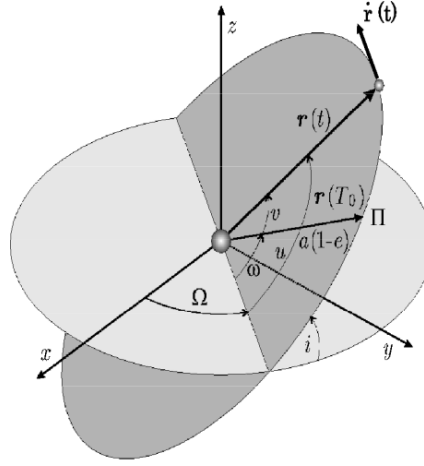


Figure 5.1: Definition of the orbital elements  $a, e, i, \Omega, \omega, u(t_0)$  and the state vector  $\mathbf{r}(t), \dot{\mathbf{r}}(t)$  [Prange, 2010].

- $\Omega$ : is the right-ascension of the ascending node. It is defined as the angle between the x-axis and the ascending node.
- $\omega$ : is the argument of perigee, defined as the angle between the ascending node and the perigee  $\Pi$  being the point closest to the Earth.
- $u_0$ : is the argument of latitude, being defined as the angle between the ascending node and the satellite's location at time  $t_0$ .

In some cases, a complete set of Keplerian elements contains the true anomaly instead of the argument of latitude. This is an equivalent description using the identity  $u_0 = \omega + \nu(t_0)$  where  $\nu(t_0)$  is the true anomaly at time  $t_0$ .

For the two-body problem, the Keplerian Elements are constant with time. The set of Keplerian Elements obtained from position and velocity of a general trajectory by the two-body problem is called osculating elements.

## 5.4 Orbit representations

### 5.4.1 Dynamic orbits

A dynamic orbit is described by the equations of motion and the underlying force models like e.g., the Earth's gravity field, third body perturbations, and non-gravitational forces, and other force models. As a dynamic orbit is force-dependent, it refers to the center of mass. Only the six initial conditions, position and velocity, six Keplerian Elements, or an equivalent set of initial conditions need to be estimated. Eventually, the satellite trajectory may be obtained by numerical integration. As a dynamic orbit is entirely dependent on the force models and the initial conditions, model deficiencies cause deviations in the computed trajectory, which are increasing with the length of the underlying orbital arc. One possible solution is to use short orbital arcs. For example the arc length selected by ITSG for GPS gravity field estimation is 30 minutes for LEO satellites [Mayer-Gürr et al., 2005]. Even though it limits the accumulation of orbital errors, this approach causes discontinuities at the arc-boundaries.

### 5.4.2 Kinematic positions

Kinematic positions, also called kinematic orbits, are pretty much the opposite of a dynamic orbit. For each observational epoch, they are a purely geometrical solution to solve for the reference point position, usually the GNSS antenna's phase center position. Knowing the satellite's attitude, e.g., from star camera measurements and the instrument offset to the center of mass, this position can be translated to the satellite's center of mass position. No force models are used to estimate LEO satellites' kinematic positions. However, for the GNSS satellites, force models are used to compute the GNSS satellite's position at transmission time. The estimated positions are also independent of each other in the case of code observations. For phase observations, the positions are not independent because they are linked by the carrier phase ambiguity parameters [Jäggi et al., 2011c]. Thus the epoch-wise covariance has to be carefully considered if the kinematic positions are used as pseudo-observations for gravity field processing [Lasser et al., 2020]. Velocity information is not available in contrast to dynamic or reduced dynamic orbits, where the velocity is given by the numerically integrated solution of the equation of motion. The kinematic position's quality heavily depends on the observational noise, the observational geometry, and the quality of the GNSS positions and clock corrections [Jäggi et al., 2011c]. If the estimation is performed carefully (i.e., outliers and ambiguities correctly identified), the kinematic positions can be assumed to scatter around the true trajectory. However, systematic deviations can be caused by the carrier phase ambiguity. As the LEO satellite's kinematic positions are not computed using a priori information like underlying force models, the kinematic positions are a natural choice for estimating gravity fields.

### 5.4.3 Reduced-dynamic orbits

The reduced dynamic orbit [Wu et al., 1991] can be considered a trade-off between dynamic orbits and kinematic positions [Jäggi, 2006]. It combines the robustness of the dynamic orbit with the capability to follow variations that are not captured in the force models. Force models are also used to estimate reduced dynamic orbits but instead of solely relying on the force models, model deficiencies can be compensated by empirical parameters. This may be realized by allowing changes in velocity or adding piece-wise constant accelerations as empirical parameters [Jäggi, 2006]. These are set up, spaced, and constrained concerning the perturbing forces and the physical models' reliability. Small spacing and weak constraints are usually considered if the satellite is highly affected by air drag, or no sufficiently precise gravity field model is available.

For example for GOCE, a spacing of only six minutes was set for the reduced dynamic orbit determination at AIUB [Bock et al., 2011]. As satellites in higher orbits are not as much affected by the gravity field's higher-order degrees and the perturbation due to air drag decreases, a larger spacing can be considered. For cannonball satellites, e.g., Starlette at 812 km altitude tracked using satellite laser ranging [eoPortal, 2021], the impact of non-gravitational forces on the motion of the satellite is also minimized by the small area to mass ratio. As empirical parameters for a 7-day solution, only 1/rev terms for along- and cross-track are estimated daily and used together with pseudo stochastic pulses in the along-track direction set up for each revolution (104 min) [Jäggi et al., 2013].

## 5.5 Orbit estimation

The motion of a satellite can be modeled using a set of differential equations, similar to 5.8. In general an initial value problem for a differential equation  $\mathbb{R}^{\geq 0} \times \mathbb{R}^{n \cdot d + m} \rightarrow \mathbb{R}^d$  of dimension  $d$  order  $n$  and  $m$  dynamical parameters is given as

$$\mathbf{r}^{(n)} = \mathbf{f}(t, \mathbf{r}, \dot{\mathbf{r}}, \ddot{\mathbf{r}}, \dots, \mathbf{r}^{(n-1)}, \tilde{p}_1, \dots, \tilde{p}_m) \quad (5.11)$$

$$\mathbf{r}^{(i)}(t_0) = \mathbf{r}_0^{(i)}, i = 0, 1, \dots, n-1. \quad (5.12)$$

here:

- $\mathbf{r}(t), \mathbb{R}^{\geq 0} \rightarrow \mathbb{R}^d$  is the solution of the system,
- $\mathbf{r}^{(i)} = \frac{d^i \mathbf{r}(t)}{dt^i}$  is the  $i$ -th time derivative,
- $\tilde{p}_j$  are the dynamical parameters,
- $\mathbf{f}: \mathbb{R}^{\geq 0} \times \mathbb{R}^{n \cdot d + m} \rightarrow \mathbb{R}^d$  is the right hand side of the differential equation,
- $\mathbf{r}_0^{(i)}$  are the initial conditions at epoch  $t_0$ .

The function  $\mathbf{f}$  can also be expressed by  $n \cdot d + m$  one dimensional parameters  $p_j, j = 1, \dots, n \cdot d + m$ . Eq. 5.11 is also called primary equation. For the sake of simplicity the first  $n \cdot d$  parameters are assigned to  $\mathbf{r}$  and its derivatives, and the last  $m$  parameters to the dynamical parameters. For any of these parameters, the variational equations

$$\mathbf{z}_j(t) := \left( \frac{\partial \mathbf{r}(t)}{\partial p_j} \right) \quad (5.13)$$

are defined. As  $\mathbf{r}$  is a solution to  $\mathbf{r}^{(n)} = \mathbf{f}$ ,  $\mathbf{z}$  is also a solution to

$$\mathbf{z}_j^{(n)} = \frac{\partial \mathbf{f}}{\partial p_j} = \sum_{i=0}^{n-1} \sum_{k=1}^d \sum_{l=1}^d \frac{\partial f_k}{\partial r_l^{(i)}} \cdot \frac{\partial r_k^{(i)}}{\partial p_j} \cdot \mathbf{e}_k + \sum_{i=1}^m \frac{\partial \mathbf{f}}{\partial p_i} \frac{\partial p_i}{\partial p_j}, \quad (5.14)$$

where  $\mathbf{e}_k$  is the  $k$ -th unit vector. In the last term it is evident, that  $\frac{\partial p_i}{\partial p_j} = 1$ , if  $i = j$  and zero otherwise. Summarizing the last term as  $f_p$ , using the identity  $\mathbf{z}^{(i)} = \frac{\partial \mathbf{r}^{(i)}}{\partial p_j}$ , this transforms to

$$\mathbf{z}^{(n)}(t) = \sum_{i=1}^{n-1} \mathbf{A}_i(t) \mathbf{z}^{(i)}(t) + \mathbf{f}_p(t) \quad (5.15)$$

with

$$\mathbf{A}_{i,(j,k)} = \frac{\partial f_j(t)}{\partial r_k^{(i)}} \quad (5.16)$$

As following from Eq. (5.14), with  $f_p$  defined as

$$\mathbf{f}_p(t) := \begin{cases} 0 & , p \in \{p_1, \dots, p_{n \cdot d}\} \\ \frac{\partial \mathbf{f}(t)}{\partial p} & , else \end{cases} \quad (5.17)$$

For both, the primary equation and the variational equations numerical integration is performed. In the celestial mechanics approach implemented in the BSW, the collocation method is utilized [Beutler, 2005]. For each sub-interval  $I_k = [t_k, t_{k+1}]$  the solution is expressed as a truncated Taylor series of order  $q$ , where  $q \geq n$ :

$$\mathbf{r}_k(t) = \sum_{l=0}^q \frac{1}{l!} (t - t_k)^l \mathbf{r}_{k0}^{(l)}. \quad (5.18)$$

The coefficients  $\mathbf{r}_{k0}^{(l)}$ , however, need to be computed by asking that the numerical solution assumes the initial values and that the numerical solution solves the differential equation system at exactly  $q+1-n$  different epochs within the integration interval [Beutler, 2005].

With the primary equation and the variational equations as truncated Taylor series, the orbit improvement process can be initialized

$$\mathbf{r}(t) = \mathbf{r}_0(t) + \sum_{i=1}^n \frac{\partial \mathbf{r}_0}{\partial p_i}(t)(p_i - p_{0,i}), \quad (5.19)$$

with  $\mathbf{r}_0$  being the a priori solution, and  $p_{0,i}$  the  $i$ -th a priori parameter. First, a priori values for the orbital parameters have to be determined. E.g. this task can be performed by estimating kinematic positions using code observations and fitting a dynamic orbit. The a priori orbit is then integrated, and the residuals to the observations linked by the observation equations are computed. Eventually, a normal equation system is set up using the variational equations and solved. The thus obtained set of orbital parameters defines the new, improved orbit, which may be obtained by Eq. 5.15. This process may be iterated.

## 5.6 Bernese Processing Engine for LEO POD

To estimate precise reduced dynamic orbits and kinematic positions for LEO satellites, a tailored combination of processing programs and scripts called LEOPOD exists in the BSW (see Fig. 5.2 [Jäggi, 2006]). The POD, as set up in the BSW, starts with the collection of required data. External products, this includes GNSS orbits and clock corrections (CODE final GNSS Orbit and 5s GPS clock corrections [Dach et al., 2020, Bock et al., 2009]), an earth gravity field model, an ocean tide model, and sensor offsets, are prepared. Satellite-specific data, such as the Receiver INdependent EXchange format (RINEX [Gurtner and Estey, 2007]) observation file, the satellite's attitude, and the receiver antenna PCV map also need to be provided. If not yet existing, such a map can be obtained by iteratively computing orbits and analyzing the residuals for elevation and azimuth of the GNSS satellites in the LEO antenna frame [Montenbruck et al., 2008]. Even if phase data is used for the orbit determination, the GPS/GNSS differential code biases (DCB) are introduced as the first a priori orbit is generated using code observations.

First, the LEO satellite's kinematic positions are computed using dual-frequency code observations in a least-squares adjustment (LSA). The ionosphere-free linear combination for the code observations is used, corrected by the DCB's provided by the IGS. These kinematic positions are then used as observations to estimate the first a priori orbit, a rather stiff reduced dynamic orbit characterized by only few empirical parameters. With that orbit as a reference, a first phase screening is performed to identify outliers and cycle slips and set up phase ambiguities. Eventually, the a priori orbit is updated. For the update of the a priori orbit, the phase observations are used, usually with a reduced sampling to reduce the computational effort. Empirical orbit parameters and also stochastic pulses or piece-wise constant accelerations may be set up and constrained depending on the satellite and the orbit perturbations. The process of screening the phase data and improving the a priori orbit may be iterated with more stringent thresholds as the orbit's quality can be assumed

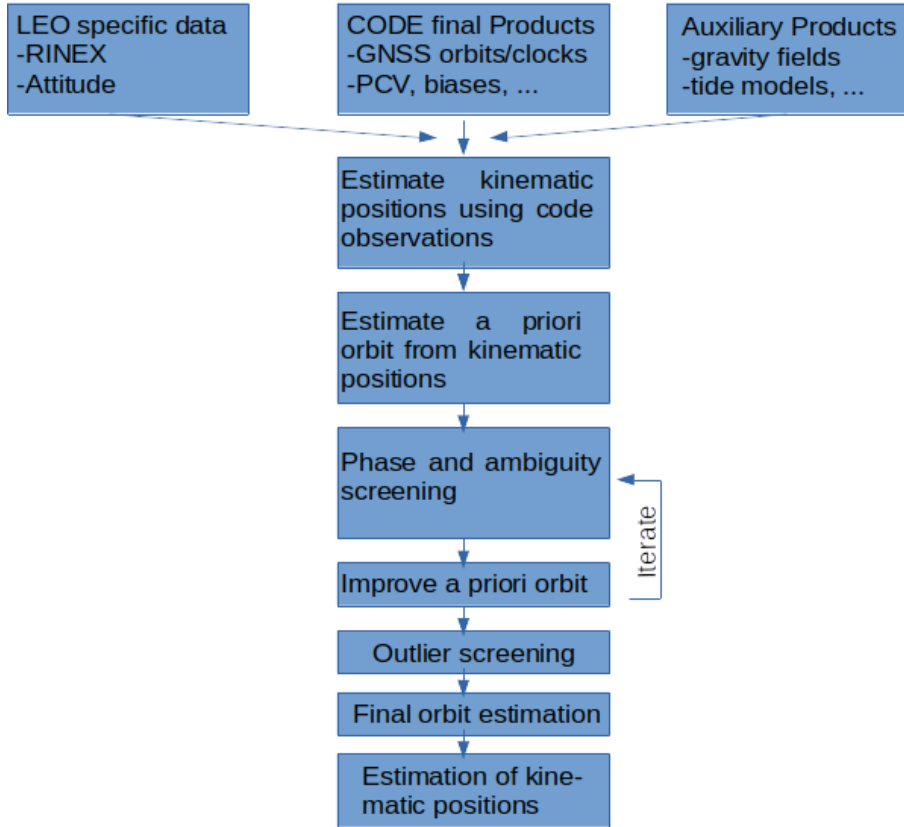


Figure 5.2: Scheme of the POD for LEO satellites at AIUB (following Jäggi [2006]).

to improve.

After the improvement of the a priori orbit is finished, a final phase screening and outlier detection are performed using the observation file's full sampling. Observations having ionosphere-free phase residuals of more than several centimeters (usually 4 cm) are rejected. The orbit used for the final screening is then used as an a priori orbit for the final orbit adjustment. The same phase observations are used for both the reduced dynamic orbit and the kinematic positions.

## 5.7 Gravity field estimation

In the Celestial Mechanics Approach, an orbit improvement is performed. First, a reduced dynamic orbit using an a priori gravity field and piece-wise constant acceleration is fitted to the kinematic positions obtained from POD. Here the covariance information of the kinematic position is used to properly weight the positions for the orbit adjustment. This reduced dynamic orbit is used to screen the kinematic positions for outliers. Two iterations are performed in this work and kinematic

positions are rejected if their residuals in radial, along-track, and cross-track directions exceed predefined thresholds. The cleaned kinematic positions are used again for a reduced dynamic orbit fit using a 24 h arc. The parameters to solve for are the orbital initial osculating elements, the empirical orbit parameters, and most importantly, the gravity field coefficients from degree 2 up to the selected degree and order. The orbital parameters and the empirical parameters are arc-wise pre-eliminated as their values are not of further interest. The daily, arc-specific normal equations are set up and stacked over longer time periods. For time-variable gravity fields, normal equations are usually stacked for one month to have sufficient geographical coverage. Several years of normal equations are stacked for static gravity fields, allowing to solve for a much higher spatial resolution of the Earth's gravity field. Eventually, the normal equation system is inverted and solved for the corrections to the a priori gravity field parameters.

## 5.8 Orbit differences and phase residuals

Especially in the case of GPS/GNSS observations used for adjusting an orbit, an internal measure of the orbit quality is obtained by comparing two types of orbits, e.g., a reduced dynamic orbit to kinematic positions. As the LEO kinematic positions are independent of the a priori force model, systematic differences can indicate potential model deficiencies, tracking artifacts, or preprocessing issues. A reduced dynamic orbit is expected to provide cm-accuracy and is much more robust than the kinematic positions. In their difference, isolated kinematic positions outside the expected noise level can be easily identified as outliers.

Particular emphasis will be put on the ionosphere-free phase residuals in the following chapters. This is the typical linear combination chosen for POD based on dual-frequency receivers in low Earth orbit, as it removes the first-order ionospheric signal. The phase advance can reach several meters even for a LEO satellite in several hundred kilometers altitude on a single frequency. Ionosphere-free phase residuals are the difference between the modeled range between receiver and GPS satellite and the measured range based on the phase observations. A reduced dynamic orbit can be used to provide the assumed best possible approximation of the true positions. However, the ionosphere-free phase residuals are affected by the estimated phase ambiguity and the epoch-specific receiver clock estimate.

## 5.9 Models and Settings used for Swarm

The precise orbit and gravity field determination for the Swarm satellites plays a key role in this work and will be frequently used in the subsequent chapters. Numerous models are used, and several parameters need to be set. As those are applied throughout this work, an overview is given at this point.

### 5.9.1 Swarm Precise orbit determination

For the POD of the Swarm satellites, daily arcs of 24 h were considered. The baseline 0401 for the Swarm RINEX and attitude files [National Space Institute - Technical University of Denmark, 2019] serving as input are used together with the final GPS orbits and clock solutions provided by CODE [Dach et al., 2020]. For the gravity field potential, the combined GOCO05S solution [Mayer-Gürr et al., 2015] is considered up to degree and order 120. For ocean tide loading, the FES2004 model [Lyard et al., 2006], and atmospheric tidal loading the Ray-Ponte model [Ray and Ponte, 2003] is used. The ocean tides are taken into account using the empirical ocean tide model EOT11a [Savcenko et al., 2012]. The sub-daily pole model is the IERS2010XY model. Nutation is modeled using the IAU2000R06 model [Petit and Luzum, 2010]. For the GNSS PCV model, the IGB08 model is used until 28th of January 2017, and afterwards replaced by the IGS14 model to ensure compatibility to the IGS orbits (see IGS Mail #6662, #6663 and #7399, <https://lists.igs.org/pipermail/igsmail>). PCV maps for the LEO satellites derived using residual stacking are also applied [Jäggi et al., 2009, 2016].

For the screening process, a reduced dynamic orbit is fitted using 96 pulses (i.e., instant changes in velocity at 15 min. spacing) in radial, along, and cross-track direction, constrained using an a priori sigma of  $5 \cdot 10^{-6}$  m/s using a 30s GPS data sampling. Eventually, the ionosphere-free phase residuals are computed at the RINEX observation file sampling (i.e., 10s sampling until 15th of July 2014, since then 1 Hz, [van den IJssel et al., 2016]), and residuals exceeding 4 cm are rejected. For the final reduced dynamic orbit, 240 piece-wise constant accelerations are set up for each day, in radial, along, and cross-track directions, which equals a 6-minute spacing. The piece-wise constant accelerations are constrained using the a priori sigma of  $5 \cdot 10^{-9}$  m/s<sup>2</sup>. The final reduced dynamic orbit is used as an a priori orbit for the kinematic positions. The Swarm orbits are also routinely computed at AIUB, IfG, and TUD in the framework of the Swarm Data, Innovation and Science Cluster (DISC) activities to provide Swarm orbit and gravity field solutions [Teixeira da Encarnação et al., 2020].

For the SLR validation, the SLRF2014 [Sinclair/RGO, 1997], consistent with the IGS14 model, is used for the whole Swarm mission. Even though this is an inconsistency when using the IGB08, the station coordinates are more accurate as post-seismic deformations can cause large deviations [Arnold et al., 2018]. For higher-order, static gravity field coefficients, the static gravity field EGM2008 is considered up to degree and order 200 [Pavlis et al., 2012]. Range corrections for the retro-reflector on-board the satellite are also applied [Arnold et al., 2018].

### 5.9.2 Swarm Gravity field estimation

In the first step, the kinematic positions obtained from POD are screened. Kinematic positions that are singular or do not have sufficient redundancy (i.e., less than 5 GPS satellites used for determination) are rejected. Furthermore, the kinematic positions are screened for gaps or already marked



positions (e.g. because of large variances, too few observations, or previous screening runs). If two marked or missing positions are less than 10 seconds apart, all observations in between are marked. The file is further screened for implausible large covariances ( $>99999$  m). The remaining positions are used to fit a reduced dynamic orbit using stochastic pulses at 30 min spacing and a constraint of 100 mm/s. The earth rotation parameters are taken from the code final product [Dach et al., 2020] and the gravity field potential from the static GRACE03S [Jäggi et al., 2010] gravity field. Ocean tides are included using the EOT11A [Savcenko et al., 2012] model, and for atmosphere and ocean de-aliasing, the AODL1B RL06 provided by GFZ [Dobslaw et al., 2017] is applied. The TIDE2000 model is used for the solid earth tides [Dehant et al., 1999].

The kinematic positions' post-fit residuals to the fitted reduced dynamic orbit are analyzed. Kinematic positions are rejected if their radial, along-, and cross-track residuals exceed 15 cm, 10 cm, and 8 cm in the first iteration and 8 cm, 5 cm, 4 cm in the second iteration. In addition, a threshold on the three-dimensional difference of 20 cm for the first and 9 cm for the second iteration is applied. These thresholds were derived empirically.

The screened orbits are further used for the gravity field improvement. The orbits are parameterized using 15 min piece-wise constant accelerations constrained by a priori RMS of  $10^{-8}$  mm/s<sup>2</sup>. Eventually, the normal equations are set up and solved for the gravity field coefficients, using the GRACE03S gravity field model again as a priori gravity field.

## 5.10 Gravity field comparison

For gravity field computations, usually, the fully normalized spherical harmonics (with coefficients  $\bar{C}_{nm}$  and  $\bar{S}_{nm}$ ) are used. Several metrics are commonly used to compare the different gravity field solution with each other: The signal degree amplitude of degree  $n$  ( $SDA_n$ ):

$$SDA_n = \sqrt{\sum_{m=0}^n (\bar{C}_{nm}^2 + \bar{S}_{nm}^2)}, \quad (5.20)$$

the error degree amplitude of degree  $n$  of the formal errors of  $\sigma_{\bar{C}_{nm}}^2$  and  $\sigma_{\bar{S}_{nm}}^2$ :

$$EDA_n = \sqrt{\sum_{m=0}^n (\sigma_{\bar{C}_{nm}}^2 + \sigma_{\bar{S}_{nm}}^2)}, \quad (5.21)$$

and, when comparing two different gravity fields a and b, the difference degree amplitude of degree  $n$

$$DDA_{ab,n} = \sqrt{\sum_{m=0}^n (\Delta\bar{C}_{nm}^2 + \Delta\bar{S}_{nm}^2)}, \quad (5.22)$$

where  $\Delta\bar{C}_{nm} = \bar{C}_{a,nm} - \bar{C}_{b,nm}$  and  $\Delta\bar{S}_{nm} = \bar{S}_{a,nm} - \bar{S}_{b,nm}$ . Frequently used in this work is the weighted RMS of geoid height differences. In order to compute the weighted RMS the geoid height

differences are computed for a grid (here  $0.5^\circ \times 0.5^\circ$ ). Towards the poles the distance between the grid points shrinks. To compensate for that effect the differences are weighted with  $\cos(\lambda)$ , where  $\lambda$  is the latitude. Other weighting functions can of course be applied depending on the objective. The weighted RMS (wRMS, see e.g. [Jean et al. \[2018\]](#)) is then computed as

$$wRMS = \sqrt{\frac{1}{\sum_{i=1}^n \cos(\lambda_i)} \sum_{i=1}^n \cos(\lambda_i) \delta_i^2}, \quad (5.23)$$

where  $n$  is the number of grid points,  $\lambda_i$  the latitude of grid point  $i$  and  $\delta_i$  the difference of geoid height of two gravity fields at grid point  $i$ .

In an analog way the weighted standard deviation is defined as

$$wSTD = \sqrt{\frac{1}{\sum_{i=1}^n \cos(\lambda_i)} \sum_{i=1}^n \cos(\lambda_i) (\delta_i - \mu_W(\delta_i))^2}, \quad (5.24)$$

where  $\mu_W(\delta_i)$  is the weighted mean, using again  $\cos(\lambda_i)$  as weighting function. The spatial resolution is either given by the resolutions of the spherical harmonics used or the filtering used. For the wSTD spherical harmonics up to degree and order 20 are taken into account in this work. For the wRMS differences up to degree and order 70 are taken into account, but a Gaussian smoothing with 400 km radius is applied, resulting in a spatial resolution of 603 km according to [Vishwakarma et al. \[2018\]](#).

## 5.11 Comparing the Swarm and GRACE monthly gravity fields

Monthly GRACE gravity fields derived using GPS and K-band are of a much higher quality than the Swarm GPS-only gravity fields. A combination of both satellite missions became attractive as the GRACE satellites could not continue collecting continuous data caused by the GRACE-B satellite's battery aging. Its accelerometer had to be switched off, and the K-band instrument had to be set inactive to keep the satellite operational when entering the Earth's shadow. Consequently, gravity fields using K-Band could not be computed for some months, starting in 2011. The gaps became more pronounced, and eventually, in October 2017 GRACE was decommissioned after exceeding the planned mission duration of five years by a factor of two. The last month for which a GRACE gravity field solution was computed by ITSG is May 2017, whereas a significant degradation was already observed from Aug 2016 on [[Mayer-Gürr et al., 2018](#)]. GRACE-FO continued the GRACE mission. However, the gap between those two missions is more than one year. The first GRACE-FO gravity field could be computed for June 2018. Due to an instrument failure, eventually recovered in October 2018, the GRACE-FO gravity fields for August and September 2018 are missing [[JPL, 2018](#)]. Those gaps of single months and more than one year between

GRACE and GRACE-FO, motivated completing the timeline of the GRACE(-FO) monthly gravity fields using Swarm GPS-only gravity fields, even though they had to rely on GPS-only. Several studies were performed comparing the monthly gravity fields obtained from GRACE and Swarm to investigate what accuracy is expected from Swarm GPS-only gravity field compared to the GRACE(-FO) Solutions. Among those, the study of [Meyer et al. \[2019\]](#), in which the Swarm time series was compared to GRACE time series. The GRACE solutions were limited to degree and order 10 for the comparison. The capability of measuring the Greenland timeline using Swarm could be demonstrated for the overlap months when even though the Swarm gravity field solutions show a somewhat larger monthly variability and can not compete with GRACE's spatial resolution. The comparison was carried out up to degree and order 6 to match the SLR-derived gravity field's resolution. Another study was performed by [Lück et al. \[2018\]](#). In this study, the ocean mass change was estimated and compared for the ITSG-GRACE solution and Swarm gravity fields from different processing centers. Among those are the Institute for Geodesy, Hannover, Germany (IfG), Institute for Geodesy and Geoinformation, Bonn, Germany (IGG), Astronomical Institute of the Czech Academy of Science (ASU), and AIUB. The comparison was carried out up to degree and order 12. Also, in this study, higher monthly variability in the Swarm gravity fields could be observed. Nevertheless, the gravitational signal of the Ocean mass change could also be observed using the Swarm timeline. The conclusion drawn is that Swarm GPS-only gravity can bridge larger gaps in the GRACE timeline, but only to a limited spatial resolution.



## Chapter 6

# Identification and mitigation of problematic GPS observations

Under certain conditions, variations in slant TEC can cause issues for accurate tracking. Besides the loss-of-lock of the signal to a certain GPS satellite [Xiong et al., 2016b], which causes gaps in the GPS observations and, therefore, can weaken the POD, also systematic artifacts in the kinematic positioning can occur. The root-cause will be further examined in Chap. 7 for GPS data of the Swarm mission. As those artifacts are deterministic, they cause systematic errors near the geomagnetic equator in the GPS-only gravity fields, especially for GOCE and Swarm because of their low altitude and, therefore, large variations in the ionospheric signal content [Zehentner and Mayer-Gürr, 2015, Jäggi et al., 2016]. How pronounced these systematic errors become depends on the receivers loop filter implementation. For the GRACE mission, having also low altitude, missing GPS observations near the geomagnetic equator were observed [Arnold et al., 2016].

Different approaches were examined to investigate how to identify and mitigate those artifacts' impact on the gravity field determination. Details on the models used and the preprocessing regarding the screening of the kinematic positions in the gravity field processing can be found in Sect. 5.9.2. In the case of Jäggi et al. [2015], differences of the geometry-free linear combination for subsequent epochs were examined for the Swarm mission, and criteria were established to identify observations that cause the artifact. In case their absolute difference exceeded 2 cm/s, the observation was removed from the receiver RINEX file used in the orbit processing. The second approach used by Zehentner and Mayer-Gürr [2015] for the GOCE mission did not reject the observations. Instead, the weight of the observations for the orbit determination was reduced. The ROTI using a 61 s symmetrical window was used to determine the weight. The ROTI value was multiplied by 20 and then used as observation specific  $\sigma$  in the least-squares orbit adjustment. Using weighting, no observational gaps were introduced compared to the "hard" screening when using epoch differences in the Swarm case.

This chapter further examines how the affected phase observations may be identified using higher-

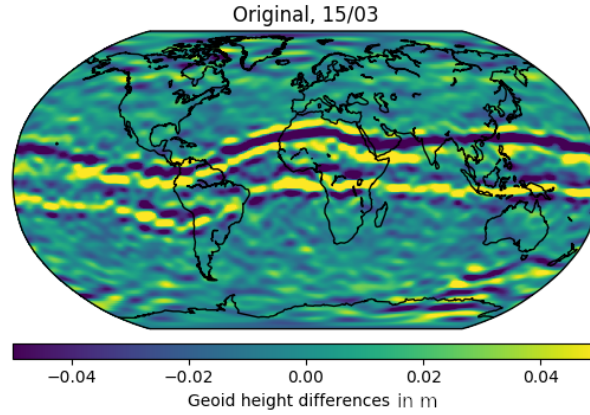


Figure 6.1: Geoid height differences between the monthly Swarm GPS-only gravity field and the JPL-GRACE-RL06 for March 2015.

order time derivatives of the geometry-free linear combination and also using the ROTI-based weighting. Instead of a strict screening, it is investigated how empirical weighting based on the time derivatives and the ROTI approach is suited to mitigate the ionospheric artifacts. The results of this study were published in [Schreiter et al. \[2019\]](#). Special emphasis is given to March 2015 (one of the most heavily affected months) and June 2016 (less solar activity, tracking loop updates already performed, similar local times as March 2015). After briefly introducing artifacts and previous studies, the cause of the artifacts is traced down to orbit solutions and the GPS phase observables. Criteria based on time derivatives of the geometry-free linear combination are developed and used to down weight and mitigate affected observations' impact. Eventually, the success will be assessed based on SLR residuals and gravity field comparisons. As a bonus, one criterion used is further developed to identify equatorial plasma depletions.

## 6.1 Ionospheric artifacts in Swarm kinematic positions and gravity fields

It was shown in earlier studies for GOCE [[Jäggi et al., 2015](#)] and Swarm [[Jäggi et al., 2016](#), [Dahle et al., 2017](#)] that the ionosphere causes the artifacts in the gravity field solutions in combination with the narrow L2 bandwidth. Modifications on the L2 bandwidth helped to reduce the artifacts (see Tab. 7.1 in Chap. 7). The region near the geomagnetic equator is well known for large values

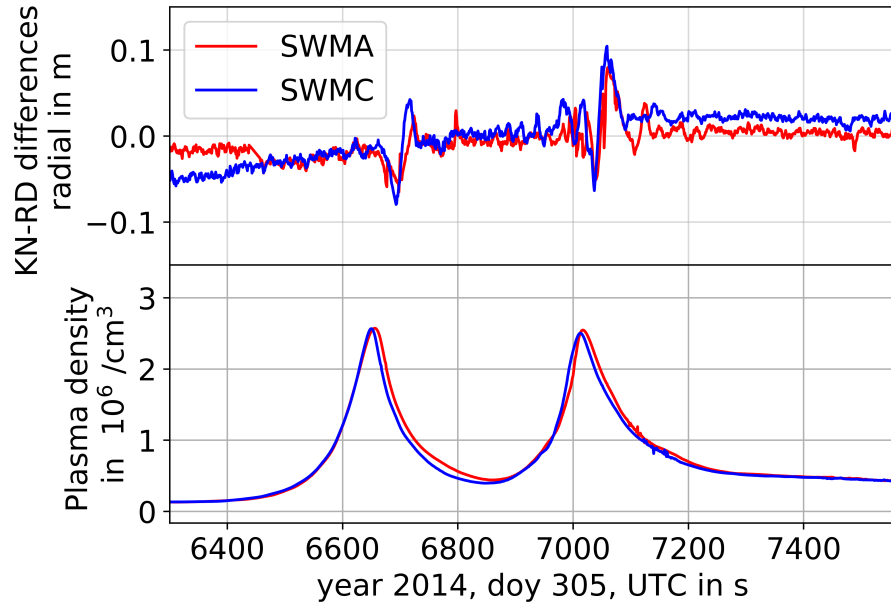


Figure 6.2: Radial differences between Swarm reduced dynamic orbits and kinematic positions for Swarm A and Swarm C (top). The bottom plot shows the ambient plasma density as measured by the Swarm Langmuir probes.

in vertical TEC and electron density. The ionization crests near the geomagnetic equator caused by the Appleton anomaly (see Sect. 2.5) can be reliably identified in the in situ Swarm plasma density measurements. The crests are usually located around  $\pm 10^\circ$  of the geomagnetic equator. This is also the region where the most significant systematic differences in the GPS-only monthly gravity fields are observed (see Fig. 6.1). The differences between kinematic positions and a reduced dynamic orbit are compared to the ambient plasma density measured by the Langmuir probes to investigate the relation between the systematic differences and the Appleton anomaly. As the reduced dynamic orbit offers more stiffness than kinematic positions, it is less susceptible to ionospheric disturbances. The piece-wise constant accelerations are spaced at six-minute time intervals. Thus variations in the orbit differences below six minutes can be attributed to the kinematic positions. For details on the orbit processing, see Sect. 5.9.1. The comparison of the orbit differences to the plasma density is shown in Fig. 6.2. Especially around the sharp peak in plasma density, spikes of a few centimeters are observed in the orbit differences. There is a notable delay of several seconds between the orbit differences and the plasma density measurements. This offset is caused by the ray geometry (most observations have an azimuth of 90 to 270 degrees in the antenna frame, thus the links "look" backward) and also by the loop filter characteristics (see Chap. 7). Investigating the ionosphere-free GPS phase residuals at the respective epochs (see Fig. 6.3, top) the epoch wise variance over all GPS-satellites is becoming larger, indicating an inconsistency

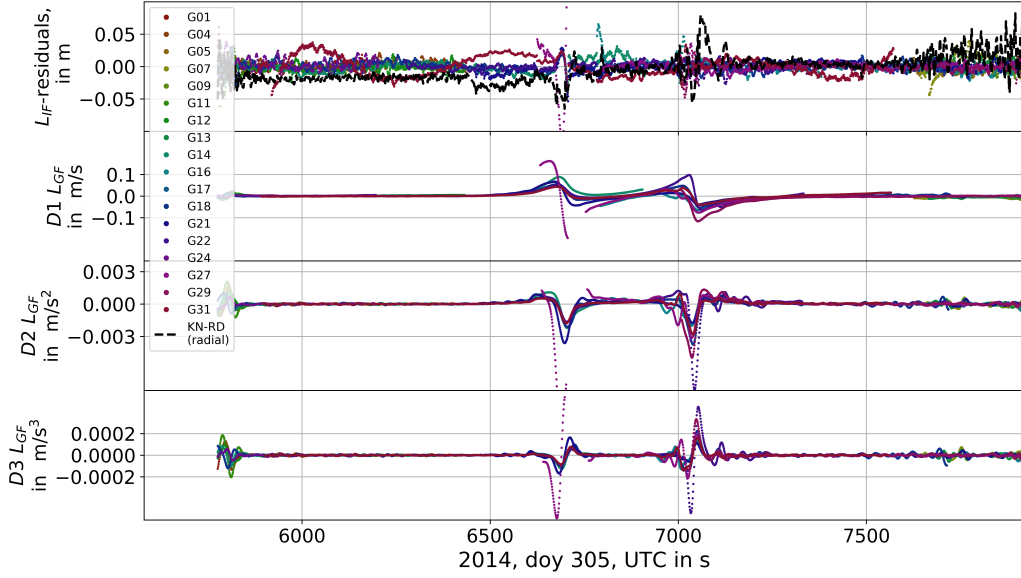


Figure 6.3: Ionosphere-free phase residuals of Swarm A reduced dynamic orbits (top) and first (D1), second (D2) and third (D3) time derivatives of the geometry-free linear combination using smoothing and a Savitzky-Golay filter for 1st of November 2014 (doy 305).

in the phase observables. The degradation occurs almost at the same epochs, where the measured plasma density has its peaks (see Figs. 6.2 and 6.3, top curves). Because the GPS-receiver moves with a large velocity in earth-centered quasi-inertial space (about 7.7 km/s), large gradients in the plasma density are clearly reflected in the geometry-free linear combination. The variability of the geometry-free linear combination of the simultaneously observed satellites is shown in Fig. 6.3, second plot. It is highly dependent on the line of sight. Thus a suited criterion needs to be able to identify the affected epochs for each LEO-GPS link independently and derive appropriate weights.

### 6.1.1 Radial variances

The weights will directly affect the covariance information of the derived kinematic positions. A short analysis of the radial variances is performed to compare the different solutions for the kinematic position directly. It may be used as an indicator for the quality of kinematic positions. Based on this, the kinematic positions may be weighted in the subsequent for gravity field determination (see Sect. 5.9.2). As shown by Jäggi et al. [2011c], this basically represents the observation scenario's geometry. Suppose some kinematic positions have a high variance regarding their x, y, and z component. In that case, their impact on the gravity field solutions is small because they get



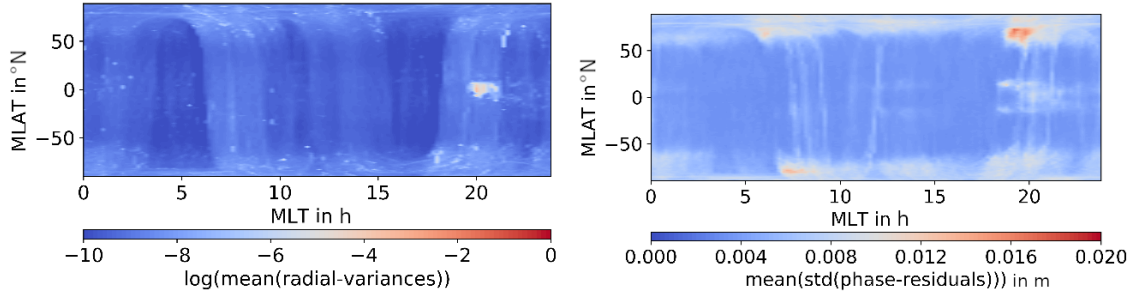


Figure 6.4: Mean radial variances (left) and mean spreading of phase residuals (right) in magnetic coordinates for the analyzed test period.

properly down-weighted according to the covariance information. This information is essential to mitigate the impact of problematic positions on the fitted orbit. Because it is shown in Sect. 6.1, that the spikes are associated with a spreading of the phase residuals (i.e., their epoch wise standard deviation increases), the radial variance obtained from the covariance information is compared to the epoch-wise standard deviation of the phase residuals over all satellites used in the orbit determination (see Fig. 6.4). Large outliers are screened in the preprocessing. Magnetic latitude and magnetic local time are used as a coordinate system because the artifacts are most prominently visible around the magnetic equator in the evening hours. For the kinematic radial variances, the formal error propagation in the radial direction

$$\sigma_r^2 = (1/r^2) \cdot (x^2 \cdot k_{xx} + y^2 \cdot k_{yy} + z^2 \cdot k_{zz} + 2 \cdot x \cdot y \cdot k_{xy} + 2 \cdot x \cdot z \cdot k_{xz} + 2 \cdot y \cdot z \cdot k_{yz}), \quad (6.1)$$

is used, where  $x, y$  and  $z$  are the coordinates in an earth fixed system and  $k_{xy}$  denotes the covariance between  $x, y$  and  $r = \sqrt{x^2 + y^2 + z^2}$  is the geocentric distance. This is used to represent the quality of the 3D-positions in the radial direction. On the other hand, the standard deviation of the phase residuals over all satellites at a specific epoch is used. These values were binned, and the mean of each box was computed. For a better visibility, the logarithm was used for the kinematic variances. The lowest values are observed in mid-latitude regions, whereas in the polar regions, the radial variances and the standard deviations increase in both figures. Besides, both figures show large values near sunset in the equatorial regions. There are notable differences, especially around the magnetic poles, where large ionosphere-free phase residuals are more frequently observed. Another difference can be seen around the geomagnetic equator. In this region, the high standard deviation in phase residuals is also affecting earlier magnetic local times. The latitudinal distribution shows deviations as well compared to the more significant variances being observed in kinematic positioning. For both plots, the same months (analyzed test period: 2015: Jan., Mar.; 2016: Feb., Mar., Jun., Jul., Aug.) were used, and only kinematic positions with a minimum redundancy of 5. No additional weighting or screening was performed apart from the outlier screening in the orbit processing. As shown by Xiong et al. [2016b], the loss of locks of the Swarm GPS

receivers is highly correlated to ionospheric plasma depletions. Loss of lock corresponds to the worst-case scenario. Even without considering loss of lock events, it is shown in Fig. 6.4 that the kinematic radial variances also generally increase in the potential bubble regions, i.e., after sunset (18 – 22 mLT) and near the geomagnetic equator. In this work, the investigations are extended by checking the radial variances of the unweighted and un-screened kinematic positions for Swarm for a longer time span. As shown in the previous section, the phase residuals increase around the peaks in plasma density, indicating a potential degradation of the phase observables or a weaker geometry due to screened GPS-observations or possible loss of locks.

In Fig. 6.5 the radial variances are binned in  $1^\circ \text{ lon} \times 1^\circ \text{ lat}$  and averaged using unweighted kinematic positions from 11/2013 – 12/2017 of all three Swarm satellites. The observations required are taken from the routinely processed unscreened Swarm kinematic positions provided on the AIUB FTP server (see Sect. 5.9.1) where only positions with sufficient redundancy were used (i.e., at least 5 GPS satellites). Figure 6.5 shows that parts of the geomagnetic equator are clearly visible, showing the most considerable radial variances. This effect is mainly caused by equatorial plasma depletions causing loss of lock, or large phase residuals leading to a rejection of the observation in the pre-processing. If one reproduces this plot in mLT and mlat (compare Fig. 6.4, left), a very pronounced peak around 18 – 22 mLT becomes visible around  $0^\circ \text{ mlat}$ . It should be noted that the period used for Fig. 6.4 is defined by the analyzed test period, and by this, it is shorter than in Fig. 6.5. Nevertheless, the observed patterns are almost identical to the results of Xiong et al. [2016b], even if loss of locks or data gaps for all GPS-satellites are by construction not included in the presented figures. These results again support the statement that the GPS data quality suffers significantly from high activity in the magnetic-equatorial ionosphere at evening hours and, of course, due to equatorial plasma bubbles (see Fig. 6.4, left). Some observations are rejected in the orbit processing because they are considered outliers and show large phase residuals of a few centimeters or due to gaps or small observation pieces. This screening is performed to avoid those data problems propagating into the orbit solution. Even though this screening process applies especially in the nighttime hours, it does not seem to detect the observations responsible for the spikes in the kinematic positioning. Fewer observations partially cause the high variances in the equatorial regions, as loss of lock caused by bubbles occurs, and also post-sunset local time observations are more frequently screened near the equator (see Fig. 6.6, right). The mean number of observations rejected in the preprocessing is shown in Fig. 6.6. As before, only valid kinematic positions with enough redundancy were used. The mean difference between the number of observations in the RINEX file and the observations used for the final kinematic positioning, after phase measurements with ionosphere-free phase residuals larger than 4 cm to a screening orbit were removed, is shown in Fig. 6.6.

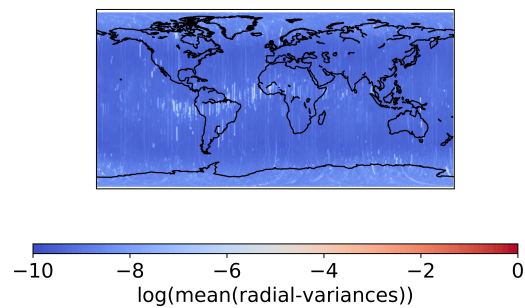


Figure 6.5: Radial variances binned for a longer time span in geographic coordinates, Nov. 2013 - Dec. 2017.

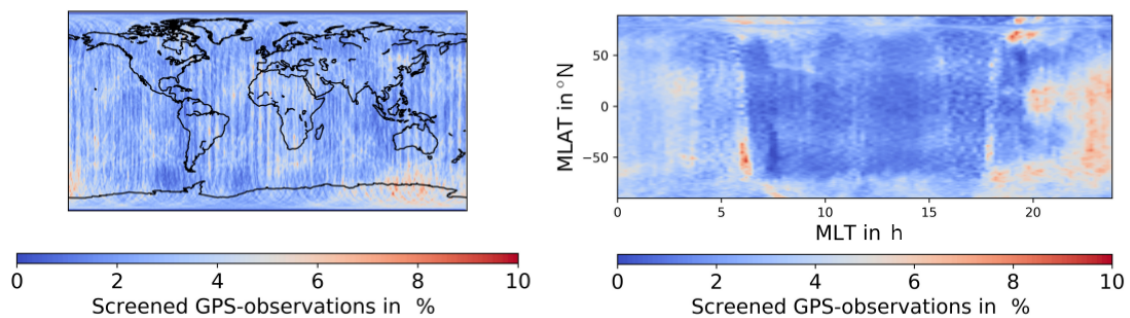


Figure 6.6: Percentage of rejected GPS-observations rejected in the preprocessing for the analyzed test period. Left: geographic coordinates, right: magnetic coordinates.

### 6.1.2 Comparing to slant TEC

It is doubtful that the ambient plasma density itself actually causes the observational artifacts in the GPS phase observables, as the in situ plasma density does enter the GPS observations. However, the integrated electron density along the line of sight, also called slant TEC, enters. In the following, criteria are established for the occurrence of the degradation in the ionosphere-free phase residuals. Numerical derivatives of the geometry-free linear combination are used because their dynamics are directly proportional to the slant TEC. An important benefit in this approach: the geometry-free linear combination can be directly computed from the GPS RINEX file. No external information, e.g., an a priori orbit based on an underlying gravity field, is needed.

### 6.1.3 AIUB standard screening

As a reference, the AIUB standard screening is used as it is published in [Jäggi et al. \[2016\]](#). It successfully removes the artifacts, although the orbit quality was weakened, and the number of ambiguities increased. Because it is a derivative-based approach, it can be used as a direct reference to our weighting solutions. In the AIUB standard screening, an approximation of the first time derivative of the geometry-free linear combination is computed without any smoothing using differences between observations of consecutive epochs

$$\dot{L}_{gf}(t_i) \approx \frac{L_{gf}(t_{i+1}) - L_{gf}(t_{i-1})}{t_{i+1} - t_{i-1}}, \quad (6.2)$$

which is equivalent to the three-point differentiating scheme shown in Sect. 6.2.1, where a quadratic polynomial is fitted to the observations at  $t_{i-1}$ ,  $t_i$  and  $t_{i+1}$  and the first time derivative is computed. Comparing this method to the differentiating scheme that is applied in the next section (compare Fig. 6.7) differences are visible, but both derivatives show similar amplitude and shape. If the first time derivative's absolute value exceeded 2 cm/s, the observation was removed from the RINEX observation files. This introduces data gaps which are mostly responsible for the increased number of ambiguity parameters due to a very conservative set up of new ambiguity parameters if data gaps are longer than 61 s. This could be overcome by setting up the ambiguity parameters based on the unscreend data. In cases in which too many observations had to be removed, the kinematic positions could not be computed anymore.

## 6.2 Appropriate weighting of the GPS phase observations

This section describes the methods applied to identify and estimate appropriate weights to apply in the orbit least squares adjustment. First, a method to reliably derive time derivatives from noisy data is developed. Furthermore the ROTI is used for weight estimation.

Table 6.1: Filter settings

Filter	window width	window type	min. points	additional
Gaussian	10.1 s	symmetric	10	bandwidth 10 s
Savitzky-Golay	12.5 s	symmetric	7	polynomial degree 1

### 6.2.1 Computation of derivatives for the geometry-free linear combination

Due to the noise of the geometry-free linear combination, the computation of meaningful derivatives is not straightforward. A combination of a Gaussian filter and a Savitzky-Golay filter is applied to obtain reliable derivatives. First, data is smoothed using the Gaussian filter, and then the Savitzky-Golay filter is applied to obtain the next order derivative. This process is iterated until the desired order of the derivative is obtained. This approach allows keeping the window size and the degree for the Savitzky-Golay filter low. Alternatively the weights from the Gaussian filter may be Incorporated into the Savitzky-Golay filter. This reduces the higher-order derivatives' sensitivity to noise, as the Savitzky-Golay filter uses a polynomial fit. A jump and outlier detection with a threshold of 0.5 m/s, applied on the differences of subsequent epochs of the geometry-free linear combination, is performed before applying the filters. If larger jumps occur, the arcs are split to avoid any contamination of the derivatives. This action was also performed in case of gaps of one or more epochs in the 1 Hz RINEX data. The filter parameters (see Tab. 6.1) were determined empirically by using an artificial signal (Fig. 6.7) and original Swarm RINEX data. Especially in the Gaussian filter case, it is essential to choose the parameters such that the window is almost entirely populated (with the mentioned setting: max. one epoch missing) and symmetrically occupied. Otherwise, the smoothed points may be biased to the previous points' mean and forcing the derivatives to zero. If it is not possible to compute the derivative due to jumps, gaps, or not enough data, the corresponding epochs are marked to set weights manually at a later stage (see Sect. 6.2.2). In the orbit processing, these observations are supposed to be down-weighted.

In Fig. 6.3 a short time series of phase residuals and the corresponding derivatives during one equatorial pass are shown. The second and third time derivative is more localized and pronounced on the epochs where the spikes occur than the first time derivative. The higher derivatives show comparatively larger amplitudes at the boundaries, which correspond to the polar regions, indicating that the derivatives' quality might suffer from observation noise.

An artificial signal is generated to check the adopted differentiating schemes' consistency and to validate them, including random jumps, observation gaps, and random noise. The signal was simulated by  $f(t) = \sin((100t)^2)$  where  $t$  is measured in days. White noise with a standard deviation of 5 cm was selected. The number of jumps and the number of gaps was set to 40, and the locations were determined randomly. A Gaussian random variable gives the jump sizes with a standard deviation of 5 m, and a Poisson random variable determines the length of gaps in seconds with the parameter  $\lambda = 100$ . The signal was chosen to be represented by a sinusoidal signal with

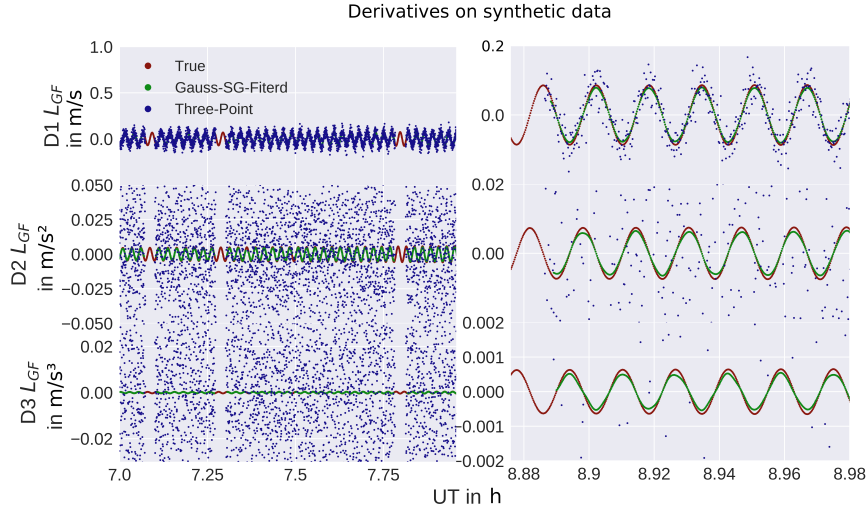


Figure 6.7: Tests on synthetic data for the first (D1), second (D2), and third (D3) time derivative of the geometry-free linear combination. Red points show the true analytic noise-free derivative, green the computed derivatives from noisy data using the filter settings from Tab. 6.1 and blue points the three-point derivative scheme. The noise in the second and third plots, visible as blue points, exceeds the axis's limit. The right side shows a zoom to compare the true derivative with the Gauss-Savitzky-Golay filtered derivative.

frequencies changing as a function of time, allowing for evaluation of the differentiating scheme's performance with frequency. In Fig. 6.7 the following two cases are compared. First, the derivatives are computed with an almost non smoothed differentiating scheme using no Gaussian filter and only three points for the Savitzky-Golay filter. Second, the differentiating scheme with the settings mentioned earlier is used. If the smoothing is too weak, as one can see in the three-point case, the derivatives become noise-dominated. With the stronger smoothing, a dampening of the higher frequencies is observed. The dampening is approximately 10%, 15% and 25% for the first, second, and third derivatives at 0.015 Hz). However, the derivatives obtained represent the signal dynamics of the true derivative. The gaps in the derivatives are given by artificial gaps in the data but were further enlarged due to the minimum number of points restriction (see Tab. 6.1).

### 6.2.2 Weights for the GPS phase observations

After numerically computing the time derivatives, empirical thresholds are applied. These thresholds were set by checking the magnitude of the derivatives, evaluating the performance on the gravity field retrieval, and the threshold used by Jäggi et al. [2016]. Appropriate thresholds were found by empirical tests to be 2 cm/s for  $|\frac{dL_{gf}}{dt}|$ , 0.025 cm/s<sup>2</sup> for  $|\frac{d^2L_{gf}}{dt^2}|$  and 0.00075 cm/s<sup>3</sup> for



$$\left| \frac{d^3 L_{gf}}{dt^3} \right|.$$

If the absolute value of the selected time derivative at a certain epoch exceeds the threshold, an observation specific  $\sigma^2$  of 21 mm<sup>2</sup> (standard  $\sigma^2$  of 1 mm<sup>2</sup> + 20 mm<sup>2</sup>) is assigned to the observation instead of a standard, uniform  $\sigma^2$  of 1 mm<sup>2</sup> to the L1 (and L2) observations. This kind of extreme down-weighting is used to reproduce a similar impact on the orbit as the standard screening. However, because the observations stay in the RINEX observation file and the resulting normal equation system, no gaps are introduced, no additional ambiguities that would weaken the orbit solution. In case an observation epoch was close to a gap or a jump, and no derivative could be computed, the data point was down-weighted as well, assuming that the observation might be affected. The third time derivative suffers most from enlarged gaps due to non-computable derivatives. The gravity field recoveries based on correspondingly generated kinematic orbits turned out to be of inferior quality. For that reason, only the first and second time derivatives are considered in the following sections.

For the first time derivative, the threshold was set to 2 cm/s to obtain similar results as with the AIUB standard screening to have a zero-test and gain additional insight into the difference between rejecting and weighing observations.

### 6.2.3 Identification using the Rate of TEC index

The ROTI-based weighting was used by Zehentner and Mayer-Gürr [2015] for the GOCE orbit processing. For GOCE, similar issues have been observed as for Swarm near the geomagnetic equator [Jäggi et al., 2015]. In analogy to Sect. 6.2.2 observations were down-weighted with a variance of 21 mm<sup>2</sup> if the number of data points was below a threshold of 10 for a 10.1 s window, and thus no reliable ROTI can be computed. For the ROTI approach, two different scaling functions are assessed. First, the scaling function that was applied by Zehentner and Mayer-Gürr [2015] for GOCE, which reads  $\sigma^2 = \max(1, 20 \cdot ROTI)$  mm<sup>2</sup>. This approach, however, turned out not to have a significant impact on the Swarm data, likely due to the number of channels or different tacking loops. Therefore the scaling is modified for the weighting using an empirical scaling factor to

$$\sigma_{AIUB-ROTI}^2 = \max(1, 60 \cdot ROTI) \text{ mm}^2. \quad (6.3)$$

Alternatively, N. Zehentner, 2017 (private communication) proposed for Swarm the following scaling function:

$$\sigma_{GRAZ-ROTI}^2 = e^{20 \cdot ROTI} \text{ mm}^2. \quad (6.4)$$

In case the ROTI is small, both approaches should return a  $\sigma^2$  close to 1 mm<sup>2</sup>. In case of high fluctuations, where ROTI gets large, the second weights are much smaller. The first set of weights will be referred to as AIUB-ROTI, the latter as Graz-ROTI. As shown in Fig. 6.8 the ROTI weights are particularly pronounced in regions where the ionosphere-free phase residuals are large. ROTI turned out to be most effective in the polar regions due to plasma density fluctuations.

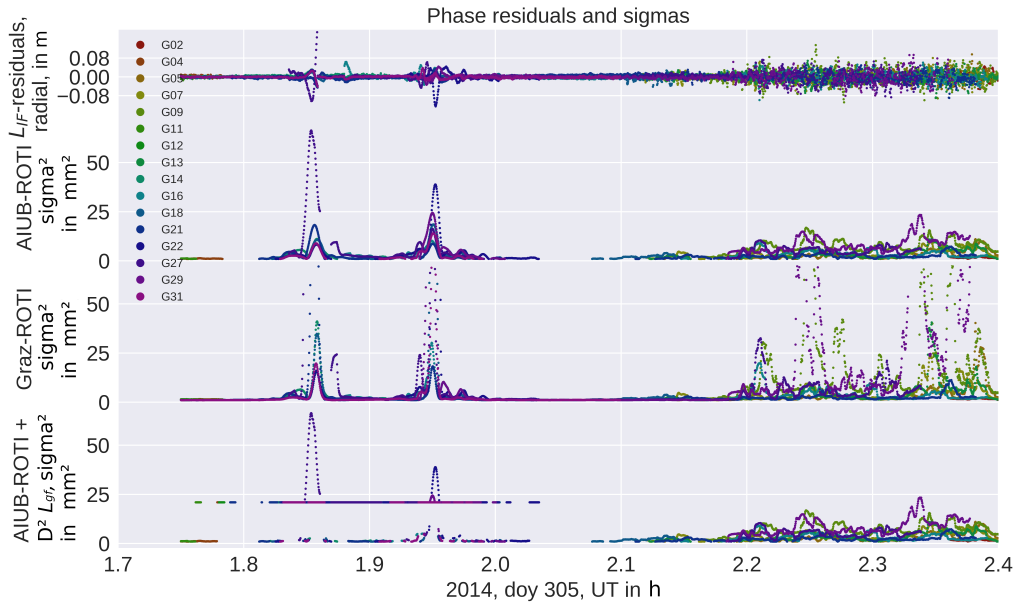


Figure 6.8: From top to bottom: Ionosphere-free phase residuals, AIUB-ROTI variance, Graz-ROTI variance, and AIUB-ROTI combined with the second derivative. The time span from 1.8 h UT to 2.0 h UT corresponds to an equatorial pass, and from 2.1 h UT to 2.4 h UT corresponds to a polar pass. The ROTI variances are larger at the polar region. The second derivative with a fixed sigma square exceeded the threshold (bottom) in near-equatorial regions. Only variance unequal to  $1\text{mm}^2$  were plotted.



### 6.2.4 Geographical restriction of down-weighting

The motivation for weighting is to reduce the impact of the artifacts induced by the equatorial ionosphere on the gravity field models and consequently improve their quality. Some of the derivative-based approaches led to a degradation of the gravity fields in polar regions, as shown in Sect. 6.3. The derivative-based weighting is limited to equatorial regions with geographic latitude between  $-50^\circ$  N and  $50^\circ$  N to avoid this degradation. Due to the shape of the geomagnetic equator (which is located between roughly  $\pm 13^\circ$  latitude) and the equatorial ionization anomaly, which is located between  $-20$  mlat and  $20$  mlat [Whalen, 2000], this covers the entire equatorial ionosphere. For the ROTI approaches, no such limitation was performed due to the positive effect in the polar regions. The localized weighting will be referred to as equatorial (eq.).

### 6.2.5 Combination of methods

The ROTI approach performs better in the polar regions, as will be shown in Sect. 6.3. The derivative-based approaches are, however, more powerful in removing the equatorial artifacts. Conclusively it is natural to combine both methods. Because the scaling function in the case of the AIUB-ROTI provides less extreme weights, it is selected for a combination with the weights obtained from the second derivative. This is achieved by taking the maximum of the AIUB-ROTI sigma square and the second derivative based sigma square in the equatorial regions (compare Fig. 6.8).

## 6.3 Gravity field recovery using weighted GPS data

In this section the orbit and gravity field solution obtained when using weighted GPS phase measurements are analyzed. The impact of the weighting approach is assessed with respect other gravity field solutions, SLR validation, consistency between reduced dynamic orbit and kinematic positions, and covariance information.

### 6.3.1 GPS-only Gravity field recovery using weighted GPS data

The corresponding monthly JPL-GRACE-RL06 [Yuan, 2018] gravity field models are used as a reference field to validate the computed gravity fields. Due to the ultra-precise K-band inter-satellite measurements, the GRACE gravity fields are of very high quality and essentially free from systematic ionospheric errors. GRACE GPS-only gravity fields are mostly free from systematic ionospheric errors, but many observations are missing around the geomagnetic equator in the GRACE RINEX files, too (Jäggi et al. [2016], Fig. 12). In Fig. 6.10 (top left), the geoid height differences between the JPL-GRACE-RL06 gravity field and a monthly Swarm GPS-only

gravity field using the reference orbits with a uniform observation specific variance (unweighted) is shown. The differences are computed by taking the gravity fields up to degree and order 70 into account. The displayed month, March 2015, is heavily affected by the artifacts, as is shown later in Fig. 6.9 and can also be seen later in Fig. 6.18. The stripes around the geomagnetic equator are clearly visible with an amplitude of more than 4 cm in geoid height when adopting a Gaussian filter radius of 400 km. These two bands have virtually disappeared in the gravity fields obtained using the AIUB standard screening (top, right).

As a first step, the AIUB standard screening is compared to the weighting based on the first derivative (Fig. 6.10, second row, left). This zero test shows similar performance as the standard AIUB screening, but it seems to add some additional small scale artifacts near Colombia and east of South America. The different behavior may be explained by Fig. 6.15 where the numbers and locations of the positions that were actually used for the gravity field recovery are compared. The standard screening removes almost all positions in that specific area, in contrast to the weighting, where the positions are preserved, but minor artifacts may appear instead.

The second derivative has a similar performance when compared to the AIUB standard screening. In particular, the artifact in the pacific region could be successfully removed. In contrast to the standard screening, the noise seems to be slightly reduced. This can be concluded from Fig. 6.10 and Tab. 6.2 and Tab. 6.3 considering the geographically weighted RMS of geoid height differences and the weighted standard deviation over the ocean. If the second derivative with no geographical restrictions is used, more significant fluctuations around the polar regions appear. For this reason, the second derivative-based weighting is limited to the equatorial regions.

The ROTI approaches are not very successful in removing the two bands around the geomagnetic equator. In the polar regions, however, the ROTI based gravity fields show reduced noise (see Fig. 6.10). The noise reduction of the ROTI approaches is confirmed by the geoid RMS as well as by the weighted standard deviation over the oceans in Tables 6.2 and 6.3. This is also supported by the different degree amplitudes shown in Fig. 6.11. For degrees above 25 the difference between both ROTI approaches are among the lowest. It implies that small-scale fluctuations are successfully reduced. A different result is obtained for spherical harmonic degree 15 to 25. In this spectral band, the derivative-based screening and weighting approaches outperform the ROTI solutions.

The AIUB screening shows a slightly better performance than the weighting based on the second time derivative in the low degrees ( $< 10$ ). However, in most higher degrees, the new approach shows a similar or even better performance. After smoothing, e.g., using a Gauss filter, errors from higher degrees may become visible in the plotted geoid height differences.

Eventually, a combination of AIUB-ROTI and the second derivative limited to the equator is considered using both approaches' maximum sigma square. The differences in the gravity field, see Fig. 6.10, still show some increased noise around the geomagnetic equator, but it is about the same level as the gravity field obtained using the second derivative based weighting. Especially in the region over Greenland, the gravity field benefits from the ROTI weighting. Looking again

Table 6.2: Gravity field evaluation and SLR-Residuals statistics for Swarm A, March 2015.

Scenario	# Kin. Pos.	L1 RMS [mm]	Geoid RMS [mm]	wStd Ocean (d/o 20) [mm]	RD mean (SLR)[mm]	RD std (SLR)[mm]	KN mean (SLR)[mm]	KN std (SLR)[mm]
Original	696060	2.78	28.6	24.9	4.6	27.3	2.4	31.1
Std. scr. $dL_{gf}/dt$	636633	2.75	18.9	21.6	3.7	26.9	0.7	31.4
Wgt. $dL_{gf}/dt$	689895	2.65	18.3	20.9	4.6	27.6	2.0	32.7
Wgt. $d^2L_{gf}/dt^2$ , eq.	693648	2.64	17.4	20.5	4.6	27.3	1.9	32.5
Wgt. AIUB-ROTI	700503	2.18	18.9	22.0	4.9	26.5	1.0	28.8
Wgt. Graz-ROTI	700155	2.11	18.6	21.8	5.0	25.8	0.9	28.7
Wgt. AIUB-ROTI + 2nd der.	700569	2.14	16.7	20.9	5.0	26.0	0.6	29.3

Table 6.3: Gravity field evaluation and SLR-Residuals statistics for Swarm A, June 2016.

Scenario	# Kin. Pos.	L1 RMS [mm]	Geoid RMS [mm]	wStd Ocean (d/o 20) [mm]	RD mean (SLR)[mm]	RD std (SLR)[mm]	KN mean (SLR)[mm]	KN std (SLR)[mm]
Original	783996	2.03	11.4	19.1	3.3	14.0	1.7	16.4
Std. scr. $dL_{gf}/dt$	783153	2.01	12.0	19.2	3.2	14.2	1.7	16.6
Wgt. $dL_{gf}/dt$	783822	1.95	11.3	19.1	3.2	14.1	1.6	16.5
Wgt. $d^2L_{gf}/dt^2$ , eq.	783714	2.01	11.8	19.1	3.3	14.0	1.7	16.4
Wgt. AIUB-ROTI	784182	1.70	9.5	19.0	3.4	14.1	1.4	16.5
Wgt. Graz-ROTI	784209	1.64	9.8	19.1	3.4	14.2	1.4	16.4
Wgt. AIUB-ROTI + 2nd der.	784128	1.69	9.7	19.2	3.3	14.2	1.3	16.7

at the degree difference amplitudes (Fig. 6.11), the light blue line is among the lowest for almost all degrees.

A longer time series of monthly Swarm gravity fields is computed and compared to the monthly JPL GRACE-RL06 gravity field solutions to assess the effect of weighting. For January and February 2015, the JPL solution was replaced by the more robust CSR GRACE-RL06 gravity field solution Bettadpur [2018]). As criteria, the wRMS of geoid height differences is used. The results are shown in Fig. 6.9. Especially in early 2015, it may be recognized that the weighting approaches achieve a wRMS at the level of 15 mm to 17 mm instead of roughly 20 mm to 30 mm for the un-weighted solution. After May 2015, Swarm C's original solution significantly improves compared to the original solution for Swarm A. This date coincides with the updates performed on the tracking loop bandwidth (see Tab. 7.1) and is also confirmed in Dahle et al. [2019]. From that point on, significant differences between the weighted and the original solution can only be observed for Swarm A, where the weighted solutions outperform the original solution. After eventually the tracking loop (TL) bandwidth was updated for Swarm A in October 2015 (see Tab. 7.1), also for Swarm A the differences between the original solution and the solution derived using weighting virtually disappear.

### 6.3.2 Weighted observations

It is favorable to remove the equatorial artifact by down-weighting as few observations as possible. A clearly defined threshold is set in the derivative-based cases, which allows deciding if an

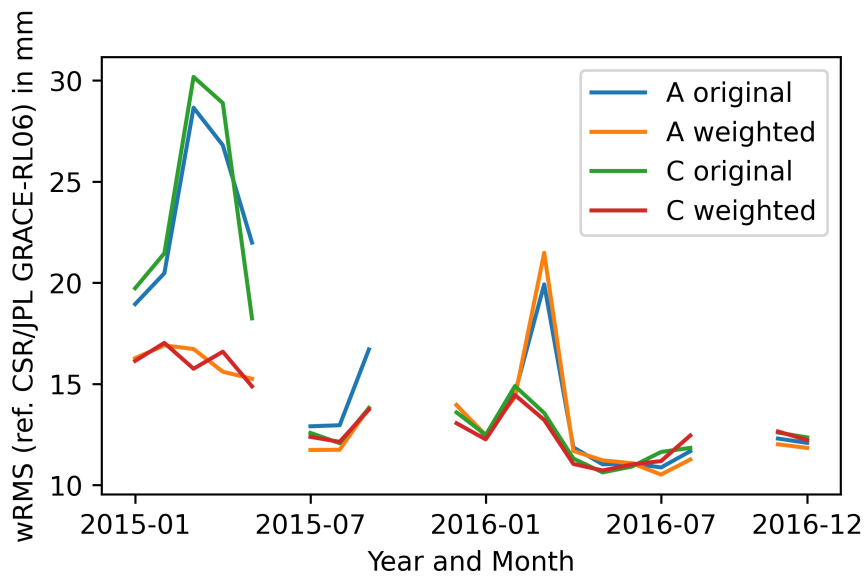


Figure 6.9: Two years (2015/2016) of monthly Swarm gravity fields for Swarm A and Swarm C compared to monthly JPL GRACE-RL06 solutions using the wRMS. With and without applying weights. Because of ground track resonance in January and February 2015, the more robust CSR GRACE-RL06 solution [Bettadpur, 2018] is used for these two months

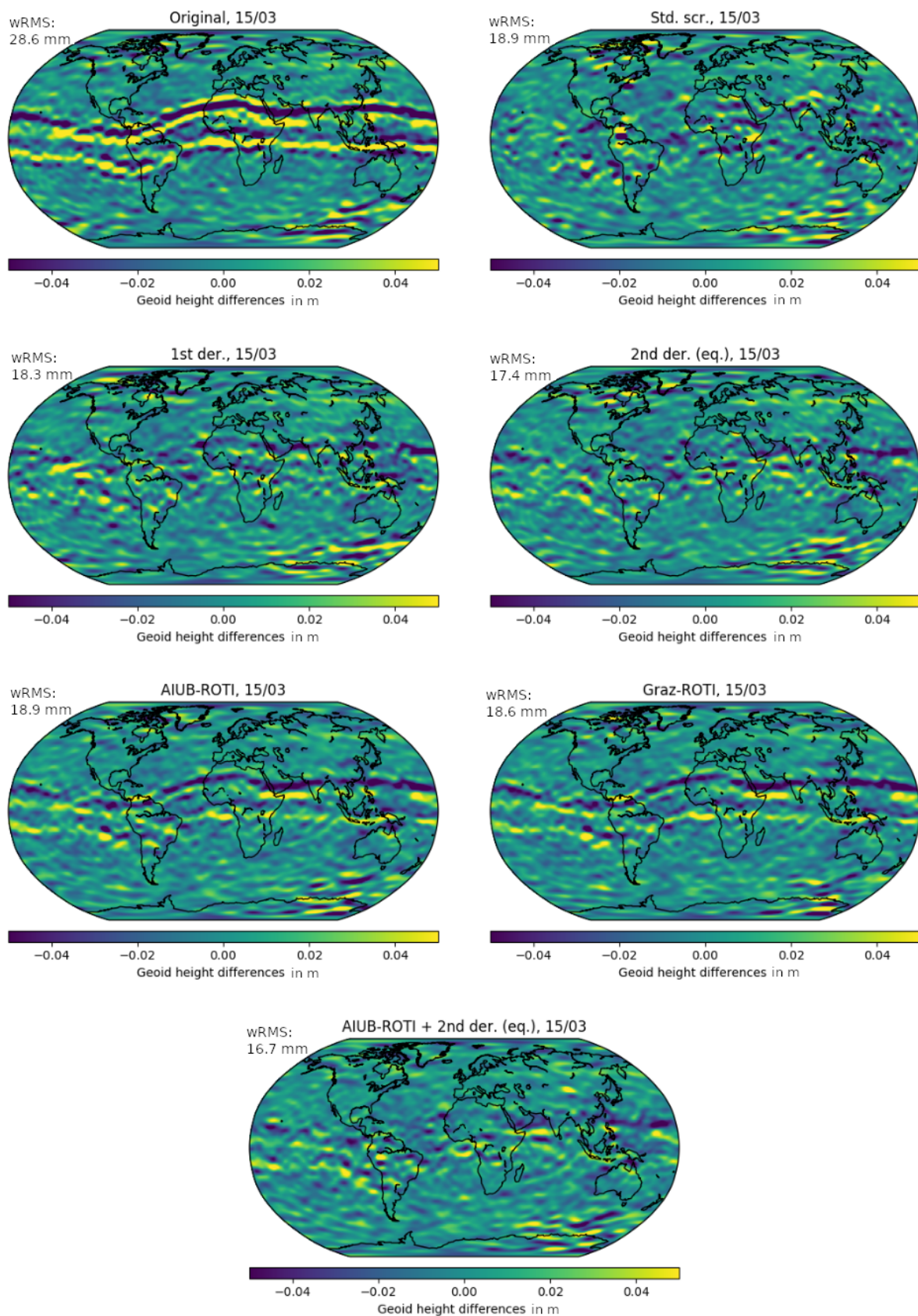


Figure 6.10: Geoid height differences between monthly Swarm A gravity field to the corresponding JPL-GRACE-RL06 solution for March 2015. Gravity field differences were computed up to degree 70.



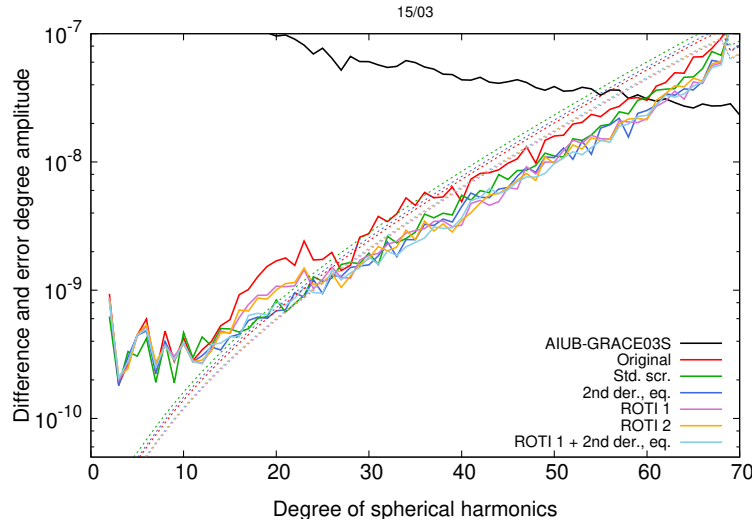


Figure 6.11: Difference (solid lines) and formal error (dashed lines) degree Amplitude for monthly Swarm A gravity field w.r.t. AIUB-GRACE03S, March 2015.

observation needs to be down-weighted or not.

However, the ROTI approach affects almost all epochs, even if most of the derived variances are close to  $1 \text{ mm}^2$ . To evaluate how many epochs are heavily down-weighted, we set thresholds to the ROTI derived weights to identify which observations are assigned substantial variances. For illustration purposes two different thresholds are selected for ROTI-based weights:  $\sigma^2 > 2 \text{ mm}^2$  and  $\sigma^2 > 5 \text{ mm}^2$ .

In Fig. 6.12 the percentage of weighted observations is illustrated in geomagnetic coordinates. Even though the first and second derivatives show similar performance, the weights based on the first derivative seem to act more specifically on the ionization crests' outer boundary than the second time derivative's weights. Therefore, using the second derivative is beneficial, assuming that the spikes in the kinematic positions are aligned with the sharp peaks in plasma density and not on the anomaly's flanks, which can be seen in Fig. 6.2. The third time derivative maximizes the number of observations that get down-weighted compared to the other approaches. Almost every observation around the pole is affected if no limitation to the equatorial region is applied.

However, the ROTI weighting approach is much more sensitive to fluctuations in the geometry-free linear combination as they occur on the poles or due to equatorial plasma bubbles. However, it is not as successful in removing the equatorial artifact.

The ratio of weighted observations is shown in Fig. 6.12 for  $\sigma_{AIUB-ROTI}^2 > 2 \text{ mm}^2$  (middle right) and  $\sigma_{AIUB-ROTI}^2 > 5 \text{ mm}^2$  (bottom). The amount of weighted observations in the polar regions decreases significantly when the threshold is increased. It implies that for most observations, only small variances are applied. This explains why the dynamic ROTI weighting shows

such a good performance around the poles. It can identify noisy observations and therefore reduce high-frequency noise in the gravity field solutions. Therefore, the ROTI information is to be used as a potential descriptor of the stochastic model of the GPS observations used for the positioning. The schemes using weighting are among the lowest curves in the difference degree amplitude for higher degrees (Fig. 6.11) Unfortunately, the systematically biased positions in the equatorial regions can not reliably be identified by a high ROTI value. This is illustrated in Fig. 6.12 when comparing the plots in the top row to the plot at the bottom.

Again a benefit from using the second derivative instead of the first derivative may be seen in Fig. 6.12. The number of weighted/screened positions is similar for both cases, but the difference and error degree amplitude are reduced, especially in higher degrees (see Fig. 6.11). Also, the geoid-RMS is reduced by 0.9 mm compared to weighting using the first derivative and 1.5 mm compared to the screening approach for March 2015, which is a heavily affected month, see Tab. 6.2 at a spatial resolution of approximately 600 km.

### 6.3.3 Orbit

In the orbit solution, the differences between kinematic and reduced dynamic positions are almost unaffected by the weighting, except for very low frequencies that are caused by the empirical accelerations in the reduced dynamic orbit (see Fig. 6.13). The spikes are still present even though their covariance information has changed, as will be shown in Sects. 6.3.4 and 6.3.5. Low-frequency differences are introduced due to differently estimated empirical accelerations, which are caused by down-weighting the problematic observations in the least-squares adjustment. It may be illustrated in particular by comparing the differences of the reduced dynamic orbits to the unweighted reference, see Fig. 6.14 (left). The comparison reveals low-frequency differences of up to 1 cm amplitude for the ROTI-based approaches. Analyzing the kinematic positions on the right-hand side, one can see significant differences in polar and equatorial regions, both of up to 10 cm. Such large differences are, however, only visible for very few epochs. In all four cases presented, the differences are spatially very localized. Considering the Graz-ROTI weighting, one can see a jump in the radial component and in the along-track component in the kinematic positions. These jumps are an indicator that the variances introduced by the scaling function are too large. Such jumps also occur at other epochs for the Graz-ROTI, but occasionally, they also occur in other weighting strategies if large variances are applied.

The differences between the kinematic positions are minimal between the polar regions and the equatorial anomaly in all other cases.

### 6.3.4 Covariances

The gravity field is determined by the used kinematic positions (pseudo-observations) but also affected by the adopted weights of the kinematic positions derived from their covariance information

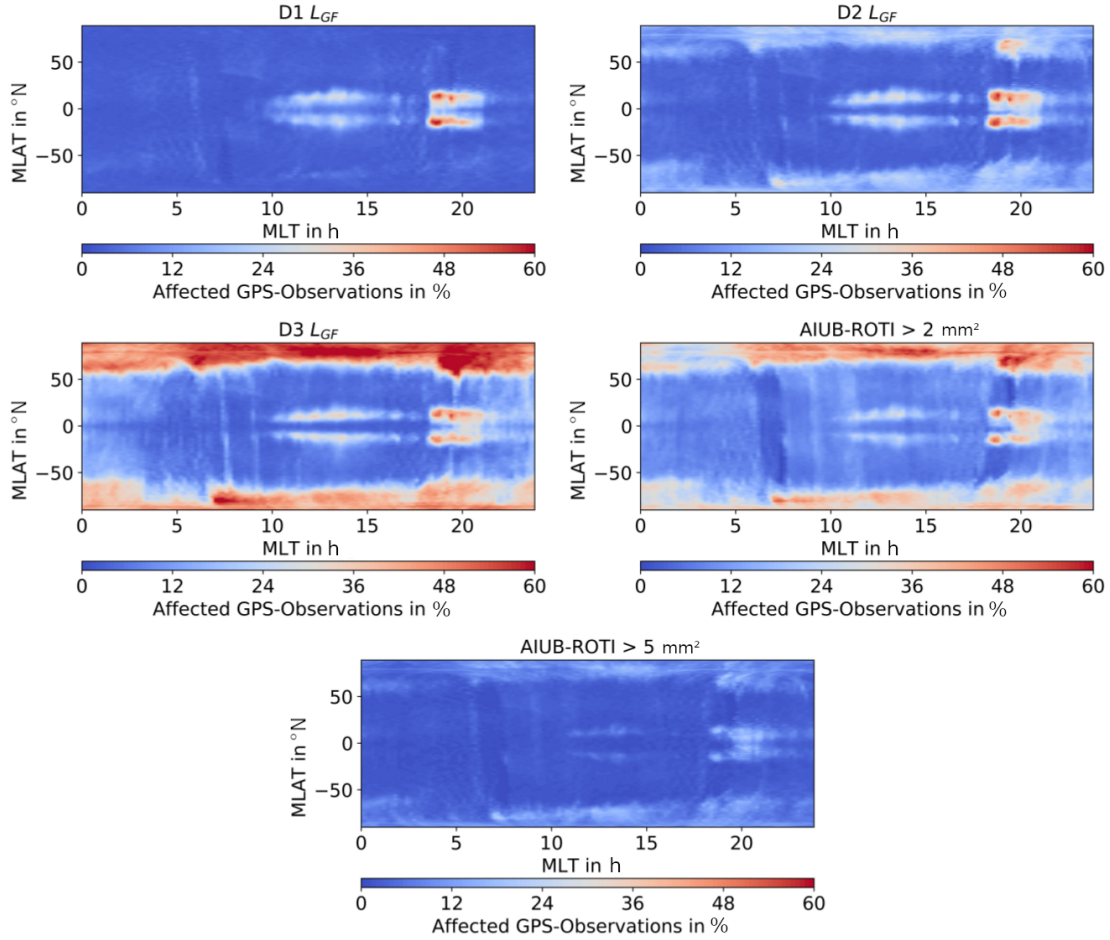


Figure 6.12: Percentage of weighted raw GPS measurements for the analyzed test period binned to the corresponding LEO position. Top: first derivative D1  $L_{GF}$  (left), second derivative D2  $L_{GF}$  (right), middle: third derivative D3  $L_{GF}$  (left), ROTI > 2 mm<sup>2</sup> (right), bottom: ROTI > 5 mm<sup>2</sup>. Bin-size 1° mlat × 0.2 h mLT.



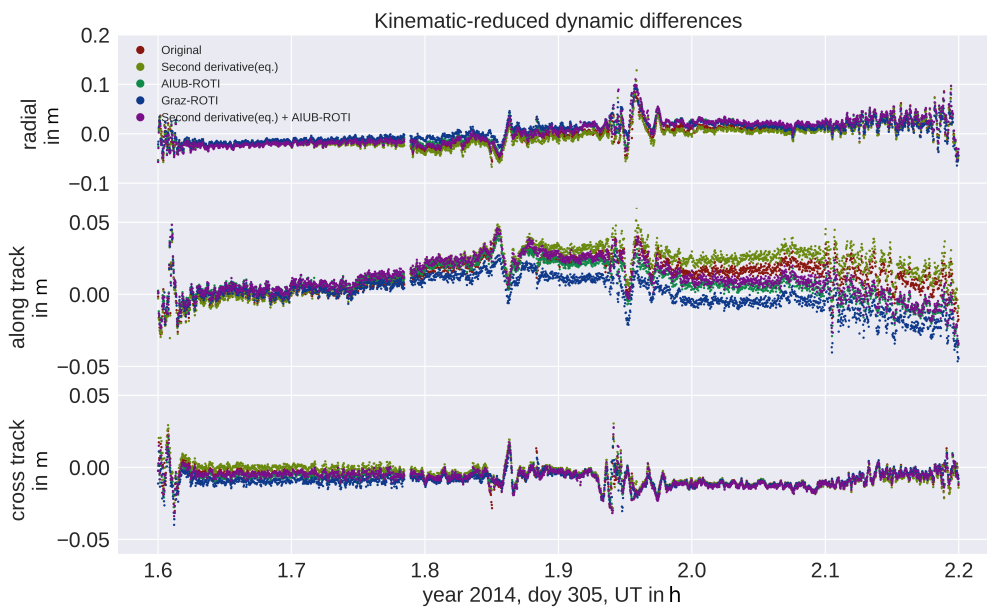


Figure 6.13: Kinematic minus reduced dynamic positions in radial, along- and cross-track direction. For both, kinematic and reduced dynamic positions, the same weighting was applied.

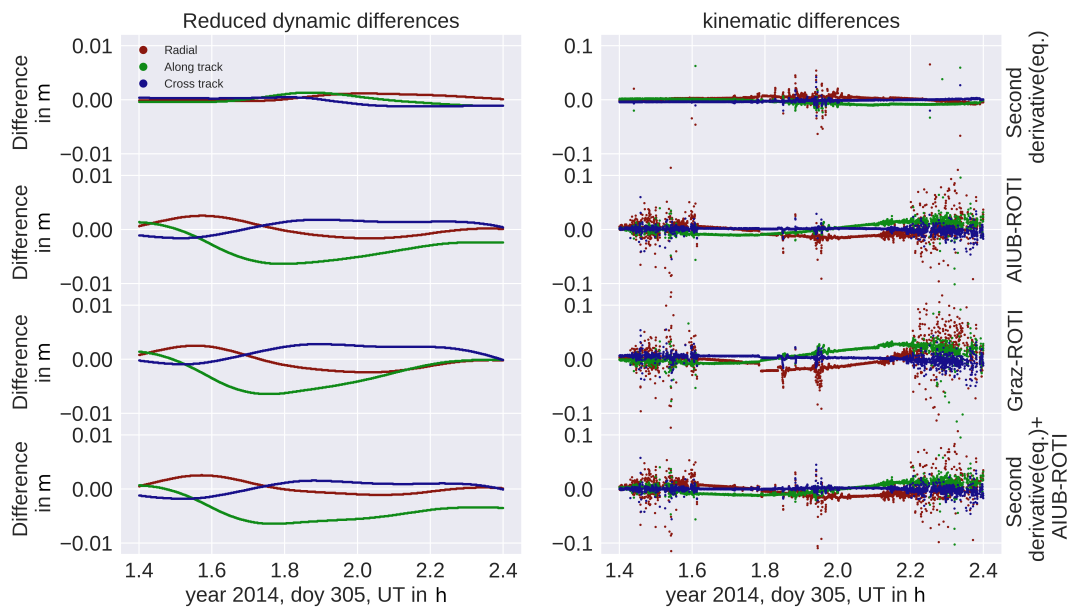


Figure 6.14: Differences between the uniformly weighted positions of reduced dynamic (left) and kinematic (right) orbits. All orbits were compared to the uniformly weighted case.

[Lasser et al., 2020]. The variances of the kinematic positions in the radial direction are analyzed as a function of their geographic and geomagnetic locations, respectively, to demonstrate how different weighting schemes affect the kinematic position's covariance matrix. The information was binned ( $1^\circ \text{ lat} \times 1^\circ \text{ lon}$  for geographic coordinates and  $1^\circ \text{ mlat} \times 0.2 \text{ h mLT}$ ) and the mean of the radial variances was computed (see Sect. 6.1.1). For a better visibility, the logarithm of that mean was taken. In Fig. 6.16 and 6.17 top left, it is shown that for the AIUB standard screening the high radial variances form a single band along the geomagnetic equator caused by the gaps in observation and the resulting large variances. One prominent ground track is visible in the radial variances caused by the Swarm *A* orbit estimation on the 20th of March 2015. On this day, the L1 RMS of the kinematic orbit is 0.022108 m, which is approximately ten times the usual RMS. The large RMS is due to many screened observations and, in turn, short observation pieces. For comparison: using the second derivative weighting in addition to the AIUB-ROTI for the same day, the L1 RMS is 0.001478 m. The other positions below and above the equator do not show high covariances, but the number of positions is significantly decreased as Fig. 6.15 illustrates. The screening acts primarily on the outer flanks of the equatorial ionization anomaly. Between the two bands, the geometry of the observations is weakened, resulting in high variances. In the two bands, too many observations are affected by the screening, resulting in a significant loss of positions. For the combined weighting approach, two bands around the geomagnetic equator are seen, compare with Figs. 6.16 and 6.17 bottom right. The positions between the two bands are of significantly better quality than those obtained using AIUB standard screening. As mentioned for the ROTI approaches, the highest variances result in areas with increased scintillation, such as the poles and equatorial regions around 18-22 mLT, which are well-known for equatorial plasma bubbles. This dependency may be well recognized when plotting the covariances in geomagnetic coordinates (Fig. 6.17). Using the second derivative and the ROTI (bottom right) results in higher covariances in the two bands around the geomagnetic equator, and higher covariances in earlier LT may be recognized. It, therefore, illustrates the different sensitivity regions of the two approaches. The weighting based on the second derivative affects primarily observations near the ionization peaks  $\pm 10^\circ$  around the geomagnetic equator explaining the two band in Fig. 6.16

### 6.3.5 SLR validation

For independent validation of the obtained orbits, measurements obtained from SLR are used as explained in Sect 5.1.4. As high-quality SLR stations we select Graz (GRZL), Greenbelt (GODL), Haleakala (HA4T), Hartebeesthoek (HARL), Herstmonceux (HERL), Matera (MATM), Mt Stromlo (STL3), Potsdam (POT3), Wettzell (SOSW), Wettzell (WETL), Yarragadee (YARL) and Zimmerwald (ZIML), following the approach of Jäggi et al. [2016]. An outlier threshold of 20 cm and an elevation-cutoff of  $10^\circ$  were applied. For March 2015, approximately 1400 normal points, and for

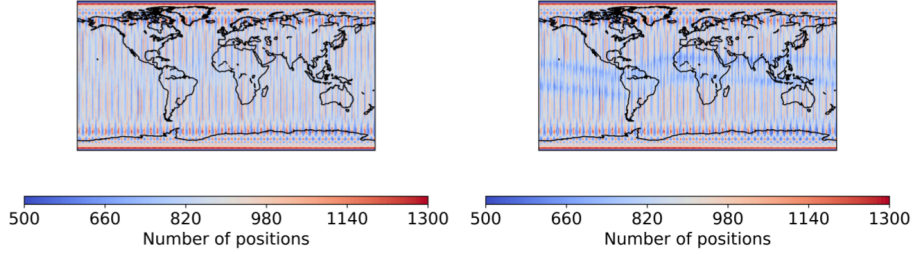


Figure 6.15: Number of kinematic positions for the analyzed test period, un-screened (left) and with AIUB standard screening (right). Binned in  $1^\circ \times 1^\circ$  grid.

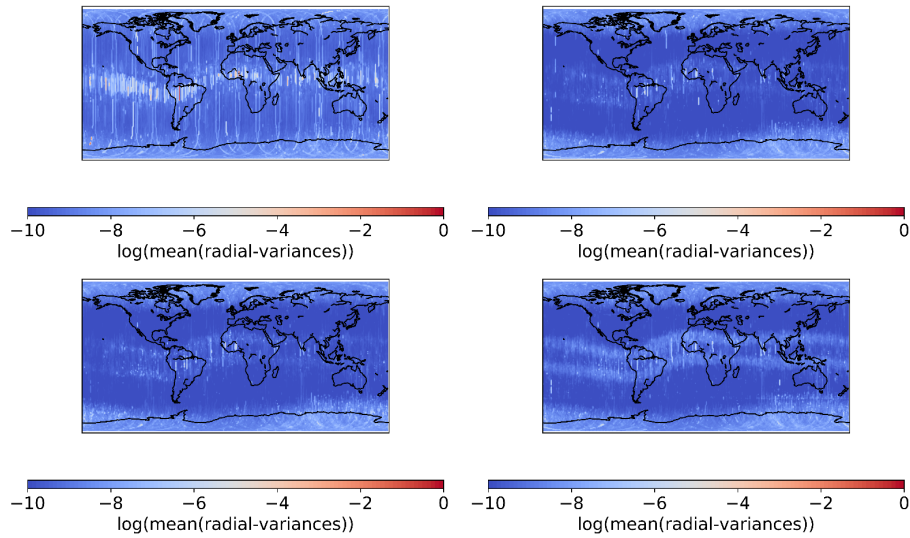


Figure 6.16: Radial variances for the analyzed test period, global. Top: AIUB standard screening (left), AIUB-ROTI (right), bottom: Graz-ROTI (left), second derivative (eq.)+AIUB-ROTI (right). The clearly visible ground track (top, left) is due to a large RMS for Swarm A, 29th of March 2015

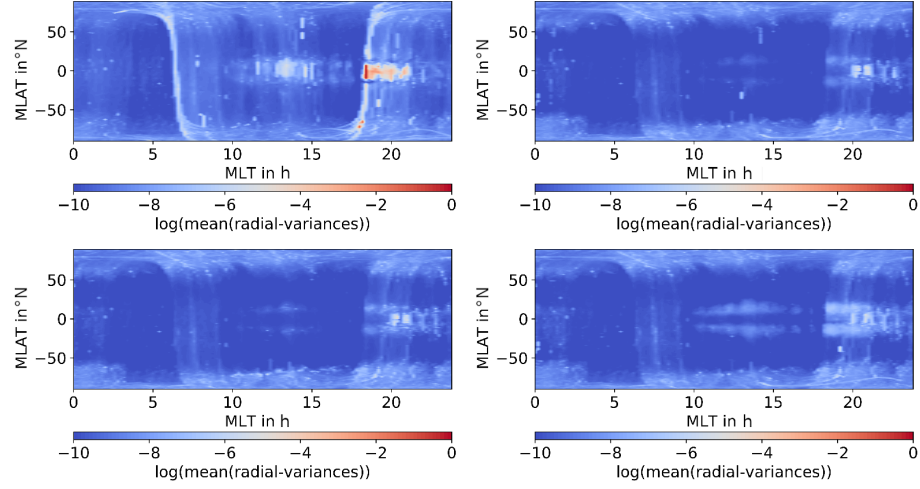


Figure 6.17: Radial variances in magnetic coordinates. Top: AIUB standard screening (left), AIUB-ROTI (right), bottom: Graz-ROTI (left), second derivative (eq.)+AIUB-ROTI (right).

June 2016, 1300 normal points are available.

Additional quality criteria are the L1-phase RMS of the gravity field adjustment, the latitude weighted RMS of the geoid height differences concerning a superior solution based on ultra-precise GRACE K-band measurements, and the latitude weighted standard deviation over the ocean, see previous Tabs. 6.2 and 6.3. The geoid RMS of the gravity field solutions using unscreened and screened GPS observations is at the same level as the values published in Dahle et al. [2017]. In the weighted scenarios for March 2015, the geoid RMS is reduced when using the second derivative for weighting or when combining the second derivative derived weights with the AIUB-ROTI derived weights. For June 2016, the second derivative derived based weights lead to almost no difference in geoid RMS. For this month, the smallest geoid RMS is obtained when using ROTI-derived weights. For both months, the geoid RMS obtained when using the combination of the AIUB-ROTI derived weights and the second derivative derived weights are among the lowest. The ROTI approaches again tend to reduce the noise, which is confirmed in reducing the geoid RMS, even if the geoid RMS for March 2015 is slightly increased compared to the second derivative. This might be due to the still existing artifacts around the geomagnetic equator. The fact that this improves by combining the AIUB-ROTI with the second derivative supports this assumption. The same effect is visible for the weighted standard deviation above the oceans.

Regarding SLR, the mean offsets and the standard deviations for the reduced dynamic orbits stay similar. The mean and SLR standard deviations show a slight improvement if the ROTI approach is used for the kinematic orbits.

In June 2016, the orbit and gravity fields' quality improved, but the orbits in June 2016 are not that much affected by the ionospheric activity. This improvement is due to the less critical local

times and reduced solar activity (the  $F10.7$  index is used as a proxy), which indicates less ionospheric activity (compare with Fig. 6.12 and Tab. 6.5). Nevertheless, even in that case, the ROTI approaches seem to improve the mean of the SLR residuals for the kinematic positions.

### 6.3.6 Weighted observations and solar activity

As shown by Jäggi et al. [2016] the amount of screened or in the presented work down-weighted observations depends on the ionospheric activity. The authors used TEC estimated to demonstrate this. Here the number of weighted observations is compared to the  $F10.7$  index and the  $Kp$  index as those indices are commonly used as a proxy for the solar activity driving ionospheric activity and geomagnetic disturbances. As shown by Stolle et al. [2006b], the probability of an equatorial plasma bubble is positively correlated to the  $F10.7$  index. Equatorial plasma bubbles usually occur during high ionospheric activity. Previous studies connect bubbles to a strong prereversal enhancement of the vertical plasma drift and an unstable E-F boundary which causes strong spatial gradients in plasma density [Whalen, 2000, Kelley, 1989, Stolle et al., 2006b]. These gradients are harmful to the quality of GPS data as shown in Fig. 6.4 (left), where the bubble region shows high variances. In conclusion, a correlation between the  $F10.7$  index and the number of observations whose variance is changed by the weighting schemes is expected.

Secondly, the  $Kp$  index represents the disturbances in the geomagnetic field. Because the motion of ionospheric plasma is connected to the magnetic field [Kelley, 1989], disturbances in the magnetic field may result again in kinematic positioning errors. Conclusively, a high number of affected observations under storm conditions is expected. These comparisons are illustrated in Fig. 6.18. All three data sets are limited to the equatorial regions ( $\phi < 50^\circ$ ) to avoid contamination due to the polar regions. The largest daily averaged  $K_p$  index in our time series is 6 (observed on 17th of March 2015, doy 76). On this day, there was a severe magnetic storm (class G4) with  $K_p$  up to 8—. Especially for the second and third time derivative-based weighting schemes, a clear increase in the relative number of affected epochs can be observed. Most probably, this is related to increased ionospheric fluctuations as they occur during storm conditions. In total, the percentage of weighted observations shows a similar behavior as the  $F10.7$  index. Some differences can be explained by local time dependence. In total, as shown in Tab. 6.4, the correlation between the percentage of weighted observations and the  $F10.7$  index is quite strong (above 0.7) for Swarm A and Swarm C but a lot weaker for Swarm B. The reason might be Swarm B's higher altitude, which leads to less free electrons and weaker gradients in the ray paths to the GPS-satellites. Besides, Swarm B passes on different local times. For March 2015 the local times are comparable, resulting in a very similar behavior (see fig. 6.18). Towards the last months (July and August 2016), Swarm B's local time is significantly different from the critical local times (18:00 mLT to 02:00 mLT), but in the same months, Swarm A and Swarm C are inside the critical local times. Here, the  $F10.7$  index peak around day 200 is reproduced in the percentage of weighted observations for Swarm A



Figure 6.18: Percentage of screened position in comparison to the  $F10.7$  and  $Kp$  indices.

Table 6.4: Correlation coefficient between the relative number of weighted observations and the  $F10.7$  index.

Method	D1 (eq.)	D2 (eq.)	D3 (eq.)
Swarm A	0.7025	0.7313	0.7564
Swarm B	0.3005	0.46400	0.6766
Swarm C	0.7925	0.7914	0.8219

and Swarm C, but no such feature is visible for Swarm B.

## 6.4 ROTI modification for identifying equatorial plasma depletion

The climatology of equatorial plasma depletions [Whalen, 2000, Kelley, 1989] is difficult to study using ground-based data. Such data lacks an equally spaced global coverage leaving large observational gaps above the oceans. The high precision magnetic field missions CHAMP and Swarm were a game-changer regarding global studies and in measuring and quantifying the magnetic field variations [Park et al., 2009, Stolle et al., 2006b]. Variations in the magnetic field connected to changes in plasma density were discussed by Lühr et al. [2003] and further studies regarding the currents induced by Park et al. [2009] and Rodríguez-Zuluaga et al. [2019]. The direct identification may only be performed if high precision magnetometers and plasma density measurements are available. However, the global, seasonal, and temporal distribution concerning solar activity



Table 6.5: Local time at middle of the month

Month	Jan.'15	Mar.'15	Feb.'16	Mar.'16	Jun.'16	Jul.'16	Aug.'16
Swarm A, C	~ 1LT, 13LT	~ 8LT, 20LT	~ 2LT, 14LT	~ 11LT, 23LT	~ 3LT, 15LT	~ 0LT, 12LT	~ 9LT, 21LT
Swarm B	~ 2.5LT, 14.5LT	~ 9LT, 21LT	~ 5LT, 17LT	~ 2LT, 14LT	~ 6LT, 18LT	~ 3LT, 15LT	~ 0LT, 12LT

is highly discussed and studied [Stolle et al., 2006b, Xiong et al., 2012]. To further improve that kind of knowledge, it is also beneficial to investigate how missions that are not dedicated to the magnetic field might be used to increase the database. Also, employing additional instruments could be used to increase the quality of detections.

The following investigations are based on Swarm and GOCE 1 Hz GPS data to derive a GPS-based ionospheric bubble index. Swarm will serve as a test case to compare the derived index to the official Level-2 IBI [DISC, 2017a] product. The derived approach will then be validated and used for the GOCE Satellite. The GOCE orbit is local time fixed with a dusk-dawn orbit. This local time may be of particular interest to the ionospheric community because plasma depletions are assumed to develop near the E-F boundary near the dusk terminator. Therefore, observations of the depletion from an altitude near that boundary and nearly fixed local time near 18:00 LT is a valuable database.

#### 6.4.1 qROTI/ROTI in equatorial regions

The ROTI approach is explained in Sect. 3.7.6 and is helpful to detect fluctuations in GPS TEC. This approach was also used in the previously discussed weighting studies. As ROTI is defined as the standard deviation of ROT over a certain time window, it is insensitive to a linear drift. However, higher-order derivatives may affect the value of ROTI. The aim is to separate regular variations from equatorial plasma depletions. They are known as small-scale fluctuations in plasma density and thus small-scale fluctuations in sTEC. Still, small scale means that the bubbles are several hundred kilometers in size. To reliably identify fluctuations, the ROTI approach needs to be adjusted. That includes selecting an appropriate time window and detrending the epoch differences so that no sensitivity to the ionization peaks is given as they are a regular phenomenon. A second-order polynomial fit performs this for each 31 s time window. The ROTI is applied on the polynomial post-fit residuals, using a 31 s symmetrical window similar to the weighting used in Sect. 6.2.2. Thus insensitivity to regular shapes, which a second-order polynomial can locally describe, is gained. In the following, this approach is referred to as quadratic ROTI or qROTI. A comparison of ROTI, qROTI, and the plasma density is shown in Figs. 6.19 and 6.20. In Fig. 6.19 a quiet equatorial pass is shown. The plasma density measurements show no fluctuations. In the plasma measurements, the equatorial ionization anomaly is well visible with two pronounced peaks in plasma density. Apart from a small fluctuation in the middle of the ionization anomaly, most likely caused by tracking issues as no screening of the GPS observations is performed, the qROTI does not show significant responses, in contrast to the classical ROTI where the ionization



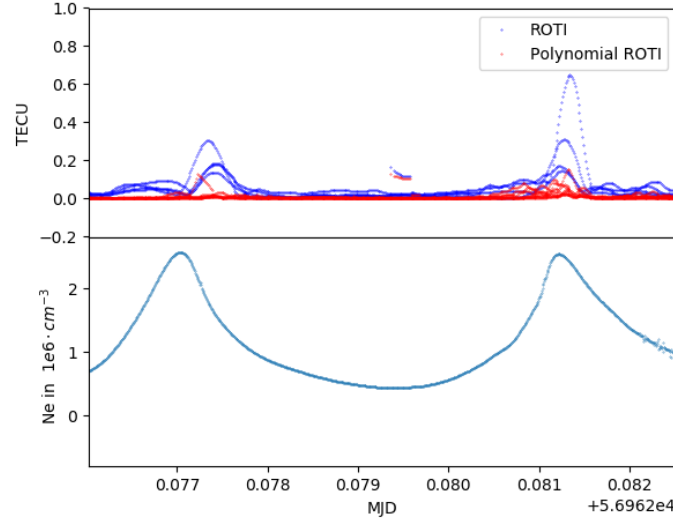


Figure 6.19: Classical ROTI and qROTI under quiet conditions (top). In situ plasma density measurements (bottom). The equatorial ionization anomaly is clearly visible, but no depletions. The response of the classical ROTI approach may be seen near the ionization peaks.

anomaly is clearly visible in the ROTI. It can be concluded that the qROTI successfully reduces the sensitivity to common phenomena like the ionization anomaly. In Fig. 6.20 an equatorial pass is shown, which is affected by bubble activity. This bubble activity can clearly be identified in the electron density measurements, where jumps and strong fluctuations are visible. In this example, it may also be seen that both ROTI and qROTI respond to the fluctuations, even if, by design, the qROTI value is in general lower. It can be concluded that the sensitivity to fluctuations is still given.

### 6.4.2 Comparing qROTI to IBI

To derive a GPS-based bubble index (GBI), an empirical threshold of 0.1 TECU is set. Since 8 GPS satellites may be simultaneously observed for the Swarm satellites and 12 for GOCE, the index is defined as the ratio between the number of affected satellites and the number of visible satellites

$$I_{GBI}(t) := \frac{\sum_{i=1}^{n_{GPS}} \mathbb{1}(qROTI^i(t) > 0.1)}{n_{GPS}}, \quad (6.5)$$

where  $n_{GPS}$  is the number of GPS satellites tracked at the specific epoch, and  $\mathbb{1}$  is the indicator function. In case the satellite directly passes the bubble, a scatter in all GPS phase observables is most likely. In such a case, both IBI and GBI should equal 1. In case the pass is quiet, both values

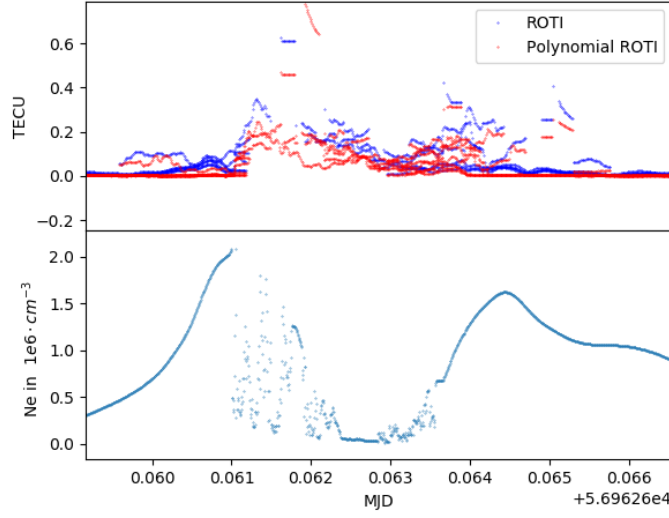


Figure 6.20: ROTI and qROTI response to a severe plasma depletion (top). In situ plasma density measured by the Swarm Langmuir probes (bottom). The depletion is clearly visible in both ROTI approaches.

should be zero. The IBI and the GBI derived for the same time window as in Fig. 6.20 is shown in Fig. 6.21. Whereas the IBI takes only the values 0 (no bubble) and 1 (bubble), the GBI provides the ratio of visible and affected satellites. The second peak's fluctuations are not visible in the IBI index, whereas they are visible in the GBI index. This can be explained by the thresholds used for the magnetic field in the IBI detection. The magnetic response is less pronounced for low plasma density than for larger values.

There is one systematic difference: The IBI is an in situ measurement, whereas the GBI is derived from the integral electron density along the line of sight. In case a bubble is located somewhere above the satellite, the IBI index does not reflect this, whereas the line of sight measurement can identify the depletion. Vice versa, if the lock on the GPS signal is lost, as it can happen due to bubble activity [Xiong et al., 2016b], no GBI can be reported. However, the in situ detection relying on magnetic and plasma density measurements can still be performed.

### 6.4.3 Distribution in geomagnetic latitude and local time

Ionospheric plasma depletions have a very distinct pattern concerning the seasonal distribution in geographical longitude and their distribution in magnetic latitude and magnetic local time. In the winter months (Nov., Dec., Jan.), ionospheric plasma depletions are confined to regions near Brazil and the Atlantic. In the summer months (Jun., Jul., Aug.), no bubbles are observed in this

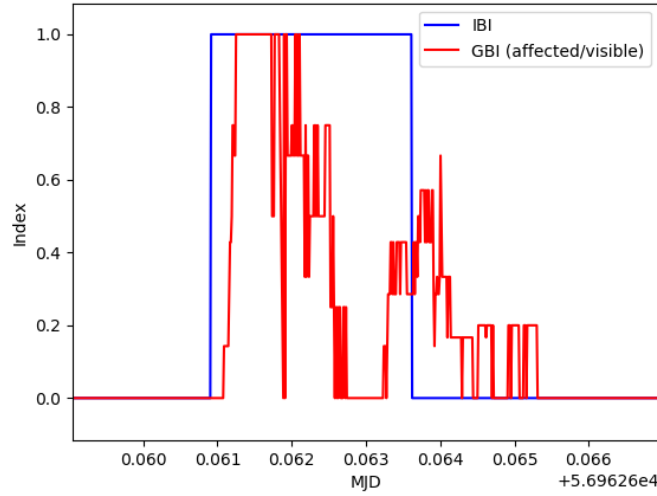


Figure 6.21: GBI compared to IBI for the same time window as shown in Fig. 6.20.

area, but in the African region. In the African region, bubbles are only rarely observed in the winter months. Ionospheric plasma depletions occur post-sunset with a maximum intensity 1-2 hours after sunset, but rarely detections are made post-midnight until sunrise. It is the subject of ongoing studies to determine if these detections are bubbles or other fluctuations related to magnetic field measurements. In comparing detections made by CHAMP and Swarm, a systematic difference in the pattern was observed. For CHAMP, the detection of ionospheric plasma depletions is performed solely on magnetic field measurements. The residual magnetic field with respect to a suited magnetic field model is extracted, high pass filtered. If the residuals exceed 0.25 nT, the observation is flagged as a bubble. This procedure utilized the preservation of plasma-pressure, where a decrease in plasma density has to be compensated by a change in the magnetic field, see Sect. 2.6, Eq. 2.9. However, this method is susceptible to fluctuations in the magnetic field, which are not related to plasma density changes. In contrast to CHAMP, Swarm can provide measurements of the plasma density at a sufficient rate. This is used to optimize the detections by correlation of the magnetic field variations to the measured plasma density. Detection in the magnetic field is only confirmed if the correlation exceeds 0.7. This additional step allowed to lower the threshold to 0.15 nT, whereas the plasma density measurements could suppress false detection caused by magnetic fluctuations near sunset. The thus obtained flags are further limited to local times between 18:00 LT and 06:00 LT and latitudes between  $-60^\circ$  N and  $+60^\circ$  N for both CHAMP and Swarm. An empirical threshold of 0.25 is selected for the ratio of affected GPS satellites to observed GPS satellites for GBI to compare the GBI and IBI data-sets. This means that at least two GPS links have to be affected for Swarm, as the SGPS receiver supports eight channels. The results of the

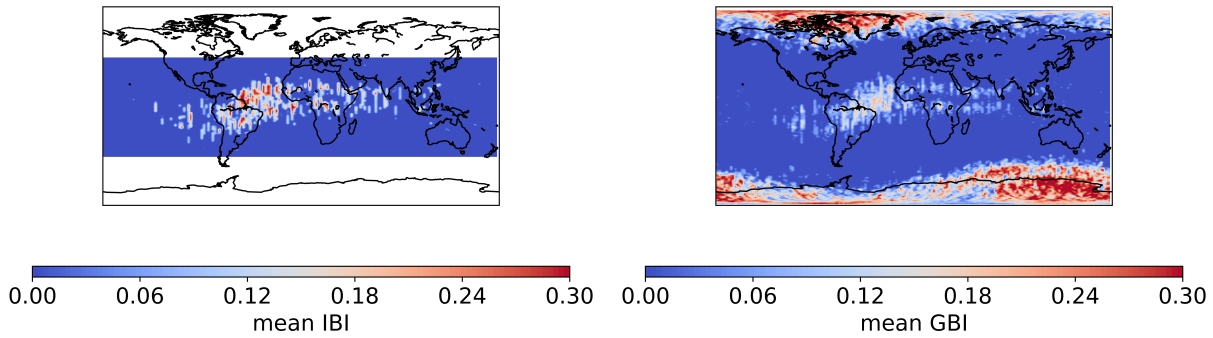


Figure 6.22: Relative number of detections binned by  $1^\circ$  in latitude and  $2^\circ$  in longitude for the IBI-index (left) and the derived GBI index (right), November 2014.

geographical and the local time distribution are shown in Figs. 6.22 and 6.23. The month used is November 2014, because the solar activity was high for this month, and the local times of the local time of Swarm orbits are near sunset. In the global distribution, the detections accumulate near Brazil for the IBI as well as the GBI. The amplitude is higher for the IBI. In the GBI, no local time-dependent masking is applied. Thus the number of used arcs is generally higher. In magnetic coordinates, both indices do not detect bubbles near 06:00 mLT. After 18:00 mLT, both derived indices show a similar pattern, a double peak centered around the geomagnetic equator. The amplitude is larger for the GBI index. This is most likely caused by the different observational scenarios: IBI uses in situ measurements, GBI uses integral measurements and therefore also responds to variations in sTEC along the line of sight. The threshold selected for GBI can of course also alter the amplitude.

For CHAMP's and Swarm's methods to detect equatorial plasma depletion, high-quality magnetometers are needed to meet the 0.25 and 0.15 nT requirement and, if available, Langmuir probes to be able to correlate magnetic field and plasma density and validate the detections. These requirements are rather demanding and require specialized magnetic field missions. On the other hand, dual-frequency GPS receivers are by default used on most satellite missions that require rather precise orbits at the few cm level. The proposed method requires at least 1 Hz sampling. Currently, such sampling is available for Swarm, GOCE, and Sentinel-3. However, Sentinel-3 is not suited for detecting plasma depletions, as the altitude is near 800 km. GOCE is of particular interest, as the altitude is only near 250 km altitude and therefore can detect bubbles in a much earlier development stage. The detections also accumulate near Brazil (Fig. 6.24), and multiple detections are seen in the northern band of the ionization anomaly. The GOCE receiver suffers more fluctuations in the observed phase triggering the detection by causing a large qROTI.

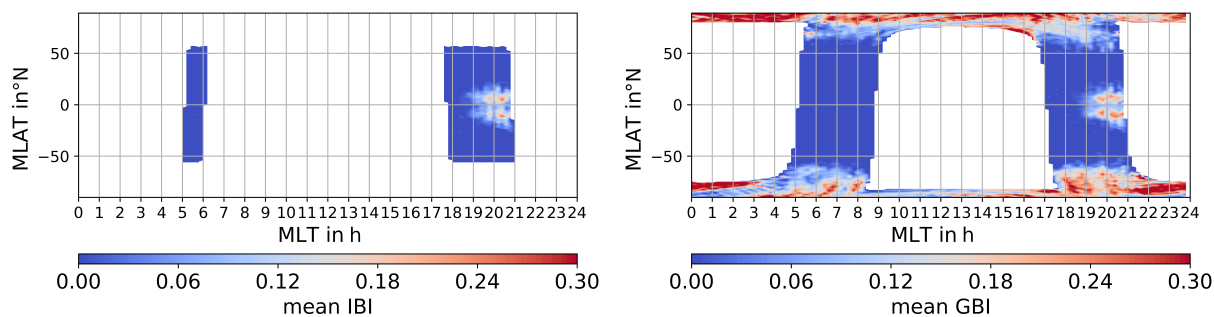


Figure 6.23: Relative number of detections binned by  $1^\circ$  in magnetic latitude and 12 min in magnetic local time for the IBI-index (left) and the derived GBI index (right), November 2014.

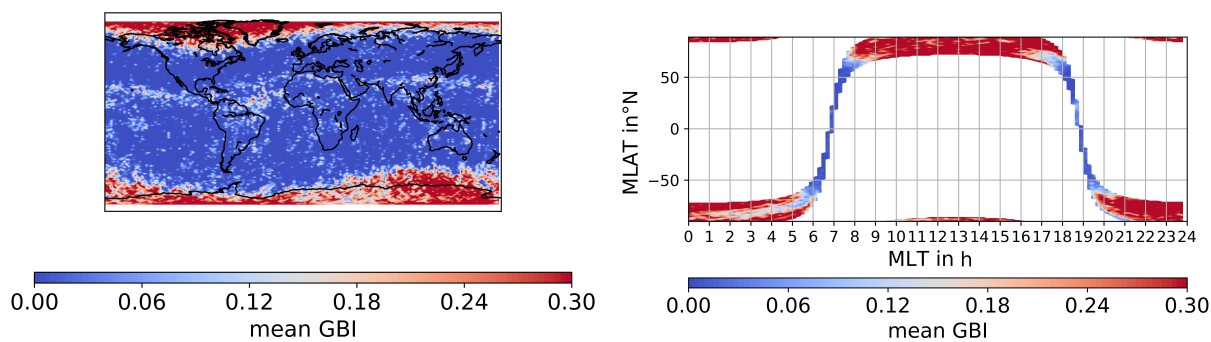


Figure 6.24: Relative number of GBI detections made by GOCE binned by  $1^\circ$  in latitude and  $2^\circ$  in longitude (left) and in magnetic coordinates binned in  $1^\circ$  in magnetic latitude and in 12 min in magnetic local (right), November 2011.



# Chapter 7

## GPS/GNSS tracking using Phase Lock Loops

This chapter analyzes the tracking loop (TL) design of a digital phase lock loop. Special emphasis is given to the loop filter implementation. It will be used to derive the amplitude and phase response of the loop filter to different frequencies of the input signal. This response is causing the ionospheric artifacts observed in the orbit and gravity field processing (see Chap. 6). Eventually, a loop-specific transfer function is derived and inverted in order to reconstruct the input L2 phase. As the bandwidth of the L1 tracking is significantly wider, tracking errors from L1 can be neglected at 1 Hz sampling (see Sect. 7.2). The impact of correcting the L2 phase observable is investigated for orbit and gravity field determination. The results were published in [Schreiter et al. \[2021\]](#). After a short introduction, the theory of digital phase lock loops is explained. The method describing the loop filter using a transfer function is utilized to invert the loop filter in frequency space. The quality of orbit and gravity field solutions using corrected observations is evaluated using ionosphere-free phase residuals from the orbit fit, orbit validation using SLR measurements, and comparing to superior GRACE gravity fields.

### 7.1 Digital Phase Lock Loops (DPLL) design

This work considers the design outlined in [Thomas \[1998\]](#). A TL typically can be divided into two parts: a counter-rotation processor (CP) and a tracking processor (TP), as illustrated in Fig. 7.1. The CP contains the number-controlled oscillator (NCO), creating a time digitized replica of the model phase obtained from the tracking processor at a sampling rate, which is typically much higher than the tracking processor's update interval. This replica is then counter-rotated and multiplied with the digitized incoming signal, such that only the difference remains. For these differences, the complex sum is formed to average the differences, reduce the impact of noise,

and downsample the signal to the TP update interval. The time interval where the counter-rotated differences are summed up is also called the pre-detection interval and matches the TP's integration time (apart from technical limitations such as dead-time when resetting the sum). The TP then takes this sum, extracts the residual phase, and eventually applies the loop filter and estimates the updated phase rate, which is then used to update the number-controlled oscillator. Also, the update interval of the tracking processor is used to reinitialize the CP's sum. The model phase from the tracking processor is then transformed and stored as an observation.

In this chapter, the loop filter response to variation in the input phase is of special interest. In the Swarm case, the Output data is available at 1 Hz sampling, whereas the TP operates at 10 Hz, the CP even higher. Therefore it may be assumed to have a perfect CP, and the phase extractor is assumed to be error-free, which holds in case the difference between the model phase and input phase is sufficiently small. The loop filter itself can have a long-lasting impact on the difference between the input and output phases, depending on the implementation. The Filter implementation typically is a trade-off between accepted noise level and signal dynamics. Increasing the loop noise bandwidth allows for a reduced observational noise due to the longer sum interval and the stronger dampening of high frequencies by the loop filter. However, the loop filter may not be able to capture the signal dynamics. This can later be seen in Fig. 7.4, where smaller values for  $B_L$  reduce the loop's capability to follow signal dynamics and lead to significant changes in amplitude. It may also be seen that high-frequency noise is less suppressed if  $B_L$  is increased. The order of the loop filter can also vary. Typically, first- or second-order loops are used in analog loops [Stephens and Thomas, 1995]. In digital loops, there is no technical limit. The higher the loop order, the more complex input signals may be, which can essentially be tracked error-free. A first order loop encounters errors in case of phase accelerations. A second-order loop can also cope with phase accelerations but cannot account for jerk stress, which is also accounted for in a third-order loop [Ward et al., 2006].

### 7.1.1 Discrete update loops

In the case of digital phase lock loops, discrete updates of the NCO are performed. These updates are performed instantaneously in case of a loop without computation delay or after one update interval. The updates typically are performed after one pre-detection interval when resetting the sum, if possible between two samples [Thomas, 1998]. However, depending on the input sampling-rate observations may be lost. In contrast, in analog loops, continuous updates can be performed, for example, when using voltage-controlled oscillators [Stephens and Thomas, 1995].

### 7.1.2 Continuous update approximation

One may consider frequency-dependent responses in terms of phase shifts and amplitude variations to study the loop behavior. For that purpose, it is beneficial to work in the frequency space domain



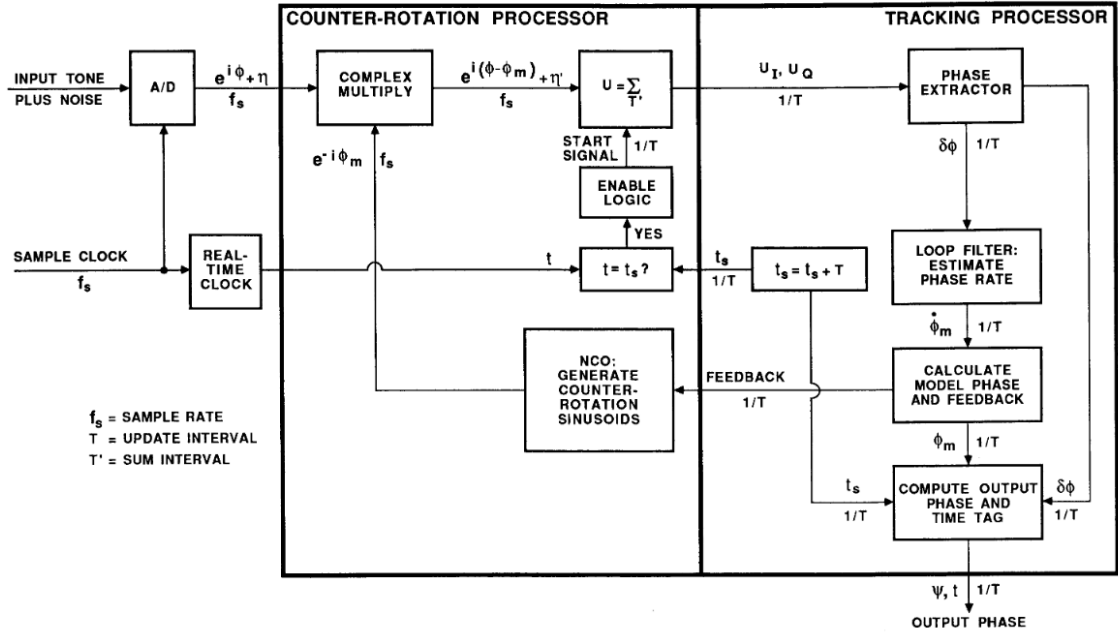


Figure 7.1: Model of a DPLL including separation in CP and TP, from Thomas [1998].

and using Fourier, Laplace, or  $z$  transforms [Stephens and Thomas, 1995]. Therefore, one may examine the limit when  $B_L T \rightarrow 0$ , where  $B_L$  is the loop bandwidth in Hz and  $T$  the integration time in s. This procedure requires  $B_L T$  to be sufficiently small. According to Stephens and Thomas [1995], this value should not exceed 0.02. However, due to the large integration time of 100 ms for the L2 tracking and the used noise Bandwidths of 0.25 Hz, 0.5 Hz, 0.75 Hz, and 1 Hz (see Tab. 7.2), this value is too large to use the CU approximation presented in Stephens and Thomas [1995] for the Swarm L2 phase tracking.

### 7.1.3 L1 aided L2 tracking

Due to the publicly available C/A code on the L1 frequency, the L1 phase observable can typically be obtained easier and much smaller loop bandwidths can be used. This allows the L1 phase tracking to follow the signal dynamics even when encountering fast variations. When tracking the L2 phase, one typically has no direct access to the code. One solution to allow robust L2 tracking is aiding the L2 tracking using the L1 phase rate such that only the difference between L1 and L2 has to be tracked. Since there is no geometry information in this difference, this can be performed, even if the receiver's position is rapidly changing, as is the case for LEO satellites.

Apart from constant offsets, the  $L_1$  and  $L_2$  carrier range  $\phi_1, \phi_2$  may be split into the sum of a frequency-independent geometry term  $g(t)$  and an frequency-dependent ionospheric term  $I(t)$  for

the carrier frequency  $f_1$ . The impact on  $\phi_2$  may be expressed as  $(f_1^2/f_2^2)I(t)$  in a first order approximation neglecting the higher order ionospheric terms

$$\phi_1(t) = g(t) - I(t) \quad (7.1)$$

$$\phi_2(t) = g(t) - (f_1^2/f_2^2)I(t). \quad (7.2)$$

When using a representation in the time domain, the measured phase  $\hat{\phi}(t)$  can be connected to the input phase using the convolution with the loop specific transfer function  $H(t)$

$$\hat{\phi}(t) = H(t) * \phi(t), \quad (7.3)$$

or in frequency domain when applying the Fourier transform

$$\hat{\Phi}(f) = H(f) \cdot \Phi(f). \quad (7.4)$$

In case of  $L_1$  carrier phase tracking the TL bandwidth is considered to be sufficiently high for both, the geometric and the ionospheric variation. Therefore the approximation

$$\hat{\phi}_1(t) = H_1(t) * g(t) - H_1(t) * I(t) \approx g(t) - I(t) = \phi_1(t) \quad (7.5)$$

holds. For the much smaller  $L_2$  bandwidth this assumption does not hold. To be insensitive to geometry related signal dynamics, the  $L_2$  PLL is therefore aided using the  $L_1$  carrier rate. The  $L_2$  carrier phase tracking may thus be described as

$$\hat{\phi}_2(t) = \hat{\phi}_1(t) + H_2(t) * (\phi_2(t) - \hat{\phi}_1(t)), \quad (7.6)$$

which expands to

$$\hat{\phi}_2(t) = g(t) - I(t) + (1 - (f_1^2/f_2^2)) \cdot H_2(t) * I(t). \quad (7.7)$$

The  $L_2$  tracking error is therefore given as

$$\hat{\phi}_2(t) - \phi_2(t) = -\frac{f_1^2 - f_2^2}{f_2^2} \cdot (H_2(t) * I(t) - I(t)). \quad (7.8)$$

To recover the true  $L_2$  carrier phase measurement, the inverse transfer function  $H_2^{-1}(t)$  is applied to Eq. 7.6 and the phase difference replaced by the geometry-free combination  $\phi_{gf} = \phi_2 - \phi_1$ . By inserting the obtained relation into the Eq. 7.8 the  $L_2$  input phase is obtained as

$$\phi_2(t) = \hat{\phi}_2(t) + [H_2^{-1}(t) * \hat{\phi}_{gf}(t) - \hat{\phi}_{gf}(t)]. \quad (7.9)$$

The inversion is best performed in the frequency domain, where the inverse transfer function is given as  $H_2^{-1}(f) = 1/H_2(f)$ .

It should be mentioned that the phase measurements as provided in the RINEX files are not the direct output of the tracking process. They are formed using mathematical operations from the NCO readout. This may be ignored due to linearity, and the transformations may be applied on the carrier phase measurements as they are provided in the RINEX files.

Table 7.1: PLL TL bandwidths of the Swarm satellites [ESA, 2015a,b, 2016, van den IJssel et al., 2016].

Since	Swarm-A	Swarm-B	Swarm-C
Launch	$B_{L1} = 10 \text{ Hz},$ $B_{L2} = 0.25 \text{ Hz}$	$B_{L1} = 10 \text{ Hz},$ $B_{L2} = 0.25 \text{ Hz}$	$B_{L1} = 10 \text{ Hz},$ $B_{L2} = 0.25 \text{ Hz}$
6 May 2015			$B_{L1} = 15 \text{ Hz},$ $B_{L2} = 0.50 \text{ Hz}$
8 Oct 2015	$B_{L1} = 15 \text{ Hz},$ $B_{L2} = 0.50 \text{ Hz}$		
10 Oct 2015		$B_{L1} = 15 \text{ Hz},$ $B_{L2} = 0.50 \text{ Hz}$	
23 June 2016			$B_{L2} = 0.75 \text{ Hz}$
11 Aug 2016	$B_{L2} = 0.75 \text{ Hz}$		$B_{L2} = 1.00 \text{ Hz}$

## 7.2 Swarm loop filter characterization

Based on the information kindly provided by F. Zangerl from the Swarm receiver manufacturer RUAG, the Swarm loop filter is of third order with super-critical dampening. The computation delay is one update interval, and the (coherent) integration time is 100 ms. The Swarm tracking loops were updated several times (see Tab. 7.1) to mitigate the ionospheric impact on the GPS tracking. These measures had a significant positive impact on the orbit and gravity field solutions generated using Swarm GPS data as shown by van den IJssel et al. [2016]. In that study, 1.3% more observations could be retrieved, and also minor improvements of kinematic and reduced-dynamic orbits concerning SLR measurements could be observed. Similar observations were made by Dahle et al. [2017], where the gravity field solutions obtained after the update outperformed the solutions generated when applying data screening. The coefficients used for implementing the digital phase lock loop used for the L1 and L2 tracking are given in Tab. 7.2. The values originate from the paper by Stephens and Thomas [1995]. However, the value used for  $B=0.75 \text{ Hz}$  is not given and was interpolated using a polynomial and eventually also confirmed by F. Zangerl. Given the short integration time and the narrow bandwidth of 10 Hz and 15 Hz for the L1 tracking, it can be concluded that the 1 Hz data sampling, which is given in the RINEX file, is not sufficient to obtain meaningful corrections for L1. A justification will be given when analyzing the transfer functions amplitude and phase feedback (see Fig. 7.3). Therefore, corrections are only derived and applied for L2.

The data processing of the Swarm loop filter is shown in Fig. 7.2, with the formulation given by Stephens and Thomas [1995]. An ideal phase extractor is assumed. The so-called  $n$ -th residual phase  $\tilde{\phi}_n$  is given by

$$\tilde{\phi}_n = \phi_n - \hat{\phi}_n, \quad (7.10)$$

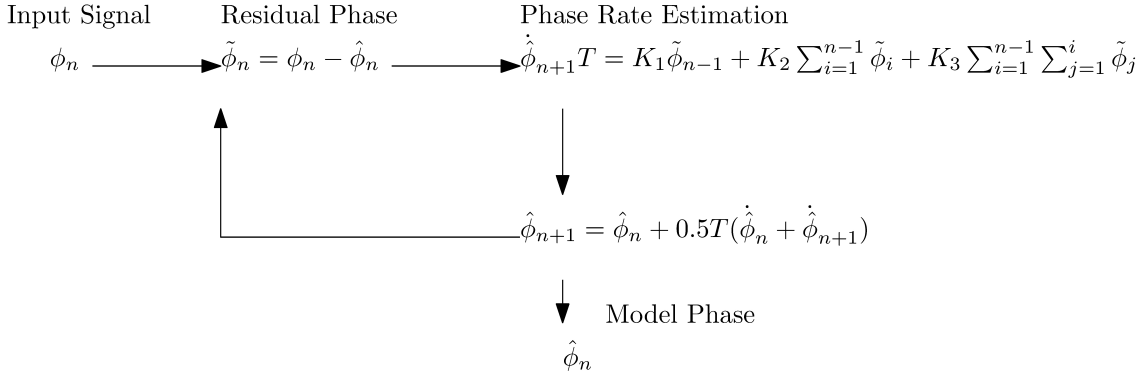


Figure 7.2: Simplified tracking processor with third-order loop filter, adopted from Fig. 3.1 in Thomas [1998].

where  $\phi_n$  is the input phase and  $\hat{\phi}_n$  is the model phase. In case of a rate-only feedback loop, the  $n + 1$ -th model phase is given by

$$\hat{\phi}_{n+1} = \hat{\phi}_n + \frac{1}{2}(\dot{\hat{\phi}}_n T + \dot{\hat{\phi}}_{n+1} T), \quad (7.11)$$

where  $T$  is the integration time and the dot denotes the first time derivative. The phase rate estimation  $\dot{\hat{\phi}}_{n+1}T$  can be obtained for a loop filter of third order with a computation delay of one update interval as

$$\dot{\hat{\phi}}_{n+1}T = K_1\tilde{\phi}_{n-1} + K_2\sum_{i=1}^{n-1}\tilde{\phi}_i + K_3\sum_{i=1}^{n-1}\sum_{j=1}^i\tilde{\phi}_j. \quad (7.12)$$

The coefficients  $K_1$ ,  $K_2$ , and  $K_3$  are characterizing the TL properties, like bandwidth, dampening, and integration time. For the TLs implemented on Swarm, the coefficients and other parameters are given in Tab. 7.2.

When deriving the empirical transfer function (see 7.2.2) and evaluating the phase and amplitude response (see Fig. 7.3 for L1 and 7.4 for L2), an overestimation of the amplitude by a factor of about 1.3 for  $B_L = 0.25$  Hz near a frequency of 0.05 Hz can be observed. With increasing  $B_L$  the peak gets larger but is shifted to higher frequencies. Also, a relatively large phase shift occurs with higher frequencies. Low frequencies below 0.01 Hz pass the loop filter virtually unaffected. For the L1 loops, this effect is also pronounced. However, because of the large  $B_L$  values of 10 Hz and 15 Hz, its impact is observed in high frequencies. No large deviations can be observed for frequencies below 1 Hz, which also holds for the phase shift (see Fig. 7.3). Given the 1 Hz sampling of the RINEX files' observations, the highest frequency that can be resolved is 0.5 Hz. Below that frequency, it can be concluded that the L1 tracking is free from systematic tracking errors.

Table 7.2: Third-order DPLL loop coefficients ( $K_1$ ,  $K_2$ ,  $K_3$ ) for different design bandwidths  $B$  based on [Stephens and Thomas \[1995\]](#). The values apply for rate-only numerically controlled oscillator (NCO) updates, super-critical damping, and a one-step computational delay. For comparison, continuous-update loop coefficients  $\omega_0$ ,  $a$ , and  $b$  as defined in [Ward et al. \[2006\]](#) are provided for the respective update intervals  $T$  (see Eq. 7.16)

$B_{DU}$ [Hz]	$K_1$	$K_2$	$K_3$	$T$ [s]	$\omega_0$ [Hz]	$a$	$b$	$B_{CU}$ [Hz]
15	0.2142	0.02208	$8.655 \cdot 10^{-4}$	0.01	9.5	2.43	2.25	8.5
10	0.1741	0.01313	$3.585 \cdot 10^{-4}$	0.01	7.1	2.60	2.45	6.5
1.00	0.1741	0.01313	$3.585 \cdot 10^{-4}$	0.1	0.71	2.60	2.45	0.65
0.75	0.14597	0.008619	$1.8455 \cdot 10^{-4}$	0.1	0.57	2.66	2.56	0.54
0.50	0.1095	0.004614	$6.745 \cdot 10^{-5}$	0.1	0.41	2.78	2.69	0.40
0.25	0.06253	0.001406	$1.075 \cdot 10^{-5}$	0.1	0.22	2.89	2.83	0.22

### 7.2.1 Simulation

Since the loop filter coefficients and implementation are known, one may directly investigate the loop filter's response to a given stimulus. A constant zero signal, with a cosine shaped pulse is used to analyze the response

$$\phi_{in}(t) = \begin{cases} -\cos((t-a)/(b-a) \cdot 2\pi) + 1, & a < t < b \\ 0, & \text{else} \end{cases} \quad (7.13)$$

The signal is sampled at 100 ms. The sum given in Fig. 7.1 can be safely ignored since its only purpose is to reduce noise. White noise with  $\sigma = 1$  cm is added to the input signal to simulate the impact of observational noise. Since the signal starts with a constant zero signal, the loop is initialized by setting all the sum terms in Eq. 7.12 to zero. As the loop's derivatives thus match the signal derivatives, a transient-free initialization is realized. The pulse's frequency is set to 0.1 Hz because all loop filter settings show significant deviations at that frequency. Large deviations up to 1 m from the input signal are observed in the loop output (see fig. 7.5). Directly evaluating the differences shows deviations up to 1 m. The capability of the loop filter to follow the signal is increased with a wider bandwidth. However, still notable differences occur over the range of 20 to 30 seconds after the pulse.

### 7.2.2 Transfer function approximation

In general, two options exist to invert the loop filter. The first option is to generate a dense (10 Hz) signal using spline interpolation and apply least squares for inversion. However, since a loop filter only affects future observations, the signal's last observation can not be reconstructed. The initial

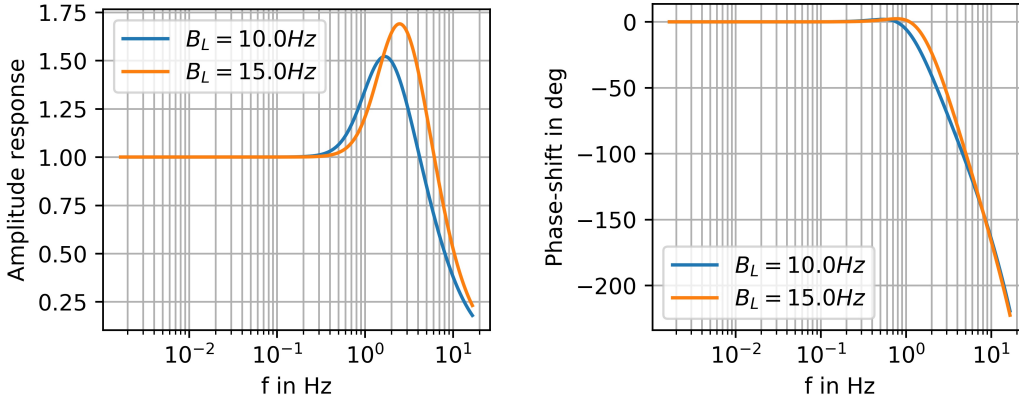


Figure 7.3: Amplitude and phase response for the different L1 TL setting used by the Swarm receivers.

conditions of the loop to estimate the phase rate are unknown. Consequently, the resulting equation system has more unknowns than observations. A second option is to investigate the frequencies of the output signal by applying the Fourier transform. Given the loop-specific transfer function, the transformed signal can be multiplied with the inverse transfer function. Eventually, after applying the inverse Fourier transform, an estimate of the original input signal is obtained as outlined in Eq. 7.9. For the discrete update loop, a continuous update approximation can be derived for the transfer function. In [Stephens and Thomas \[1995\]](#) such an approximation is given for small values of  $B_L T$ :

$$H(s) = \frac{\kappa_1 s^{-1} + \kappa_2 s^{-2} + \dots + \kappa_N s^{-N}}{1 + \kappa_1 s^{-1} + \kappa_2 s^{-2} + \dots + \kappa_N s^{-N}}, \quad (7.14)$$

where  $\kappa_i = K_i/T^i$  and  $s = 2i\pi f$ . This leads to the CU loop bandwidth

$$B_{CU} = \frac{\kappa_1^2 \kappa_2 - \kappa_1 \kappa_3 + \kappa_2^2}{4(\kappa_1 \kappa_2 - \kappa_3)}. \quad (7.15)$$

The classical formulation, as given in [Ward et al. \[2006\]](#), is

$$B_{CU} = \frac{\omega_0(ab^2 + a^2 - b)}{4(ab - 1)}, \quad (7.16)$$

where  $a$  and  $b$  are filter constants that determine the damping and overshoot of the output signal in response to a step change of the input signal. The coefficient  $\omega_0$  denotes the filter's natural frequency and defines the filter bandwidth for given values of  $a$  and  $b$ .

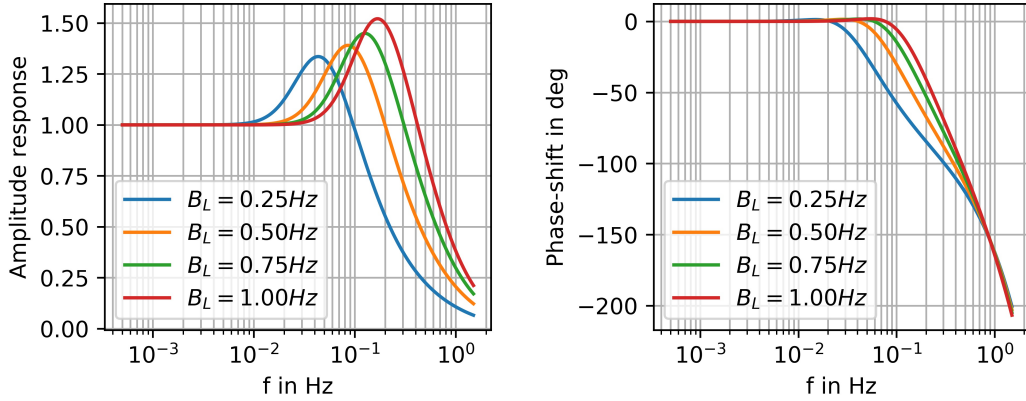


Figure 7.4: Amplitude and phase response for the different L2 TL setting used by the Swarm receivers.

Comparing Eqs. 7.15 and 7.16, the following equations hold:

$$\omega_0 = \kappa_3^{\frac{1}{3}}, \quad (7.17)$$

$$a = \frac{\kappa_2}{\kappa_3^{\frac{2}{3}}}, \quad (7.18)$$

$$b = \frac{\kappa_1}{\kappa_3^{\frac{1}{3}}}. \quad (7.19)$$

Typical values are  $a = 1.1$  and  $b = 2.4$  [Ward et al., 2006], whereas values of 2.5-3 for  $a$  and  $b$  (Tab. 7.2) apply for the Swarm TL in accordance with the choice of super-critical damping.

The long integration time of 100 ms in the case of the Swarm L2 TL violates the condition  $B_L T \ll 1$  (Stephens and Thomas [1995] specifies a limit of 0.02) for this sort of CU approximation. An empirical approximation of the transfer function with sufficiently high order is derived to obtain a sufficiently precise CU approximation for the DU loop filter. Following the studies made by Aguirre and Hurd [1984], a transfer function using a third-order numerator and a fifth-order denominator can be used to describe a third-order DPLL with computation delay. To estimate the coefficients of the transfer function an artificial signal at 10 Hz sampling is generated, which can be processed by the loop implementation used in Sect. 7.2.1. The artificial signal is defined by a Fourier series over a sufficiently large time interval  $T$  to cover also the very low frequencies with periods in the range of a few minutes:

$$\phi_{test}(t) = \sum_{i=1}^n a_i \sin\left(t \cdot \frac{i}{T} \cdot 2\pi\right) + \sum_{i=1}^n b_i \cos\left(t \cdot \frac{i}{T} \cdot 2\pi\right). \quad (7.20)$$

Here  $a_i$  and  $b_i$  are determined randomly. The length of the time interval  $T$  is set to 3000 s, which is longer than all phase arcs observed by the Swarm mission, usually shorter than 30 min. Also,

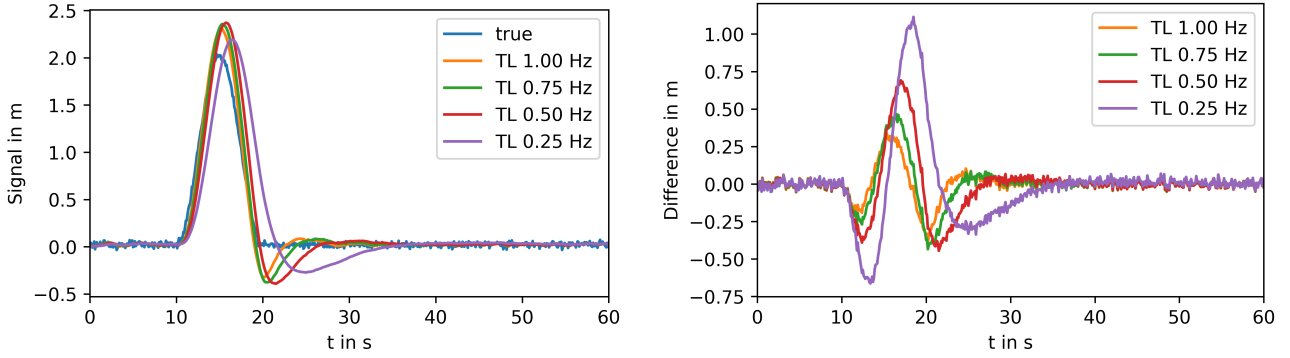


Figure 7.5: TL response and differences for different bandwidths to a synthetic cosine-shaped pulse.

the signal is extrapolated to avoid uncertainties by initializing the loop. For a given input signal  $\phi(t)$  the signal  $\hat{\phi}(t)$  at the output of the TL can be computed by means of the Fourier-transform  $\mathcal{F}$  using the relation

$$\hat{\phi}(t) = \mathcal{F}^{-1}(H(s) \cdot \mathcal{F}(\phi(t))). \quad (7.21)$$

Given the test function and the TL output, one can directly derive the empirical transfer function  $H_{emp}$  as

$$H_{emp}(s) = \frac{\mathcal{F}(\hat{g}_{test})(s)}{\mathcal{F}(g_{test})(s)}. \quad (7.22)$$

The following formulation for an empirical transfer function of order 4/6 as described in [Aguirre and Hurd \[1984\]](#) is used:

$$H_{fit}(s) = \frac{b_2 s^3 + b_3 s^2 + b_4 s + b_5}{s^5 + a_1 s^4 + a_2 s^3 + a_3 s^2 + a_4 s + a_5}. \quad (7.23)$$

The coefficients for the empirical transfer function were estimated using a least-squares fit to minimize the difference between the phase and amplitude response of the empirical transfer function and the fitted transfer function. The empirical transfer function ( $H_{emp}$ ), the CU approximation ( $H_{CU}$ ) and the fitted transfer function are shown in Fig. 7.6. It may be recognized that the CU approximation leads to underestimating the amplitude response and the phase shift. When using an approximation, no significant deviations between the empirical transfer function and the fitted transfer function can be observed.



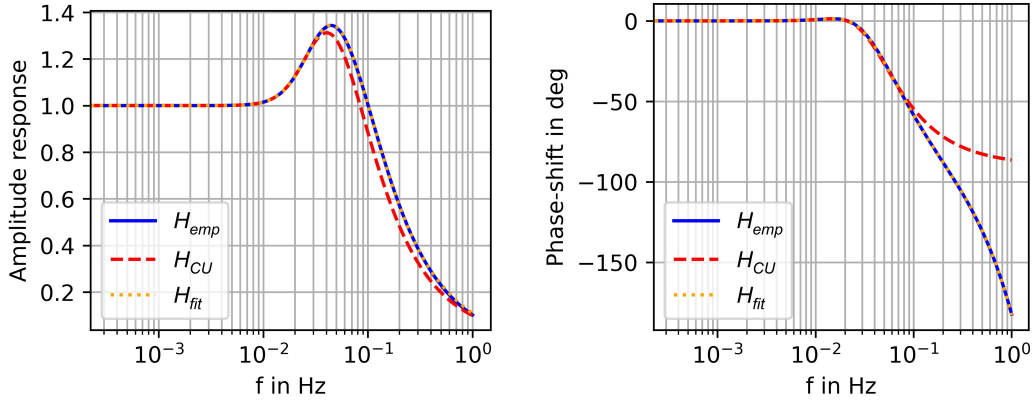


Figure 7.6: Amplitude and phase response for the  $B_L = 0.25$  Hz for the empirical transfer function, CU approximation and the fitted transfer function.

### 7.2.3 Loop filter inversion

Once the transfer function is known, one may directly invert the filter using

$$\phi(t) = \mathcal{F}^{-1}\left(\frac{1}{H(s)}\mathcal{F}(\hat{\phi})(s)\right). \quad (7.24)$$

For synthetic data, an example is shown in Fig. 7.7. The data was reduced to 1 Hz sampling to match the sampling of the Swarm RINEX files. It may be seen that even with the reduced sampling, the original signal can be reconstructed within the cm range. Because the original signal and its derivatives are 0 m at the edges, boundary effects do not need to be considered. This boundary condition, however, is different when the procedure is applied to real data.

### 7.2.4 Correction of the L2 phase observable

For applying the inverse transfer function, the observations were separated into connected phase arcs, with no gap ( $> 1.5$  s) or jumps ( $> 1$  m in  $L_{gf}$ ). The phase arcs were detrended (i.e. a linear polynomial subtracted, such that  $\tilde{\phi}(t_0) = \tilde{\phi}(t_n) = 0$ ). The drawback of the option using the transfer function is mainly related to boundary effects. The loop filter has a certain range (in theory infinity, but due to dampening 30s can be considered as range as may be seen in Figs. 7.4 and 7.5). The FFT assumes the signal to be periodic. Therefore observations from the end of the phase arc may affect the reconstructed signal at the beginning of the arc and vice versa. A reliable correction for the first 30 s can not be performed. However, the loop filter needs previous observations in order to follow the signal. Jumps in phase or phase rate at the boundary can introduce large deviations at the beginning of a phase arc (see Fig. 7.8). To mitigate this effect, the signal should be extrapolated

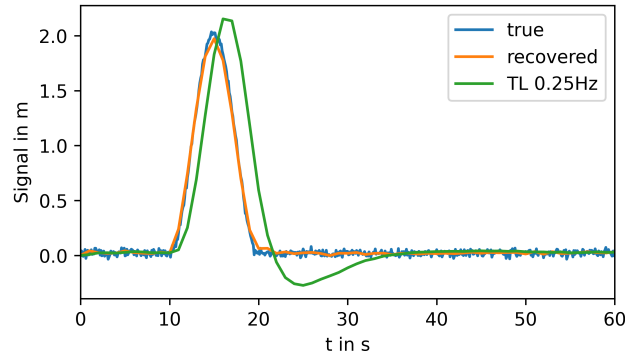


Figure 7.7: Inversion of the  $B_L = 0.25$  Hz loop filter using the inverse transfer function with 1 Hz data sampling.

using an adequate function to ensure a smooth transition. Because the loop is of third-order, such an extrapolation should be continuous and at least two times continuously differentiable. Several options for extrapolation were examined after detrending and removing the offset of the first epoch. Such modifications do not change the loop filter's tracking error since a loop filter of order three has no velocity-related tracking error [Ward et al., 2006]. The investigated options are:

1. no extrapolation
2. 300 seconds of zero values
3. point mirroring at the edges
4. 60 second linear polynomial, with 10 second blending

The derived corrections using the methods mentioned above are shown in Fig. 7.8 for a real Swarm data arc. Between these four option deviations can be observed at the beginning of the arc. After this first 30 seconds, all four options lead to essentially the same corrections for the L2 phase. Its corrections are that large at the beginning that it takes up to 60 seconds for this option to agree with the other options on mm level. Depending on the signal dynamics, the first option may introduce discontinuities in the first time derivative, which cause unrealistic large corrections (blue curve). This is due to the Fourier transform, which assumes a periodic signal and consequently the signal dynamics at the end of the phase arc influence the corrections at the beginning of the arc. The second option is separating the first and last observation by prolonging the signal with a constant value. As in option 1, this approach can cause discontinuities in the first time derivative at the edges which lead to relatively large corrections (orange curve). The third option doubles the signal

length. The obtained signal is defined as

$$\tilde{\phi}(t_i) = \begin{cases} \tilde{\phi}(t_i) & , i \leq n \\ -\tilde{\phi}(t_{n-(i-n)}) & , i > n \end{cases} \quad (7.25)$$

It is preserving the odd derivatives while setting the even derivatives to zero. Therefore only sinus terms propagate into the Fourier transform, whereas the cosine terms are 0. This procedure allows an infinite continuously differentiable extrapolation. It should be noted that symmetric data is generated, which may not be realistic. The last option, proposed by C. Siemes (personal communication), fits a linear polynomial to the first and last 20 seconds of an arc and extrapolate for 60 seconds at the ends. The signal is blended in using a linear weighting function for the first and last 10 seconds of the arc to ensure a smooth transition. The resulting signal  $\tilde{phi}(t)$  is:

$$\tilde{\phi}(t) = \begin{cases} \phi^s(t), & t < t_s \\ \frac{(10-(t_s-t)) \cdot \phi^s(t) + (t_s-t) \cdot \phi_t}{10}, & t_s \leq t < t_s + 10 \\ \phi(t), & t_s + 10 \leq t \leq t_e - 10 \\ \frac{(10-(t-t_e)) \cdot \phi^e(t) + (t-t_e) \cdot \phi(t)}{10}, & t_e - 10 > t \geq t_e \\ \phi^e(t), & t > t_e \end{cases} \quad (7.26)$$

Here  $t_s$  and  $t_e$  are the times of the first and the last observation in the original arc and  $\phi_s$  and  $\phi_e$  are the fitted linear polynomial at start and end of the arc. This approach shows the smallest corrections caused by edge effects and introduces only little a priori information (i.e. first derivative preserved) and was therefore selected.

The inverse transfer function is applied for each phase arc, and the differences between the input and output signal are computed to reconstruct the L2 phase measurements. Since the differences are generated solely by the L2 phase observable, all so derived corrections are applied to L2 and written into a corrected RINEX file. In case no correction was possible due to missing L2 or the arc was shorter than 20s, the arc was completely removed from the RINEX file. The number of short arcs is relatively small (for example, on the 1st of March 2015, in total 40 arcs were affected). Besides, also rejecting each the first and last 30 s was tested. Due to the low redundancy in the Swarm case, this resulted in a significant loss of positions ( $\sim 6\%$ ). Therefore this approach is not examined in more detail.

## 7.3 Impact on orbit and gravity field determination

The POD is performed using the Swarm GPS RINEX files (baseline 0401) and attitude files (baseline 0401) provided by ESA. Further details on the processing strategy used can be found in Sect. 5.9.1. A first estimate for the corrections needed is the ionosphere-free (IF) phase residuals to a reduced dynamic (RD) orbit and the associated receiver clock solution. Since the RD orbit shows

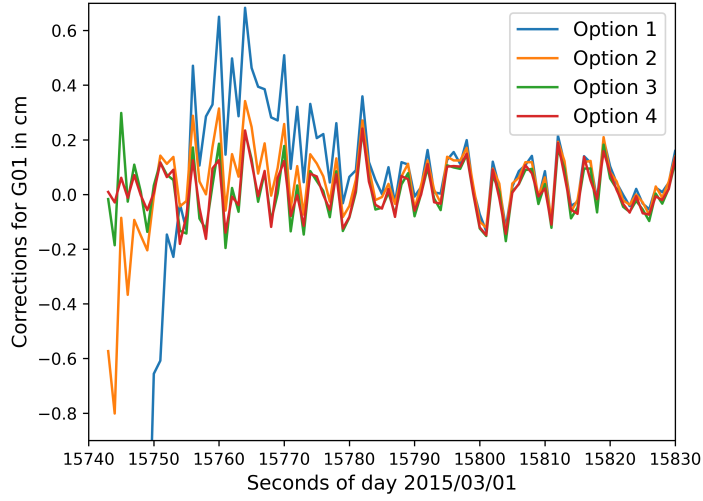


Figure 7.8: Impact of four different methods to treat the edges (Swarm A, 1st of March 2015) for G01. Option 1: no extrapolation, Option 2: 300 seconds of zero values, Option 3: point mirroring at the edges, Option 4: 60 second linear polynomial with 10 second blending.

more dynamical stiffness than a KN orbit, it better represents the satellite's assumed "true" position. At the locations where artifacts occur, the IF phase residuals may become large [Schreiter et al., 2019], but due to the estimation of epoch-wise receiver clock offsets, they have an approximately epoch-wise zero mean considering all simultaneously observed GPS satellites. Figure 7.9 (top) shows an example of IF phase residuals for the GPS satellite G01 and the associated TL corrections derived previously. The corrections are scaled by approximately  $-1.546$  for comparing the corrections to the IF phase residuals. This factor is the  $\phi_2$  pre-factor in the IF linear combination. At the locations where the IF phase residuals are getting large, the corrections show very similar behavior. However, earlier on that day (around second 12200), opposite corrections for G01 are observed, which are caused by another GPS satellite (G23). G23 shows large phase residuals, too, and consequently has large corrections. The phase residuals are linked by epoch-wise clock corrections, resulting in a range error for observations of other GPS satellites. In order to evaluate the impact on orbit fitting level, the post-fit RMS for RD and KN orbits (see Fig. 7.11, RD left, KN right) and the number of observations used for the final orbit computation (see Fig. 7.10) are compared for three scenarios: The uncorrected reference solution, the correction, when using the point mirroring, and the correction when using the extrapolation. By construction, the latter two should result in very similar results. First, it can be noted that more observations could be used for the POD for almost all days. For the first and worst month (March 2015/Swarm A), the number of used observations increases by 6% to 7%. For the weaker ionospheric condition

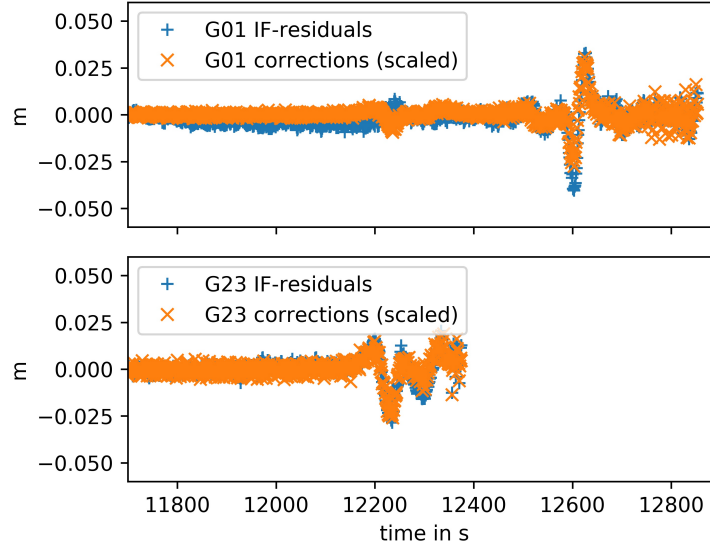


Figure 7.9: TL corrections scaled to IF linear combination and IF Phase residuals for G01 and G23 to a reduced dynamic orbit for Swarm A, 1st of November 2014.

in the later months and also after the TL updates corrections were applied. Still, a few hundred more observations could be used when applying our corrections. The increased number of useable observations is remarkable because the correction scenarios contain by construction fewer observations in the RINEX file due to the rejection of short arcs, where no reliable corrections could be derived. For the post-fit RMS, both TL correction scenarios show an improvement from 3 mm RMS down to 2 mm RMS (see Fig. 7.11) for the reduced dynamic orbit (March 2015). Even the strongly disturbed days (17th to 19th of March 2015) show an improvement. However, the RMS is still high above typical levels due to a geomagnetic storm taking place on 17th of March 2015 with Kp-indices up to 8–, [GFZ-Potsdam, 2019]. For August 2015, an RMS level of 1.4 mm can be achieved instead of approximately 1.9 mm (Swarm A) or 1.6 mm (Swarm C). For November 2016 also an improvement of 0.2 mm can be observed. For the kinematic positions, an improvement from 2.1 mm down to 1.6 mm can be observed for March 2015. Also, the RMS for August 2015 and November 2015 drops. Even if the impact is relatively small, there is not even a single day where the corrected solution is worse than the original reference solution. In the corrected cases in general, fewer ambiguities were set. The difference is up to 5% less for some days. The differences are again more minor with updated settings and less ionospheric activity.

An external assessment of the orbit quality is performed using SLR validation (see Sect. 5.9.1) The selection of the subset of available SLR stations includes the station numbers 7090, 7105, 7119, 7501, 7810, 7825, 7827, 7839, 7840, 7841, 7941 and 8834. Among those stations are Herstmonceux, Graz, Greenbelt, Mount Stromlo, Yarragadee, and Zimmerwald known for particularly high

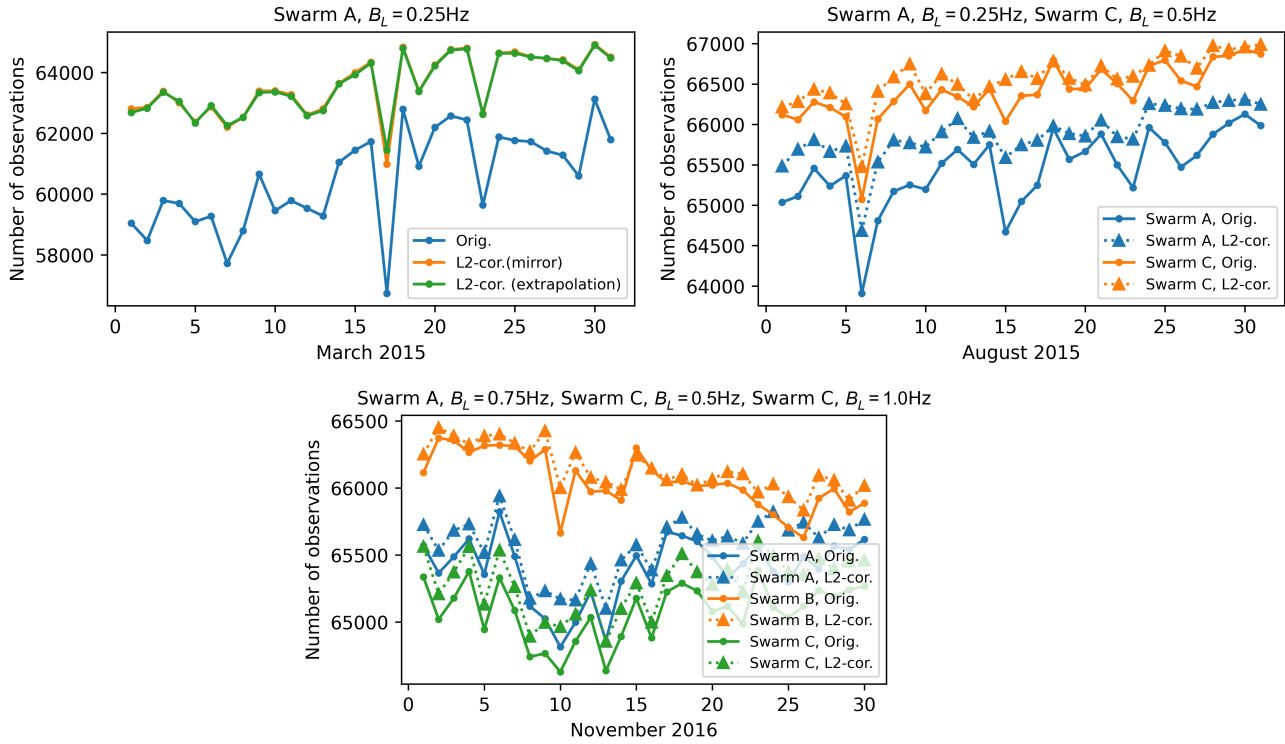


Figure 7.10: Number of observation usable for reduced dynamic orbit fit.

quality and amount of SLR observations. An outlier threshold of 200 mm is used. A selection of stations near the geomagnetic equator could not be performed due to the minimal number of active SLR stations in equatorial regions. For the reduced dynamic orbits in March 2015, the results are given in Tab. 7.3 and 7.4. For the reduced dynamic orbits, a systematic offset between the original and the corrected solutions of 0.4 mm to 0.6 mm may be observed. The standard deviation shows an improvement of 1 mm to 1.2 mm, and also, a small improvement can be seen in the RMS. For the kinematic orbit, standard deviations and RMS also improve in the corrected scenarios. Here the difference is much more significant, with approximately 1 mm in mean offset and 3.6 mm in standard deviation and RMS. For August 2015 (see Tab. 7.6 and 7.5) and November 2016 (see Tab. 7.8 and 7.7), almost no difference can be observed for the reduced dynamic orbits. Only minor improvements in the range of 0.1 mm for the kinematic positions are visible, apart from November 2016, where the standard deviation for Swarm A's kinematic positions is improved by 0.6 mm. This test, however, is not of utmost significance because not sufficient SLR observations from near-equatorial stations are available. Still, it could be shown that the orbits do not degrade and also that the kinematic positions better agree with the SLR measurements.

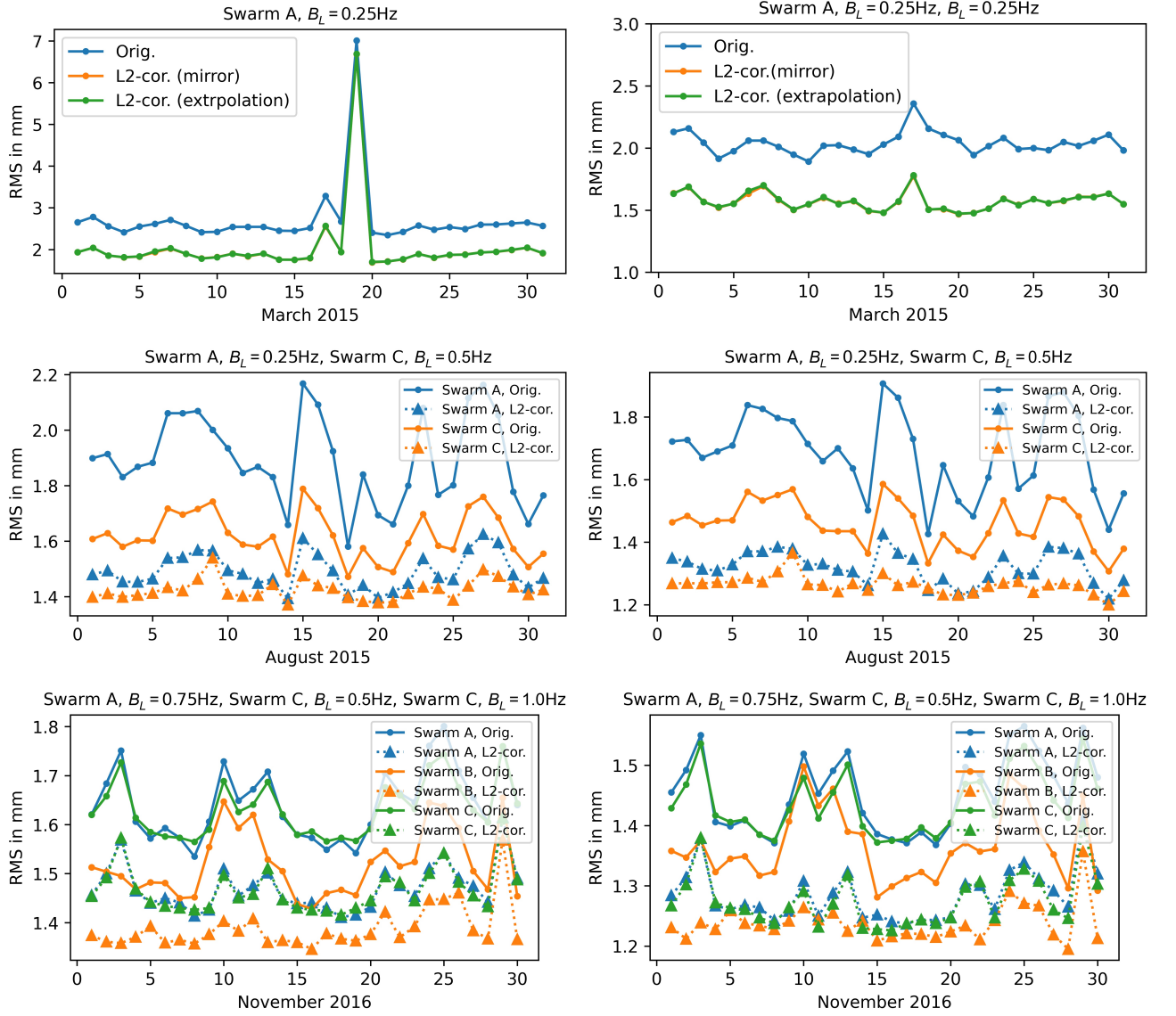


Figure 7.11: Posteriori RMS reduced dynamic orbit (left) and kinematic orbit (right) fit.

Table 7.3: SLR residual statistics for March 2015, Swarm reduced dynamic orbits.

<b>March 2015</b>	number of observations	mean [mm]	std [mm]	RMS [mm]
Swarm A, Original	1433	4.93	26.09	26.54
Swarm A, L2-Cor. (mirror)	1433	4.55	24.91	25.32
Swarm A, L2-Cor. (extrapolation)	1433	4.34	25.05	25.41



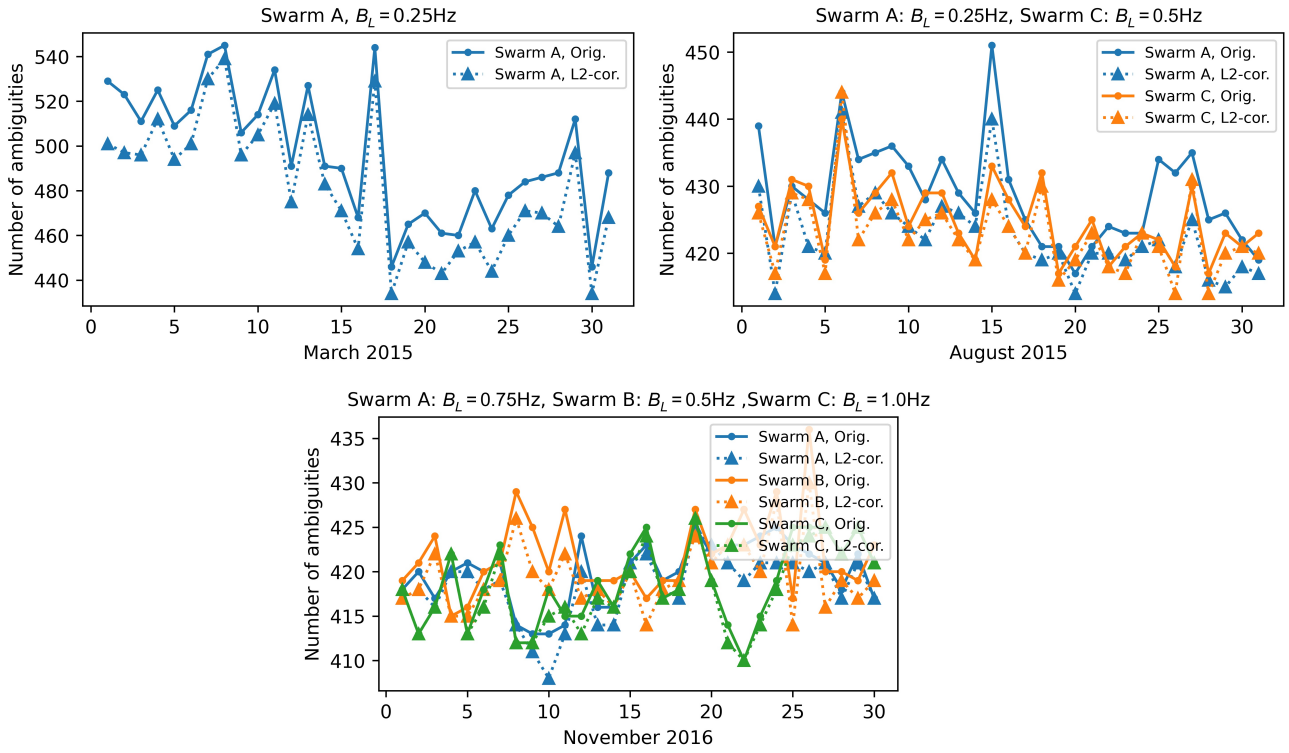


Figure 7.12: Number of ambiguities set up.

Table 7.4: SLR residual statistics for March 2015, Swarm kinematic orbits.

<b>March 2015</b>	number of observations	mean [mm]	std [mm]	RMS [mm]
Swarm A, Original	1408	2.47	30.02	30.12
Swarm A, L2-Cor. (mirror)	1408	1.56	26.42	26.45
Swarm A, L2-Cor. (extrapolation)	1408	1.29	26.46	26.48

Table 7.5: SLR residual statistics for Aug. 2015, Swarm reduced dynamic orbits.

<b>August 2015</b>	number of observations	mean [mm]	std [mm]	RMS [mm]
Swarm A, Original	1775	7.01	14.23	15.86
Swarm A, L2-Cor. (mirror)	1775	6.86	14.41	15.95
Swarm A, L2-Cor. (extrapolation)	1775	6.78	14.33	15.85
Swarm C, Original	2047	5.00	14.67	15.49
Swarm C, L2-Cor. (mirror)	2047	5.04	14.71	15.54
Swarm C, L2-Cor. (extrapolation)	2047	5.00	14.75	15.57



Table 7.6: SLR residual statistics for Aug. 2015, Swarm kinematic orbits.

<b>August 2015</b>	number of observations	mean [mm]	std [mm]	RMS [mm]
Swarm A, Original	1775	4.95	18.75	19.39
Swarm A, L2-Cor. (mirror)	1775	4.62	18.49	19.04
Swarm A, L2-Cor. (extrapolation)	1775	4.63	18.48	19.04
Swarm C, Original	2047	4.39	16.54	17.11
Swarm C, L2-Cor. (mirror)	2047	4.21	16.34	16.87
Swarm C, L2-Cor. (extrapolation)	2047	4.21	16.37	16.90

Table 7.7: SLR residual statistics for Nov. 2016, Swarm reduced dynamic orbits.

<b>November 2016</b>	number of observations	mean [mm]	std [mm]	RMS [mm]
Swarm A, Original	1662	7.83	10.76	13.31
Swarm A, L2-Cor. (mirror)	1662	7.71	10.91	13.36
Swarm A, L2-Cor. (extrapolation)	1662	7.77	10.91	13.39
Swarm B, Original	4075	6.12	10.87	12.47
Swarm B, L2-Cor. (mirror)	4075	6.04	10.74	12.32
Swarm B, L2-Cor. (extrapolation)	4075	6.12	10.75	12.37
Swarm C, Original	1432	5.06	10.69	11.82
Swarm C, L2-Cor. (mirror)	1432	5.14	10.61	11.79
Swarm C, L2-Cor. (extrapolation)	1432	5.13	10.49	11.68

Table 7.8: SLR residual statistics for Nov. 2016, Swarm kinematic orbits.

<b>November 2016</b>	number of observations	mean [mm]	std [mm]	RMS [mm]
Swarm A, Original	1660	4.68	22.21	22.69
Swarm A, L2-Cor. (mirror)	1660	3.22	20.59	20.84
Swarm A, L2-Cor. (extrapolation)	1660	3.28	20.59	20.84
Swarm B, Original	4075	7.16	13.78	15.53
Swarm B, L2-Cor. (mirror)	4075	6.99	13.63	15.32
Swarm B, L2-Cor. (extrapolation)	4075	7.01	13.64	15.34
Swarm C, Original	1432	1.33	15.21	15.26
Swarm C, L2-Cor. (mirror)	1432	1.30	15.10	15.15
Swarm C, L2-Cor. (extrapolation)	1432	1.33	15.13	15.19

The gravity field solutions were computed based on the procedure outlined in Sect. 5.9.2. To evaluate the gravity field solutions, we compare them to the monthly JPL-RL06 GRACE gravity field solution [Yuan, 2018]. First, we perform a visual inspection of the resulting geoid height differences, smoothed using a 400 km Gaussian filter, checking if the equatorial artifact is mitigated and if other artifacts occur (see Fig. 7.13). We also compare to a solution obtained in a previous study using weighting of observations ([Schreiter et al., 2019], Chap. 6). The correction scenario is capable of reducing the equatorial artifact to a limited extent. Still, the equatorial artifact is least visible in the weighting solution. However, the polar regions' noise patterns are less pronounced when correcting L2 measurements based on the inverse loop transfer function. Due to insignificant differences and no pronounced artifact, the geoid height differences are not displayed for August 2015.

In the difference and error degree amplitudes (Fig. 7.14) the corrected observations lead to a reduction of the difference w.r.t. the reference gravity fields and show minor error degree variances (dashed line, Fig. 7.14). In the very low degrees, the weighting scenario is slightly better for March 2015 than the L2 correction and the original scenario. In contrast, in the higher degrees, the L2 correction scenario and the weighting solution become comparable. However, the difference amplitudes are still significantly smaller using the weighting strategy for degrees 12 to 30. The solution based on L2 phase corrections and the solution based on weighting the observations shows improvement compared to the original solution (see Fig. 7.14). Formal errors are smaller at all degrees when using the corrected L2 data compared to the original data due to a larger number of accepted observations. For the actual errors, the benefit of the L2 correction can primarily be seen in higher degrees ( $>10$ ). However, this may be expected. The correction mainly affects frequencies near 1/30 Hz, which equals a few hundred kilometers in spatial resolution and is therefore invisible in the low degrees, covering larger scales. For August 2015 for Swarm C (Fig. 7.14 (right)), after the first TL update was performed, the L2 correction is also capable of reducing the error degree variance. However, the differences between the original scenario and the original solution are minor. For this month, also degradation in the low degrees is observed for the weighting scenario. Comparing the weighted RMS of geoid height differences (wRMS) for March 2015, see Tab. 7.9, again, the weighting solution shows the lowest value with 16.64 mm compared to the monthly GRACE JPL-RL06 gravity field solution. The best fit concerning the kinematic positions and the maximum number of kinematic positions used are obtained in the correction scenario. When comparing the results for August 2015 (Tab. 7.10), one may see that the wRMS of 12.15 mm is lower than the weighted solution's value of 13.82 mm, for Swarm A. A similar result is obtained for Swarm C, where the weighted RMS is 14.33 mm for the weighted solution and 12.12 mm for the correction scenario. However, the wRMS for the original solution is approximately 0.4 mm lower than for the correction. In the wSTD over the oceans, the corrected scenario shows the smallest value in all cases for August 2015. The number of positions used is similar in all cases, but the best fit concerning the kinematic positions could be obtained using the correction.

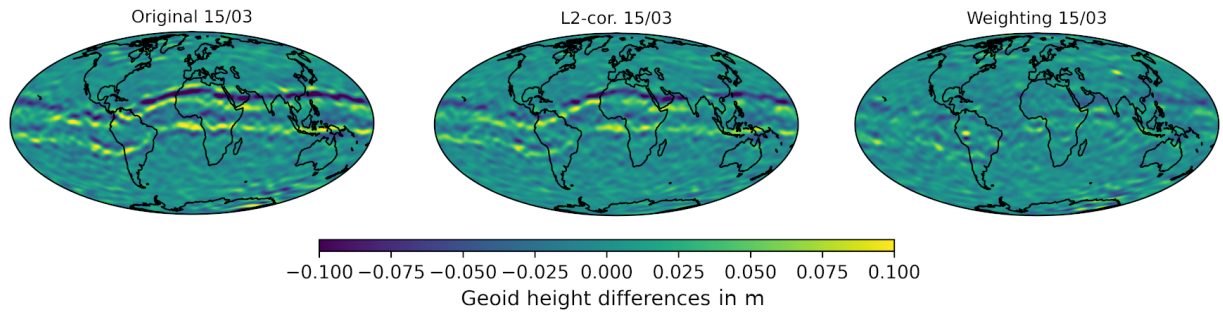


Figure 7.13: Geoid height differences for a Swarm A GPS-only gravity field solution compared to the monthly GRACE JPL-RL06 solution. The original reference scenario is shown on the left, based on L2 corrected RINEX files in the middle and the gravity field obtained using weighting on the right.

Table 7.9: Gravity field comparison for March 2015

Scenario	wRMS (monthly) <sup>1</sup> mm	wSTD (monthly) <sup>1,2</sup> mm	No. kin. pos.	RMS kin. pos. mm
A Original	28.49	25.87	695673	2.61
A L2-correction	22.57	24.56	761586	2.27
A Weighting	16.64	20.66	706698	2.58

<sup>1</sup> Compared to the monthly GRACE JPL-RL06 gravity field solution

<sup>2</sup> Resolved up to degree and order 20

<sup>3</sup> Weighting using the second derivative combined with the Rate-of-TEC Index

It can be concluded that correcting the L2 phase observable using the loop filter's inverse transfer function is beneficial in orbit and gravity field processing. In general, more observations could be used for orbit processing. The post-fit RMS is lower for all TL settings, and in terms of SLR validation, the orbits were not degraded. In gravity field processing, mitigation of ionospheric errors is observed, but the weighting approach was still more successful for a heavily affected month. For a less affected month after the TL update, weighting leads to a degradation of the gravity field. In contrast, no degradation is observed for the gravity field based on corrected L2 observations.

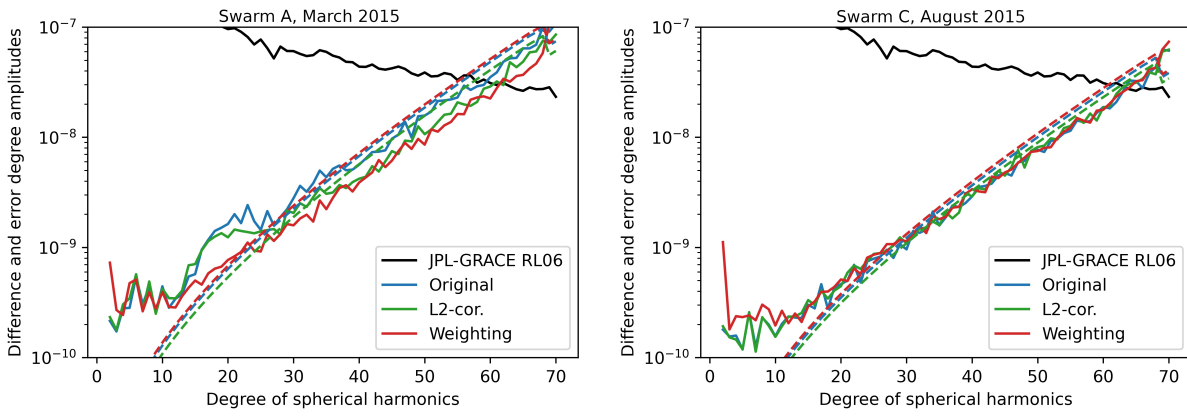


Figure 7.14: Difference- (solid) and error degree (dashed) amplitude for a Swarm A GPS-only gravity field solution for March 2015 (left) and a Swarm C GPS-only gravity field for August 2015 (right).

Table 7.10: Gravity field comparison for August 2015

Scenario	wRMS (monthly) <sup>1</sup> mm	wSTD (monthly) <sup>1,2</sup> mm	No. kin. pos.	RMS kin. pos. mm
A Original	13.08	18.58	796761	1.97
A L2-correction	12.15	18.46	801294	1.59
A Weighting	13.82	18.89	799398	2.05
C Original	11.76	18.21	801576	1.70
C L2-correction	12.14	18.05	802515	1.52
C Weighting	14.33	18.45	802695	1.78

<sup>1</sup> Compared to the monthly GRACE JPL-RL06 gravity field solution

<sup>2</sup> Resolved up to degree and order 20

<sup>3</sup> Weighting using the second derivative combined with the Rate-of-TEC Index

## Chapter 8

# Measuring and modelling the ionosphere using LEO-GPS

This chapter will discuss how LEO GPS-TEC can be used to gain insight into the electron density of the topside ionosphere and plasmasphere. A selection of current state-of-the-art and well-validated models was shown in Sect. 2.8, how they are calibrated, and subsequently their limitations. Existing empirical models rely mostly on ground-based observations, except for the Neustrelitz Plasmasphere model [Jakowski and Hoque, 2018], a climatological model based on CHAMP topside GPS. For the IRI model, also topside sounding was utilized using, e.g., the INTERCOSMOS 19 topside sounder that was operating from 1979 to 1982 [Bilitza et al., 2006], and also the IMAGE satellite carrying the radio plasma imager (RPI) instrument was operating from 2000 to 2005 [Reinisch et al., 2007]. Topside radar TEC from the TOPEX mission (1992-2006) is compared to IRI [Bilitza et al., 2011, Jee et al., 2005]. An overview of topside sounding missions is given in Themens et al. [2018]. More recent or more extended data sets of topside sounding do not exist.

Nowadays, many low Earth-orbiting satellites, among them Swarm, GRACE (-FO), and Sentinel, can provide slant TEC observations employing dual-frequency GPS observations. Due to a large number of observations, the different altitude regimes, and the fast orbital revolution time of about 90-100 min, they provide a sizeable continuous database to estimate the topside electron density on relatively short time scales of a few hours. The approach presented considers the numerically integrated electron content along the line of sight instead of mapped vertical TEC, as used, e.g., in the CODE TEC maps. A priori symmetries introduced by elevation-dependent mapping functions can be avoided by using numerical integration, however, the computational effort increases significantly. Tracing is essential for LEO satellite slant TEC when using low elevation data (see Sect. 3.7.3). The integration is a major difference to the multi LEO model proposed by Ren et al. [2020]. In his publication mapping functions (of similar design as the mapping function proposed by Foelsche and Kirchengast [2002], see Eq. 3.35) were applied to estimate two TEC maps of different altitude regimes based on vertical TEC. Their model is based on Swarm, GRACE,

TerraSAR-X, and Kompsat-5 for the 500 km upward altitude regime, and COSMIC and MetOp for the 800 km upward altitude regime. Also, the choice of the mapping parameters, such as layer height and layer thickness, can be avoided as it would have to be performed for each altitude regime and can only locally be validated as only radar observations can sound above peak altitude, but they do not provide global coverage.

A second challenge is the accuracy of code leveled slant TEC, which is limited by the code noise. Also not negligible is the uncertainty of the receiver's P1-P2 bias, which is required to estimate the absolute slant TEC. This error can be arbitrary depending on the leveling method used (see Sect. 3.7) and reach several TECU. As plasmaspheric TEC may only reach very few TECU, leveling uncertainties exceeding these values are considered too large. Therefore, a leveling bias for each phase arc is co-estimated with the model parameters in this work. Eventually, the obtained results are evaluated and validated by comparing the estimated electron density to DMSP in situ measurements. The model dynamics during the geomagnetic storm occurring on the 5th of August 2019 are included in the analysis. After introducing the model approach and the adjustment process, the obtained electron density is validated using other models and measurement types. The stability of the estimated P1-P2 receiver bias is assessed, and as another result, geometry-free PCV maps are derived. As an application, the importance of plasmasphere estimation is shown for a tomographic approach, and a link is drawn to the earlier discussed artifacts in the GPS phase observations (see Chaps. 6 and 7).

## 8.1 Topside formulation

The model developed in this work makes use of a variation of a single Epstein layer (see Sect. 2.2.2) similar to the formulation that is used in the NeQuick model

$$N_e(h) = 4N_m \frac{e^{\alpha \cdot z(h)}}{(1 + e^{z(h)})^2} \cdot \frac{e^{\bar{z}(h)}}{1 + e^{\bar{z}(h)}}, \quad (8.1)$$

where

$$z(h) = \frac{h - h_m}{H_0} \quad (8.2)$$

and

$$\bar{z}(h) = \frac{h - h_{cut}}{H_{cut}}, \quad (8.3)$$

where

- $N_m$  is the peak electron density,
- $h_m$  is the height of the peak electron density,

- $H_0$  is the reference scale height,
- $h_{cut}$  is the altitude, below which no significant electron density is to be assumed, and
- $H_{cut}$  defines the cutoff rate at  $h_{cut}$ .

The purpose of the last term is to smoothly cut the electron density below a certain altitude, where significant electron density is to be expected un-physical. Values of  $h_{cut} = 90$  km and  $H_{cut} = 5$  km are selected, such that no significant electron density may be observed below 80 km as a significant ionization below that altitude is considered to be unrealistic. For altitudes above 80 km, the cut-off function quickly converges to 1 and consequently the Epstein layer in the higher altitudes is virtually unaffected by the cut-off function. A second modification to the Epstein layer is the shape parameter  $\alpha$ . This parameter can be used to slow down the decay with higher altitudes. In the limit case, where  $\alpha$  is set to 2, no decay with higher altitudes takes place and the electron density is basically  $2 \cdot N_m$  for altitudes significant above  $h_m$ . An  $\alpha$  larger than 2 would lead to an exponential increase with altitude and a value smaller than 0 to an exponential decay with no ionization peak. Therefore,  $\alpha$  is limited to values between 0 and 2. The impact of the parameters on the profile is shown in Fig. 8.1.

Profilers using the Epstein layer formulation are already in use in several topside models like the IRI-Plas and the NeQuick topside. Even though the ionosphere consists of several layers (D/E/F1/F2-layer) this may be ignored for the topside. The measurements taken from the LEO satellite missions cover altitudes above 450 km, which is above the F2 peak at approximately 350 km. An Epstein layer is selected instead of a Chapman layer, because it better represents the topside decay. Contributions of lower layers can be assumed to be sufficiently small to be neglected due to their exponential decay with altitude. In contrast to the Chapman layer function, the Epstein layer does not take the solar zenith angle into account. Nevertheless, the variability is given in our model approach when varying the parameters, namely the maximum electron density  $N_m$ , the peak altitude  $h_m$ , scale height  $H_0$ , and the shape parameter  $\alpha$ . Also, composition changes are compensated for by varying the parameters.

A change in ion composition mostly affects the scale height of the electron density. The scale height is linked to the temperature by

$$H = \frac{k_B T}{mg}, \quad (8.4)$$

where  $k_B$  is the Boltzmann constant,  $T$  is the temperature in Kelvin,  $m$  is the mean molecule mass (in kg), and  $g$  is the gravitational acceleration. For our simplistic modeling, the unknown temperature and composition are thus compensated by a variation in scale height combined with the shape parameter  $\alpha$ .

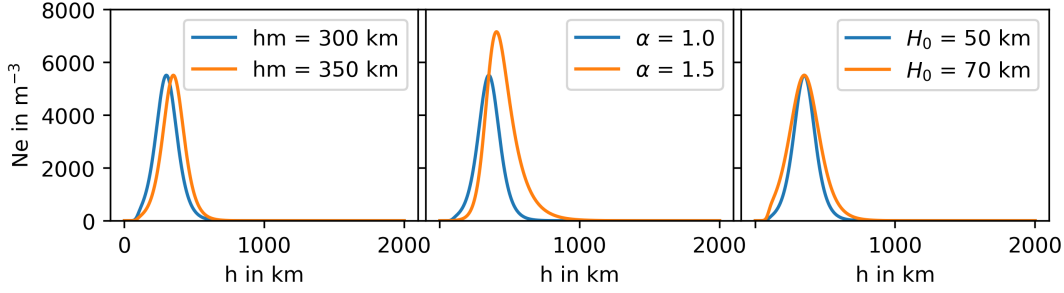


Figure 8.1: Changes in the profile function when adjusting the parameters  $hm$ ,  $H_0$ , and  $\alpha$ .  $Nm$  is fixed to  $e^{10}/4 \text{ m}^{-3}$ ,  $H_0 = 50 \text{ km}$ ,  $\alpha = 1$  and  $hm = 350 \text{ km}$  unless varied.

## 8.2 Model approach

The model provides an empirical three-dimensional electron density with a reasonably fast time resolution of currently 3 h. The future aim is to match the 1 h time resolution of the CODE TEC maps, such that the model may be seen as a three-dimensional counterpart to the CODE TEC maps. In this work, the time resolution is set to 3 h to have about two full revolutions of each LEO satellite used. The model is intended to be derived mostly, but not exclusively, from LEO GNSS TEC. Further data-sources are ground-based TEC and, if available, Langmuir electron density measurement data collected by the Swarm satellites. The observations used are shown in Tab 8.1. Model-assisted arc-wise leveling of the LEO slant TEC observations can be seen as a key feature. The absolute calibration of GNSS TEC remains one of the most challenging parts and will be discussed in Sect. 8.2.1. Bias parameters are set up for each phase arc independently. A simple empirical approach, similar to the CODE TEC maps, describes the electron density. Instead of using a single or slab layer model, a vertical profiler similar to an Epstein layer is used. The layer function requires modeling the peak electron density, the height of the peak electron density, and the scale height. The profile's shape can be adjusted using the parameter  $\alpha$  for accounting for the plasmasphere transition.

The global variability employs a very similar approach as the CODE TEC maps. As a reference coordinate system, magnetic local time and magnetic latitude (based on IGRF-13) are used (for comparison, the CODE TEC maps use local time and dipole latitude [Schaer et al., 1996]). The global representation of the parameters defining the layers' properties is modeled using spherical harmonics, which is also employed for CODE TEC maps.



Table 8.1: Observation types used for fitting the topside ionosphere-plasmasphere model. The in situ plasma density is taken from the Swarm Langmuir Probes. The Ne values obtained by the Langmuir probes are corrected by the factors published in [Lomidze et al. \[2018\]](#).

Obs. type	Mission/Source
relative sTEC	Swarm A/B/C, GRACE-FO A/B, Sentinel 1A/1B/2A/2B/3A/3B
in situ Ne	Swarm A/B/C
vertical TEC	CODE TEC map ( $5^\circ \times 5^\circ$ grid)

### 8.2.1 Consideration regarding slant TEC

The slant TEC was obtained by the procedure outlined in Sect. 3.7. Connected phase arcs are identified and down-sampled to a 30 s sampling. When using the full available 0.1 Hz or even 1 Hz sampling for certain missions, the computational effort increases, but the effect on the model results is limited because of the model's limited spatial resolution (here spherical harmonics up to degree and order 8). If the sampling rate is higher than 30 s the signal is further pre-processed to get rid of higher frequencies in the signal. For that purpose, the Fast Fourier Transform (FFT) is used and the coefficients for frequencies above 1/60 Hz are set to zero (Nyquist frequency for 30 s sampling). The filtered signal is then evaluated converted into a 30 s sampling. There are two benefits of this procedure. First, as shown in Chap. 7 the observations can be highly correlated in the range of several seconds, and second: outliers and observational noise is mitigated. The observations are assumed to be uncorrelated and also free of high-frequency noise when using the 30 s filtered down-sampled signal.

Code leveling is considered to have too large uncertainties. Especially for the high-flying Sentinel satellites, where the observed slant TEC values are in general small, the error from code-based leveling can even easily exceed the maximum sTEC. A more accurate adjustment is required. In the worst case, the leveled TEC's absolute accuracy is expected to be in the range of several TECU when using code leveling techniques, dominated by the leveling uncertainty given by the code noise. That accuracy is far below GNSS TEC's potential obtained by phase measurements, which has a relative accuracy better than 0.01 TECU, assuming an L1 phase noise below 1 mm, a reasonable value for Blackjack receivers (e.g., CHAMP [[Montenbruck and Kroes, 2003](#)]). It may be expected that the further developed TriRO-GNSS receivers as they are flying on GRACE-FO match this level as they have Blackjack heritage, and the Swarm SGPS receivers are expected to provide similar accuracy. The remaining receiver-dependent P1-P2 (C1W-C2W) bias needs to be estimated to obtain absolute slant TEC using code leveling (see Sect. 3.7). A common approach is to shift the relative slant TEC, such that it fits assumptions like non-negativity, by setting the lowest observed TEC value to 0. When working with LEO satellites at different altitudes, this only holds if the electron density along the line of sight is exactly 0, which is unrealistic due to the nature of the F2-layer and the plasmasphere. Combining different LEO satellites, relative offsets

of the calibration between the LEO satellites, and of course, the absolute unknown offset have to be considered. One bias parameter is set up for each connected phase arc to allow precise leveling. These bias parameters are eventually solved in the model adjustment. As the biases are estimated in a least-squares adjustment by comparing the model slant TEC to the observed slant TEC they are not singular. However, they rely on the model approach. These parameters are an essential outcome of the adjustment process, as they can be used to obtain calibrated LEO GNSS TEC.

### 8.2.2 Tracing and integration

Due to the ionosphere's three-dimensional structure, the profile's variation can only fully be seen in the slant TEC instead of mapped vertical TEC. Two different layers can result in the same vertical TEC but can differ in scale height and peak density. Besides, the classical elevation-dependent mapping functions to obtain vertical TEC from slant TEC assume that the receiver is located below the ionosphere and that the electron density does not have a more significant spatial gradient in the antennas field of view. This assumption might be a valid assumption for ground receivers. However, GNSS receivers on-board LEO satellites are directly located inside the ionosphere and sensitive to spatial gradients in slant TEC, especially when using low elevation data. This can partially be compensated using slab layer mapping functions (see Sect. 3.7.3), but requires adjusting the layer thickness and peak height for each satellite mission or ground station. Nevertheless, the peak height needs also to be adjusted, but ground stations are rather insensitive to peak height variations.

Numerical line of sight integration is used to obtain model slant TEC values and compare them to the measured slant TEC to avoid using vertical TEC. To solve the integral, numerical integration

$$sTEC = \int_{LEO}^{GPS} Ne(l)dl \approx \sum_{i=1}^N w_i \cdot Ne(s_i) \quad (8.5)$$

will be used. Here  $w_i$  are the weights, and  $s_i$  are the support points along the line of sight. Since the model is restricted to large scales, changes in slant TEC caused by a different path by ray bending effects can be ignored. Gauss-Legendre quadrature with 8 support points is used to solve the numerical integration. The integration is carried out for the ray path below 2000 km and above 2000 km separately, and eventually, both parts are added up. The reason for this approach will be discussed in the following subsection 8.2.3. This order allows a perfect integration up to a polynomial degree of 15 (Gauss-Legendre quadrature) for each interval, thus keeping the integration error sufficiently low. Simple approaches, like the box-rule, should not be used because of systematic differences when integrating a function as an exponential decay.

### 8.2.3 Order of the numerical integration

The optimal order  $N$  of the numerical integration is a trade-off. The most accurate integration is obtained by pushing  $N$  to infinity, neglecting numerical limitations. This, however, leads to an immense computational effort. A simulation using an Epstein layer with a scale height of 120 km and  $h_m = 350$  km is performed to estimate the required degree for the quadrature rule. The relatively large scale height was selected to account for larger plasmaspheric scale heights [Wu et al., 2021]. For evaluation purposes, the absolute relative error

$$|\epsilon_{rel}| = \left| \frac{I_{num} - I_{ana}}{I_{ana}} \right| \quad (8.6)$$

is used, where  $I_{ana}$  is the analytical integral and  $I_{num}$  the numerical approximation. At least 29 support points need to be set (see Fig. 8.2), to ensure an error below 0.1 % without splitting. This situation can drastically be improved when separating the top and the bottom side at 2000 km altitude. In that case, a low degree of 8 is sufficient for both parts, which in total means 16 function evaluations instead of 29 that would have been required to achieve similar accuracy without splitting. The reason for that behavior is the fast decay which causes the polynomial fitted for quadrature to oscillate. When assuming large slant TEC values in the range of 100 TECU, as Swarm observed them, an integration error below 0.1 TECU can be realized. When considering a LEO satellite at 450 km, i.e. above the peak, this can be even improved, and the error may be pushed below 0.01 %. For a slant TEC of 100 TECU, this results in an integration error below 0.01 TECU, which is even below the TEC noise level derived from GPS phase observations.

### 8.2.4 Parameters

The parameters to be estimated may be divided into two categories: model coefficients and calibration biases. The model coefficients are required to define the density profile, namely  $Nm$ ,  $H_0$ ,  $\alpha$ , and  $h_m$ . As the model is supposed to provide a global representation, these parameters may vary with location, which is accounted for using spherical harmonics for the global representation. As TEC, or more specifically the electron density, is largely sun fixed and bound to the magnetic field, magnetic latitude and magnetic local time are a suited reference frame. A similar approach is utilized in the generation of the CODE TEC maps. In this reference frame, the key parameters

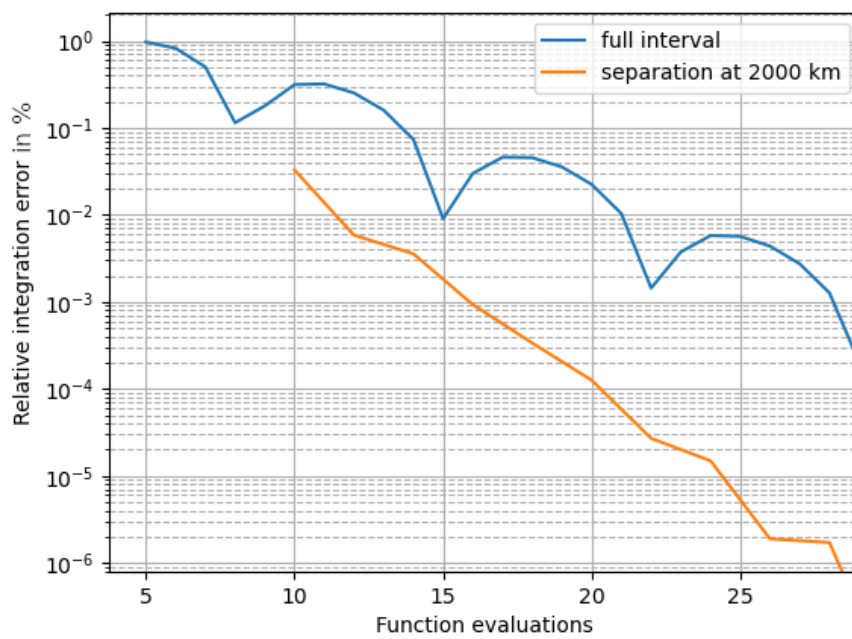


Figure 8.2: Relative numerical integration error tested on Epstein layer function. Note that in case of the separate integration the number of support points in each interval is the number of function evaluation divided by 2.

are expressed using the spherical harmonics

$$Nm(mlat, mLT) = \exp \left( \sum_{i=0}^{n_{Ne}} \sum_{j=-i}^i c_{Nm}^{(ij)} f_{ij}(mlat, mLT) \right), \quad (8.7)$$

$$H_0(mlat, mLT) = f_{H_0} \left( \sum_{i=0}^{n_{H_0}} \sum_{j=-i}^i c_{H_0}^{(ij)} f_{ij}(mlat, mLT) \right), \quad (8.8)$$

$$\alpha(mlat, mLT) = f_{\alpha} \left( \sum_{i=0}^{n_{\alpha}} \sum_{j=-i}^i c_{\alpha}^{(ij)} f_{ij}(mlat, mLT) \right), \quad (8.9)$$

$$hm(mlat, mLT) = f_{hm} \left( \sum_{i=0}^{n_{hm}} \sum_{j=-i}^i c_{hm}^{(ij)} f_{ij}(mlat, mLT) \right), \quad (8.10)$$

where  $f_{ij}$  are the fully normalized spherical harmonic base functions and  $c_*^{(ij)}$  are the model coefficients. In total  $n_{Ne}^2 + n_{H_0}^2 + n_{sH}^2 + n_{hm}^2$  model coefficients have to be estimated. In addition, also the calibration biases need to be estimated. Their number equals the number of continuous phase arcs, which is equivalent to the number of GPS phase ambiguities to be solved for. The exponential in  $Nm$  is selected for two reasons. First, the electron density is nonnegative, and second, as  $H_0$ ,  $\alpha$ , and  $hm$  are in the exponential of the profiler, therefore, having the coefficients for  $Nm$  in the exponential supports the least-squares adjustment. As the values for  $\alpha$  should be restricted to values between 0 and 2 the function

$$f_{\alpha}(x) = 2 \cdot \frac{e^x}{1 + e^x} \quad (8.11)$$

is applied to  $\alpha$  as a bijective mapping from  $\mathbb{R}$  to  $(0, 2)$  and avoid values for  $\alpha$  that would cause numerical issues. As the height of the maximum electron density can be assumed to be well above 100 km, the values of  $hm$  are restricted to values above 100 km. This is done using a infinitely differentiable soft-max function

$$f_{hm}(x, x_{min}, \beta) = \beta \cdot \log(\exp(x/\beta) + \exp(x_{min}/\beta)). \quad (8.12)$$

The parameter  $\beta$  is used as a shape parameter in the soft-maximum. Larger values lead to a smoother transition, whereas small values lead to a sharp bend. This value for  $\beta$  is to be selected concerning the scale of  $x$ , in this case  $\beta = 10$ . A similar method is used to limit  $H_0$  to values larger than 10 km to avoid the singularity at 0, where also the density is not differentiable with respect to the parameter  $H_0$ .

## 8.2.5 Parameter estimation

The minimization problem for the parameter estimation setup can be decomposed into density calculation and integration. The optimization goal is to find the model that best fits the observed

relative slant TEC. The vector  $\mathbf{y}$  is containing the observed relative slant TEC values. For the computation of the slant TEC, the electron density along the line of sight between the receiver (LEO) and transmitter (GNSS satellite) needs to be evaluated at the sampling points defined by the quadrature rule (see Sect. 8.2.2). The integers  $n, i, p, o \in \mathbb{N}$  are defined as follows:  $n$  is the number of slant TEC observations,  $i$  is the number of function evaluations used for the numerical integration,  $p$  is the number of model parameters, and  $o$  is the number of offsets. One offset is estimated for each connected phase arc. The numerical integration may be written as a matrix  $\mathbf{L}$  containing the integration weights of dimension  $n \times (n \cdot i) + o$  (the offsets are not needed for the integration, but they need to be applied when computing the difference to slant TEC values). Then the matrix  $\mathbf{D}$  evaluating the electron density at the sampling points is of dimension  $(n \cdot i) + o \times p + o$ . The offsets are passed to  $\mathbf{L}$  through the additional dimensions of  $\mathbf{D}$ . This sums up to the minimization problem

$$\|\mathbf{F} \cdot \mathbf{x} - \mathbf{y}\| = \|\mathbf{L} \cdot \mathbf{D} \cdot \mathbf{x} - \mathbf{y}\| \rightarrow \min. \quad (8.13)$$

The vector  $\mathbf{x}$  contains the model parameters and the phase offsets. A solution is then performed using non-linear least squares. Here, the number of integration points drives the complexity of the problem. Due to the non-linearity, the matrix  $\mathbf{D}$  has to be recomputed for each minimization step. Therefore, it is crucial to minimize the number of integration points and, in turn, also reduce the dimension of the matrix  $\mathbf{F}$ . Even if the dimension of the matrix  $\mathbf{L}$  may be huge, this is not much of an issue. The matrix does only have  $n \cdot i + n$  non-zero entries (the last  $n$  originates from the offsets) and is therefore sparse. Furthermore, the matrix is static and does not have to be recomputed each step. The minimization algorithm used is an iterative least-squares, namely the Levenberg-Marquardt algorithm [Levenberg, 1944, Marquardt, 1963]. The minimization is initialized, with  $Nm, hm, H_0$  and  $\alpha$  assumed to be globally constant.

### 8.2.6 Regularization

The proposed model includes three major challenges:

- The model is highly non-linear.
- Some model coefficients may only be estimated with large uncertainties or may even be singular.
- Several local time and magnetic latitude areas are not well observed (see Fig. 8.3).

These points may affect the minimization and might as well lead to numerically singular matrices. To overcome these issues, Tikhonov regularization is applied. Two regularization types are used. The model is nested because of the spherical harmonics, meaning that higher resolution can be obtained when increasing the number of spherical harmonics used. The penalization is quadratic, meaning that a the factor penalizing degree  $i$  is  $i^2$  to limit the high degrees' power. As the model

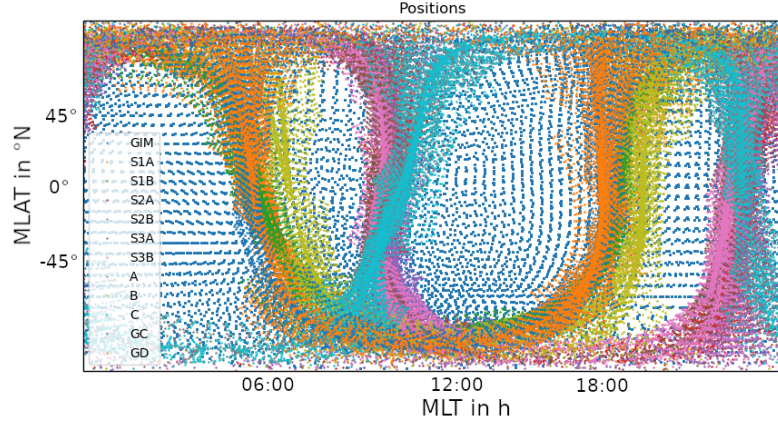


Figure 8.3: Positions of the sampled points in mlat/mL T for 2nd of July 2019 from 00:00 UT to 03:00 UT. The blue dots originate from the CODE TEC map, which is a rough constraint for the large unobserved areas. Furthermore, the figure includes the satellites from Tab. 8.1. This includes Sentinel 1 A/B, 2 A/B, 3 A/B as S1A, S1B, S2A, S2B, S3A, S3B, Swarm A/B/C as A, B, C, and GRACE-FO as GC and GD.

slant TEC's sensitivity concerning the model parameters is of a different order of magnitude, the constraints must be scaled. The factors selected are  $1/25$ ,  $1/50$ ,  $1$ ,  $1/100$  for  $c_{Ne}$ ,  $c_{H0}$ ,  $c_{\alpha}$ , and  $c_{hm}$  with respect to their typical values. A typical value for the maximum electron density can be expected roughly around  $e^{28} \approx 1.5 \cdot 10^{12}$  in non-equatorial regions. Values for the scale height can be expected around 50 km, a shape parameter near 1 for a purely Epstein layer representation, and the height of the peak density between 80 km and 350 km. Therefore, the reference value for the scaling was selected to be 100 km. The constant parameters  $c_{Ne}^{(00)}$ ,  $c_{H0}^{(00)}$ ,  $c_{sH}^{(00)}$  in the spherical harmonic representation are not constrained and also the calibration biases remain unconstrained. The coefficient  $c_{hm}^{(00)}$  is weakly constraint to 180 km. This penalization is necessary because, under certain conditions,  $hm$  can be set to extremely small values during the first minimization steps. Such unrealistic values can cause the normal equation matrix to become numerically singular because of numerical issues. The constraints are summarized in the constraining matrix  $\Omega$ , whereas  $\|\lambda\Omega\mathbf{x}\|$  is the penalization term. Its penalization parameter  $\lambda$  is determined empirically.

## 8.3 Results

This section evaluates the fit's quality and validates the model results by comparing them to independent data obtained by the IRI model and DMSP-F18 in situ electron density measurements [Rich, 1994]. Eventually, also a direct comparison to the CODE TEC map will be drawn. However, it should be mentioned that vertical TEC obtained using the CODE TEC maps evaluated as



a  $5^\circ \times 5^\circ$  grid was utilized as a weak background to assist in the model's parameter estimation and obtain a grip on TEC below satellite altitude. In the presented work it is required to support altitudes below approximately 450 km.

### 8.3.1 Quality of fit

As a first indication of the quality of fit, the post-fit RMS is evaluated. The results depending on the regularization parameter  $\lambda$  are shown in Fig. 8.4. These results were also used to determine a proper regularization parameter  $\lambda$ . Solutions for two days, containing eight three-hour solutions per day, were computed, resulting in 16 solutions. The black line indicates the mean residual norm. As expected, a more stringent choice leads in general to larger post-fit RMS. However, setting  $\lambda = 1.0$ , numerical instabilities and singularities occur. That causes the post-fit RMS to increase above the levels of more stable regularized solutions.

Further internal validation is performed by comparing the time series of computed TEC values directly to the observed slant TEC. In Fig. 8.5 a time series for Swarm A (the lowest satellite used) and Sentinel 3A (the highest satellite used) is shown. It needs to be mentioned that the estimated calibration biases are already applied to the observed TEC. Thus only the shape should be considered. For Swarm, the model is capable of reproducing the observed slant TEC values with TECU accuracy. A weaker performance is observed for Sentinel 3A, here also negative slant TEC values are observed. Besides the TEC values for Sentinel 3A are much lower than those by Swarm. The negative values caused by leveling inaccuracies caused by limitations of the profiler. The profiler is not fully capable of reproducing the electron densities observed at low elevations by Sentinel 3A. The bias is estimated such that the mean difference between the modeled and observed slant TEC for the arc is zero. As the shape of the observed slant TEC is not fully reproducible by the model, negative values can occur after leveling, especially with the in general low TEC values observed by Sentinel 3. As the model resolution is limited to degree 8 in spherical harmonics, which equals scale lengths of several hundred kilometers, it can not be assumed to reproduce small-scale features like fluctuations caused by plasma depletions. Also, one should investigate the magnitude of residuals depending on elevation to determine if an elevation-dependent bias is present. The results are displayed in Fig. 8.6, no significant bias is observed. However, the residuals increase with low elevation and especially at the edges of continuous phase arcs. This may be expected since the GPS data quality is generally known to degrade with low elevation. Also, remaining higher-order ionospheric effects primarily affect the observations selected at low elevations due to the increased slant TEC, however, their impact is small (see Sect. 3.6).

### 8.3.2 Choice of regularization parameter

As the problem is ill-posed, i.e., some parameters may be singular or close to singular, regularization is required. However, the regularization parameter needs to be adjusted. The L-curve criterion



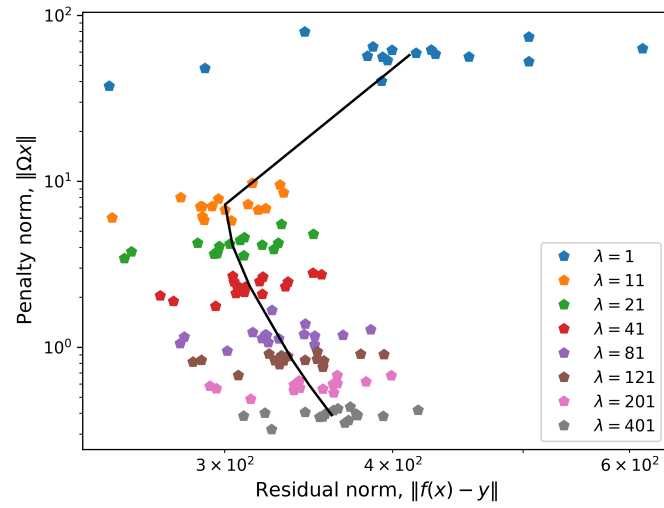


Figure 8.4: Norm of post-fit residuals compared to the norm of the scaled parameter vector. The black line indicates the mean values. Solution for the 1st and 2nd of July 2019 considered.

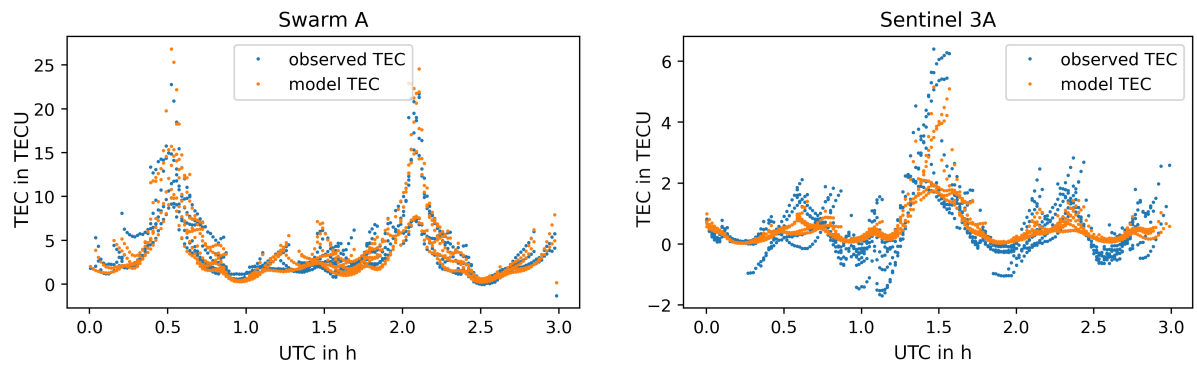


Figure 8.5: Observed TEC versus model TEC for Swarm A and Sentinel 3A (2nd of July 2019, doy 183).

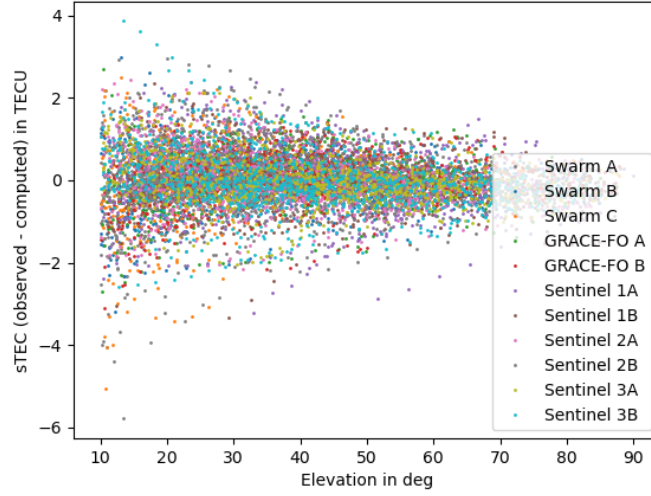


Figure 8.6: Differences between observed and model TEC versus elevation. 2nd of July 2019 from 00:00 UT to 03:00 UT.

Table 8.2: Correlation coefficient for different regularization parameters  $\lambda$  between the derived model and DMSP observations for 2nd of July 2019.

$\lambda$	1	11	21	41	81	121	201	401
corr. coeff.	0.673	0.834	0.832	0.821	0.830	0.826	0.781	0.812

is used to compare the residual norm to the norm of the parameter vector multiplied with the penalization matrix  $\Omega$  in log-scale (see Fig. 8.4). The optimum is assumed at the point where the resulting curve shows an L-like bend. As is shown in Fig. 8.4 a choice of 1 for  $\lambda$  is too weak and leads to singular or close to singular parameters causing the minimization to terminate before a minimum is reached. Apart from that, no pronounced bend can be observed. The in situ plasma density measurements obtained by the DMSP mission are used to determine a suitable regularization parameter.

As the Langmuir probe calibration is unknown, the regularization parameter is considered to be suited if the correlation between the in situ plasma density measurements and the model is maximized. The correlation coefficients for a full day are shown in Tab 8.2. The correlation is used because scaling parameters may be off for Langmuir probes on-board satellites. In some cases, corrections for the Langmuir probe were derived from model or ground comparisons. E.g. Swarm A underestimates the electron density by almost 11 % [Lomidze et al., 2018]. No information about such studies is available for DMSP. As the correlation is equally good for  $\lambda$  between 11 and 121 eventually the more restrictive value of 81 is selected not to risk instabilities. The spherical

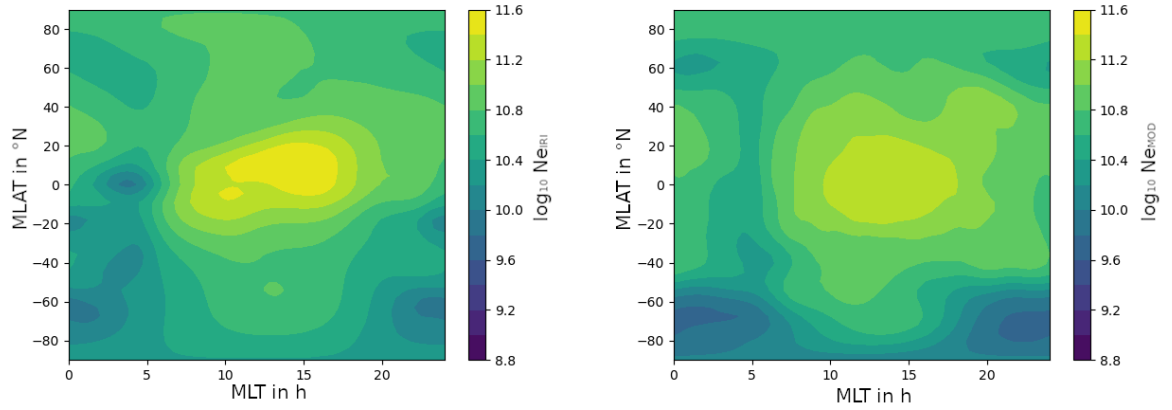


Figure 8.7: Electron density predicted by the IRI model (left) and by the LEO GPS reconstruction at an altitude of 500 km. For 2nd of July 2019 valid from 03:00h to 06:00h.

harmonics were resolved up to degree and order 8.

### 8.3.3 Evaluation of electron density using IRI

As the IRI model is currently the well-established standard ionospheric model, a comparison of the electron densities obtained by our empirical model and the electron density predicted by the IRI model is performed. Indeed, differences are expected, but in general electron density measurements with a similar amplitude should be reproduced. The electron densities obtained are shown in Fig. 8.7. For both cases, the peak in electron density is around 14-15 LT. The peak in the derived model is not as high as in the IRI model. Also, the gradients in electron density are smaller. A minimum near 5 LT is observed in both cases, also the decay towards the polar regions. The observed minimum around the south pole is much deeper in the derived model, which becomes more evident when considering the relative difference (see Fig. 8.8). Also clearly visible are several localized minima, e.g. during sunrise near the equator, which are evident in the IRI model, but not in the derived model. As the IRI model relies mainly on ground-based observations such as GPS-TEC, ionosondes (digisondes), and radar, it is biased towards the northern hemisphere (digisonde station distribution shown in Bilitza et al. [2017]). Near the southern pole, only very few stations contribute, which may explain the rather significant differences between IRI and the presented model. However, as the presented model has substantial limitations concerning the LEO satellite's covered local times, as shown in Fig. 8.3, small-scale variations can not be resolved.

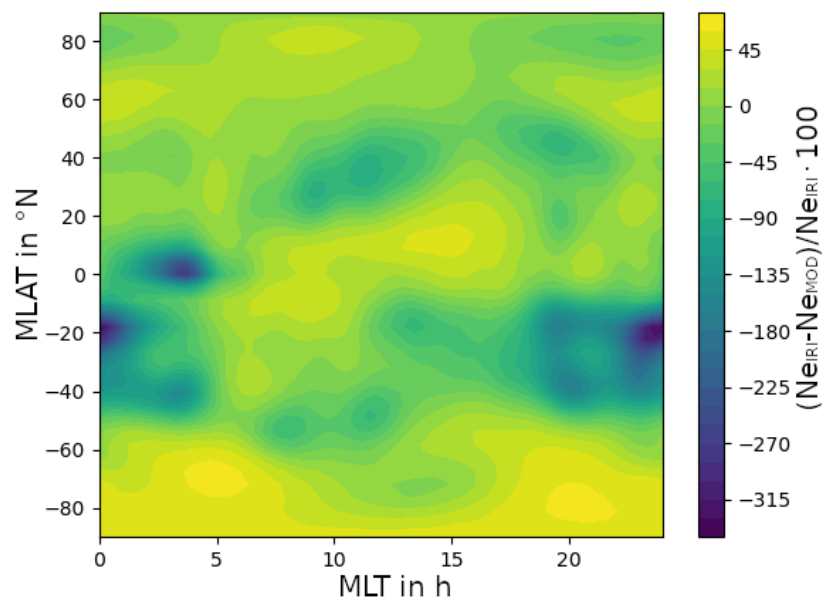


Figure 8.8: Electron density difference in percent relative to IRI at an altitude of 500 km. For the 2nd of July 2019 valid from 03:00h to 06:00h.

### 8.3.4 Evaluation of electron density using DMSP

The estimated electron density of the derived model is compared to plasma density observation taken by the DMSP-F18 satellite to validate the altitude dependency estimated in the model. The satellite is located at an orbital altitude of 857 km near-polar with 99° inclination and sun-synchronous with local times near 6 LT and 18 LT. To assess the quality, again, the correlation is used. The results for the 2nd of July 2019 are shown in Fig. 8.9. The prominent peaks visible are near 18 LT. These peaks are co-located in all three cases. The model value is significantly above the IRI value, which again is above the measurements of DMSP. This overshoot is most likely due to model limitations caused by the single-layer assumption. Because the model is aided by the CODE-TEC map, the missing E-Layer as has to be compensated by the scale height and shape parameter in the single layer approach. Additionally, further adjusting the constraints might be required in order to lower the output. The secondary double-peak features in between the more prominent peaks are the equatorial passing near 6 LT. At the local maximum at 14:30 UT, it may be seen that the model and also the DMSP measurements show significant electron densities, whereas no such increase can be seen for the IRI model. This is also the spot where the deep minimum in Fig. 8.7 is present for the IRI model. In total, the correlation between DMSP and the proposed model is 83.5%. Still, the IRI shows a slightly better correlation with 86%. In total, one may conclude that even if the model is rather simplistic, electron densities can be obtained, which are in proximity to the densities obtained by DMSP.

### 8.3.5 Comparison to CODE TEC maps

The CODE TEC map is not an independent validation as a coarse grid of vertical TEC observations was taken to substitute the pronounced observational gaps in the mlat/mL T frame. The TEC maps (see Fig. 8.10) are very similar. Some negative values for the CODE TEC map are not anymore present due to the model design. Those negative values appear in areas, which are not well observed by ground-based observations as those values are determined by extrapolation of the spherical harmonics. Taking a TEC error map into account might help. The TEC map also has a similar issue as the IRI model. The observations are taken from ground stations, which induces gaps over the oceans. For example, a peak in the northern Atlantic can be observed. The TEC map was introduced to the model with an unknown offset to be estimated. However, the amplitude of the CODE TEC map and the model TEC map are almost identical. Additionally the weighting between CODE TEC map and the satellite observations is to be adjusted. Currently this is performed by the number of observations of each source. The number of observation taken from a CODE TEC map is similar to the number of observations from one satellite in a three hour window.

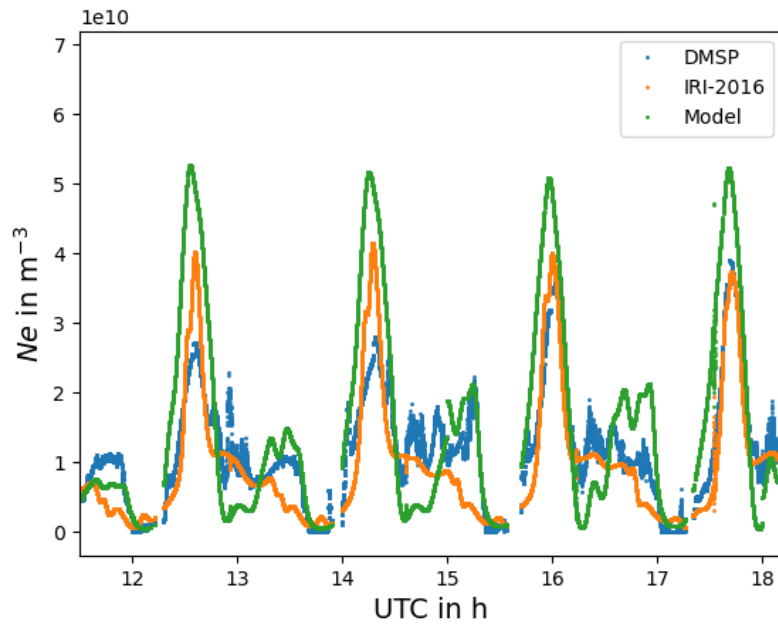


Figure 8.9: DMSP observations compared to IRI-2016 Electron density and the model predictions, 1nd of July 2019. The correlation between observations and IRI is 86 %, whereas to the proposed model the correlation is 83.5 %.

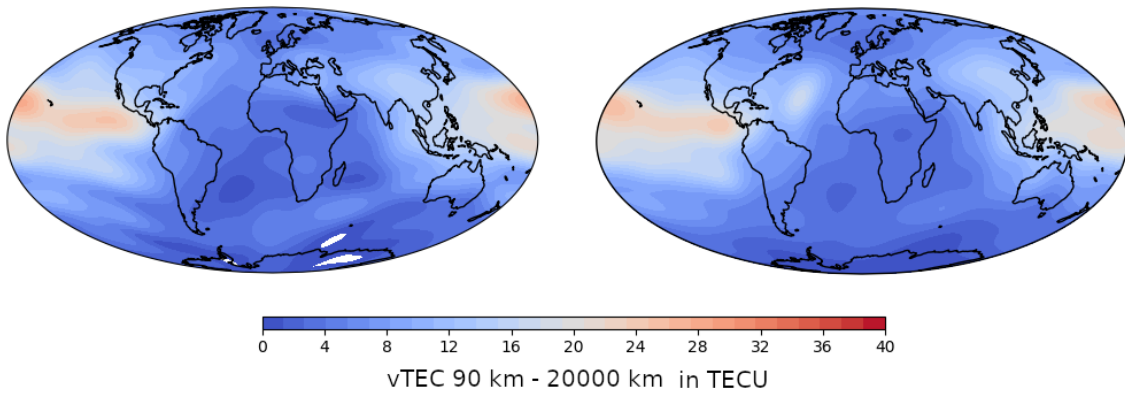


Figure 8.10: TEC of the CODE TEC map (left) and the proposed model (right) for 2nd of July 2019, at 01:30 UT. Evaluated from 90 km to approximately GPS altitude (20000km). White areas in the CODE TEC map are negative values.

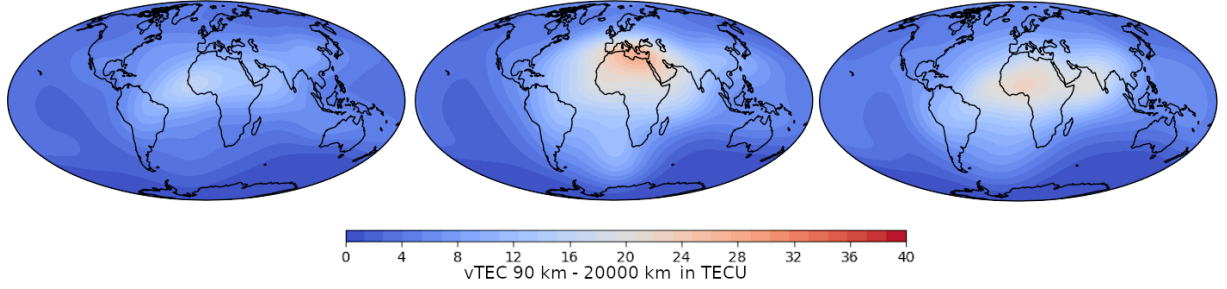


Figure 8.11: Estimated global TEC map for 4th (left), 5th (middle), and 6th (right) of August 2019, at 12:00 UT.

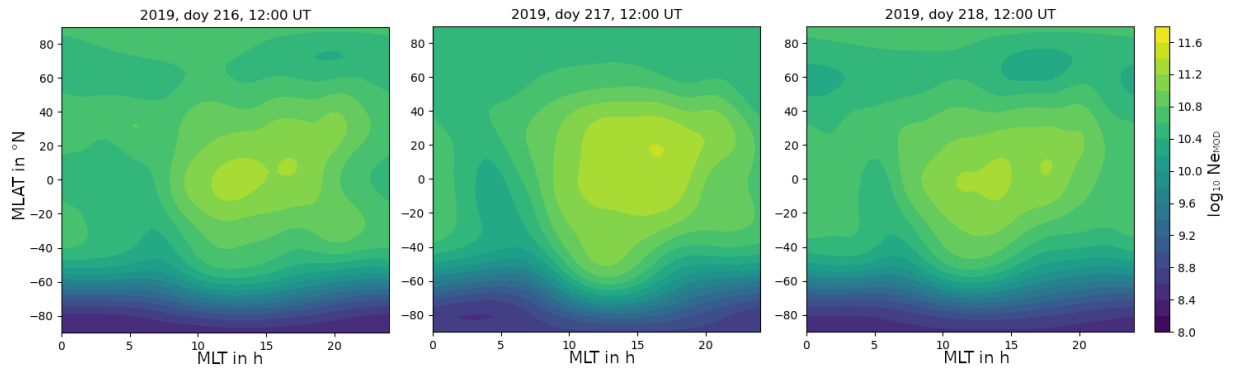


Figure 8.12: Estimated electron density for 4th (left), 5th (middle), and 6th (right) of August 2019, at 12:00 UT and 500 km altitude.

### 8.3.6 Storm response

On the 5th of August 2019, near 12 UT a minor geomagnetic storm took place. The largest Kp values observed were 5+ compared to 2- on the previous day and 3 on a subsequent day. TEC outbursts during geomagnetic storms were studied. It was shown that an increase in TEC could be observed on a larger scale covering latitudes from -60 to 60 degrees, especially for weaker geomagnetic storms [Blagoveshchensky et al., 2018]. The best correlation was observed in the Eurasian sector. According to Prol et al. [2021] an increase in electron density is expected. In his study he used a tomographic approach based on METOP GPS TEC. As the storm on the 5th of August 2019 was rather weak, an increase of TEC and F2-layer electron density is expected. The model result for TEC is shown in Fig. 8.11, and for the electron density in Fig. 8.12. Compared to the day before and after, an apparent increase in TEC by roughly 10 TECU is visible. Also, the peak in electron density at 500 km altitude becomes wider and increases. The amplitude of the electron density increase in equatorial regions is observed to be around 50%. This increase is at the same level as observed for equatorial regions in Prol et al. [2021]. The results are, therefore, in accordance with previous studies by Blagoveshchensky et al. [2018] and Prol et al. [2021].

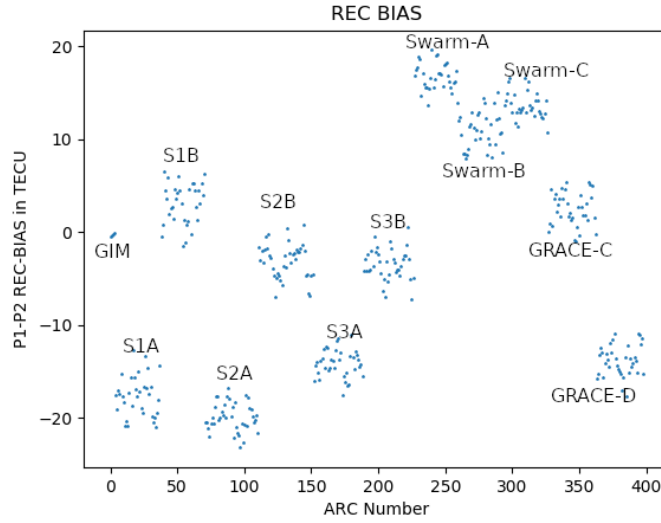


Figure 8.13: Estimated Receiver biases for Sentinel 1A/1B/2A/2B/3A/3B, Swarm A/B/C and GRACE C/D. Also the estimated offsets for the CODE TEC maps are shown. Time period used: 1st of July 2019, 00:00 UT to 03:00 UT.

### 8.3.7 P1-P2 receiver bias

One major effort during the development of the model was to improve the relative slant TEC leveling. As long as one can assume the receiver's P1-P2 bias to be constant, this accuracy is determined by the code noise and the arc length. For Swarm, the achieved accuracy is in the range of 1-2 TECU [DISC, 2017b]. For receivers with a reduced sampling of 10 s, an accuracy near 5 TECU is more realistic. However, this uncertainty is also the range of plasmaspheric TEC seen by the Sentinel satellites (see Fig. 8.5). Therefore, code leveling alone must be assumed not to be sufficiently precise. The estimated biases can be seen in Fig. 8.13. The biases stay relatively close to a constant level. Surprisingly, the differences between, for example, Sentinel 1A and Sentinel 1B are pretty significant even though they have the same satellite design and equipment. Similarly large differences are observed for Sentinel 2A and 2B and Sentinel 3A and 3B. As the B satellites are in general newer than the A satellites, the hardware might slightly differ. Nevertheless, such differences are even observed for the identical GRACE-FO satellites that have the same age. It may be that the bias is very sensitive to even the smallest deviations during manufacturing (e.g., resistance, length of wires, tolerances of the processor, or others). The scatter of the bias for the satellites is in the range of up to five TECU, close to the expected levels. As shown in Fig. 8.5, the values for Sentinel 3A are only in the range from 0 to 5 TECU. This concludes that code leveling is not suited for relatively high flying LEO satellites with orbital altitudes above 800 km and under solar minimum conditions with limited sampling frequency.



### 8.3.8 Geometry-free PCV maps

Empirical elevation and azimuth-dependent PCV maps for the antenna are estimated to account for antenna-specific effects. In POD they are estimated and applied, e.g., for the ionosphere-free linear combination. These maps can be derived by subtracting the signal dynamics using a sufficiently precise orbit model, computing the theoretical observations, and evaluating the residuals with respect to the observed values. In POD, the ionosphere-free phase residuals are analyzed by binning them and computing the mean residual for each bin [Montenbruck et al., 2008]. This residual stacking approach can also be applied to the geometry-free linear combination. In the case of the geometry-free linear combination, the same procedure can be utilized. The post-fit residuals of the model are used to derive the geometry-free PCV map. The map is computed using bin-wise average means, similar to the approach used to derive ionosphere-free PCV maps for POD. To compensate for model deficiencies, a long period of two months, July and August 2019, is considered. This long period is also important, as the observations were down-sampled to 30 s sampling, and thus fewer residuals may be analyzed to derive the PCV map. The sampling could be increased by evaluating the model also for the observations that were not used for the model fit. However, as seen in Chap. 7, observations may be strongly correlated at higher sampling. Even if this was derived for the Swarm GPS receivers, one might assume a similar behavior for the Sentinel satellites' receiver. Their receivers are also provided by RUAG and have a similar design.

In case PCV maps for the ionosphere-free linear and the geometry-free linear combination were derived, they can be decomposed into single-frequency PCV maps for L1 and L2. Therefore, the matrix form of the linear combinations

$$\begin{pmatrix} \frac{f_1^2}{f_1^2 - f_2^2} & \frac{-f_2^2}{f_1^2 - f_2^2} \\ 1 & -1 \end{pmatrix} \begin{pmatrix} L_1 \\ L_2 \end{pmatrix} = \begin{pmatrix} L_{if} \\ L_{gf} \end{pmatrix}. \quad (8.14)$$

can be written. Via inversion of the matrix L1 and L2 PCV maps can be obtained. The decomposition for Sentinel 1 A is shown in Fig. 8.14. The noise in the PCV map for the geometry-free linear combination is primarily due to the limited 30 s sampling, which leads to only around 100 residuals in each  $1^\circ \times 1^\circ$  bin for two months. This is the sampling used for the model adjustment, but it could be increased to the RINEX file sampling, i.e., to 0.1 Hz and 1 Hz. Another noticeable feature is the gap near  $225^\circ$  azimuth. This is caused by the screening before TEC processing. In this region strong multi-path effects are observed, which affects the Melbourne-Wuebbena linear combination used for screening. In turn, the observations are rejected. It can also be observed that PCV for L2 is more pronounced than the PCV for L1.

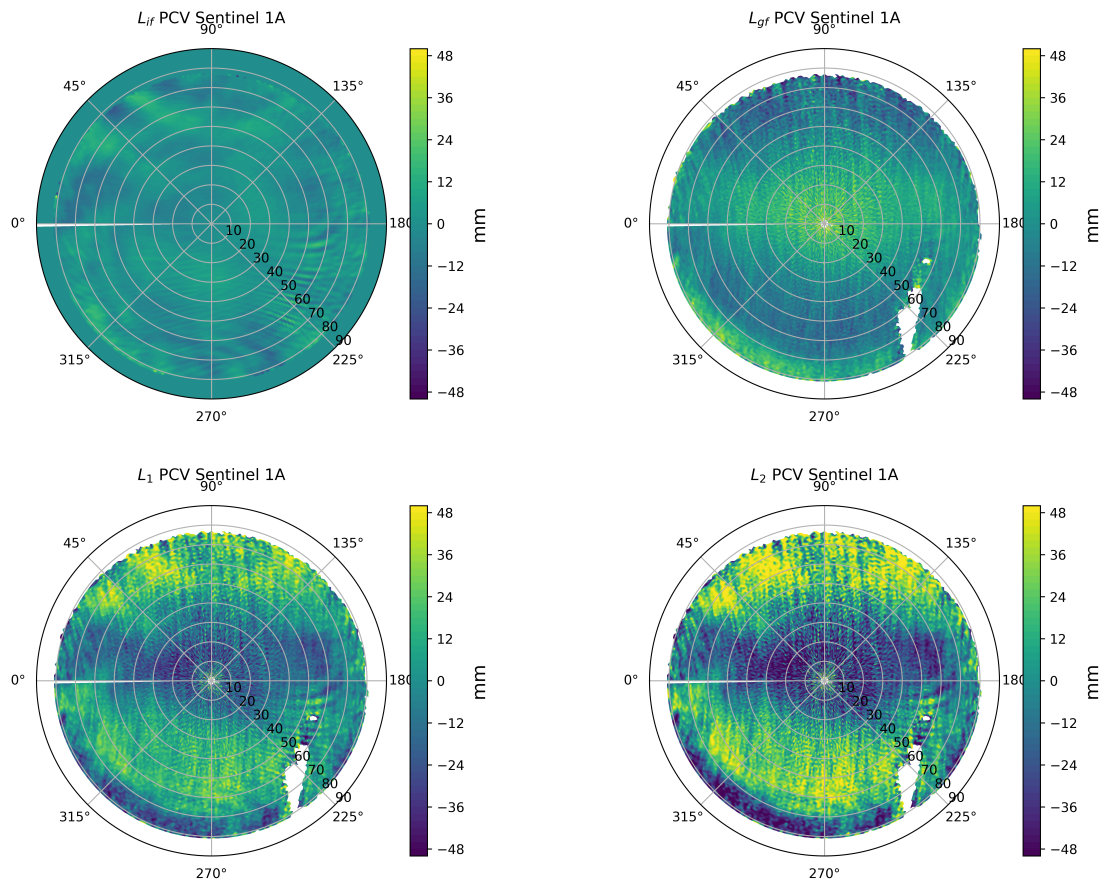


Figure 8.14: Ionosphere-free (top, left), geometry-free (top, right), L1 (bottom, left) and L2 (bottom, right) PCV maps. July and August 2019.

### 8.3.9 Outlook

The model in its current state lacks a plasma-pause model. Recently, studies were conducted [[Heilig and Lühr, 2013, 2018](#), [PRISM, 2020](#)] to derive the plasma-pause (PP) location and mid-latitude ionospheric trough (MIT) from CHAMP and Swarm observations. The Swarm results were validated to observations taken by the van Allen probes. However, Swarm can detect the plasma-pause much more frequently than the van Allen probes, which were deactivated in 2019 [[NASA, 2019](#)]. The PRISM project outcomes can be utilized to investigate the PP and MIT detection from Swarm GPS TEC or constrain the model and limit the representation to inward the PP. Outward in the polar regions, the regular layer assumption used for the model approach may be violated. As the PP is highly dependent on the solar activity, a precise knowledge of its location is required when including the location as an external product into the empirical model.

The global coverage in the magnetic coordinate system is currently one of the largest issues for a good topside estimation. GPS TEC collected by COSMIC-2 or Spire will help to fill the observational gaps in magnetic latitude and magnetic local time and improve the reconstruction. Their low inclination of  $24^\circ$  can provide the missing local times in the equatorial regions. Its orbit is not local time fixed or only slowly progressing, as it is the case for the missions currently used.

## 8.4 Application: Tomography using Swarm

Another approach to gain insight into the ionospheric electron density distribution is ionospheric tomography. In this approach, the electron density distribution is assumed to be constant over a small time interval. The area of interest is discretized, typically a grid resulting in voxels, and the numerous slant TEC measurements are used to adjust the electron density inside the voxels such that the integrated electron density matches the slant TEC. Previous studies were performed using CHAMP data [[Schlüter et al., 2003](#), [Stolle et al., 2006a](#)] to investigate polar patches. In [Minkwitz et al. \[2015\]](#) for example, slant TEC observations from ground stations were used in combination with a NeQuick background model to improve the electron density estimation. A kriging approach (Gaussian Regression) was applied to solve the ill-posed problem [[Minkwitz et al., 2015](#)]. A study using the COSMOS beacon and the TomoScand receiver network was performed in [Norberg et al. \[2016\]](#). In that study, a Bayesian statistical inversion was used, as also an ill-posed inverse problem had to be solved. Due to the receivers' locations near the EISCAT incoherent scatter radar in Svalbard, a direct validation was possible. It could be observed that the peak altitude could be improved compared to the IRI prior model using tomography.

In this work, an approach similar to [Schlüter et al. \[2003\]](#) and [Stolle et al. \[2006a\]](#) is shown. In contrast to CHAMP studies, a two-dimensional tomography is performed, focusing on equatorial slices. Only altitudes above the satellite's trajectory are considered. The upper altitude limit for the reconstruction is set to 1000 km. The plasmaspheric electron content above 1000 km is removed

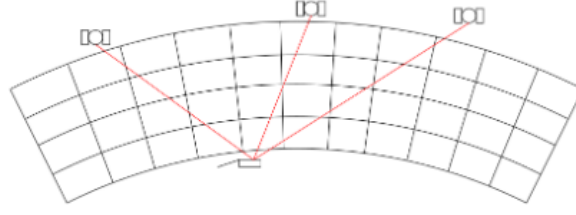


Figure 8.15: Observational scenario for tomography using a vertical grid.

using a model derived from Sentinel slant TEC observations, using the same approach as in Sect. 8.2. As the tomography in this work uses a two-dimensional approach, mapping is also required to map rays to the plane spanned by the radial and along-track direction. A single equatorial pass of the Swarm satellite is considered. Each equatorial pass spans a time interval of approximately 25 minutes (limiting the observation taken to  $\pm 60^\circ$  lat.). The observational scenario is illustrated in Fig. 8.15.

The electron density in each box is to be estimated, such that the slant TEC values equal the sum of the electron densities ( $N_e(i)$ ) over all  $N$  boxes of the product of the length  $l(i)$  (weight) of the ray inside the  $i$ -th box and the electron density. The basic approach is again to approximate the integral by a finite sum

$$sTEC = \int N_e dl + b_{arc} = \sum_{i=1}^N l(i) N_e(i) + b_{arc}. \quad (8.15)$$

From this equation, the design matrix  $A$  is set up. The constant  $b_{arc}$  contains biases and ambiguities terms that are assumed to be constant for each phase arc.

#### 8.4.1 Ray geometry

The main reason why ionospheric tomography usually results in an ill-posed problem is that with higher altitudes, the rays tend to be more concentrated due to the relatively slow-moving GPS satellites. Even if the voxel's size is increased with altitude (here exponentially), larger gaps occur, which will cause an unconstrained linear equation system to become singular. The situation is shown in Fig. 8.16. Here, one complete equatorial pass and all available observations at 30 s sampling are mapped to the two-dimensional vertical plane. Good coverage in low altitudes directly above the Swarm A satellite is observed, but the rays leave out large areas with higher altitudes.

#### 8.4.2 Removing the topside

As the tomography can not provide a reliable reconstruction for higher altitudes due to the poor ray geometry, these high altitudes should be fixed or even removed. The Sentinel satellites are

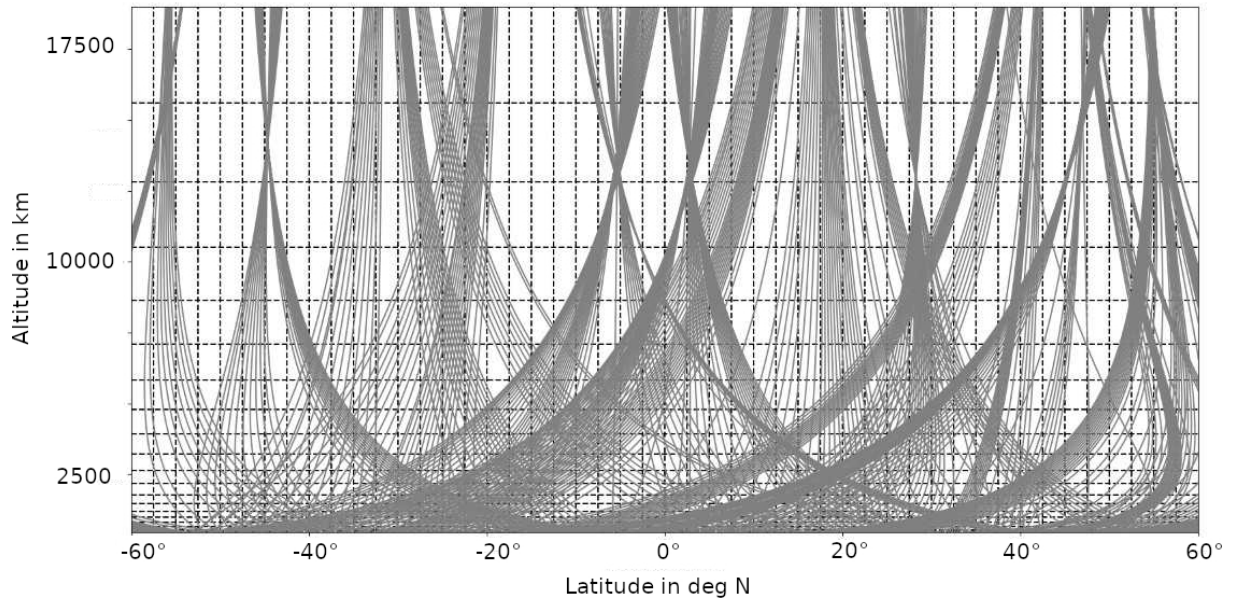


Figure 8.16: Real observational scenario with boxes increasing exponentially in height for Swarm A, 2nd of November 2014. Equator crossing at 1:12 UT. The rays were mapped to the vertical plane.

highly useful for that purpose, as their high altitude near 700 km to 800 km almost exclusively contains the plasmasphere. Based on those data, a model similar to the one previously presented in this chapter (see Sect. 8.2) is computed. The plasmaspheric profiler is simplified as exponential decay, as no observations from lower altitudes enter. Only a reference electron density at 1000 km is modeled together with a plasmaspheric scale height. The model is evaluated along the line of sight from Swarm and integrated starting at 1000 km to estimate the plasmaspheric contribution to the observed slant TEC. The plasmaspheric content is afterwards removed from Swarm slant TEC observations. The thus reduced slant TEC is shown in Fig 8.17. As can be seen, the TEC values with the plasmasphere removed (red) are significantly lower near the peak by several TECU than the original slant TEC (blue). This peak is co-located with the geomagnetic equator, which is also the area where the plasmaspheric TEC is highest. The ray geometry only allows good coverage in lower altitude regimes. If the plasmaspheric TEC is not removed, the grid has to be extended or neglecting the plasmaspheric contribution results in too large densities within the grid. The extension would result in many not well-observed voxels, which cause peaks of electron density near the nearly stationary GPS satellites' locations to compensate for plasmaspheric TEC.



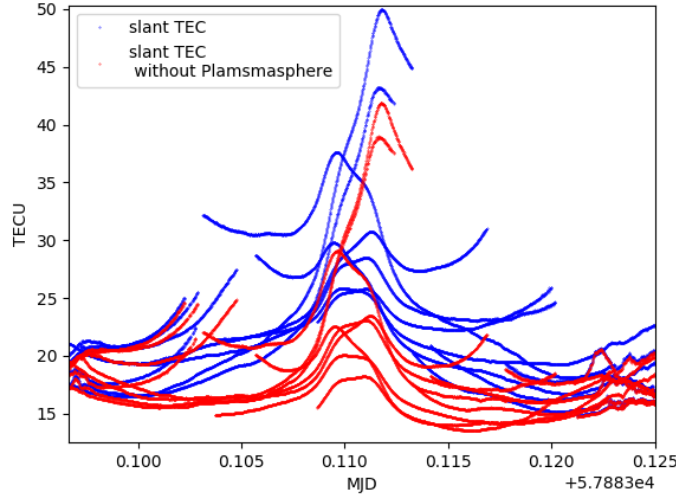


Figure 8.17: GPS TEC observed by Swarm with and without plasmaspheric electron content. 10th of May 2017, equatorial pass at 2:40 UT (9:05 LT)

### 8.4.3 Mapping and masking

As only the two-dimensional shape is considered for the tomography, mapping needs to be applied to observations not embedded in the reconstruction plane. A line of sight is not in the plane defined by the flight path and in a vertically upward direction. First, all intersections of the three-dimensional line of sight with the latitudes and altitudes defining the grid cells are computed. Then the three-dimensional distance is computed and used as a multiplier. As low elevations with azimuths near  $90^\circ$  or  $270^\circ$  can be expected to suffer from mapping errors, only observations, where  $\sin(a)^2 + \cos(e)^2 < 1.5$ , where  $a$  is the azimuth angle, and  $e$  is the elevation, are used. The resulting mask is shown in Fig. 8.18. As shown in the previous chapters, the GPS data quality may be affected by ionospheric gradients. Therefore, the weighting matrix  $\mathbf{P}$  derived in Chap. 6 using the second time derivative and ROTI is introduced to mitigate ionospheric induced observational errors.

### 8.4.4 Algorithm description and reconstruction

Starting from Eq. 8.15 a design matrix  $A$  is derived, that contains the weights  $l_i$  and also applies the  $b_{arc}$  parameters to the slant TEC. The method used for the tomography is the multiplicative algebraic reconstruction technique (MART [Gordon et al., 1970, Gerzen and Minkwitz, 2016]).

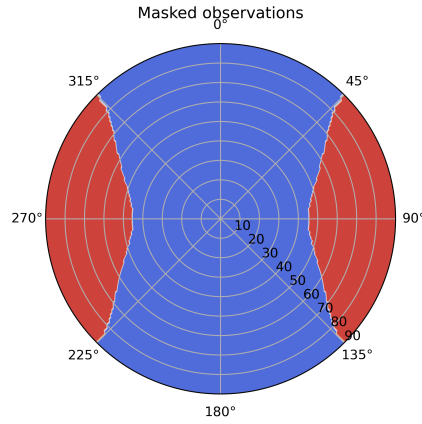


Figure 8.18: Rejected observations (red) and accepted observations (blue) with respect to elevation and azimuth.

Instead of minimizing a norm, MART is designed to minimize the entropy, which is defined as

$$E(\mathbf{u}) = - \sum_{i=1}^N \mathbf{u}_i \log(\mathbf{u}_i). \quad (8.16)$$

The parameter  $\mathbf{u}$  is hereby given as

$$\mathbf{u}_i = \mathbf{y}_i / (\mathbf{A} \cdot \mathbf{x})_i. \quad (8.17)$$

In this notation, the  $\cdot_i$  denotes the  $i$ -th row. The iteration is then defined as

$$\mathbf{x}_j^{k+1} = \mathbf{x}_j^k \cdot \prod_{i=1}^m \left( \frac{\mathbf{y}_i}{(\mathbf{A}\mathbf{x}^k)_i} \right)^{\lambda \mathbf{A}_{i,j} / \|\mathbf{A}_i\|}. \quad (8.18)$$

The parameter  $\lambda$  is an empirical parameter to adjust the step size and ensure convergence. Here, the condition that all  $\mathbf{y}_i$  and  $\mathbf{A} \cdot \mathbf{x}$  have to be strictly positive is obvious. For the electron density, this is reasonable as well as for the slant TEC. For the offsets, an appropriate leveling of the slant TEC values can be performed to ensure that these are also positive. When considering constraints this is not valid as the constraining matrix includes negative values. These constraints are for example the electron density in the bottom boxes, that are constrained to Langmuir probe measurements. A further constraint can be applied by constraining the electron density in one box to the neighboring boxes. In that case the entries of the constraining matrix  $\mathbf{\Omega}$  read as

$$\mathbf{\Omega}_{ij} = \begin{cases} w_{ij}, i \neq j \\ -\sum_{k=1}^n w_{kj}, i = j \end{cases}, \quad (8.19)$$

where  $w_{ij}$  is the length of the common edge between box  $i$  and box  $j$  (0 if box  $i$  and box  $j$  are not adjacent). Consequently, the matrix constrains the value inside one box to the weighted mean of the neighbouring boxes. As this constraining matrix  $\mathbf{\Omega}$  contains the difference of observations, the positive requirement for the entries is not fulfilled. However, one may use a workaround by separating the constraining matrix  $\mathbf{\Omega}$  into two parts  $\mathbf{\Omega} = \mathbf{\Omega}^+ + \mathbf{\Omega}^-$ , where  $\mathbf{\Omega}^+$  contains all the positive entries and  $\mathbf{\Omega}^-$  the negative ones. When using  $\mathbf{\Omega}^- \cdot \mathbf{x}$  as temporary observations, the resulting formula can be written as

$$\mathbf{x}_j^{k+1} = \mathbf{x}_j^k \cdot \prod_{i=1}^m \left( \frac{\mathbf{y}_i}{(\mathbf{A}\mathbf{x}^k)_i} \right)^{\lambda \mathbf{A}_{i,j} / \|\mathbf{A}_i\|} \prod_{i=1}^k \left( \frac{(-\mathbf{\Omega}^- \mathbf{x}^k)_i}{(\mathbf{\Omega}^+ \mathbf{x}^k)_i} \right)^{\lambda \mathbf{\Omega}_{i,j}^+ / \|\mathbf{\Omega}_i^+\|} \quad (8.20)$$

as iteration step for MART including the constraints. The constraints matrix is used to derive a prior in the least-squares approach with the bottom side electron density given by the Langmuir probes. The model gives the topside electron density derived of Sentinel slant TEC observation to initialize the tomography. Additional constraints are set such that the difference between two adjacent boxes weighted by the length of the common edge is minimized. These formations and constraints are used to estimate an a priori reconstruction using classical least-squares. With the a priori solution, the MART algorithm is initialized. In case weighting is used, the observed slant TEC values and the  $\mathbf{A}$  matrix are multiplied using the weighting matrix  $\mathbf{P}$ . The result of this reconstruction method can be seen in Figs. 8.19 and 8.20. In Fig. 8.20 (left) artifacts along the line of sight become visible. They virtually disappear, when the weighting matrix is used (Fig. 8.20, right).

The application of ionospheric tomography sums up some key features of this work. It was shown that the affected L2 phase observations, which were discussed in Chaps. 6 and 7, are also affecting the tomographic approach. Identification and the weighting are performed with exactly the same matrix derived in Sect. 6.2.2 for the gravity field processing and is also capable of removing the artifacts in the tomography. Secondly, the inferior line of sight geometry points out the need for a topside estimation by an accurate LEO GNSS-based model. How such a model can be designed is shown in Sect. 8.2. It is modified for the plasmaspheric estimation to be used in the tomography.



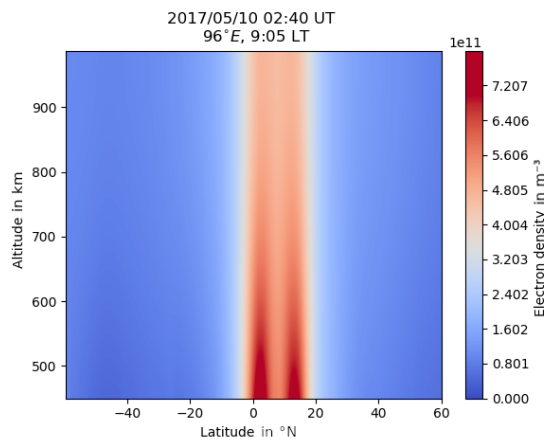


Figure 8.19: Electron density of the reconstruction before MART is applied, based on Langmuir probe measurements at the bottom-side of the reconstruction plane (10th of May 2017).

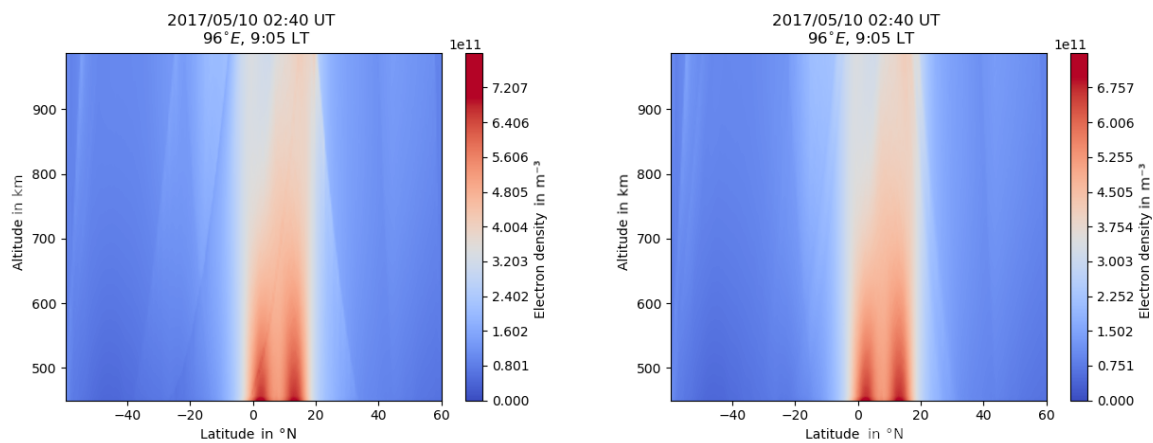


Figure 8.20: MART applied to unweighted (left) and weighted (right) Swarm GPS observations using the prior given by the Langmuir probes (10th of May 2017).



# Chapter 9

## Summary, Conclusions and Outlook

This work assesses the interactions between ionosphere and GPS with a focus on geophysical and ionospheric applications. It consists of three main aspects associated with the three questions:

1. How can the quality of GNSS observations be assessed a priori using only the GNSS free linear combination? (Chap. 6)
2. Given a tracking scenario and a loop filter implementation, how does the tracking respond to ionospheric stimuli. Moreover, are those responses deterministic and can be removed? (Chap. 7)
3. How can LEO-based GNSS TEC reliably be determined to estimate the electron density in the topside ionosphere and plasmasphere? (Chap. 8)

The first question is addressed in Chap. 6. Systematic differences in the Swarm GPS-only gravity fields could be associated with systematic, small-scale errors in the Swarm kinematic positions. Those systematic errors are observed near the geomagnetic equator and caused by variations in slant TEC. As the ionosphere-free linear combination is used for the orbit determination, only a minor impact of the higher-order ionospheric terms should be included in the observations. However, the impact of HOI contributions was found to be insufficient to cause that sort of artifact. Triggers in the geometry-free linear combination were identified using time derivatives and quantifying the observation's noise level using the ROTI index providing the standard deviation over a predefined time window. Eventually, observation-specific weights were derived and included in the orbit processing. The weights affect the covariance information for the kinematic positions, and subsequently, the weight of the presumably affected positions is lowered in the gravity field solutions. The difference between the obtained Swarm GPS-only gravity field and a superior GRACE solution confirmed the findings, as the equatorial artifact is significantly mitigated. Besides, the noise near the polar regions is less pronounced. The presented approach has been further adapted

an refined at AIUB by T. Grombein [Arnold et al. \[2021\]](#) for GOCE orbit and gravity field determination.

The second question further addresses how the receiver's observations are affected by the receiver design (see Chap. 7). Franz Zangerl (private communication) kindly provided details on the loop filter and the Swarm GPS receivers' tracking procedure. These details allowed us to simulate the tracking and to investigate the filter response. The geometry-free linear combination was found to be an appropriate indicator in Chap. 6, this is supported by the fact that the L2 tracking is performed not directly on the L2 phase itself but the L1-L2 phase difference. The narrow bandwidth of the loop filter combined with the relatively long integration interval of 100 ms was found to cause systematic tracking errors in the L2 phase when encountering fast variations of slant TEC. Given the knowledge of the loop filter implementation, the response was further investigated in the frequency domain, and the amplitude and phase response was derived.

Signals with a period of 10 s to 30 s were found to be most affected by the amplitude shift. Longer periods pass the loop filter almost unaffected, whereas shorter periods experience a dampening. From the frequency domain representation, the loop filter transfer function was estimated. The classical continuous update formulation did not fit the actual loop transfer. Its integration time of 100 ms is too long. A suited higher-order transfer function was eventually derived and used to invert the loop filter. The differences between the observed output and the estimated input coincide with the phase residuals observed in the precise orbit determination. This points out the capability of reducing tracking errors via inversion of the loop filter. Eventually, a gravity field determination pointed out that systematic errors were mitigated. However, the performance compared to the previously derived weighting was limited. This can be attributed to the limited time resolution of the Swarm RINEX files of 1 Hz. The loop filter itself uses a 10 Hz sampling. A full reconstruction would therefore require 10 Hz data.

The ionospheric contribution to the GPS/GNSS phase observations is not only introducing tracking errors. It is also a valuable source of ionospheric measurements with an accuracy of down to 0.01 TECU (see Chap. 8). The theoretical accuracy of 0.01 TECU is usually not met, as leveling errors in the sTEC estimation using code observations easily reach up to 5 TECU. The total electron content observed by LEO satellited for the topside ionosphere can range from around 100 TECU for low flying satellites near solar max (e.g. Swarm in 2014) down to only a few TECU in solar min for higher flying satellites (e.g. Sentinel 3 in 2019). Code leveling uncertainties can therefore be considered to be too large. It is also unknown how robust the receiver DCB estimate for an LEO satellite is, as such biases are sensitive to temperature changes. In Chap. 8, a model-based approach is developed to estimate those biases. The model is mostly based on sTEC observations from several LEO missions, such as Sentinel 1A/B, 2A/B, 3A/B, Swarm, and GRACE-FO. It provides a three-dimensional reconstruction of the topside electron density using a variation of a single Epstein layer and spherical harmonics for the global representation of the layer defining parameters. This model is further used to calibrate the sTEC measurements by leveling each phase

arc independently. This approach also provides a consistent leveling for different LEOs at different altitudes, and thus the absolute sTEC becomes directly comparable. The model uses small time windows, thus providing short time snapshots, which is a significant difference from the commonly used models like IRI and NeQuick-2, which rely on long-term averages.

In this work, the interaction between GPS observations and the ionosphere was examined from both sides: How they may be utilized to optimize LEO positioning and how constellations of LEO satellites equipped with GPS receivers can be used to gain insight into the topside electron density. The COSMIC-2 mission was launched in June 2019 with low inclination orbits around 500 km. In this work, this data has not been included in the model estimation. As all satellites used for the model estimation are near-polar, the 24° inclined orbits would undoubtedly help fill the observational gaps in the not well observed local times. Subsequently, the model is expected to become more robust, and also, the sTEC leveling would be consistent with the other LEO missions used in the estimation. For this purpose, the Fleet of Lemur cube-sats at 500 km altitude operated by the private company Spire Global Inc. (<https://spire.com/>) can be included. Their CubeSats are equipped with STRATOS dual-frequency GNSS receivers providing 1 Hz sampling and can track GPS satellites down to  $-20^\circ$  elevation. An agreement to provide the data for the scientific community was conducted with ESA <sup>1</sup>.

Another natural continuation of this work estimates the loop filter responses for GOCE and Sentinel 3 as they also provide 1 Hz sampling. The GPS receiver mounted on-board Sentinel 3 is also provided by RUAG and of similar design and settings as the Swarm receivers. For the Lagrange receiver on-board GOCE, this is more difficult. However, the ionosphere free phase residuals can provide the necessary information to obtain a rough guess on the loop filters implementation, also assuming an L1 aided L2 tracking. Especially for GOCE similar issues with the phase observables were observed near the geomagnetic equator as for Swarm. GOCE kinematic position could also benefit from a reconstruction of the original phase using loop filter inversion.

To sum up: The ionosphere is challenging the GPS/GNSS receivers on-board LEO satellites, but at the same time, they also provide a unique insight into the not yet well observable topside ionosphere.

---

<sup>1</sup><https://earth.esa.int/eogateway/missions/spire>, accessed 11th of May 2021.



# Bibliography

- J. Aarons. Equatorial scintillations: A review. *IEEE Transactions on Antennas and Propagation*, 25(5):729–736, 1977. 13
- J. Aarons, H. E. Whitney, E. MacKenzie, and S. Basu. Microwave equatorial scintillation intensity during solar maximum. *Radio Science*, 16(5):939–945, 1981. doi: 10.1029/RS016i005p00939. URL <https://agupubs.onlinelibrary.wiley.com/doi/abs/10.1029/RS016i005p00939>. 13
- K. Abich, A. Abramovici, B. Amparan, A. Baatzsch, B. B. Okihiro, D. C. Barr, M. P. Bize, C. Bogan, C. Braxmaier, M. J. Burke, K. C. Clark, C. Dahl, K. Dahl, K. Danzmann, M. A. Davis, G. de Vine, J. A. Dickson, S. Dubovitsky, A. Eckardt, T. Ester, G. F. Barranco, R. Flatscher, F. Flechtner, W. M. Folkner, S. Francis, M. S. Gilbert, F. Gilles, M. Gohlke, N. Grossard, B. Guenther, P. Hager, J. Hauden, F. Heine, G. Heinzel, M. Herding, M. Hinz, J. Howell, M. Katsumura, M. Kaufer, W. Klipstein, A. Koch, M. Kruger, K. Larsen, A. Lebeda, A. Lebeda, T. Leikert, C. C. Liebe, J. Liu, L. Lobmeyer, C. Mahrtdt, T. Mangoldt, K. McKenzie, M. Mischfeldt, P. R. Morton, V. Müller, A. T. Murray, D. J. Nguyen, K. Nicklaus, R. Pierce, J. A. Ravich, G. Reavis, J. Reiche, J. Sanjuan, D. Schütze, C. Seiter, D. Shaddock, B. Sheard, M. Sileo, R. Spero, G. Spiers, G. Stede, M. Stephens, A. Sutton, J. Trinh, K. Voss, D. Wang, R. T. Wang, B. Ware, H. Wegener, S. Windisch, C. Woodruff, B. Zender, and M. Zimmermann. In-Orbit Performance of the GRACE Follow-on Laser Ranging Interferometer. *Phys. Rev. Lett.*, 123:031101, Jul 2019. doi: 10.1103/PhysRevLett.123.031101. URL <https://link.aps.org/doi/10.1103/PhysRevLett.123.031101>. 44
- S. Aguirre and W. Hurd. Design and Performance of Sampled Data Loops for Subcarrier and Carrier Tracking. *TDA progress report 42-79*, 1984. URL [https://ipnpr.jpl.nasa.gov/progress\\_report/42-79/79H.PDF](https://ipnpr.jpl.nasa.gov/progress_report/42-79/79H.PDF). 107, 108
- D. N. Anderson, M. Mendillo, and B. Herniter. A semi-empirical low-latitude ionospheric model. *Radio Science*, 22(2):292–306, 1987. doi: 10.1029/RS022i002p00292. URL <https://agupubs.onlinelibrary.wiley.com/doi/abs/10.1029/RS022i002p00292>. 9

- D. Arnold, A. Jäggi, G. Beutler, and U. Meyer. Impact of the ionosphere on GPS-based precise orbit determination of Low Earth Orbiters. *ESA Living Planet Symposium, Prague, Czech Republic, May 09 - 13, 2016*, 2016. 65
- D. Arnold, O. Montenbruck, S. Hackel, and et al. Satellite laser ranging to low Earth orbiters: orbit and network validation. *Journal of Geodesy*, 93:2315–2334, 2018. doi: 10.1007/s00190-018-1140-4. 60
- D. Arnold, O. Montenbruck, S. Hackel, and K. Sośnica. Satellite laser ranging to low Earth orbiters: orbit and network validation. *Journal of Geodesy*, 93(11):2315–2334, Nov 2019. ISSN 1432-1394. doi: 10.1007/s00190-018-1140-4. URL <https://doi.org/10.1007/s00190-018-1140-4>. 50
- D. Arnold, T. Grombein, L. Schreiter, V. Sterken, and J. A. Reprocessed precise science orbits and gravity field recovery for the entire GOCE mission. 2021. 152
- T. Bandikova, C. McCullough, G. L. Kruizinga, H. Save, and B. Christophe. GRACE accelerometer data transplant. *Advances in Space Research*, 64(3):623 – 644, 2019. ISSN 0273-1177. doi: 10.1016/j.asr.2019.05.021. URL <http://www.sciencedirect.com/science/article/pii/S0273117719303485>. 44
- S. Bassiri and G. Hajj. Modeling the global positioning system signal propagation through the ionosphere. *The Telecommunications and Data Acquisition*, pages 92–103, 1992. 27
- S. Bassiri and G. Hajj. Higher-Order Ionospheric Effects on the GPS Observable and Means of Modeling Them. *Manuscripte Geodaetica*, 18:280–289, 1993. 27
- S. Bettadpur. GRACE 327-742, Gravity Recovery And Climate Experiment, UTCSR Level-2 Processing Standards Document. 2018. xv, 79, 80
- G. Beutler. *Methods of Celestial Mechanics*. 2005. ISBN ISBN 978-3-540-26870-3. doi: 10.1007/b138225. 52, 56
- G. Beutler, I. I. Mueller, and R. E. Neilan. The International GPS Service for Geodynamics (IGS): The Story. In G. Beutler, W. G. Melbourne, G. W. Hein, and G. Seeber, editors, *GPS Trends in Precise Terrestrial, Airborne, and Spaceborne Applications*, pages 3–13, Berlin, Heidelberg, 1996. Springer Berlin Heidelberg. ISBN 978-3-642-80133-4. 38
- D. Bilitza. A correction for the IRI topside electron density model based on Alouette/ISIS topside sounder data. *Advances in Space Research*, 33(6):838 – 843, 2004. ISSN 0273-1177. doi: 10.1016/j.asr.2003.07.009. URL <http://www.sciencedirect.com/science/article/pii/S0273117703010111>. Path Toward Improved Ionosphere Specification and Forecast Models. 16



- D. Bilitza. IRI the International Standard for the Ionosphere. *Advances in Radio Science*, 16:1–11, 2018. doi: 10.5194/ars-16-1-2018. URL <https://ars.copernicus.org/articles/16/1/2018/>. 13, 15
- D. Bilitza, B. W. Reinisch, S. M. Radicella, S. Pulinets, T. Gulyaeva, and L. Triskova. Improvements of the international reference ionosphere model for the topside electron density profile. *Radio Science*, 41(5), 2006. doi: 10.1029/2005RS003370. URL <https://agupubs.onlinelibrary.wiley.com/doi/abs/10.1029/2005RS003370>. 121
- D. Bilitza, L. McKinnell, B. Reinisch, and T. Fuller-Rowell. The international reference ionosphere today and in the future. *Journal of Geodesy*, 85:909–920, 2011. 14, 16, 35, 121
- D. Bilitza, D. Altadill, V. Truhlik, V. Shubin, I. Galkin, B. Reinisch, and X. Huang. International Reference Ionosphere 2016: From ionospheric climate to real-time weather predictions. *Space Weather*, 15(2):418–429, 2017. doi: 10.1002/2016SW001593. URL <https://agupubs.onlinelibrary.wiley.com/doi/abs/10.1002/2016SW001593>. 15, 16, 135
- D. V. Blagoveshchensky, O. A. Maltseva, and M. A. Sergeeva. Impact of magnetic storms on the global TEC distribution. *Annales Geophysicae*, 36(4):1057–1071, 2018. doi: 10.5194/angeo-36-1057-2018. URL <https://angeo.copernicus.org/articles/36/1057/2018/>. 139
- H. Bock, R. Dach, A. Jäggi, and G. Beutler. High-rate GPS clock corrections from CODE: support of 1 Hz applications. *Journal of Geodesy*, 83(11):1083, Jun 2009. ISSN 1432-1394. doi: 10.1007/s00190-009-0326-1. URL <https://doi.org/10.1007/s00190-009-0326-1>. 57
- H. Bock, A. Jäggi, U. Meyer, P. Visser, J. van den IJssel, T. van Helleputte, M. Heinze, and U. Hugentobler. GPS-derived orbits for the GOCE satellite. *Journal of Geodesy*, 85(11):807, May 2011. ISSN 1432-1394. doi: 10.1007/s00190-011-0484-9. URL <https://doi.org/10.1007/s00190-011-0484-9>. 55
- H. Bock, A. Jäggi, G. Beutler, and U. Meyer. GOCE: precise orbit determination for the entire mission. *Journal of Geodesy*, 88(11):1047–1060, Nov 2014. ISSN 1432-1394. doi: 10.1007/s00190-014-0742-8. URL <https://doi.org/10.1007/s00190-014-0742-8>. 47
- C. Bruyninx, Z. Altamimi, C. Boucher, E. Brockmann, A. Caporali, W. Gurtner, H. Habrich, H. Hornik, J. Ihde, A. Kenyeres, J. Mäkinen, G. Stangl, H. van der Marel, J. Simek, W. Söhne, J. Torres, and G. Weber. *The European Reference Frame: Maintenance and Products*, pages 131–136. Springer Berlin Heidelberg, Berlin, Heidelberg, 2009. ISBN 978-3-642-00860-3. doi: 10.1007/978-3-642-00860-3\_20. URL [https://doi.org/10.1007/978-3-642-00860-3\\_20](https://doi.org/10.1007/978-3-642-00860-3_20). 15

- C. Cai, Z. Liu, P. Xia, and W. Dai. Cycle slip detection and repair for undifferenced GPS observations under high ionospheric activity. *GPS Solutions*, 17:247–260, 2013. doi: 10.1007/s10291-012-0275-7. 30
- D. P. Chambers. Evaluation of new GRACE time-variable gravity data over the ocean. *Geophysical Research Letters*, 33(17), 2006. doi: 10.1029/2006GL027296. URL <https://agupubs.onlinelibrary.wiley.com/doi/abs/10.1029/2006GL027296>. 49
- S. Chapman. The absorption and dissociative or ionizing effect of monochromatic radiation in an atmosphere on a rotating earth. *Proceedings of the Physical Society*, 43(1):26–45, jan 1931. doi: 10.1088/0959-5309/43/1/305. 8
- C. H. Chen, A. Saito, C. H. Lin, J. Y. Liu, H. F. Tsai, T. Tsugawa, Y. Otsuka, M. Nishioka, and M. Matsumura. Long-distance propagation of ionospheric disturbance generated by the 2011 off the Pacific coast of Tohoku Earthquake. *Earth, Planets and Space*, 63(7):67, Sep 2011. ISSN 1880-5981. doi: 10.5047/eps.2011.06.026. URL <https://doi.org/10.5047/eps.2011.06.026>. 6
- C.-Z. F. Cheng, Y.-H. Kuo, R. A. Anthes, and L. Wu. Satellite constellation monitors global and space weather. *Eos, Transactions American Geophysical Union*, 87(17):166–166, 2006. doi: 10.1029/2006EO170003. URL <https://agupubs.onlinelibrary.wiley.com/doi/abs/10.1029/2006EO170003>. 46
- L. Ciruolo, F. Azpilicueta, and C. e. a. Brunini. Calibration errors on experimental slant total electron content (TEC) determined with GPS. *Journal of Geodesy*, 81:111–120, 2007. doi: 10.1007/s00190-006-0093-1. 35
- K. Cook, C. Fong, M. J. Wenkel, P. Wilczynski, N. Yen, and G. S. Chang. FORMOSAT-7/COSMIC-2 GNSS radio occultation constellation mission for global weather monitoring. In *2013 IEEE Aerospace Conference*, pages 1–8, 2013. 46
- Copernicus. 2020. <https://www.copernicus.eu/>, accessed December 31, 2020. 44
- A. J. Coster, E. M. Gaposchkin, and L. E. Thronton. Real-Time Ionospheric Monitoring System Using GPS. *NAVIGATION*, 39(2):191–204, 1992. doi: 10.1002/j.2161-4296.1992.tb01874.x. URL <https://onlinelibrary.wiley.com/doi/abs/10.1002/j.2161-4296.1992.tb01874.x>. 33
- P. Coisson, S. Radicella, R. Leitinger, and B. Nava. Topside electron density in IRI and NeQuick: Features and limitations. *Advances in Space Research*, 37(5):937 – 942, 2006. ISSN 0273-1177. doi: 10.1016/j.asr.2005.09.015. URL <http://www.sciencedirect.com/science/>

- [article/pii/S0273117705011270](#). Advances in Specifying Plasma Temperatures and Ion Composition in the Ionosphere. 16
- R. Dach, S. Lutz, P. Walser, and P. F. (Eds). *Bernese GNSS Software Version 5.2 User manual*. Astronomical Institute, University of Bern, Bern Open Publishing, 2015. 28, 29, 32, 39
- R. Dach, S. Schaer, D. Arnold, M. Kalarus, L. Prange, P. Stebler, A. Villiger, and A. Jäggi. CODE final product series for the IGS, 2020. 57, 60, 61
- C. Dahle, D. Arnold, and A. Jäggi. Impact of tracking loop settings of the Swarm GPS receiver on gravity field recovery. *Advances in Space Research*, 59(12):2843 – 2854, 2017. ISSN 0273-1177. doi: 10.1016/j.asr.2017.03.003. URL <http://www.sciencedirect.com/science/article/pii/S027311771730176X>. 66, 89, 103
- C. Dahle, M. Murböck, F. Flechtner, H. Dobsław, G. Michalak, K. Neumayer, O. Abrykosov, A. Reinhold, R. König, R. Sulzbach, and C. Förste. The GFZ GRACE RL06 Monthly Gravity Field Time Series: Processing Details and Quality Assessment. *Remote Sensing*, 11, 2019. doi: 10.3390/rs11182116. 32, 79
- V. Dehant, P. Defraigne, and J. M. Wahr. Tides for a convective Earth. *Journal of Geophysical Research: Solid Earth*, 104(B1):1035–1058, 1999. doi: 10.1029/1998JB900051. URL <https://agupubs.onlinelibrary.wiley.com/doi/abs/10.1029/1998JB900051>. 61
- DISC. Swarm Level 2 IBI product description. Technical report, ESA, BGS, DTU, DUT, GFZ, ETH, IPGP, IRF, Leti, UoC, VZLU, 2017a. 13, 42, 92
- DISC. Swarm Level 2 TEC product description. Technical report, ESA, BGS, DTU, DUT, GFZ, ETH, IPGP, IRF, Leti, UoC, VZLU, 2017b. 32, 36, 37, 38, 140
- DLR. 2020a. [https://www.dlr.de/rd/desktopdefault.aspx/tabid-2440/3586\\_read-5330/](https://www.dlr.de/rd/desktopdefault.aspx/tabid-2440/3586_read-5330/), accessed Decmeber 16 2020. xiii, 41
- DLR. 2020b. <https://www.gfz-potsdam.de/en/grace/>, accessed Decmeber 16, 2020. 42
- H. Dobsław, I. Bergmann-Wolf, R. Dill, L. Poropat, M. Thomas, C. Dahle, S. Esselborn, R. König, and F. Flechtner. A new high-resolution model of non-tidal atmosphere and ocean mass variability for de-aliasing of satellite gravity observations: AOD1B RL06. *Geophysical Journal International*, 211(1):263–269, 07 2017. ISSN 0956-540X. doi: 10.1093/gji/ggx302. URL <https://doi.org/10.1093/gji/ggx302>. 61
- E. Doornbos. Daedalus mission proposal, mini-iswat virtual meeting series: G2a atmosphere variability, 22-26 february 2021, 2021. URL [https://iswat-cospar.org/virtual-meeting-series\\_G2A](https://iswat-cospar.org/virtual-meeting-series_G2A). 14

- J. Dow, R. Neilan, and G. Gendt. The International GPS Service: Celebrating the 10th anniversary and looking to the next decade. *Advances in Space Research*, 36(3):320–326, 2005. ISSN 0273-1177. doi: 10.1016/j.asr.2005.05.125. URL <http://www.sciencedirect.com/science/article/pii/S0273117705007684>. Satellite Dynamics in the Era of Interdisciplinary Space Geodesy. 38
- M. Drinkwater, R. Haagmans, D. Muzi, A. Popescu, R. Floberghagen, M. Kern, and M. Fehringer. The GOCE gravity mission: ESA’s first core explorer, 2006. 42, 49
- eoPortal. 2020. <https://directory.eoportal.org/web/eoportal/-/dmisp>, accessed December 31, 2020. 45
- eoPortal. 2021. <https://earth.esa.int/web/eoportal/satellite-missions/s/starlette>, accessed January 3, 2021. 55
- E. Erdogan, M. Schmidt, A. Goss, B. Görres, and F. Seitz. Adaptive Modeling of the Global Ionosphere Vertical Total Electron Content. *Remote Sensing*, 12(11), 2020. doi: 10.3390/rs12111822. 18
- ESA. New GPSR settings on Swarm A and B satellites, 29 October 2015. <https://earth.esa.int/web/guest/missions/esa-operational-eo-missions/swarm/news>, 2015a. accessed 23 Nov. 2019. xix, 103
- ESA. Swarm GPSR update, 1 July 2015. <https://earth.esa.int/web/guest/missions/esa-operational-eo-missions/swarm/news>, 2015b. accessed 23 Nov. 2019. xix, 103
- ESA. New GPSR settings on Swarm A and C satellites. <https://earth.esa.int/web/guest/missions/esa-operational-eo-missions/swarm/news>, 2016. accessed 23 Nov. 2019. xix, 103
- ESA. Galileo enhancing Sentinel-6’s sea level monitoring mission. [https://www.esa.int/Applications/Navigation/Galileo\\_enhancing\\_Sentinel-6\\_s\\_sea\\_level\\_monitoring\\_mission](https://www.esa.int/Applications/Navigation/Galileo_enhancing_Sentinel-6_s_sea_level_monitoring_mission), 2020a. accessed 2 Mar. 2021. 24
- ESA. 2020b. [https://www.esa.int/Applications/Observing\\_the\\_Earth/GOCE/Introducing\\_GOCE](https://www.esa.int/Applications/Observing_the_Earth/GOCE/Introducing_GOCE), accessed September 17, 2020. xiii, 42
- ESA. 2020c. <https://sentinel.esa.int/web/sentinel/missions/sentinel-1>, accessed December 31, 2020. 45
- ESA. 2020d. <https://sentinel.esa.int/web/sentinel/missions/sentinel-2>, accessed December 31, 2020. 45

- ESA. 2020e. <https://sentinel.esa.int/web/sentinel/missions/sentinel-3>, accessed December 31, 2020. 45
- ESA. 2020f. [https://www.esa.int/Enabling\\_Support/Operations/Swarm\\_operations](https://www.esa.int/Enabling_Support/Operations/Swarm_operations), accessed September 17, 2020. xiii, 42
- ESA. 2020g. <https://directory.eoportal.org/web/eoportal/satellite-missions/c-missions/copernicus-sentinel-1>, accessed September 17, 2020. xiv, 44
- ESA. 2020h. <https://sentinel.esa.int/web/sentinel/missions/sentinel-3/overview/mission-summary>, accessed September 17, 2020. xiv, 44
- ESA. 2020i. [http://www.esa.int/Space\\_in\\_Member\\_States/Germany/Sentinel-2\\_im\\_Dienste\\_der\\_Ernaehrung](http://www.esa.int/Space_in_Member_States/Germany/Sentinel-2_im_Dienste_der_Ernaehrung), accessed September 17, 2020. xiv, 44
- ESA. Esa moves forward with harmony, 23.02.2021, 2021. URL [https://www.esa.int/Applications/Observing\\_the\\_Earth/ESA\\_moves\\_forward\\_with\\_Harmony](https://www.esa.int/Applications/Observing_the_Earth/ESA_moves_forward_with_Harmony). 14
- S. Esterhuizen, G. Franklin, K. Hurst, A. Mannucci, T. Meehan, F. Webb, and L. Young. TriG - A GNSS Precise Orbit and Radio Occultation Space Receiver. *Proceedings of the 22nd international technical meeting of the Satellite Division of the Institute of Navigation, ION GNSS 2009*, pages 1442–1446, 2009. URL <https://authors.library.caltech.edu/21729/>. 24
- M. Falcone, J. Hahn, and T. Burger. *Galileo*, pages 247–272. Springer International Publishing, Cham, 2017. ISBN 978-3-319-42928-1. doi: 10.1007/978-3-319-42928-1\_9. URL [https://doi.org/10.1007/978-3-319-42928-1\\_9](https://doi.org/10.1007/978-3-319-42928-1_9). 24
- J. Fernandez, C. Fernandez, H. Peter, and P. Féménias. The Copernicus Sentinel-3 Mission POD Service. *20th International Workshop on Laser Ranging, October 9-14, 2016, Potsdam, Germany*, 2016. URL [https://cddis.nasa.gov/lw20/docs/2016/posters/P32-Fernandez\\_poster.pdf](https://cddis.nasa.gov/lw20/docs/2016/posters/P32-Fernandez_poster.pdf). 47
- U. Foelsche and G. Kirchengast. A simple “geometric” mapping function for the hydrostatic delay at radio frequencies and assessment of its performance. *Geophysical Research Letters*, 29(10):111–1–111–4, 2002. doi: 10.1029/2001GL013744. URL <https://agupubs.onlinelibrary.wiley.com/doi/abs/10.1029/2001GL013744>. 33, 121
- E. Friis-Christensen, H. Lühr, D. Knudsen, and R. Haagmans. Swarm – An Earth Observation Mission investigating Geospace. *Advances in Space Research*, 41(1):210 – 216, 2008. ISSN 0273-1177. doi: 10.1016/j.asr.2006.10.008. URL <http://www.sciencedirect.com/science/article/pii/S0273117706005497>. 43

- M. Fritsche, R. Dietrich, C. Knöfel, A. Rülke, S. Vey, M. Rothacher, and P. Steigenberger. Impact of higher-order ionospheric terms on GPS estimates. *Geophysical Research Letters*, 32(23), 2005. doi: 10.1029/2005GL024342. URL <https://agupubs.onlinelibrary.wiley.com/doi/abs/10.1029/2005GL024342>. 19
- C. Förste, O. Abrykosov, S. Bruinsma, C. Dahle, R. König, and J.-M. Lemoine. ESA's Release 6 GOCE gravity field model by means of the direct approach based on improved filtering of the reprocessed gradients of the entire mission (GO<sub>C</sub>ONS<sub>G</sub>CF<sub>2D</sub>IR<sub>R</sub>6), 2019. 49
- M. Garcia-Fernández and O. Montenbruck. Low Earth orbit satellite navigation errors and vertical total electron content in single-frequency GPS tracking. *Radio Science*, 41(5), 2006. doi: 10.1029/2005RS003420. URL <https://agupubs.onlinelibrary.wiley.com/doi/abs/10.1029/2005RS003420>. 15, 28, 34
- A. García-Rodríguez. On Board Radio Navigation Receivers, TEC-ETN/2007.65. *European Space Agency*, 2008. 42
- T. Gerzen and D. Minkwitz. Simultaneous multiplicative column-normalized method (SMART) for 3-D ionosphere tomography in comparison to other algebraic methods. *Annales Geophysicae*, 34(1):97–115, 2016. doi: 10.5194/angeo-34-97-2016. URL <https://angeo.copernicus.org/articles/34/97/2016/>. 18, 146
- T. Gerzen, V. Wilken, D. Minkwitz, M. M. Hoque, and S. Schlüter. Three-dimensional data assimilation for ionospheric reference scenarios. *Annales Geophysicae*, 35(2):203–215, 2017. doi: 10.5194/angeo-35-203-2017. URL <https://angeo.copernicus.org/articles/35/203/2017/>. 15, 18
- GFZ. 2020. <http://op.gfz-potsdam.de/grace/payload/payload.html>, accessed December 31, 2020. 44
- GFZ-Potsdam. <https://www.gfz-potsdam.de/en/kp-index/>, last access: 6. November 2019. 2019. 113
- R. Gordon, R. Bender, and G. T. Herman. Algebraic Reconstruction Techniques (ART) for three-dimensional electron microscopy and X-ray photography. *Journal of Theoretical Biology*, 29(3):471 – 481, 1970. ISSN 0022-5193. doi: 10.1016/0022-5193(70)90109-8. URL <http://www.sciencedirect.com/science/article/pii/0022519370901098>. 146
- A. Goss, M. Schmidt, E. Erdogan, and F. Seitz. Global and Regional High-Resolution VTEC Modelling Using a Two-Step B-Spline Approach. *Remote Sensing*, 12(7), 2020. doi: 10.3390/rs12071198. 18

- GSC. <https://www.gsc-europa.eu/news/latest-batch-of-galileo-satellites-enters-service>. *European GNSS Service Centre*, 2019. 24
- W. Gurtner and L. Estey. RINEX, The Receiver Independent Exchange Format, Version 3.00. *IGS Data Format description*, 2007. URL <ftp://igs.org/pub/data/format/rinex300.pdf>. 57
- B. Heilig and H. Lühr. New plasmopause model derived from CHAMP field-aligned current signatures. *Annales Geophysicae*, 31(3):529–539, 2013. doi: 10.5194/angeo-31-529-2013. URL <https://angeo.copernicus.org/articles/31/529/2013/>. 143
- B. Heilig and H. Lühr. Quantifying the relationship between the plasmopause and the inner boundary of small-scale field-aligned currents, as deduced from Swarm observations. *Annales Geophysicae*, 36(2):595–607, 2018. doi: 10.5194/angeo-36-595-2018. URL <https://angeo.copernicus.org/articles/36/595/2018/>. 143
- W. A. Heiskanen and H. Moritz. *Physical Geodesy*. San Francisco W. H. Freeman and Company, 1967. 51
- J. Herman, A. Davis, K. B. Chin, M. Kinzler, S. Scholz, and M. Steinhoff. Life with a weak Heart, Prolonging the Grace Mission despite degraded Batteries. *SpaceOps 2012; Stockholm, Sweden – June 11 - 15*, 2012. 44
- M. M. Hoque and N. Jakowski. Estimate of higher order ionospheric errors in GNSS positioning. *Radio Science*, 43(5), 2008. doi: 10.1029/2007RS003817. URL <https://agupubs.onlinelibrary.wiley.com/doi/abs/10.1029/2007RS003817>. 28
- M. M. Hoque and N. Jakowski. A new global empirical NmF2 model for operational use in radio systems. *Radio Science*, 46(6), 2011. doi: 10.1029/2011RS004807. URL <https://agupubs.onlinelibrary.wiley.com/doi/abs/10.1029/2011RS004807>. 18
- M. M. Hoque and N. Jakowski. A new global model for the ionospheric F2 peak height for radio wave propagation. *Annales Geophysicae*, 30(5):797–809, 2012. doi: 10.5194/angeo-30-797-2012. URL <https://angeo.copernicus.org/articles/30/797/2012/>. 18
- IGS. IGS Analysis Centers. <https://www.igs.org/acc/>, 2020a. accessed 29 Dec. 2020. 39
- IGS. IGS Products. <https://www.igs.org/products/>, 2020b. accessed 29 Dec. 2020. 38, 39
- J. ISAS. Sounding Rockets. [http://www.isas.jaxa.jp/en/missions/sounding\\_rockets/](http://www.isas.jaxa.jp/en/missions/sounding_rockets/), 2020. accessed 23 Dec. 2020. 14



- N. Jakowski and M. M. Hoque. A new electron density model of the plasmasphere for operational applications and services. *J. Space Weather Space Clim.*, 8:A16, 2018. doi: 10.1051/swsc/2018002. URL <https://doi.org/10.1051/swsc/2018002>. 5, 6, 17, 121
- Y. Jean, U. Meyer, and A. Jäggi. Combination of GRACE monthly gravity field solutions from different processing strategies. *Journal of Geodesy*, 92(11):1313–1328, Nov 2018. ISSN 1432-1394. doi: 10.1007/s00190-018-1123-5. URL <https://doi.org/10.1007/s00190-018-1123-5>. 62
- G. Jee, R. W. Schunk, and L. Scherliess. Comparison of iri-2001 with topex tec measurements. *Journal of Atmospheric and Solar-Terrestrial Physics*, 67(4):365 – 380, 2005. ISSN 1364-6826. doi: 10.1016/j.jastp.2004.08.005. URL <http://www.sciencedirect.com/science/article/pii/S1364682604002640>. 121
- G. Johnston, A. Riddell, and G. Hausler. *The International GNSS Service*, pages 967–982. Springer International Publishing, Cham, 2017. ISBN 978-3-319-42928-1. doi: 10.1007/978-3-319-42928-1\_33. URL [https://doi.org/10.1007/978-3-319-42928-1\\_33](https://doi.org/10.1007/978-3-319-42928-1_33). 15
- JPL. GRACE-FO Resumes Data Collection, accessed 5th of January 2021. 2018. URL <https://gracefo.jpl.nasa.gov/news/140/grace-fo-resumes-data-collection/>. 62
- JPL. 2020. <https://gracefo.jpl.nasa.gov/mission/overview/>, accessed September 17, 2020. xiii, 43
- A. Jäggi. *Pseudo-stochastic orbit modelling of Low Earth Satellites using the Global Positioning System*. PhD thesis, University of Bern, 2006. xiv, 21, 55, 57, 58
- A. Jäggi, R. Dach, O. Montenbruck, U. Hugentobler, H. Bock, and G. Beutler. Phase center modeling for LEO GPS receiver antennas and its impact on precise orbit determination. *Journal of Geodesy*, 83(12):1145, Jul 2009. ISSN 1432-1394. doi: 10.1007/s00190-009-0333-2. URL <https://doi.org/10.1007/s00190-009-0333-2>. 60
- A. Jäggi, L. Prange, U. Meyer, L. Mervart, G. Beutler, T. Gruber, R. Dach, and R. Pail. Gravity Field Determination at AIUB: From annual to multi-annual solutions. *EGU General Assembly 2010*, 12, 2010. 61
- A. Jäggi, H. Bock, and R. Floberghagen. GOCE orbit predictions for SLR tracking. *GPS Solutions*, 15(2):129–137, Apr 2011a. ISSN 1521-1886. doi: 10.1007/s10291-010-0176-6. URL <https://doi.org/10.1007/s10291-010-0176-6>. 42
- A. Jäggi, H. Bock, L. Prange, U. Meyer, and G. Beutler. GPS-only gravity field recovery with GOCE, CHAMP, and GRACE. *Advances in Space Research*, 47(6):1020 – 1028, 2011b.



- ISSN 0273-1177. doi: 10.1016/j.asr.2010.11.008. URL <http://www.sciencedirect.com/science/article/pii/S0273117710007350>. 48
- A. Jäggi, L. Prange, and U. Hugentobler. Impact of covariance information of kinematic positions on orbit reconstruction and gravity field recovery. *Advances in Space Research*, 47(9):1472 – 1479, 2011c. ISSN 0273-1177. doi: 10.1016/j.asr.2010.12.009. URL <http://www.sciencedirect.com/science/article/pii/S0273117710007969>. 54, 68
- A. Jäggi, H. Bock, D. Thaller, K. Sośnica, U. Meyer, C. Baumann, and R. Dach. Precise Orbit Determination of Low Earth Satellites at AIUB using GPS and SLR. *ESA Living Planet Symposium 2013-14 September 2013, Edinburgh, U.K.*, 2013. doi: 10.7892/boris.44881. 55
- A. Jäggi, H. Bock, U. Meyer, G. Beutler, and J. van den IJssel. GOCE: assessment of GPS-only gravity field determination. *Journal of Geodesy*, 89(1):33–48, Jan 2015. ISSN 1432-1394. doi: 10.1007/s00190-014-0759-z. URL <https://doi.org/10.1007/s00190-014-0759-z>. 28, 65, 66, 75
- A. Jäggi, C. Dahle, D. Arnold, H. Bock, U. Meyer, G. Beutler, and J. van den IJssel. Swarm kinematic orbits and gravity fields from 18months of GPS data. *Advances in Space Research*, 57(1):218 – 233, 2016. ISSN 0273-1177. doi: 10.1016/j.asr.2015.10.035. URL <http://www.sciencedirect.com/science/article/pii/S0273117715007541>. 60, 65, 66, 72, 74, 77, 87, 90
- E. Kaplan and C. J. Hegarty. *Understanding GPS/GNSS: Principles and Applications, Third Edition*. Artech House, Inc., Norwood, MA, USA, 3rd edition, 2017. ISBN 1630810584, 9781630810580. 23
- M. C. Kelley. *The Earth's Ionosphere*. Academic Press, 1989. ISBN 978-0-12-404013-7. doi: 10.1016/B978-0-12-404013-7.X5001-1. xiii, 5, 7, 10, 11, 12, 90, 91
- P. M. Kintner, B. M. Ledvina, and E. R. de Paula. GPS and ionospheric scintillations. *Space Weather*, 5(9), 2007. doi: 10.1029/2006SW000260. URL <https://agupubs.onlinelibrary.wiley.com/doi/abs/10.1029/2006SW000260>. 6
- F. Landerer, F. Flechtner, H. Save, C. Dahle, and M. Watkins. GRACE Follow-On Science Data System Newsletter Report: April/May2020(No. 13). 13, 2020a. URL [https://www.gfz-potsdam.de/fileadmin/gfz/sec12/pdf/GRACE-FO/GRACE\\_FO\\_SDS\\_newsletter\\_No13.pdf](https://www.gfz-potsdam.de/fileadmin/gfz/sec12/pdf/GRACE-FO/GRACE_FO_SDS_newsletter_No13.pdf). 44
- F. W. Landerer, F. M. Flechtner, H. Save, F. H. Webb, T. Bandikova, W. I. Bertiger, S. V. Bettadpur, S. H. Byun, C. Dahle, H. Dobslaw, E. Fahnestock, N. Harvey, Z. Kang, G. L. H. Kruizinga, B. D. Loomis, C. McCullough, M. Murböck, P. Nagel, M. Paik, N. Pie, S. Poole,

- D. Strelakov, M. E. Tamisiea, F. Wang, M. M. Watkins, H.-Y. Wen, D. N. Wiese, and D.-N. Yuan. Extending the Global Mass Change Data Record: GRACE Follow-On Instrument and Science Data Performance. *Geophysical Research Letters*, 47(12):e2020GL088306, 2020b. doi: 10.1029/2020GL088306. URL <https://agupubs.onlinelibrary.wiley.com/doi/abs/10.1029/2020GL088306>. e2020GL088306 2020GL088306. 44
- M. Lasser, U. Meyer, D. Arnold, and A. Jäggi. Stochastic noise modelling of kinematic orbit positions in the Celestial Mechanics Approach. *Advances in Geosciences*, 50:101–113, 2020. doi: 10.5194/adgeo-50-101-2020. URL <https://adgeo.copernicus.org/articles/50/101/2020/>. 54, 87
- J.-M. Lemoine, S. Bruinsma, S. Loyer, R. Biancale, J.-C. Marty, F. Perosanz, and G. Balmino. Temporal gravity field models inferred from GRACE data. *Advances in Space Research*, 39(10):1620–1629, 2007. ISSN 0273-1177. doi: 10.1016/j.asr.2007.03.062. URL <http://www.sciencedirect.com/science/article/pii/S0273117707003067>. 49
- K. Levenberg. A method for the solution of certain non-linear problems in least squares. *Quarterly of Applied Mathematics*, 2(2):164–168, 1944. ISSN 0033569X, 15524485. URL <http://www.jstor.org/stable/43633451>. 130
- H.-L. Liu, C. G. Bardeen, B. T. Foster, P. Lauritzen, J. Liu, G. Lu, D. R. Marsh, A. Maute, J. M. McInerney, N. M. Pedatella, L. Qian, A. D. Richmond, R. G. Roble, S. C. Solomon, F. M. Vitt, and W. Wang. Development and Validation of the Whole Atmosphere Community Climate Model With Thermosphere and Ionosphere Extension (WACCM-X 2.0). *Journal of Advances in Modeling Earth Systems*, 10(2):381–402, 2018. doi: 10.1002/2017MS001232. URL <https://agupubs.onlinelibrary.wiley.com/doi/abs/10.1002/2017MS001232>. 15
- M. Liu, Y. Yuan, X. Huo, M. Li, and Y. Chai. Simultaneous estimation of gps p1-p2 differential code biases using low earth orbit satellites data from two different orbit heights. *Journal of Geodesy*, 94(12):121, Nov 2020. ISSN 1432-1394. doi: 10.1007/s00190-020-01458-5. URL <https://doi.org/10.1007/s00190-020-01458-5>. 36
- L. Lomidze, D. J. Knudsen, J. Burchill, A. Kouznetsov, and S. C. Buchert. Calibration and Validation of Swarm Plasma Densities and Electron Temperatures Using Ground-Based Radars and Satellite Radio Occultation Measurements. *Radio Science*, 53(1):15–36, 2018. doi: 10.1002/2017RS006415. URL <https://agupubs.onlinelibrary.wiley.com/doi/abs/10.1002/2017RS006415>. xix, 13, 125, 134
- C. Lück, J. Kusche, R. Rietbroek, and A. Löcher. Time-variable gravity fields and ocean mass change from 37 months of kinematic Swarm orbits. *Solid Earth*, 9(2):323–339, 2018. doi: 10.5194/se-9-323-2018. URL <https://www.solid-earth.net/9/323/2018/>. 43, 63

- F. Lyard, F. Lefevre, T. Letellier, and O. Francis. Modelling the global ocean tides: modern insights from FES2004. *Ocean Dynamics*, 56(5):394–415, Dec 2006. ISSN 1616-7228. doi: 10.1007/s10236-006-0086-x. URL <https://doi.org/10.1007/s10236-006-0086-x>. 60
- H. Lühr, M. Rother, S. Maus, W. Mai, and D. Cooke. The diamagnetic effect of the equatorial Appleton anomaly: Its characteristics and impact on geomagnetic field modeling. *Geophysical Research Letters*, 30(17), 2003. doi: 10.1029/2003GL017407. URL <https://agupubs.onlinelibrary.wiley.com/doi/abs/10.1029/2003GL017407>. 10, 91
- A. J. Mannucci, B. D. Wilson, D. N. Yuan, C. H. Ho, U. J. Lindqwister, and T. F. Runge. A global mapping technique for GPS-derived ionospheric total electron content measurements. *Radio Science*, 33(3):565–582, 1998. doi: 10.1029/97RS02707. URL <https://agupubs.onlinelibrary.wiley.com/doi/abs/10.1029/97RS02707>. 33
- D. W. Marquardt. An Algorithm for Least-Squares Estimation of Nonlinear Parameters. *Journal of the Society for Industrial and Applied Mathematics*, 11(2):431–441, 1963. doi: 10.1137/0111030. URL <https://doi.org/10.1137/0111030>. 130
- T. Mayer-Gürr, K. H. Ilk, A. Eicker, and M. Feuchtinger. ITG-CHAMP01: a CHAMP gravity field model from short kinematic arcs over a one-year observation period. *Journal of Geodesy*, 78(7):462–480, Mar 2005. ISSN 1432-1394. doi: 10.1007/s00190-004-0413-2. URL <https://doi.org/10.1007/s00190-004-0413-2>. 54
- T. Mayer-Gürr, A. Kvas, B. Klinger, D. Rieser, and N. Zehentner. The new combined satellite only model GOCO05s. 4 2015. EGU General Assembly 2013 ; Conference date: 07-04-2013 Through 12-04-2013. 60
- T. Mayer-Gürr, S. Behzadpur, M. Ellmer, A. Kvas, B. Klinger, S. Strasser, and N. Zehentner. ITSG-Grace2018 - Monthly, Daily and Static Gravity Field Solutions from GRACE. 2018. doi: 10.5880/ICGEM.2018.003. 49, 62
- U. Meyer, K. Sosnica, D. Arnold, C. Dahle, D. Thaller, R. Dach, and A. Jäggi. SLR, GRACE and Swarm Gravity Field Determination and Combination. *Remote Sens.*, 11, 2019. doi: 10.3390/rs11080956. 63
- D. Minkwitz, K. G. van den Boogaart, T. Gerzen, and M. Hoque. Tomography of the ionospheric electron density with geostatistical inversion. *Annales Geophysicae*, 33(8):1071–1079, 2015. doi: 10.5194/angeo-33-1071-2015. URL <https://angeo.copernicus.org/articles/33/1071/2015/>. 143
- I. A. Mironova, A. A. Artamonov, G. A. Bazilevskaya, E. V. Rozanov, G. A. Kovaltsov, V. S. Makhmutov, A. L. Mishev, and A. V. Karagodin. Ionization of the Polar Atmosphere by

- Energetic Electron Precipitation Retrieved From Balloon Measurements. *Geophysical Research Letters*, 46(2):990–996, 2019. doi: 10.1029/2018GL079421. URL <https://agupubs.onlinelibrary.wiley.com/doi/abs/10.1029/2018GL079421>. 6
- C. Mitchell and P. Cannon. Multi-Instrument Data Analysis System (MIDAS) Imaging of the Ionosphere. 2002. doi: 10.21236/ada445580. 15
- O. Montenbruck and B. González Rodríguez. NeQuick-G performance assessment for space applications. *GPS Solutions*, 24(13), 2020. doi: 10.1007/s10291-019-0931-2. 16, 17
- O. Montenbruck and R. Kroes. In-flight performance analysis of the CHAMP BlackJack GPS Receiver. *GPS Solutions*, 7:74–86, 2003. doi: 10.1007/s10291-003-0055-5. 30, 32, 125
- O. Montenbruck, M. Garcia-Fernandez, Y. Yoon, S. Schön, and A. Jäggi. Antenna phase center calibration for precise positioning of LEO satellites. *GPS Solutions*, 13(1):23, Jun 2008. ISSN 1521-1886. doi: 10.1007/s10291-008-0094-z. URL <https://doi.org/10.1007/s10291-008-0094-z>. 57, 141
- O. Montenbruck, S. Hackel, and A. Jäggi. Precise orbit determination of the Sentinel-3A altimetry satellite using ambiguity-fixed GPS carrier phase observations. *Journal of Geodesy*, 92(7): 711–726, Jul 2018. ISSN 1432-1394. doi: 10.1007/s00190-017-1090-2. URL <https://doi.org/10.1007/s00190-017-1090-2>. 47
- NASA. 2019. <https://www.nasa.gov/feature/goddard/2019/first-of-two-van-allen-probes-spacecraft-ceases-operations>, accessed January 31, 2021. 143
- NASA. 2020. <https://earthobservatory.nasa.gov/features/GRACE>, accessed September 17, 2020. xiii, 43
- National Space Institute - Technical University of Denmark. Swarm Level 1b Processor Algorithms, SW-RS-DSC-SY-0002. 2019. 31, 60
- NOAA. 2020. <https://www.ospo.noaa.gov/Operations/DMSP/index.html>, accessed September 17, 2020. xiv, 45
- J. Norberg, I. I. Virtanen, L. Roininen, J. Vierinen, M. Orispää, K. Kauristie, and M. S. Lehtinen. Bayesian statistical ionospheric tomography improved by incorporating ionosonde measurements. *Atmospheric Measurement Techniques*, 9(4):1859–1869, 2016. doi: 10.5194/amt-9-1859-2016. URL <https://amt.copernicus.org/articles/9/1859/2016/>. 143
- NSPO. 2020. <https://directory.eoportal.org/web/eoportal/satellite-missions/content/-/article/formosat-3>, accessed September 17, 2020. xiv, 46

- G. Olivares-Pulido, M. Hernández-Pajares, A. Aragón-Ángel, and A. Garcia-Rigo. A linear scale height Chapman model supported by GNSS occultation measurements. *Journal of Geophysical Research: Space Physics*, 121(8):7932–7940, 2016. doi: 10.1002/2016JA022337. URL <https://agupubs.onlinelibrary.wiley.com/doi/abs/10.1002/2016JA022337>. 9
- J. Park, H. Lühr, C. Stolle, M. Rother, K. W. Min, and I. Michaelis. The characteristics of field-aligned currents associated with equatorial plasma bubbles as observed by the CHAMP satellite. *Annales Geophysicae*, 27(7):2685–2697, 2009. doi: 10.5194/angeo-27-2685-2009. URL <https://www.ann-geophys.net/27/2685/2009/>. 91
- J. Park, M. Noja, C. Stolle, and H. Lühr. The Ionospheric Bubble Index deduced from magnetic field and plasma observations onboard Swarm. *Earth, Planets and Space*, 65(11):13, Nov 2013. ISSN 1880-5981. doi: 10.5047/eps.2013.08.005. URL <https://doi.org/10.5047/eps.2013.08.005>. 13
- N. K. Pavlis, S. A. Holmes, S. C. Kenyon, and J. K. Factor. The development and evaluation of the Earth Gravitational Model 2008 (EGM2008). *Journal of Geophysical Research: Solid Earth*, 117(B4), 2012. doi: 10.1029/2011JB008916. URL <https://agupubs.onlinelibrary.wiley.com/doi/abs/10.1029/2011JB008916>. 60
- M. Pearlman, J. Degnan, and J. Bosworth. The International Laser Ranging Service. *Advances in Space Research*, 30(2):135 – 143, 2002. ISSN 0273-1177. doi: 10.1016/S0273-1177(02)00277-6. URL <http://www.sciencedirect.com/science/article/pii/S0273117702002776>. 50
- G. Petit and B. Luzum. IERS Conventions. *IERS Conventions Centre*, 36, 2010. URL <https://www.iers.org/SharedDocs/Publikationen/EN/IERS/Publications/tn/TechnNote36/tn36.pdf>. 60
- E. J. Petrie, M. Hernández-Pajares, P. Spalla, P. Moore, and M. A. King. A Review of Higher Order Ionospheric Refraction Effects on Dual Frequency GPS. *Surveys in Geophysics*, 32:197–253, 2011. doi: 10.1007/s10712-010-9105-z. 27, 28
- M. Pezzopane and A. Pignalberi. The ESA Swarm mission to help ionospheric modeling: a new NeQuick topside formulation for mid-latitude regions. *Scientific Reports*, 9(12253), 2019. doi: 10.1038/s41598-019-48440-6. 9
- X. Pi, A. J. Mannucci, U. J. Lindqwister, and C. M. Ho. Monitoring of global ionospheric irregularities using the Worldwide GPS Network. *Geophysical Research Letters*, 24(18):2283–2286, 1997. doi: 10.1029/97GL02273. 38

- X. Pi, C. D. Edwards, G. A. Hajj, C. Ao, L. Romans, J. Callas, A. Mannucci, S. Asmar, and D. Kahan. A Chapman-Layers Ionospheric Model for Mars. *JPL Publication*, 08(24), 2008. 8
- W. E. Potter. Rocket measurements of auroral electric and magnetic fields. *Journal of Geophysical Research (1896-1977)*, 75(28):5415–5431, 1970. doi: 10.1029/JA075i028p05415. URL <https://agupubs.onlinelibrary.wiley.com/doi/abs/10.1029/JA075i028p05415>. 14
- L. Prange. *Global Gravity Field Determination Using the GPS Measurements Made Onboard the Low Earth Orbiting Satellite CHAMP*. PhD thesis, University of Bern, 2010. xiv, 42, 48, 53
- PRISM. <https://www.gfz-potsdam.de/en/section/geomagnetism/projects/prism-plasmapause-related-boundaries-in-the-topside-ionosphere-as-derived-from-swarm-measurements/>, last access: 2. November 2020. 2020. 143
- F. Prol, M. Hoque, and A. Ferreira. Plasmasphere and topside ionosphere reconstruction using metop satellite data during geomagnetic storms. *J. Space Weather Space Clim.*, 11:5, 2021. doi: 10.1051/swsc/2020076. URL <https://doi.org/10.1051/swsc/2020076>. 139
- S. Radicella and R. Leitinger. The evolution of the DGR approach to model electron density profiles. *Advances in space research*, 27:35–40, 2001. 16
- S. M. Radicella and M. L. Zhang. The improved DGR analytical model of electron density height profile and total electron content in the ionosphere. *Annals of Geophysics*, 38(1), 1995. ISSN 2037-416X. doi: 10.4401/ag-4130. URL <https://www.annalsofgeophysics.eu/index.php/annals/article/view/4130>. 9, 16, 17, 35
- K. Rawer. Replacement of the present sub-peak plasma density profile by a unique expression. *Advances in space research*, 2(10):183–190, 1983. 9
- K. Rawer, D. Bilitza, and S. Ramakrishnan. Goals and status of the International Reference Ionosphere. *Reviews of Geophysics*, 16(2):177–181, 1978. doi: 10.1029/RG016i002p00177. URL <https://agupubs.onlinelibrary.wiley.com/doi/abs/10.1029/RG016i002p00177>. 15
- R. D. Ray and R. M. Ponte. Barometric tides from ECMWF operational analyses. *Annales Geophysicae*, 21(8):1897–1910, 2003. doi: 10.5194/angeo-21-1897-2003. URL <https://angeo.copernicus.org/articles/21/1897/2003/>. 60
- C. Reigber, P. Schwintzer, and H. Lühr. The CHAMP geopotential mission. *Bollettino Di Geofisica Teorica ed Applicata*, 40:285–289, 1999. 41



- C. Reigber, R. Schmidt, F. Flechtner, R. König, U. Meyer, K.-H. Neumayer, P. Schwintzer, and S. Y. Zhu. An Earth gravity field model complete to degree and order 150 from GRACE: EIGEN-GRACE02S. *Journal of Geodynamics*, 39(1):1 – 10, 2005. ISSN 0264-3707. doi: 10.1016/j.jog.2004.07.001. URL <http://www.sciencedirect.com/science/article/pii/S0264370704000754>. 49
- B. Reinisch, P. Nsumei, X. Huang, and D. Bilitza. Modeling the f2 topside and plasmasphere for iri using image/rpi and isis data. *Advances in Space Research*, 39(5):731 – 738, 2007. ISSN 0273-1177. doi: 10.1016/j.asr.2006.05.032. URL <http://www.sciencedirect.com/science/article/pii/S0273117706006028>. 121
- X. Ren, J. Chen, X. Zhang, M. Schmidt, X. Li, and J. Zhang. Mapping topside ionospheric vertical electron content from multiple LEO satellites at different orbital altitudes. *Journal of Geodesy*, 94(9):86, Aug 2020. ISSN 1432-1394. doi: 10.1007/s00190-020-01415-2. URL <https://doi.org/10.1007/s00190-020-01415-2>. 121
- S. Revniviykh, A. Bolkunov, A. Serdyukov, and O. Montenbruck. *GLONASS*, pages 219–245. Springer International Publishing, Cham, 2017. ISBN 978-3-319-42928-1. doi: 10.1007/978-3-319-42928-1\_8. URL [https://doi.org/10.1007/978-3-319-42928-1\\_8](https://doi.org/10.1007/978-3-319-42928-1_8). 24
- F. Rich. Users guide for the topside ionospheric plasma monitor (SSIES, SSIES-2 and SSIES-3) on spacecraft of the Defense Meteorological Satellite Program (DMSP). Volume I: Technical Description; PL-TR-94-2187. 1994. URL <https://satdat.ngdc.noaa.gov/dmsp/docs/Rich%20-%201994%20-%20Users%20Guide%20SSIES-1%20SSIES-2%20SSIES-3%20-%20PL-TR-94-2187.pdf>. 131
- J. Rodríguez-Zuluaga, C. Stolle, Y. Yamazaki, H. Lühr, J. Park, L. Scherliess, and J. L. Chau. On the Balance Between Plasma and Magnetic Pressure Across Equatorial Plasma Depletions. *Journal of Geophysical Research: Space Physics*, 124(7):5936–5944, 2019. doi: 10.1029/2019JA026700. URL <https://agupubs.onlinelibrary.wiley.com/doi/abs/10.1029/2019JA026700>. 5, 91
- RUAG. Swarm GPSR TE-12 Instrument L1b Algorithms Definition, SW-TN-SES-GP-0018, 2008. 31
- R. Rummel. *GOCE: Gravitational Gradiometry in a Satellite*, pages 93–103. Springer Berlin Heidelberg, Berlin, Heidelberg, 2010. ISBN 978-3-642-01546-5. doi: 10.1007/978-3-642-01546-5\_4. URL [https://doi.org/10.1007/978-3-642-01546-5\\_4](https://doi.org/10.1007/978-3-642-01546-5_4). 42
- R. Rummel, G. Balmino, J. Johannessen, P. Visser, and P. Woodworth. Dedicated gravity field missions—principles and aims. *Journal of Geodynamics*, 33(1):3 – 20, 2002. ISSN 0264-3707.

- doi: 10.1016/S0264-3707(01)00050-3. URL <http://www.sciencedirect.com/science/article/pii/S0264370701000503>. Earth's Gravity and Magnetic Fields from Space. 49
- T. E. Sarris, E. R. Talaat, M. Palmroth, I. Dandouras, E. Armandillo, G. Kervalishvili, S. Buchert, S. Tourgaidis, D. M. Malaspina, A. N. Jaynes, N. Paschalidis, J. Sample, J. Halekas, E. Doornbos, V. Lappas, T. Moretto Jørgensen, C. Stolle, M. Clilverd, Q. Wu, I. Sandberg, P. Pirnaris, and A. Aikio. Daedalus: a low-flying spacecraft for in situ exploration of the lower thermosphere–ionosphere. *Geoscientific Instrumentation, Methods and Data Systems*, 9(1):153–191, 2020. doi: 10.5194/gi-9-153-2020. URL <https://gi.copernicus.org/articles/9/153/2020/>. 14
- R. Savcenko, W. Bosch, D. Dettmering, and F. Seitz. EOT11a - Global Empirical Ocean Tide model from multi-mission satellite altimetry, with links to model results, 2012. URL <https://doi.org/10.1594/PANGAEA.834232>. Supplement to: Savcenko, Roman; Bosch, Wolfgang (2012): EOT11a - Empirical Ocean Tide Model from Multi-Mission Satellite Altimetry. Deutsches Geodätisches Forschungsinstitut (DGFI), München, 89, 49 pp, hdl:10013/epic.43894.d001. 60, 61
- S. Schaer. *Mapping and Predicting the Earth's Ionosphere using the Global Positioning System*. PhD thesis, University of Bern, 1999. xiii, 18, 32, 34
- S. Schaer. Activities of IGS Bias and Calibration Working Group. In: Meindl M, Dach R, Jean Y (eds) IGS Technical Report 2011., 2011. 29
- S. Schaer. Overview of Relevant GNSS Biases. In: Proceedings of IGS Workshop on GNSS Biases, 2012. 29
- S. Schaer, G. Beutler, M. Rothacher, and T. Springer. Daily Global Ionosphere Maps based on GPS carrier phase data routinely produced by the CODE analysis center. *IGS AC Workshop*, 1996. 18, 124
- S. Schlüter, C. Stolle, N. Jakowski, and C. Jacobi. *Monitoring the 3 Dimensional Ionospheric Electron Distribution based on GPS Measurements*, pages 521–527. Springer Berlin Heidelberg, Berlin, Heidelberg, 2003. ISBN 978-3-540-38366-6. doi: 10.1007/978-3-540-38366-6\_71. URL [https://doi.org/10.1007/978-3-540-38366-6\\_71](https://doi.org/10.1007/978-3-540-38366-6_71). 143
- T. Schmidt, J. Wickert, G. Beyerle, R. König, R. Galas, and C. Reigber. *The CHAMP Atmospheric Processing System for Radio Occultation Measurements*, pages 597–602. Springer Berlin Heidelberg, Berlin, Heidelberg, 2005. ISBN 978-3-540-26800-0. doi: 10.1007/3-540-26800-6\_95. URL [https://doi.org/10.1007/3-540-26800-6\\_95](https://doi.org/10.1007/3-540-26800-6_95). 42



- L. Schreiter, D. Arnold, V. Sterken, and A. Jäggi. Mitigation of ionospheric signatures in Swarm GPS gravity field estimation using weighting strategies. *Annales Geophysicae*, 37(1):111–127, 2019. doi: 10.5194/angeo-37-111-2019. URL <https://www.ann-geophys.net/37/111/2019/>. 66, 112, 118
- L. Schreiter, O. Montenbruck, F. Zangerl, C. Siemes, D. Arnold, and A. Jäggi. Bandwidth correction of Swarm GPS carrier phase observations for improved orbit and gravity field determination. *GPS Solutions*, 25(2):70, Mar 2021. ISSN 1521-1886. doi: 10.1007/s10291-021-01107-0. URL <https://doi.org/10.1007/s10291-021-01107-0>. 99
- A. T. Sinclair/RGO. Re-Statement of Herstmonceux Normal Point Recommendation. 1997. URL [https://ilrs.gsfc.nasa.gov/data\\_and\\_products/data/npt/npt\\_algorithm.html](https://ilrs.gsfc.nasa.gov/data_and_products/data/npt/npt_algorithm.html). 50, 60
- A. Spicher, T. Cameron, E. M. Grono, K. N. Yakymenko, S. C. Buchert, L. B. N. Clausen, D. J. Knudsen, K. A. McWilliams, and J. I. Moen. Observation of polar cap patches and calculation of gradient drift instability growth times: A Swarm case study. *Geophysical Research Letters*, 42(2):201–206, 2015. doi: 10.1002/2014GL062590. URL <https://agupubs.onlinelibrary.wiley.com/doi/abs/10.1002/2014GL062590>. 5
- S. A. Stephens and J. B. Thomas. Controlled-root formulation for digital phase-locked loops. *IEEE Transactions on Aerospace and Electronic Systems*, 31(1):78–95, 1995. doi: 10.1109/7.366295. xix, 100, 101, 103, 105, 106, 107
- C. Stolle, J. Lilensten, S. Schlüter, C. Jacobi, M. Rietveld, and H. Lühr. Observing the north polar ionosphere on 30 october 2003 by gps imaging and is radars. *Annales Geophysicae*, 24(1):107–113, 2006a. doi: 10.5194/angeo-24-107-2006. URL <https://angeo.copernicus.org/articles/24/107/2006/>. 143
- C. Stolle, H. Lühr, M. Rother, and G. Balasis. Magnetic signatures of equatorial spread F as observed by the CHAMP satellite. *Journal of Geophysical Research: Space Physics*, 111(A2), 2006b. doi: 10.1029/2005JA011184. URL <https://agupubs.onlinelibrary.wiley.com/doi/abs/10.1029/2005JA011184>. 6, 12, 13, 90, 91, 92
- T. Tanimoto, K. Heki, and J. Artru-Lambin. 4.16 - Interaction of Solid Earth, Atmosphere, and Ionosphere. In G. Schubert, editor, *Treatise on Geophysics (Second Edition)*, pages 421 – 443. Elsevier, Oxford, second edition edition, 2015. ISBN 978-0-444-53803-1. doi: 10.1016/B978-0-444-53802-4.00083-X. URL <http://www.sciencedirect.com/science/article/pii/B978044453802400083X>. 6

- B. D. Tapley, S. Bettadpur, J. C. Ries, P. F. Thompson, and M. M. Watkins. GRACE Measurements of Mass Variability in the Earth System. *Science*, 305(5683):503–505, 2004a. ISSN 0036-8075. doi: 10.1126/science.1099192. URL <https://science.sciencemag.org/content/305/5683/503>. 43, 48
- B. D. Tapley, B. E. Schutz, and G. H. Born. *Statistical Orbit Determination*. 2004b. ISBN 0-12-683630-2. 21
- J. Teixeira da Encarnação, P. Visser, D. Arnold, A. Bezdek, E. Doornbos, M. Ellmer, J. Guo, J. van den IJssel, E. Iorfida, A. Jäggi, J. Klokocník, S. Krauss, X. Mao, T. Mayer-Gürr, U. Meyer, J. Sebera, C. K. Shum, C. Zhang, Y. Zhang, and C. Dahle. Description of the multi-approach gravity field models from Swarm GPS data. *Earth System Science Data*, 12(2):1385–1417, 2020. doi: 10.5194/essd-12-1385-2020. URL <https://essd.copernicus.org/articles/12/1385/2020/>. 51, 60
- J. Teixeira da Encarnação, D. Arnold, A. Bezděk, C. Dahle, E. Doornbos, J. van den IJssel, A. Jäggi, T. Mayer-Gürr, J. Sebera, P. Visser, and N. Zehentner. Gravity field models derived from Swarm GPS data. *Earth, Planets and Space*, 68, 2016. doi: 10.1186/s40623-016-0499-9. 43, 48
- E. Thébaud, C. C. Finlay, C. D. Beggan, P. Alken, J. Aubert, O. Barrois, F. Bertrand, T. Bondar, A. Boness, L. Brocco, E. Canet, A. Chambodut, A. Chulliat, P. Coisson, F. Civet, A. Du, A. Fournier, I. Fratter, N. Gillet, B. Hamilton, M. Hamoudi, G. Hulot, T. Jager, M. Korte, W. Kuang, X. Lalanne, B. Langlais, J.-M. Léger, V. Lesur, F. J. Lowes, S. Macmillan, M. Manda, C. Manoj, S. Maus, N. Olsen, V. Petrov, V. Ridley, M. Rother, T. J. Sabaka, D. Saturnino, R. Schachtschneider, O. Sirol, A. Tangborn, A. Thomson, L. Tøffner-Clausen, P. Vigneron, I. Wardinski, and T. Zvereva. International Geomagnetic Reference Field: the 12th generation. *Earth, Planets and Space*, 67(1):79, May 2015. ISSN 1880-5981. doi: 10.1186/s40623-015-0228-9. URL <https://doi.org/10.1186/s40623-015-0228-9>. 28
- D. R. Themens, P. T. Jayachandran, I. Galkin, and C. Hall. The Empirical Canadian High Arctic Ionospheric Model (E-CHAIM): NmF2 and hmF2. *Journal of Geophysical Research: Space Physics*, 122(8):9015–9031, 2017. doi: 10.1002/2017JA024398. URL <https://agupubs.onlinelibrary.wiley.com/doi/abs/10.1002/2017JA024398>. 17
- D. R. Themens, P. T. Jayachandran, D. Bilitza, P. J. Erickson, I. Häggström, M. V. Lyashenko, B. Reid, R. H. Varney, and L. Pustovalova. Topside Electron Density Representations for Middle and High Latitudes: A Topside Parameterization for E-CHAIM Based On the NeQuick. *Journal of Geophysical Research: Space Physics*, 123(2):1603–1617, 2018. doi: 10.1002/2017JA024817. URL <https://agupubs.onlinelibrary.wiley.com/doi/abs/10.1002/2017JA024817>. 17, 121

- J. B. Thomas. An analysis of digital phase-locked loops. *JPL Publication 89-2*, 1998. URL <https://trs.jpl.nasa.gov/bitstream/handle/2014/40039/JPL-PUB-89-2.pdf?sequence=3&isAllowed=y>. xvi, 99, 100, 101, 104
- UCAR. 2020. <https://www.cosmic.ucar.edu/what-we-do/cosmic-2/>, accessed September 17, 2020. xiv, 46
- J. van den IJssel, J. Encarnação, E. Doornbos, and P. Visser. Precise science orbits for the Swarm satellite constellation. *Advances in Space Research*, 56(6):1042 – 1055, 2015. ISSN 0273-1177. doi: 10.1016/j.asr.2015.06.002. URL <http://www.sciencedirect.com/science/article/pii/S0273117715004068>. 43
- J. van den IJssel, B. Forte, and O. Montenbruck. Impact of Swarm GPS receiver updates on POD performance. *Earth, Planets and Space*, 68(1):85, May 2016. ISSN 1880-5981. doi: 10.1186/s40623-016-0459-4. URL <https://doi.org/10.1186/s40623-016-0459-4>. xix, 60, 103
- B. D. Vishwakarma, B. Devaraju, and N. Sneeuw. What is the spatial resolution of grace satellite products for hydrology? *Remote Sensing*, 10(6), 2018. ISSN 2072-4292. doi: 10.3390/rs10060852. URL <https://www.mdpi.com/2072-4292/10/6/852>. 62
- P. W. Ward, J. W. Betz, and C. J. Hegarty. Satellite Signal Acquisition , Tracking , and Data Demodulation. In E. Kaplan and C. Hegarty, editors, *Understanding GPS: Principles and Applications*. Artech, 2006. xix, 100, 105, 106, 107, 110
- J. P. Weiss, D. Hunt, B. Schreiner, T. VanHove, A. Jäggi, and D. Arnold. COSMIC-2 Precise Orbit Determination. *AGU Fall Meeting 2019. San Francisco, CA, USA.*, 2019. doi: 10.7892/boris.143173. 24, 46
- J. A. Whalen. An equatorial bubble: Its evolution observed in relation to bottomside spread F and to the Appleton anomaly. *Journal of Geophysical Research: Space Physics*, 105(A3):5303–5315, 2000. doi: 10.1029/1999JA900441. URL <https://agupubs.onlinelibrary.wiley.com/doi/abs/10.1029/1999JA900441>. 6, 12, 77, 90, 91
- A. Witze. Legendary Arecibo telescope will close forever — scientists are reeling. *Nature*, 587:529–530, 2020. doi: 10.1038/d41586-020-03270-9. URL <https://www.nature.com/articles/d41586-020-03270-9>. 13
- K. T. Woo. Optimum Semicodeless Carrier-Phase Tracking of L2. *NAVIGATION*, 47(2):82–99, 2000. doi: 10.1002/j.2161-4296.2000.tb00204.x. URL <https://onlinelibrary.wiley.com/doi/abs/10.1002/j.2161-4296.2000.tb00204.x>. 23

- M. Wu, X. Xu, F. Li, P. Guo, and N. Fu. Plasmaspheric scale height modeling based on cosmic radio occultation data. *Journal of Atmospheric and Solar-Terrestrial Physics*, 217: 105555, 2021. ISSN 1364-6826. doi: <https://doi.org/10.1016/j.jastp.2021.105555>. URL <https://www.sciencedirect.com/science/article/pii/S1364682621000201>. 127
- S. C. Wu, T. P. Yunck, and C. L. Thornton. Reduced-dynamic technique for precise orbit determination of low earth satellites. *Journal of Guidance, Control, and Dynamics*, 14(1):24–30, 1991. doi: 10.2514/3.20600. URL <https://doi.org/10.2514/3.20600>. 55
- C. Xiong, H. Lühr, S. Y. Ma, C. Stolle, and B. G. Fejer. Features of highly structured equatorial plasma irregularities deduced from CHAMP observations. *Annales Geophysicae*, 30(8): 1259–1269, 2012. doi: 10.5194/angeo-30-1259-2012. URL <https://www.ann-geophys.net/30/1259/2012/>. 92
- C. Xiong, C. Stolle, H. Lühr, J. Park, B. G. Fejer, and G. N. Kervalishvili. Scale analysis of equatorial plasma irregularities derived from Swarm constellation. *Earth, Planets and Space*, 68(1):121, Jul 2016a. ISSN 1880-5981. doi: 10.1186/s40623-016-0502-5. URL <https://doi.org/10.1186/s40623-016-0502-5>. 6
- C. Xiong, C. Stolle, and H. Lühr. The Swarm satellite loss of GPS signal and its relation to ionospheric plasma irregularities. *Space Weather*, 14(8):563–577, 2016b. doi: 10.1002/2016SW001439. URL <https://agupubs.onlinelibrary.wiley.com/doi/abs/10.1002/2016SW001439>. 13, 65, 69, 70, 94
- D. Yuan. GRACE 327-744, Gravity Recovery And Climate Experiment, JPL Level-2 Processing Standards Document. 2018. URL [https://podaac-tools.jpl.nasa.gov/drive/files/GeodeticsGravity/grace/docs/L2-JPL\\_ProcStds\\_v6.0.pdf](https://podaac-tools.jpl.nasa.gov/drive/files/GeodeticsGravity/grace/docs/L2-JPL_ProcStds_v6.0.pdf). 77, 118
- X. Yue, W. S. Schreiner, D. C. Hunt, C. Rocken, and Y.-H. Kuo. Quantitative evaluation of the low Earth orbit satellite based slant total electron content determination. *Space Weather*, 9(9), 2011. doi: 10.1029/2011SW000687. URL <https://agupubs.onlinelibrary.wiley.com/doi/abs/10.1029/2011SW000687>. 35, 37
- N. Zehentner and T. Mayer-Gürr. Mitigation of ionospheric scintillation effects in kinematic LEO precise orbit determination. EGU General Assembly 12. - 17. April 2015, Vienna, 2015. 38, 65, 75
- A. J. Zmuda. Ionization enhancement from Van Allen electrons in the South Atlantic Magnetic Anomaly. *Journal of Geophysical Research (1896-1977)*, 71(7):1911–1917, 1966. doi: 10.1029/JZ071i007p01911. URL <https://agupubs.onlinelibrary.wiley.com/doi/abs/10.1029/JZ071i007p01911>. 6

- J. F. Zumberge, M. B. Heflin, D. C. Jefferson, M. M. Watkins, and F. H. Webb. Precise point positioning for the efficient and robust analysis of GPS data from large networks. *Journal of Geophysical Research: Solid Earth*, 102(B3):5005–5017, 1997. doi: 10.1029/96JB03860. URL <https://agupubs.onlinelibrary.wiley.com/doi/abs/10.1029/96JB03860>. 48



# Publications

**Mitigation of ionospheric signatures in Swarm GPS gravity field estimation using weighting strategies.** L. Schreiter, D. Arnold, V. Sterken, and A. Jäggi. *Annales Geophysicae*, 37(1):111–127, 2019. doi: 10.5194/angeo-37-111-2019. <https://www.ann-geophys.net/37/111/2019/>.

**Bandwidth correction of Swarm GPS carrier phase observations for improved orbit and gravity field determination.** L. Schreiter, O. Montenbruck, F. Zangerl, C. Siemes, D. Arnold, and A. Jäggi. *GPS Solutions*, 25(2):70, Mar 2021. ISSN 1521-1886. doi: 10.1007/s10291-021-01107-0. <https://link.springer.com/article/10.1007/s10291-021-01107-0>.